

**UNIVERSIDADE FEDERAL DO RIO GRANDE DO SUL
INSTITUTO DE GEOCIÊNCIAS
PROGRAMA DE PÓS-GRADUAÇÃO EM GEOCIÊNCIAS**

**EVOLUÇÃO TERMOTECTÔNICA FANEROZOICA DOS
ESCUDOS URUGUAIO E SUL-RIO-GRANDENSE**

JOÃO PACÍFICO SILVEIRA LUIZ MACHADO

ORIENTADORA - Profa. Dra. Andréa Ritter Jelinek

Porto Alegre, 2020

**UNIVERSIDADE FEDERAL DO RIO GRANDE DO SUL
INSTITUTO DE GEOCIÊNCIAS
PROGRAMA DE PÓS-GRADUAÇÃO EM GEOCIÊNCIAS**

**EVOLUÇÃO TERMOTECTÔNICA FANEROZOICA DOS
ESCUDOS URUGUAIO E SUL-RIO-GRANDENSE**

JOÃO PACÍFICO SILVEIRA LUIZ MACHADO

ORIENTADORA - Profa. Dra. Andréa Ritter Jelinek

BANCA EXAMINADORA

Prof. Dr. Mauricio Parra Amézquita - Instituto de Energia e Ambiente, Universidade de São Paulo

Prof. Dr. Felipe Guadagnin - Universidade Federal do Pampa

Prof. Dr. Léo Afraneo Hartmann - Instituto de Geociências, Universidade Federal do Rio Grande do Sul

Tese de Doutorado apresentada como
requisito parcial para a obtenção do
Título de Doutor em Ciências.

Porto Alegre, 2020

CIP - Catalogação na Publicação

Machado, João Pacífico Silveira Luiz
Evolução termotectônica Fanerozoica dos escudos
Uruguaio e Sul-Rio-Grandense / João Pacífico Silveira
Luiz Machado. -- 2020.
246 f.
Orientadora: Andréa Ritter Jelinek.

Tese (Doutorado) -- Universidade Federal do Rio
Grande do Sul, Instituto de Geociências, Programa de
Pós-Graduação em Geociências, Porto Alegre, BR-RS,
2020.

1. termocronologia. 2. escudo. 3. rifte. 4.
Atlântico Sul. 5. sísmica. I. Jelinek, Andréa Ritter,
orient. II. Título.

AGRADECIMENTOS

O processo de pesquisa e desenvolvimento de uma tese é majoritariamente individual, mas dificilmente exitoso se não contar com a colaboração de diversas pessoas e instituições. A todos que de alguma forma me auxiliaram nessa jornada, direta ou indiretamente, obrigado!

Agradeço o suporte da Shell Brasil, dado através do projeto “BG05: UoA-UFRGS-SWB Sedimentary Systems”, a parceria entre a Universidade Federal do Rio Grande do Sul e a University of Aberdeen, o apoio da ANP através de sua regulação de R&D e dados da Bacia de Pelotas, assim como o auxílio do CNPq durante o intercâmbio na University of Aberdeen (SWE 204254/2017). Muitas pessoas estiveram envolvidas nesse projeto, e sou grato a todas, especialmente aos professores Ben Kneller, Karin Goldberg e Juliana Marques, os quais superaram diversos obstáculos na coordenação do projeto nas universidades.

Muito obrigado aos meus orientadores, professora Andréa Jelinek na Universidade Federal do Rio Grande do Sul, e professor Randell Stephenson na University of Aberdeen, os quais abriram muitas portas para o desenvolvimento de minha pesquisa, forneceram valiosas orientações e tornaram-se, além de colegas de pesquisa, amigos. Obrigado também ao professor Peter Reiners e sua equipe do Arizona Radiogenic Helium Dating Laboratory pelas análises (U-Th)/He e assistência na interpretação dos resultados, e ao professor Kerry Gallagher pelo suporte durante a modelagem térmica. Além disso, agradeço ao doutor Marcos Bicca pela parceria no trabalho de campo e discussão dos resultados, assim como a ajuda dos professores Claudio Gaucher e Letícia Chiglino em relação ao trabalho no Uruguai.

Durante o doutorado fui auxiliado por muitos amigos, novos e antigos, nas mais variadas formas e necessidades. Também contei com a colaboração de uma miríade de profissionais e pesquisadores. Com isso em vista, seria uma injustiça listar alguns nomes e esquecer outros por lapso de memória. Portanto eu apenas gostaria de agradecer enormemente a todos que me acompanharam nos últimos anos: obrigado!

Por fim, eu agradeço a minha família, que me apoiou e permitiu que eu seguisse meus sonhos. Muito obrigado!

RESUMO

A margem passiva Sul-Americana foi formada devido à abertura do Oceano Atlântico durante a ruptura do Gondwana Ocidental, no final do Mesozoico. O rifte propagou-se de sul para norte, seguindo estruturas associadas à formação do Gondwana Ocidental no Neoproterozóico, e é vinculado a volumoso magmatismo no Cretáceo Inferior. Através da aplicação de análises termocronológicas de baixa temperatura em rochas do continente e análises sísmicas na bacia oceânica, a presente tese visa aprimorar a compreensão sobre as forças geodinâmicas associadas à ruptura do megacontinente Gondwana, relacionando o resfriamento/soerguimento continental à formação e desenvolvimento da margem. A área de estudo compreende os escudos cristalinos Uruguai e Sul-Rio-Grandense e a Bacia de Pelotas. Análises termocronométricas sugerem temperaturas inferiores a 200 °C nos escudos no início do Paleozoico. A principal fase de resfriamento, associada ao soerguimento e exumação do embasamento continental, precede a abertura do Atlântico na região. Os resultados indicam que desde o Permiano os escudos resfriaram continuamente, alcançando temperaturas abaixo dos 60 °C na transição Jurássico/Cretáceo, imediatamente antes do vulcanismo da Bacia do Paraná e abertura do rifte na região. Isso indica que as amostras analisadas estavam próximas à superfície durante o rifteamento, e sugere que os escudos formavam um alto topográfico regional na época. Análises sísmicas na Bacia de Pelotas indicam baixa deposição siliciclástica e volumoso magmatismo durante o rifteamento. Modelos termocronológicos sugerem um sutil reaquecimento após a abertura do Oceano Atlântico, com amostras alcançando 75 °C no final do Cretáceo/Paleogeno. Isso poderia ser resultado de uma perturbação geotérmica causada pela pluma mantélica Tristão da Cunha e os magmatismos continental e oceânico associados ao rifte, persistentes até o final do Cretáceo nos escudos. O resfriamento final da região tem baixa resolução nos modelos, mas aparenta iniciar-se no Eoceno. Dados da Bacia de Pelotas sugerem um aumento na taxa de sedimentação a partir do Oligoceno, o que pode ser associado ao resfriamento/exumação final dos escudos e subsequente maior disponibilidade sedimentar para a bacia.

Palavras-chave: termocronologia; sísmica; escudo; Atlântico Sul; rifte.

ABSTRACT

The South American passive margin was formed due the West Gondwana breakup, in the late Mesozoic. The rift propagated from south to north, following basement structures that were formed during the assembly of West Gondwana (Neoproterozoic), and is associated to broad magmatism in the early Cretaceous, onshore and offshore. Using low-temperature thermochronometry onshore and seismic analysis offshore, this work aims to improve our comprehension about the geodynamic forces associated with the breakup, linking continental cooling/uplift to the Atlantic marginal basins development. The study area covers the shields in Uruguay and southernmost Brazil, as well as the adjacent and marginal Pelotas Basin. Thermochronometric analysis suggests that the shields reached temperatures below 200°C in the early Palaeozoic. The main cooling event, associated to basement uplift and exhumation, proceeds the South Atlantic opening in the region. The results indicate that since the Permian the shields went through a continuous cooling/uplift, with most of the analysed samples reaching temperatures below 60°C in the Jurassic-Cretaceous transition, immediately before the extrusion of the Paraná-Etendeka Large Igneous Province and rift propagation in the region. This indicates that the samples were near the surface during rifting, and suggests that the region was a topographic high before the opening. Seismic analysis in the Pelotas Basin indicate very limited siliciclastic deposition during rifting and broad magmatism along the forming coast. Inverse models suggest a subtle reheating phase after the South Atlantic opening, rising the shields temperatures up to 75°C in the late Cretaceous/Palaeogene. This can be related to a regional geothermal disturbance caused by the presence of the Tristan da Cunha mantle plume during rifting and the magmatism onshore and offshore, persistent until the late Cretaceous. A final cooling phase of the shields is poorly constrained by the thermochronometric analysis, but appears to start by the Eocene. Seismic analysis in the Pelotas Basin suggest an increase in the sedimentation rates from the Oligocene onwards, which might be linked to the final cooling/exhumation of the shields and subsequent increase of sediment supply to the basin.

Key words: thermochronology; seismic; shield; South Atlantic; rift.

LISTA DE FIGURAS

Figura 1.1: Mapa composto da América do Sul, com área de estudo delimitada pelo polígono vermelho	14
Figura 2.1: Estágios tectônicos da margem brasileira durante o Fanerozóico.....	16
Figura 2.2: Principais blocos crustais e cinturões orogênicos durante a colisão entre a América do Sul e África no Neoproterozóico.....	17
Figura 2.3: Principais fases do Ciclo Brasiliense e eventos colisionais que levaram à formação do Gondwana Ocidental.....	18
Figura 2.4: Extensão geográfica da Província Mantiqueira, com unidades geotectônicas da parte sul da Província.....	20
Figura 2.5: Taxas de espalhamento do Atlântico Sul de acordo com diferentes modelos de reconstrução de placas.....	22
Figura 2.6: Entidades magmáticas ao longo da margem do Atlântico Sul.....	23
Figura 2.7: Abrangência da Bacia do Paraná, destacando o magmatismo da Província Ígnea Paraná-Etendeka e as principais estruturas tectônicas em uma reconstrução pré-drifte.....	25
Figura 2.8: Carta estratigráfica da Bacia do Paraná.....	27
Figura 2.9: Carta estratigráfica da Bacia de Pelotas.....	29
Figura 3.1: Intervalo de temperatura de detecção (ou zona de retenção parcial) de alguns sistemas isotópicos em diferentes minerais.....	33
Figura 3.2: Etapas analíticas do método do detector externo.....	36
Figura 3.3: Materiais para análise de termocronometria	38
Figura 4.1: Interpolação por krigagem de todas as idades centrais de AFT disponíveis para a região.....	42
Figura 4.2: Reconstrução do Atlântico Sul durante o rifte.....	44
Figura 4.3: Reconstrução paleogeográfica do Gondwana Ocidental no final do período Paleozoico.....	46
Figura 4.4: Correlação entre as taxas de sedimentação na Bacia de Pelotas e o padrão médio de resfriamento observado no Batólito de Pelotas, adjacente à área da análise sísmica.....	48

Figura 5.1: Panel with DEM image of the study area in the South 92 Atlantic margin, with schematic boundaries of the Paraná Basin and Rio de La Plata Craton indicated.....	65
Figura 5.2: Simplified geological map of Uruguay with sample locations and new thermochronometry ages.....	67
Figura 5.3: Compilation of AFT data available for the Uruguayan shield and its relations with elevation and distance to the South Atlantic.....	79
Figura 5.4: Compilation of AFT data available for the Uruguayan shield and its relations with mean track lengths.....	81
Figura 5.5: Photomicrographs of apatites showing factors that can affect the (U-Th/He) analysis and cause significant age inaccuracies.....	85
Figura 5.6. Plots of (U-Th/He) corrected ages against effective uranium content (eU).....	89
Figura 5.7: Panel of representative inverse thermal models from Group 1.....	90
Figura 5.8: Mean cooling trajectories of inverse models for samples from Group 1.....	92
Figura 5.9: Mean cooling trajectories of inverse models for samples from Group 2.....	93
Figura 5.10: Chronological chart of cooling phases in the Uruguayan Shield observed in inverse thermal models.....	99
Figura 6.1: Geotectonic and aeromagnetic maps of the study region.....	117
Figura 6.2: Geotectonic map of the SRGS with sample location and thermochronometry ages.....	120
Figura 6.3: Plots of AFT central ages for southernmost Brazil against MTLs uncorrected for their c-axis orientation, and against the distance to the coast.....	130
Figura 6.4: Plot of single crystal AHe corrected ages against eU.....	134
Figura 6.5: Plot of ZHe corrected ages against eU, showing negative correlation for the Pelotas Batholith zircons.....	136
Figura 6.6: Mean cooling trajectory of inverse models for samples from Camaquã Basin, São Gabriel, Taquarembó and Tijucas Terranes, with representative models.....	139
Figura 6.7: Mean cooling trajectory of inverse models from each of Pelotas Batholith, with representative models.....	142
Figura 6.8. Kriging interpolation of the dataset of all AFT central ages available for the SRGS.....	144

Figura 6.9. Chronological chart of cooling phases in the SRGS observed in inverse thermal models.....	147
Figura A1.1: Conjunto de dados no extremo sul do Brasil utilizado para a análise da Bacia de Pelotas	166
Figura A1.2: Tipos de terminações de um refletor sísmico.....	167
Figura A1.3: Seismic line of dip direction located between the Rio Grande Terrace and Rio Grande Cone.....	171
Figura A1.4: Set of maps showing the depth to the top of each seismic unit mapped.....	174
Figura A1.5: Set of isopach maps of the volcano-sedimentary infill of the Pelotas Basin.....	177
Figura A1.6: Panel of representative seismic lines of the Pelotas Basin.....	182

LISTA DE TABELAS

Table 5.1: Details of each location and analysis made in Uruguay.....	73
Table 5.2: Apatite fission track data from the Uruguayan shield.....	78
Table 5.3: Summary of Apatite (U-Th)/He ages and parameters in Uruguay.....	82
Table 5.4: Summary of Zircon (U-Th)/He ages and parameters in Uruguay.....	87
Table 6.1: Details of each location and analysis made in the Sul -Rio-Grandense Shield....	123
Table 6.2: Apatite fission track data from the Sul -Rio-Grandense Shield.....	128
Table 6.3: Summary of AHe ages and parameters in the Sul -Rio-Grandense Shield.....	132
Table 6.4: Summary of ZHe ages and parameters in the Sul -Rio-Grandense Shield.....	135
Table A1.1: Comparative between the different interpretations of the seismic units within the Pelotas Basin.....	170
Table A1.2: Estimates of the extension of each seismic unit mapped in the Pelotas Basin....	180

SUMÁRIO

ESTRUTURA DA TESE.....	10
<i>Capítulo 1 – Introdução.....</i>	11
1.1 Introdução	11
1.2 Objetivos.....	15
<i>Capítulo 2 – Contexto Geológico</i>	16
2.1 Introdução	16
2.2 Formação do Gondwana Ocidental: o Ciclo Brasiliano.....	16
2.3 Ruptura do Gondwana Ocidental: a abertura do Oceano Atlântico Sul	20
2.4 A cobertura vulcana-sedimentar	24
<i>Capítulo 3 – Métodos.....</i>	32
3.1 Introdução	32
3.2 Termocronometria de baixa temperatura.....	32
3.3 Modelagem térmica inversa.....	39
<i>Capítulo 4 – Síntese integradora</i>	41
4.1 Introdução	41
4.2 Termocronologia dos escudos Uruguai e Sul-Rio-Grandense	41
4.3 Integração, conclusões e limitações	45
4.4 Sugestões para pesquisas futuras.....	49
<i>Referências.....</i>	51
<i>Capítulo 5 - Low-temperature thermochronology of the South Atlantic margin along Uruguay and its relation to tectonic events in West Gondwana.....</i>	62
Nota explicativa	62
Abstract.....	62
5.1 Introduction	63
5.2 The Uruguayan Shield	66
5.3 Previous thermochronometry studies in Uruguay	71
5.4 Materials and methods.....	73
5.5 Thermochronometry results	77
5.6 Inverse thermal history modelling.....	89
5.7 Discussion and integration.....	93
5.8 Conclusions	102
5.9. Acknowledgments	102

5.10 References	103
5.11 Email de submissão	114
 <i>Capítulo 6 - West Gondwana orogenies and Pangaea breakup: thermotectonic effects on the southernmost Mantiqueira Province, Brazil.....</i> 115	
Nota explicativa	115
Abstract.....	115
6.1 Introduction	116
6.2 Geological Setting.....	118
6.4 Material and methods	123
6.5 Thermochronometry results	127
6.6 Thermal modelling results.....	136
6.7 Discussion	143
6.8 Conclusions	151
6.9 Acknowledgments	152
6.10 References	152
6.11 Email de publicação	162
 <i>Apêndices.....</i>	164
A1 - Seismostratigraphy of the Pelotas Basin	164
Nota explicativa	164
Abstract.....	164
A1.1 Introduction.....	165
A1.2 Method and Dataset.....	165
A1.3 Seismic units	168
A1.4 Depositional sequences.....	176
A1.5 Discussion	181
A1.6 Summary & Conclusions	184
A1.7 References	185
A2 Uruguay data	187
A2.1 Uruguay radial plots	187
A2.2 Uruguay fission-tracks distribution	192
A2.3 Uruguay inverse models	202
A3 Rio Grande do Sul data	212
A3.1 Rio Grande do Sul radial plots.....	212
A3.2 Rio Grande do Sul fission-tracks distribution	216

A3.3 Rio Grande do Sul inverse models	225
<i>A4 Resumos publicados</i>	234
A4.1 XVI Simpósio Nacional De Estudos Tectônicos	234
A4.2 AGU Fall Meeting 2017	238
A4.3 16th International Conference on Thermochronology	239
A4.4 49º Congresso Brasileiro de Geologia	240
A4.5 EGU General Assembly 2019	241
A4.6 XVII Simpósio Nacional De Estudos Tectônicos	242
A4.7 Goldschmidt 2019	243

ESTRUTURA DA TESE

A presente tese de doutorado está estruturada em torno de dois artigos, estando um publicado no periódico *Journal of the Geological Society*, classificado no estrato Qualis-CAPES A2, e outro submetido e em processo avançado de revisão no periódico *Tectonophysics*, também classificado no estrato Qualis-CAPES A2.

Esta tese é apresentada como resultado de um projeto de cotutela entre a Universidade Federal do Rio Grande do Sul e a University of Aberdeen (UK). Dessa forma, além da orientação, na UFRGS, da Profa. Dra. Andréa Ritter Jelinek, o projeto contou com a orientação do Prof. Dr. Randell Stephenson na University of Aberdeen.

A organização da tese compreende as seguintes partes:

- Texto integrador: composto pelo Capítulo 1) Introdução, com a formulação do problema de investigação, hipóteses e objetivos da pesquisa; Capítulo 2) Contexto geológico da área de estudo; Capítulo 3) Métodos utilizados; Capítulo 4) Síntese integradora, com os principais resultados obtidos, interpretações e conclusões; e Referências do texto integrador.
- Artigos: corpo principal da tese, constituído pelos artigos desenvolvidos durante o doutorado. O Capítulo 6 corresponde ao artigo submetido ao periódico *Tectonophysics*; o Capítulo 7 corresponde ao artigo publicado pelo periódico *Journal of the Geological Society*.
- Apêndices: compreende 1) um manuscrito sobre a Bacia de Pelotas, o qual será aprimorado após a defesa da tese para a sua futura submissão a um periódico internacional; 2) as análises estatísticas das idades (*radial plots*) e distribuição de comprimentos de traços de fissão em apatita; 3) os modelos termocronológicos de cada localidade; e 4) resumos publicados em congressos derivados desse doutorado.

Capítulo 1 – Introdução

1.1 Introdução

A formação da margem Atlântica Sul-Americana ocorreu no Mesozoico em consequência da ruptura do Gondwana Ocidental e desenvolvimento do Oceano Atlântico Sul. Essa margem passiva apresenta uma extensão de mais de 6.000 km e grande variedade de feições geológicas e topográficas de sul a norte (Fig. 1.1). Na Argentina, porção mais meridional da margem, situa-se o montanhoso Terreno Patagônio ao sul, e no nordeste vastas planícies sedimentares. Mais ao norte na margem, o Uruguai apresenta topografia suave e exposições do Cráton do Rio de La Plata e do Cinturão Dom Feliciano, associadas à formação do Gondwana Ocidental durante o Neoproterozóico (Ciclo Orogênico Brasiliense/Pan-Africano, referenciado aqui apenas como Ciclo Brasiliense). No Brasil, a margem mais ao sul é correlata à geologia do Uruguai, as margens sudeste e leste são dominadas por cinturões orogênicos Brasilienses, representados pelos altos topográficos da Província Mantiqueira e, finalmente, a margem nordeste é caracterizada por amplos planaltos e planícies, associados ao Cráton São Francisco e mais cinturões orogênicos Brasilienses. A geodiversidade não se restringe apenas às características continentais ao longo da margem, visto que as bacias oceânicas também apresentam elementos arquiteturais e estratigrafia distintas. A diferença mais notável, provavelmente, é a ausência de depósitos evaporíticos e reservas economicamente viáveis de hidrocarbonetos nas bacias da Argentina, Uruguai e sul do Brasil, enquanto as bacias do sudeste do Brasil (especialmente as bacias de Santos e Campos) compreendem camadas e diápiros de sal que atuam como armadilhas para volumosas reservas de petróleo e gás na plataforma oceânica.

Apesar dessa ampla variedade de características ao longo da costa, tanto *onshore* quanto *offshore*, é possível especificar uma região de mudança significativa na configuração da margem passiva Sul-Americana. Essa área é localizada perto da cidade de Florianópolis, no sul do Brasil, e representa um limite entre a porção sul, de baixa topografia, e a norte, de relevo alto e acidentado (Fig. 1.1). Essa região também marca o limite entre a Bacia de Pelotas, no sul, e a Bacia de Santos, no norte, pobre e rica em reservas de hidrocarbonetos, respectivamente. Além disso, representa uma conexão entre a crosta continental e a Dorsal Mesoatlântica, através da Zona de Fratura do Rio Grande (também conhecida como Zona de Fratura de Florianópolis),

uma estrutura de E-W que se propaga no fundo oceânico e também limita a Elevação de Rio Grande e o Platô de São Paulo, dois altos batimétricos no Oceano Atlântico.

A geodiversidade ao longo da margem passiva da América do Sul tem sido estudada com diversos objetivos e a partir dos mais variados métodos. Uma grande quantidade desses estudos se concentrou na margem sudeste do Brasil, ao norte de Florianópolis, região com alta topografia *onshore* e reservas volumosas de hidrocarbonetos *offshore*. Muitos desses estudos tiveram o objetivo de compreender os processos e fases da abertura do Atlântico Sul, e relacioná-los com o desenvolvimento das altas escarpas da Província Mantiqueira e também com o acúmulo de hidrocarbonetos nas bacias marginais adjacentes (e.g. Gallagher *et al.* 1994, 1995; Saenz *et al.* 2003; Jelinek *et al.* 2003; Hackspacher *et al.* 2007; Hiruma *et al.* 2010; Cogné *et al.* 2011, 2012; Karl *et al.* 2013; Soares *et al.* 2016). Para tal, os métodos comumente aplicados incluem análise sísmica e correlação de poços *offshore*, para avaliar as estruturas e os padrões deposicionais nas bacias costeiras, e a termocronologia de baixa temperatura *onshore*, para estimar o resfriamento, exumação e erosão do continente.

Por outro lado, a região mais ao sul de Florianópolis não despertava maior interesse até recentemente. Os estudos de termocronometria são escassos no extremo sul do Brasil (de Borba *et al.* 2002, 2003; de Oliveira *et al.* 2016), Uruguai (Kollenz 2015; Hueck *et al.* 2017; Gomes & Almeida 2019) e Argentina (Kollenz *et al.* 2017), e o resfriamento do embasamento nessas regiões é pouco conhecido. De qualquer forma, os dados disponíveis sugerem que o resfriamento e a exumação dessa ampla área continental antecedem a ruptura do Gondwana Ocidental e a abertura do Atlântico Sul em até centenas de milhões de anos. Na região *offshore* adjacente ao Uruguai e sul do Brasil, a Bacia de Pelotas possui apenas uma dúzia de poços de exploração e os estudos sísmicos publicados também são escassos, mas sugerem o acúmulo de um espesso pacote sedimentar pós-rifte, composto principalmente por sedimentos de granulometria fina (e.g. Bueno *et al.* 2007; Contreras *et al.* 2010; Beglinger *et al.* 2012; Morales *et al.* 2017). Portanto, devido à carência de dados, o processo de rifteamento e o desenvolvimento da margem na região ainda são motivo de debate. Todavia, a presença de hidratos de gás na Bacia de Pelotas (Miller *et al.* 2015) e os primeiros resultados de estudos termocronométricos na última década aumentaram o interesse na área.

O presente estudo foi proposto com o intuito de expandir nossa compreensão sobre a evolução do rifte no Uruguai e sul do Brasil (Fig. 1.1). O objetivo inicial inclui

elucidar os efeitos termotectônicos da ruptura do Gondwana Ocidental e do magmatismo associado, assim como o desenvolvimento da Bacia de Pelotas. Compreender a evolução da margem continental nesta região não é apenas essencial para o entendimento da geodinâmica de ruptura do Gondwana Ocidental e da propagação do rifte para o norte, mas também tem implicações diretas para a indústria de petróleo e gás natural.

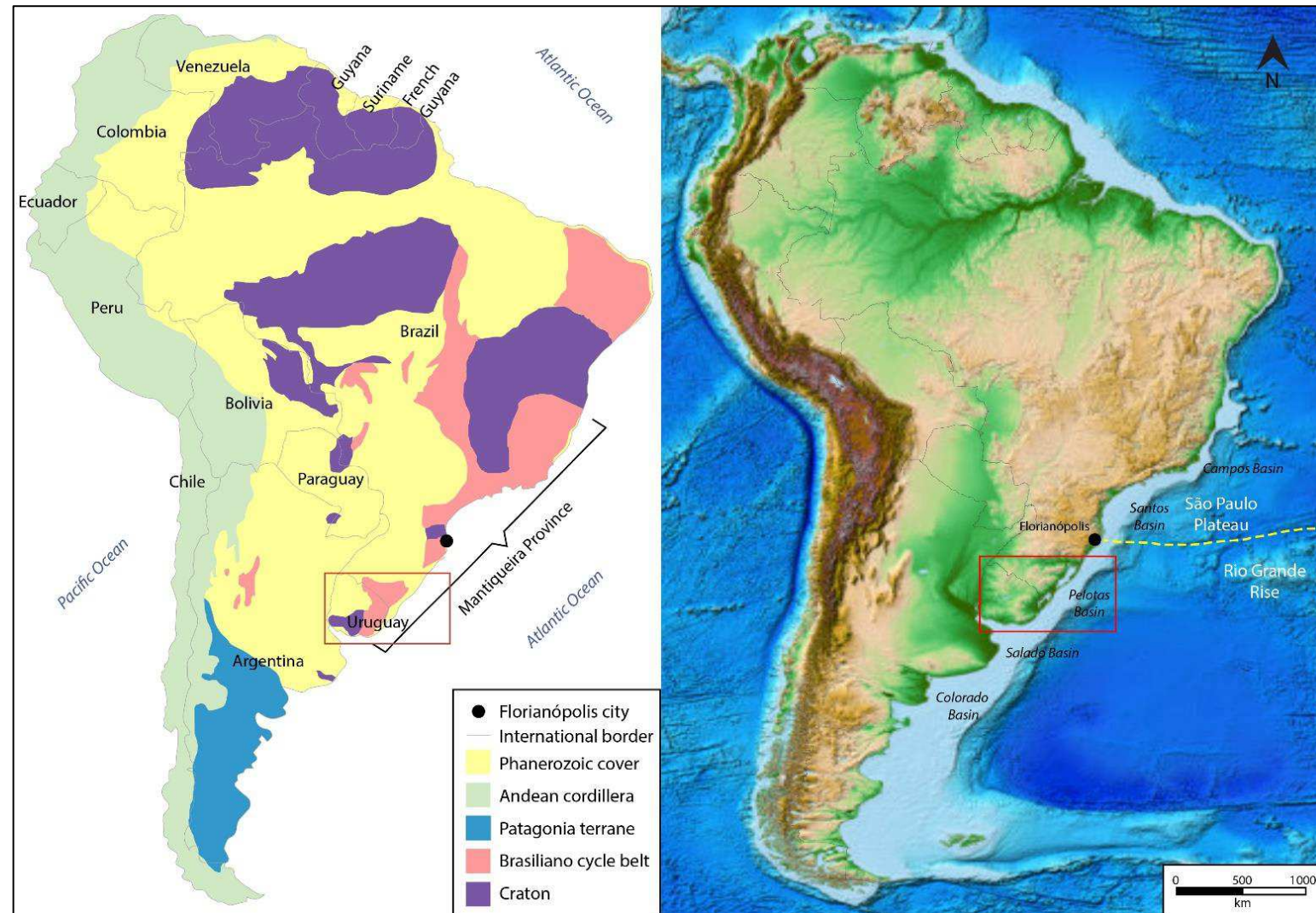


Figura 1.1: Mapa composto da América do Sul, com área de estudo delimitada pelo polígono vermelho. À esquerda, os principais domínios geológicos e, à direita, a topografia e as bacias marginais adjacentes ao estudo, com a Zona de Fratura do Rio Grande indicada pela linha amarela tracejada. Mapas detalhados da região de estudo são encontrados nos capítulos 2, 5 e 6. Modificado a partir de Hartmann et al. (2001) e Amante & Eakins (2009).

1.2 Objetivos

O principal objetivo do presente estudo é melhorar nossa compreensão sobre a margem passiva Sul-Americana, desde a sua formação até os dias atuais. Especificamente, a investigação se concentra na evolução termotectônica das rochas do embasamento na região ao sul de Florianópolis, no extremo sul do Brasil, estendendo-se até o Uruguai (Fig. 1.1). Visto que os trabalhos publicados na região (de Borba *et al.* 2002, 2003; Kollenz 2015; de Oliveira *et al.* 2016; Hueck *et al.* 2017; Gomes & Almeida 2019) sugerem resfriamento/exumação anterior ao rifte do Oceano Atlântico Sul, este projeto busca melhor identificar o início, as causas e a duração desse comportamento termotectônico. Além disso, idealmente, o projeto visa apoiar a equação entre a exumação e erosão do continente e o preenchimento da Bacia de Pelotas, em um modelo *source to sink*.

A hipótese central é que os dados termocronométricos continentais permitem determinar o resfriamento das rochas do embasamento e, consequentemente, o padrão de exumação e erosão deste nas fases pré-, sin- e pós-rifte. Esses resultados podem ser correlacionados com os processos geodinâmicos no Gondwana Ocidental e a abertura do Oceano Atlântico Sul, assim como com o acúmulo de sedimentos na bacia *offshore*, que por sua vez é analisada usando dados sísmicos e de poço.

Considerando a ideia descrita acima, esta tese foi desenvolvida com as seguintes linhas específicas de pesquisa:

- Estimar as fases de soerguimento e a exumação dos embasamentos Uruguai e do extremo sul do Brasil, usando uma abordagem de multi-termocronômetros;
- Determinar os efeitos térmicos do rifte do Atlântico Sul e magmatismo associado no embasamento da região;
- Definir a arquitetura da Bacia de Pelotas, taxas de deposição e evolução de depocentros, utilizando informações de sísmica 2D e poços;
- Associar o soerguimento e a erosão do embasamento continental ao desenvolvimento e preenchimento da Bacia de Pelotas, vinculando a geodinâmica do rompimento do Gondwana Ocidental e a propagação do rifte à evolução da margem passiva Sul-Americana.

Capítulo 2 – Contexto Geológico

2.1 Introdução

A investigação aqui apresentada focou na porção sul da margem passiva Sul-Americana. Este capítulo apresenta uma breve revisão da origem da margem passiva e dos eventos tectonomagnéticos que levaram à formação do embasamento na região de estudo. A cobertura vulcâno-sedimentar também é aqui apresentada. Descrições detalhadas dos terrenos tectonoestratigráficos mais relevantes para este estudo são fornecidas nos capítulos 5 e 6.

Os principais estágios evolutivos da margem Sul-Americana durante o Fanerozóico, com foco na porção sudeste da costa, estão resumidos na Figura 2.1, após Carneiro *et al.* (2012). O Ciclo Brasiliano (Neoproterozóico a Cambriano) e a abertura do Atlântico Sul (Mesozoico) são os dois eventos em escala de tectônica de placa responsáveis pela maioria das características geológicas na região, e são discutidos abaixo.

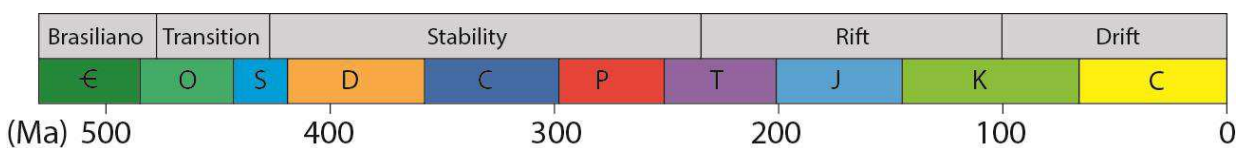


Figura 2.1: Estágios tectônicos da margem brasileira durante o Fanerozóico.

2.2 Formação do Gondwana Ocidental: o Ciclo Brasiliano

Embora a configuração atual da margem passiva da América do Sul seja uma consequência direta da ruptura do Gondwana Ocidental e do subsequente desenvolvimento do Oceano Atlântico Sul, a maioria das estruturas e características geológicas presentes ao longo da margem são derivadas da formação do megacontinente Gondwana durante o Ciclo Brasiliano (Neoproterozóico a Cambriano) (Cordani *et al.* 1968, de Almeida *et al.* 1981; de Almeida & Hasui 1984). Esse prolongado ciclo orogênico envolveu o fechamento de oceanos, convergência de cratons e colisões de vários microcontinentes e arcos vulcânicos, o que levou à união final dos continentes da América do Sul e África (Fig. 2.2) (Santos *et al.* 2017; de Brito Neves *et al.* 2014; Oriolo *et al.* 2017). Portanto, o Ciclo Brasiliano representa um período de eventos diacrônicos ao longo das duas margens continentais e que, de acordo com Hasui (2010), pode ser dividido em três fases principais de convergência, resumidas abaixo (Fig 2.3):

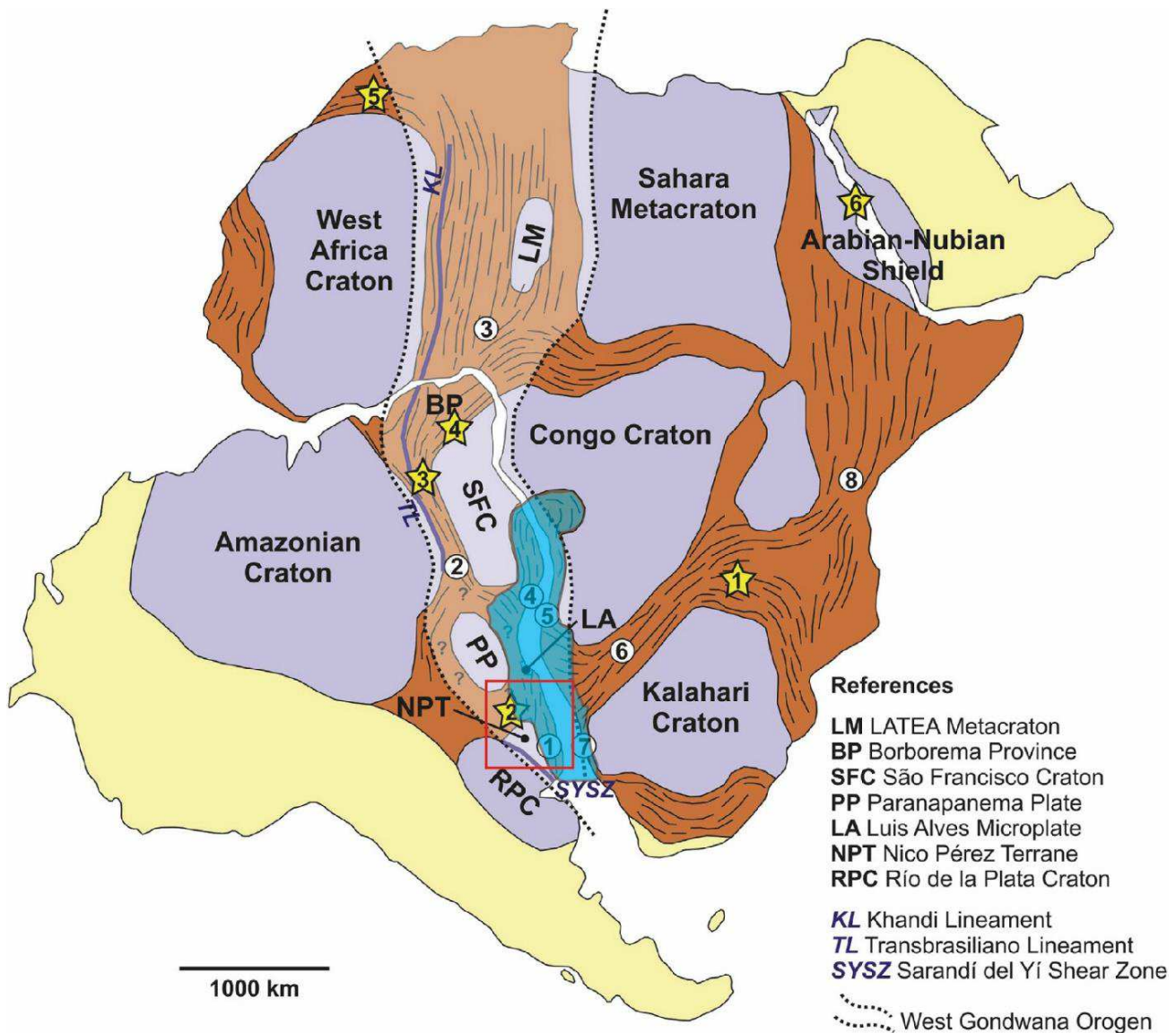


Figura 2.2: Principais blocos crustais e cinturões orogênicos durante a colisão entre a América do Sul e a África no Neoproterozóico. A região em tom cinza claro representa a principal zona afetada pelo Ciclo Brasiliense, enquanto o tom azul indica a província Mantiqueira e a caixa vermelha marca a área de estudo. Os pontos brancos rotulam os cinturões Brasilianos/Pan-Africanos (1 - Dom Feliciano, 2 - Brasília, 3-Dahomey, 4-Ribeira, 5-Kaoko, 6-Damara, 7-Gariep, 8-Leste-Africano-Antártico) e as estrelas amarelas representam ofiolitos ou complexos de arco de ilhas (1 - Zambezi, 2 - São Gabriel, 3 - Araguaia, 4 - Borborema, 5 - Anti-Atlas, 6 - Arábico-Núbia). Extraído de Oriolo et al. (2017).

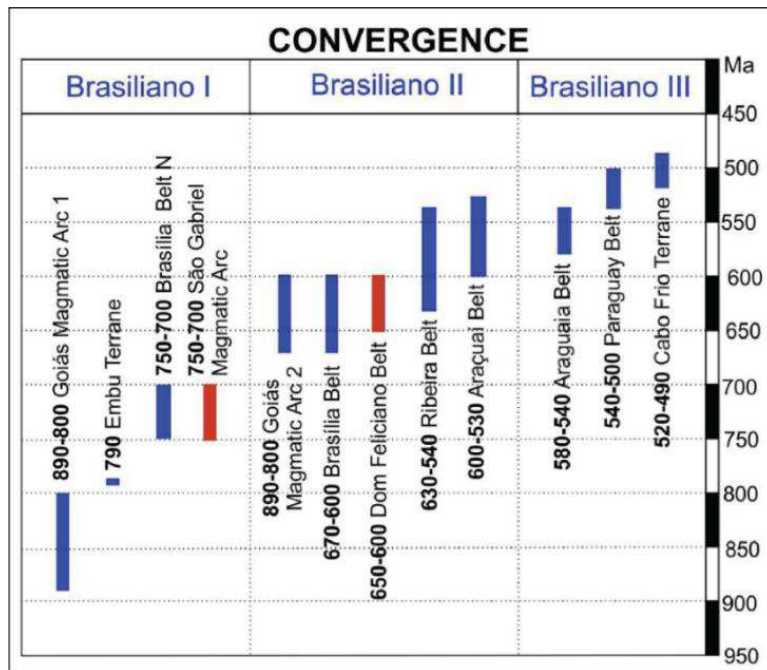


Figura 2.3: Principais fases do Ciclo Brasiliano e eventos colisionais que levaram à formação do Gondwana Ocidental. Eventos marcados em vermelho são responsáveis pela formação da região de estudo. A partir de Hasui (2010).

Fase 1) Brasiliano I (900-700 Ma): com exposições limitadas e esparsas, é reconhecido principalmente no Cinturão de Brasília e no Terreno São Gabriel, no estado do Rio Grande do Sul. O Terreno São Gabriel representa um evento de colisão que envolveu arcos vulcânicos e o Cráton de La Plata, e iniciou a formação da área de estudo (Figs. 2.2 e 2.4).

Fase 2) Brasiliano II (670-530 Ma): principal fase colisional do ciclo orogênico, é registrada em toda a margem brasileira e foi responsável pelas principais estruturas presentes ao longo da costa. Inclui as colisões entre os cráticos Paranapanema, São Francisco, Congo, Kalahari e Rio de La Plata. O cinturão Dom Feliciano, uma importante entidade tectônica na região de estudo (Figs. 2.2 e 2.4) foi formado durante esta fase.

Fase 3) Brasiliano III (580-490 Ma): etapa final do ciclo orogênico, representa a convergência do Cráton Amazônico, bem como alguns eventos tectônicos no Cinturão Ribeira. Essa fase envolve o fechamento tardio de bacias de retro-arco e ainda é motivo de debate no meio acadêmico.

Naturalmente, o Ciclo Brasiliano levou à formação de cinturões orogênicos, cordilheiras, metamorfismo regional e magmatismo generalizado nas margens Sul-Americana e Africana (de Almeida *et al.* 1981; Basei *et al.* 2010). Apesar das frequentes mudanças nos campos de tensão durante as colisões diacrônicas entre os diferentes blocos crustais, as estruturas formadas ao longo da margem sudeste da

América do Sul geralmente apresentam direção NE-SW, incluindo falhas de empurrao e zonas de cisalhamento de deformação dúctil e rúptil (de Almeida *et al.*, 1981; Hasui 2010). Grande parte da margem passiva Sul-Americana é domínio da Província Mantiqueira (Figs. 1.1 e 2.2), que representa um extenso cinturão desenvolvido principalmente durante o Brasiliano II, como resultado da convergência entre os cráticos Paranapanema, São Francisco, Congo, Kalahari e Rio de La Plata.

A Província Mantiqueira inclui três cinturões orogênicos e é a principal entidade tectônica ao longo da margem brasileira, com extensão de mais de 3.000 km, largura entre 200 e 600 km e topografia quase que inteiramente montanhosa (Fig. 1.1) (de Almeida *et al.* 1981; Basei *et al.* 2010; Hasui 2010; de Brito Neves *et al.* 2014). De sul a norte, a Província Mantiqueira compreende os cinturões Dom Feliciano, Ribeira e Araçuaí. Esses cinturões são compostos principalmente por rochas metamórficas e ígneas pré-Silurianas de alto grau. Eles registram eventos geotectônicos que datam até o Arqueano, mas esses cinturões passaram por intensas transformações durante o Ciclo Brasiliano (de Almeida *et al.* 1981; Hasui 2010, 2012). A parte mais meridional da Província Mantiqueira, ou seja, o cinturão Dom Feliciano, juntamente com o cráton Rio de La Plata correspondem à região investigada neste trabalho (Fig. 2.4).

No Uruguai, as exposições do embasamento cristalino composto pelo cinturão e pelo cráton supracitados são chamadas coletivamente de Escudo Uruguaio (UYS), enquanto no Brasil são conhecidas como Escudo Sul-Rio-Grandense (SRGS), em referência ao estado do Rio Grande do Sul. A geologia desses escudos é detalhada nos capítulos 5 e 6, mas em resumo, e a partir de Heilbron *et al.* (2004) e Hasui (2012), as unidades aflorantes na região podem ser organizadas cronologicamente da seguinte maneira:

- Arqueano: restritas exposições de complexos metamórficos de alto grau, principalmente no Terreno Nico Pérez;
- Paleoproterozóico: complexos metamórficos e ígneos do Cráton Rio de La Plata e exposições mais limitadas nos terrenos Nico Pérez e Tijucas, bem como no norte do batólito de Pelotas;
- Mesoproterozóico: alguns poucos granitos e anortositos característicos de condições intraplaca, localizados no Terreno Nico Pérez e Batólito Pelotas;
- Neoproterozóico ao Ordoviciano (Ciclo Brasiliano): amplo magmatismo e metamorfismo nas unidades do cinturão Dom Feliciano, bem como no Terreno Nico Pérez.

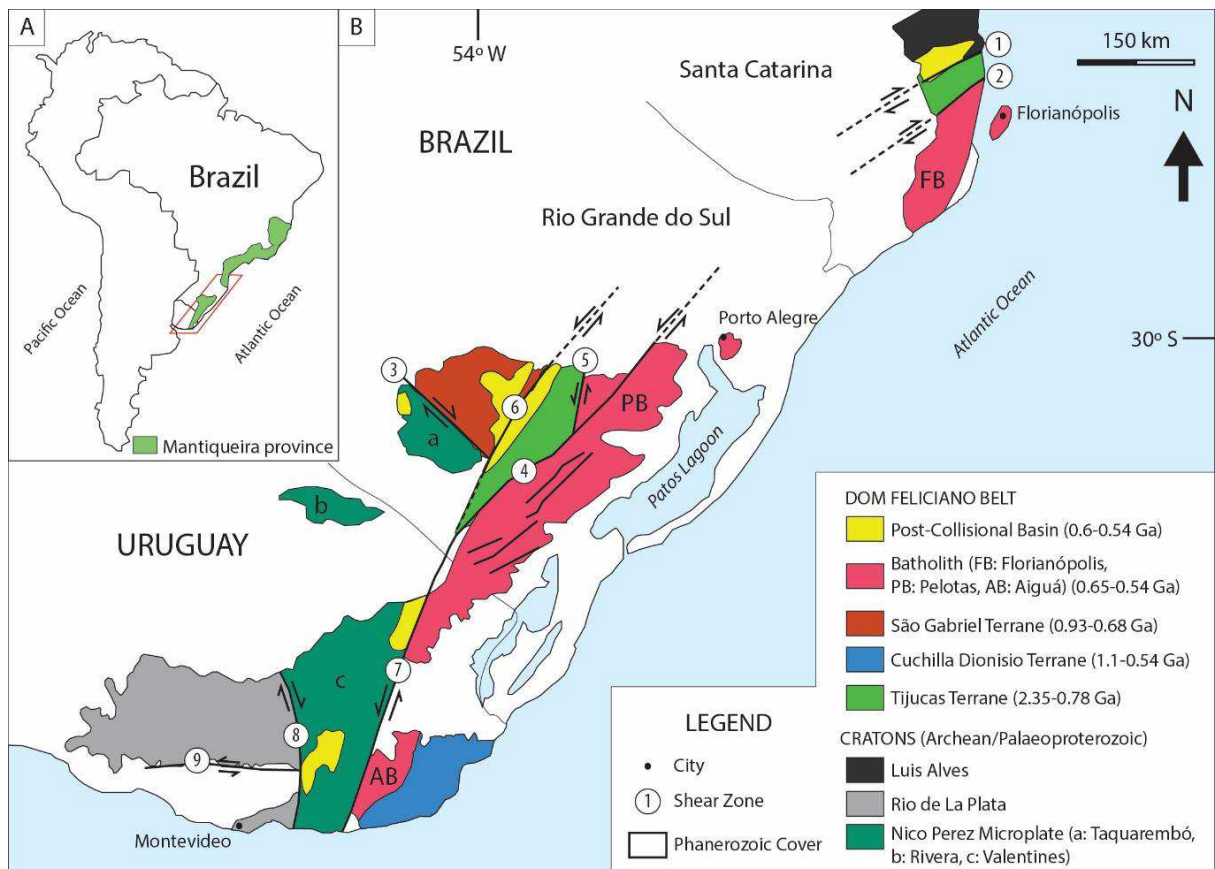


Figura 2.4: A) Extensão geográfica da Província Mantiqueira, com B) unidades geotectônicas da parte sul da Província. Principais falhas e zonas de cisalhamento: 1) Itajaí-Perimbó, 2) Major Gercino, 3) Ibaré, 4) Dorsal de Canguçu, 5) Passo do Marinheiro, 6) Caçapava, 7) Serra Ballena, 8) Sarandí del Yí, 9) Colônia. Modificado após Chemale (2000) e Philipp et al. (2013).

Após o Ordoviciano e a aglutinação final do Gondwana Ocidental, a região estudada passou por uma fase de estabilidade tectônica que durou a maior parte do Paleozoico, a qual foi dominada por intemperismo e erosão e correlacionada com o desenvolvimento da Bacia do Paraná, de natureza intracontinental (Milani & Ramos 1998; Hackspacher *et al.* 2004; Hasui 2010). Esse estágio de estabilidade durou até o Triássico, quando o início da ruptura do Gondwana Ocidental causou estiramento crustal e reativou estruturas do embasamento. No início do Mesozoico, a margem Sul-Americana passou por um processo de soerguimento geral associado ao rifteamento e ao desenvolvimento do Oceano Atlântico Sul (Carneiro *et al.* 2012).

2.3 Ruptura do Gondwana Ocidental: a abertura do Oceano Atlântico Sul

Um dos primeiros registros do fim do estágio de estabilidade tectônica da placa Sul-Americana é o início da atividade ígnea durante o Triássico Médio no noroeste da Bacia do Paraná, onde complexos alcalinos intrusivos e extrusivos de idade $^{40}\text{Ar} / {^{39}\text{Ar}}$ em biotita de 241 ± 1 Ma são associados à reativação de antigas estruturas regionais

(Comin-Chiaramonti *et al.* 2005; de Almeida *et al.* 2012). No entanto, o rifte do Gondwana Ocidental foi desenvolvido ao leste da Bacia do Paraná, e somente após o Triássico. O rompimento continental entre a América do Sul e África foi diacrônico, com a abertura do Atlântico Sul iniciando-se na Argentina durante o Jurássico e propagando-se para o norte no Mesozoico (Mizusaki *et al.* 1988; Stica *et al.* 2014). O rifte seguiu uma tendência geral para NNE, de acordo com lineamentos do embasamento e zonas de fraqueza litosférica formadas durante o Ciclo Brasiliano (Chang *et al.* 1992; Mohriak *et al.* 2008; Buiter & Torsvik 2014; Will & Frimmel 2018).

A ruptura do Gondwana Ocidental é marcada por volumosa atividade ígnea na Bacia do Paraná e nas bacias marginais em formação (por exemplo, bacias de Pelotas, Santos e Campos), onde o vulcanismo precedeu ou foi concomitante à abertura do Atlântico Sul (Mohriak 2012). As causas e os mecanismos atuantes durante o rifte permanecem em debate, mas há um consenso geral de que a dinâmica do manto está envolvida na quebra do megacontinente. O início do rifte é frequentemente relacionado à presença da pluma mantélica Tristão da Cunha, cujo posicionamento inicial sob a placa Sul-Americana provavelmente está ligado ao magmatismo Paraná-Etendeka *Large Igneous Province* (LIP), por volta de 132 Ma (Chang *et al.* 1992; Brown *et al.* 2000; Pérez-Díaz & Eagles 2014; Buiter & Torsvik 2014).

Durante o rifteamento a margem Sul-Americana foi hiperextendida, com significativo adelgaçamento da crosta e exumação da litosfera devido à influência da pluma mantélica, o que provocou a elevação topográfica da margem até a ruptura final (Aslanian *et al.* 2009; Mohriak 2012). A ruptura entre os continentes também envolveu “saltos” do rifte para leste, e provavelmente é responsável pela geração da Elevação de Rio Grande (Fig. 1.1), um controverso fragmento continental cercado por crosta oceânica (Nurnberg & Muller 1991; Mohriak *et al.* 2010; Graça *et al.* 2019). O movimento para noroeste da placa Sul-Americana e a expansão da crosta oceânica são marcados por um lineamento NW-SE de elevações batimétricas ao longo do fundo oceânico (Fig. 2.6), o qual conecta a crosta continental à Elevação de Rio Grande e à cordilheira Mesoatlântica, e provavelmente é o resultado da litosfera passando sobre a pluma mantélica (Brown *et al.* 2000; Graça *et al.* 2019).

Com base em diferentes métodos, vários modelos foram propostos para movimentação das placas e taxas de abertura durante e após o rompimento do Gondwana Ocidental, alguns dos quais foram resumidos por Colli *et al.* (2014) e são apresentados na Figura 2.5. Os modelos, oriundos de estudos independentes,

concordam com um aumento da velocidade de abertura durante a transição Jurássico Superior/Cretáceo Inferior. A maioria dos estudos sugere um aumento contínuo, mas não linear, da taxa de abertura durante o Cretáceo, seguido por um período de velocidade alta e constante e, em seguida, uma diminuição de volta a uma taxa mínima no limite Cretáceo/Paleogeno. Mais recentemente, modelos numéricos de Brune *et al.* (2016) sugerem uma fase inicial de lenta ruptura, iniciada durante a transição Jurássico/Cretáceo (145 a 126 Ma), seguida por um aumento abrupto da velocidade de divergência de placas no início do Cretáceo (126 a 120 Ma) e uma subsequente fase de rápida abertura durante o Cretáceo. Anomalias magnéticas também indicam um aumento nas taxas de abertura do oceano no Cretáceo Inferior (~ 120 Ma), com uma queda acentuada em torno de 80 Ma (Granot & Dyment 2015). A expansão do fundo oceânico na região adjacente ao Uruguai teve início em torno de 127 Ma, enquanto na área de Florianópolis a geração de crosta oceânica foi iniciada apenas em torno do limite Aptiano/Albiano (113 Ma) (Chang *et al.* 1992; Stica *et al.* 2014). Portanto, na região de interesse, a taxa de abertura manteve um alta taxa por cerca de 30 Ma após a separação entre as placas da América do Sul e da África (~ 110 Ma) (Nürnberg & Müller 1991; Granot & Dyment 2015). A causa das mudanças nas taxas de abertura ainda não é clara, mas possivelmente foi causada por diferenças de pressão e fluxo instável da astenosfera durante a ruptura (Colli *et al.* 2014).

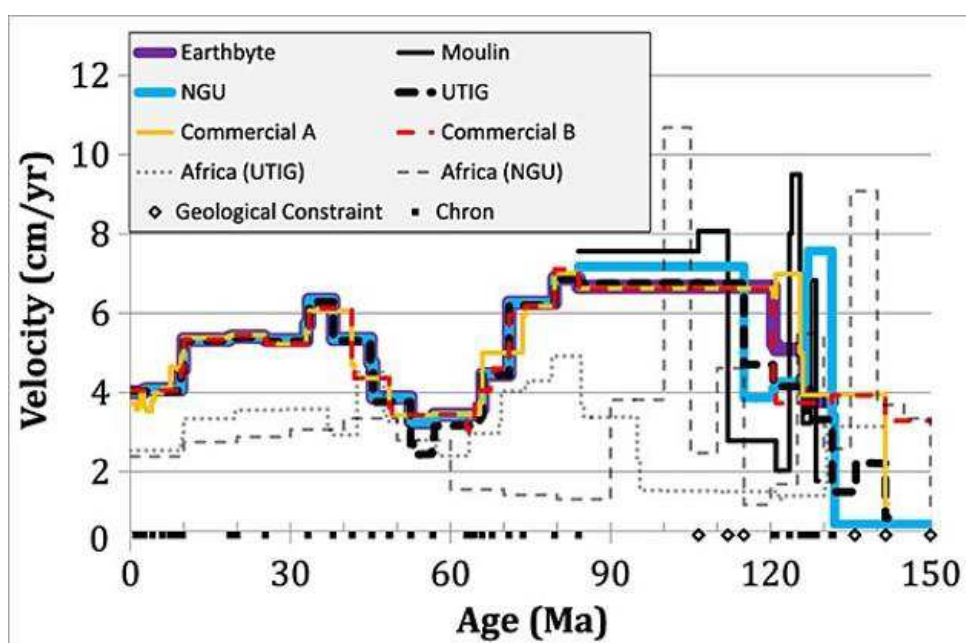


Figura 2.5: Taxas de espalhamento do Atlântico Sul de acordo com diferentes modelos de reconstrução de placas. Observe a variabilidade dos modelos entre 150 e 110 Ma, e subsequente semelhança. As taxas diminuem após 80 Ma, alcançando um mínimo no Paleoceno. Extraído de Colli *et al.* (2014).

Ao longo da margem estudada, o processo de ruptura do megacontinente Gondwana pode ser classificado como de um rifte ativo, com 1) espessas cunhas de refletores mergulhantes ao mar (*seaward-dipping reflectors*, ou SDRs) que marcam o vulcanismo concomitante à divergência das placas, 2) uma zona de alta velocidade na base da crosta e 3) uma anomalia gravitacional positiva paralela à costa (Mohriak *et al.* 2008; Soto *et al.* 2011; Morales *et al.* 2017; McDermott *et al.* 2019). A área de estudo está localizada entre dois grandes corpos magmáticos (Fig. 2.6): ao norte e oeste, os volumosos depósitos vulcânicos da Paraná-Etendeka LIP, e ao leste e sudeste as espessas cunhas dos SDRs (Gladchenko *et al.* 1997). Além disso, pesquisas de sensoriamento remoto revelaram um enxame de diques no sul do Brasil, o que provavelmente está relacionado ao evento da LIP (Hartmann *et al.* 2016). O magmatismo continuou até o Campaniano, com o posicionamento de *plugs* fonolíticos no sul do Brasil (entre 99 e 76 Ma) (Barbieri *et al.* 1987) e riolitos subalcalinos no Uruguai (77 ± 1 Ma) (Gaucher *et al.* 2016). Dessa forma, a área investigada foi diretamente afetada pelo magmatismo antes e depois da ruptura, sendo exposta aos efeitos térmicos desses eventos por alguns milhões de anos.

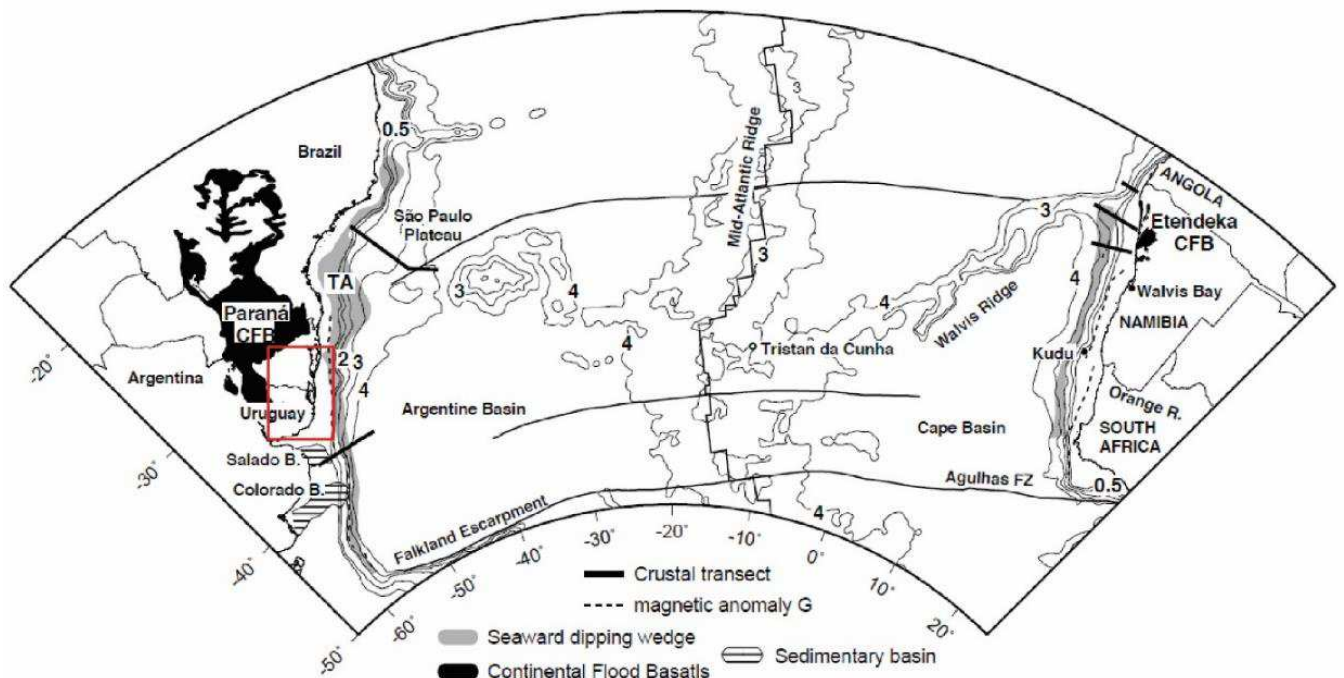


Figura 2.6: Entidades magmáticas ao longo da margem do Atlântico Sul. A caixa vermelha marca a região do estudo, e números a batimetria. Observe o alinhamento NW-SE das elevações do fundo do mar, marcando o movimento das placas continentais sobre a pluma mantélica de Tristão da Cunha. CFB, basaltos continentais (ou LIP); TA, Arco de Torres. Extraído de Gladchenko *et al.* (1997).

2.4 A cobertura vulcano-sedimentar

As exposições do embasamento Uruguaio e Sul-Rio-Grandense são limitadas à norte e oeste principalmente pelos depósitos Paleozoicos e Mesozoicos da Bacia do Paraná. Já a margem Atlântica na região é domínio da Bacia de Pelotas (Meso-Cenozóica), formada como consequência da separação da América do Sul e África. O evento de ruptura também está relacionado à formação de outras duas bacias menores no Uruguai. Remanescentes de outras bacias, de idade Paleozoica, recobrem também pequenas porções de ambos os escudos.

2.4.1 A Bacia do Paraná

A principal bacia na área de estudo é a Bacia do Paraná, uma ampla bacia intracontinental que se espalha pela Argentina, Brasil, Paraguai e Uruguai (Fig. 2.7); e que foi desenvolvida no interior de Gondwana Ocidental durante o Paleozoico e o Mesozoico. O registro vulcano-sedimentar da Bacia do Paraná atinge uma espessura máxima de cerca de 6.000 m, e a natureza do seu embasamento ainda está em debate (Pereira *et al.* 2012). O pacote deposicional desta bacia é dividido em seis supersequências separadas por discordâncias inter-regionais (Fig. 2.8): Rio Ivaí (Ordoviciano a Siluriano), Paraná (Devoniano), Gondwana I (Carbonífero Superior a Triássico Inferior), Gondwana II (Triássico Médio a Superior), Gondwana III (Jurássico ao Cretáceo Inferior) e Bauru (Cretáceo Superior) (Milani 1997; Milani *et al.* 2007). As três primeiras supersequências estão relacionadas a ciclos transgressivo-regressivos, enquanto as três últimas compreendem depósitos sedimentares e vulcânicos continentais (Milani *et al.* 2007).

Na região de interesse afloram unidades das supersequências Paraná a Gondwana III. Esta última foi depositada imediatamente antes da ruptura do Gondwana Ocidental e compreende a Formação Botucatu, caracterizada por arenitos eólicos (Scherer 2000), e a Formação Serra Geral (Fig. 2.7), que é essencialmente uma sequência basáltica que cobre o paleodeserto de Botucatu. A Formação Serra Geral se estende por mais de 1 milhão de km² e pode atingir uma espessura de mais de 1.500 m, sendo relacionada ao vulcanismo da Paraná-Etendeka LIP (Ponte & Asmus 2004). Os fluxos de lava da Formação Serra Geral são sub-horizontais, com mergulho <10 ° para o centro da bacia (NNW), e estão associados a vários enxames de diques ao longo das margens brasileira e africana (Pereira *et al.* 2012).

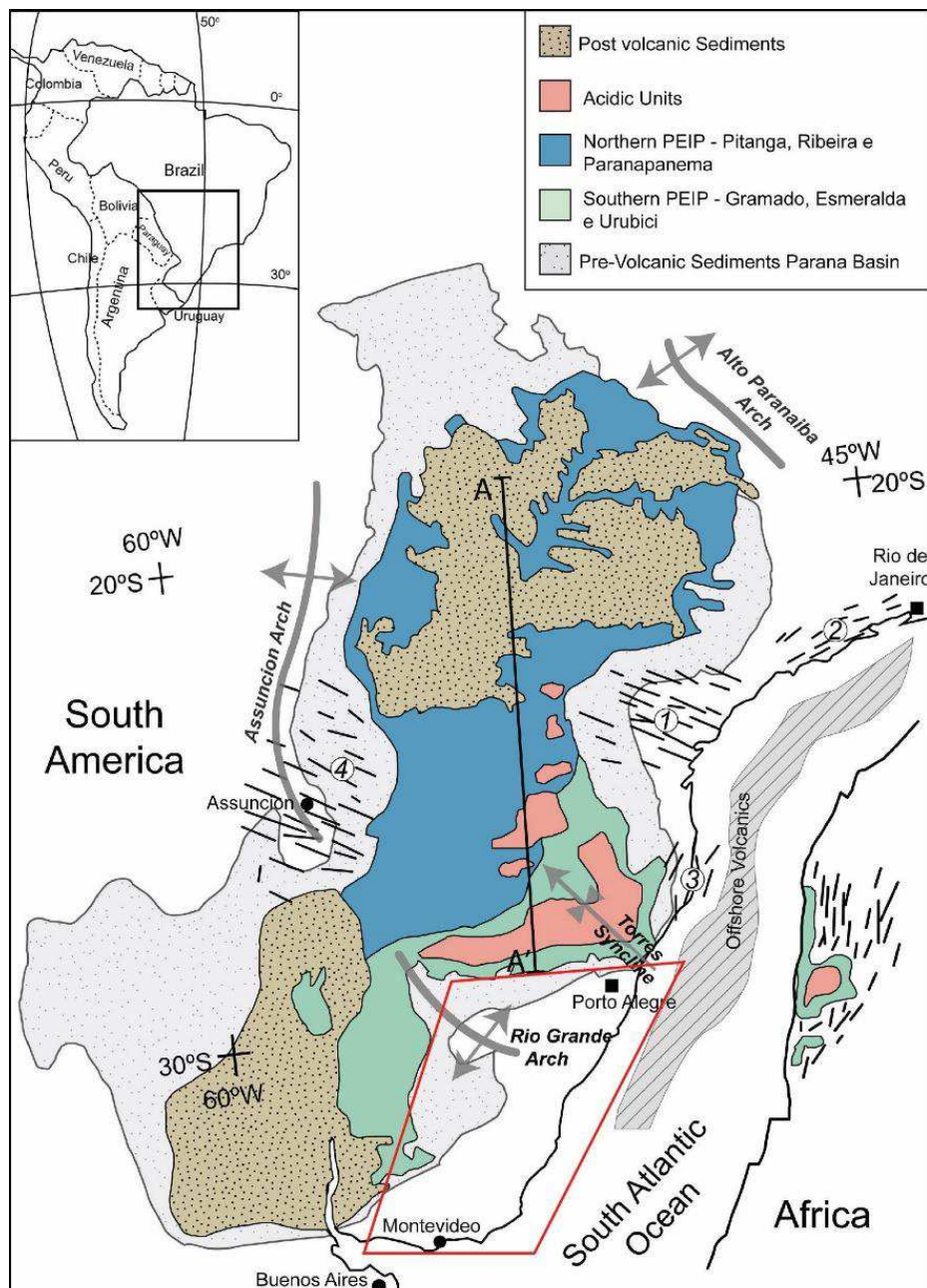


Figura 2.7: Abrangência da Bacia do Paraná, destacando o magmatismo da Província Ígnea Paraná-Etendeka (PEIP) e as principais estruturas tectônicas em uma reconstrução pré-drifte. O polígono vermelho marca a região do estudo. Enxames principais de diques: 1- Ponta Grossa; 2- Santos-Rio de Janeiro; 3- Florianópolis; 4- Paraguai. Os diques no Rio Grande do Sul são mostrados na Figura 6.1. Extraído de Rossetti (2018).

No Uruguai, a Bacia do Paraná, conhecida localmente como Bacia do Norte, é representada por depósitos que cobrem a maior parte do noroeste do país e que estão associados às supersequências Paraná a Gondwana III, atingindo uma espessura máxima entre 2.300 e 3.000 m (de Santa Ana *et al.* 2006). Os depósitos mais antigos e inferiores aflorantes na região correspondem ao Grupo Durazno, que ocorre na margem SE da bacia e é relacionado à Supersequência Paraná. Este grupo

compreende uma sequência transgressiva-regressiva de depósitos continentais a marinhos rasos, com paleocorrentes para o noroeste e proveniência siliciclástica dos próprios terrenos uruguaios, sendo depositadas dentro de um regime de subsidência extensional (Sprechmann *et al.* 1993; Uriz *et al.* 2016). Separada por uma discordância, a sobrejacente Supersequência Gondwana I também representa um ciclo transgressivo-regressivo. Ela compreende depósitos do Carbonífero tardio ao Permiano que registram a transição de ambientes glaciolacustrinos a marinho e, por fim, depósitos fluviais e eólicos (de Santa Ana *et al.* 2006; Beri *et al.* 2011). As exposições do Gondwana II são escassas no Uruguai e correspondem a depósitos finos (<50 m) de amplos sistemas aluviais com paleocorrentes leste-nordeste, desenvolvidas em uma planície de baixo gradiente (Zerfass *et al.* 2004). Por último, em discordância com as unidades inferiores, encontram-se os depósitos continentais da Supersequência Gondwana III, que compreendem formações fluviais e eólicas cobertas pelos fluxos basálticos da Paraná-Etendeka LIP (Sprechmann *et al.* 1981), cujo vulcanismo atingiu o pico em c. 133 Ma e está relacionada à pluma mantélica Tristão da Cunha e à abertura do Atlântico Sul (Turner *et al.* 1994; Rossetti *et al.* 2014; Cernuschi *et al.* 2015).

No extremo sul do Brasil, circundando o Escudo Sul-Rio-Grandense, estão expostas unidades das supersequências Gondwana I, II e III, com características semelhantes às encontradas no Uruguai e paleocorrentes principalmente para o noroeste. A Supersequência Gondwana II é mais expressiva aqui do que no Uruguai, com depósitos fluviais e lacustres rasos associados a grabens dentro do Escudo Sul-Rio-Grandense e com evidências de deposição intermitente (Zerfass *et al.* 2004). O Gondwana III é a sequência mais proeminente da região, cobrindo o oeste e o norte do estado do Rio Grande do Sul, onde estão situados depósitos vulcânicos espessos (mais de 500 m) da Paraná-Etendeka LIP (Turner *et al.* 1994; Renne *et al.* 1996 ; Florisbal *et al.* 2014; Rossetti *et al.* 2014). Dados aeromagnéticos (CPRM 2010) revelam um sistema de diques com direção WNW-ESE no Escudo, e que seriam alimentadores da Paraná-Etendeka LIP (Fig. 6.1), indicando que o SRGS foi diretamente afetado pelo magmatismo da Supersequência Gondwana III no Cretáceo Inferior (Hartmann *et al.* 2016).

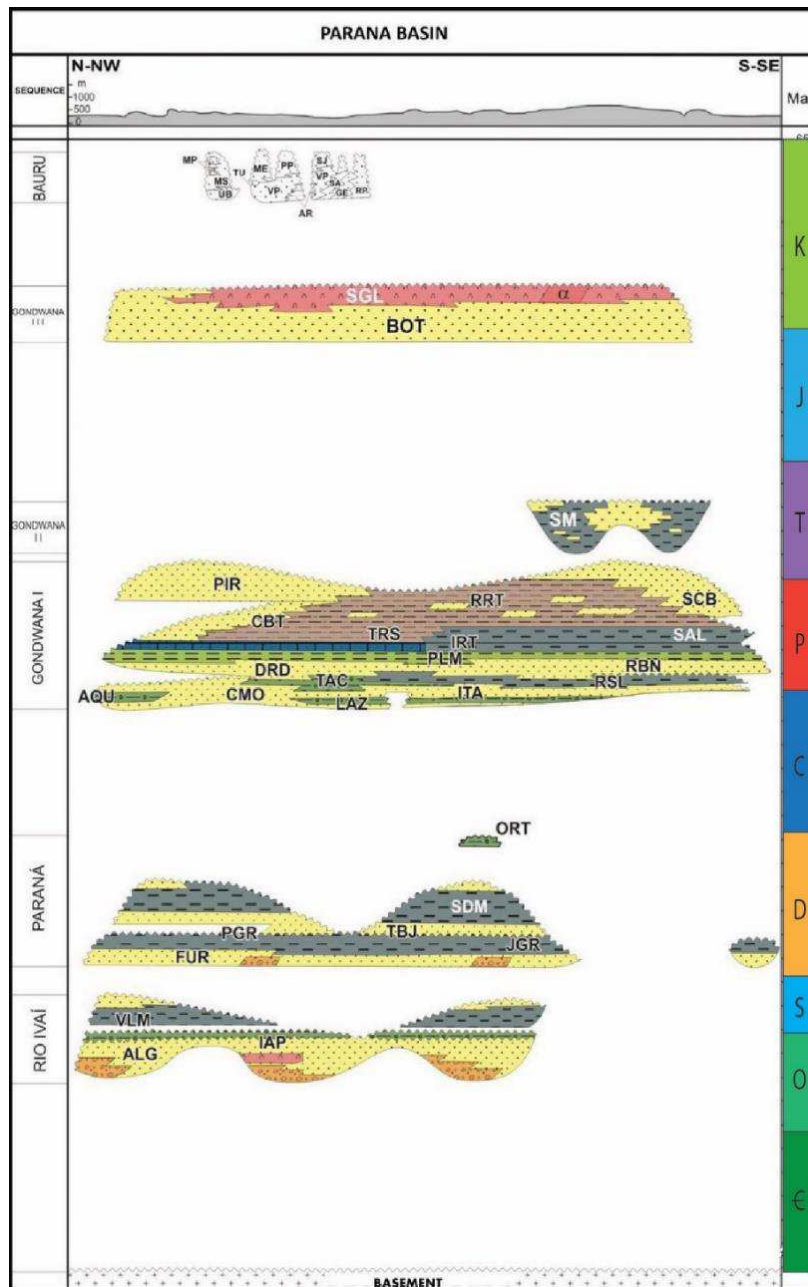


Figura 2.8: Carta estratigráfica da Bacia do Paraná, apóis Milani et al. (2007).

2.4.2 Bacias associadas ao rifte

A ruptura entre a América do Sul e África levou à formação de várias bacias oceânicas ao longo da costa dos dois continentes. A Bacia de Pelotas é a bacia oceânica localizada ao leste dos escudos do Uruguai e Sul-Rio-Grandense (Fig. 1.1). Aqui ela é discutida brevemente, enquanto que o Capítulo 7 inclui uma descrição mais detalhada da estrutura e unidades da bacia.

A Bacia de Pelotas é uma bacia de margem continental passiva que estende-se da Zona da Fratura de Florianópolis, no norte, Brasil, até o Alto de Polônio, no sul, Uruguai. O embasamento da Bacia de Pelotas é caracterizado pelo Cinturão Dom

Feliciano e depósitos da Bacia do Paraná, especialmente as rochas vulcânicas da Paraná-Etendeka LIP (Stica *et al.* 2014; Rosa *et al.* 2017). Ao contrário de outras bacias marginais mais ao norte da costa brasileira, a Bacia de Pelotas carece de extensos depósitos evaporíticos e apresenta abundante sedimentação siliciclástica, principalmente de granulometria fina (Bueno *et al.* 2007). Reservas economicamente viáveis de hidrocarbonetos não foram encontradas nesta bacia, mas há um interesse crescente na exploração de hidratos de gás na Bacia de Pelotas (Beglinger *et al.* 2012; Miller *et al.* 2015).

A sequência deposisional da Bacia de Pelotas compreende nove unidades litoestratigráficas definidas por Dias *et al.* (1994), que por sua vez foram agrupadas por Bueno *et al.* (2007) nas Supersequências Pré-Rifte, Rifte, Pós-Rifte e Drifte (Fig. 2.9). A Supersequência Pré-Rifte representa o embasamento da Bacia de Pelotas e é caracterizada por unidades da Supersequência Gondwana III da Bacia do Paraná, principalmente pelo vulcanismo fissural da Formação Serra Geral, ligado à ascensão da astenosfera nos estágios iniciais da ruptura. A Supersequência Rifte inclui basaltos de idade Barremiana-Aptiana da Formação Imbituba e depósitos siliciclásticos da Formação Cassino. Os depósitos ígneos da Formação Imbituba são correlacionados aos *seaward dipping reflectors* (SDRs) e podem ser identificados facilmente nos perfis sísmicos da Bacia de Pelotas. A Formação Cassino compreende depósitos siliciclásticos grosseiros com abundantes fragmentos vulcânicos e é restrita a meio-grabens de idade Aptiana. A Supersequência Pós-Rifte é caracterizada por mais magmatismo (Formação Curumim) intercalado com depósitos lacustres, gradando a calcários marinhos e arenitos característicos de um ambiente de águas rasas (formações Ariri e Portobelo). A análise da fauna de ostracodes sugere águas mornas e rasas na Bacia de Pelotas durante o Cretáceo e início do Paleogeno. Nesta época, a bacia era caracterizada por um ambiente nerítico com condições normais de salinidade (Ceolin *et al.* 2011). Por fim, a Supersequência Drifte corresponde ao principal depósito da Bacia de Pelotas. Ela pode ser dividida nas fases inicial (rasa, durante o Albiano), intermediária (transgressiva, do Albiano ao Oligoceno) e final (regressiva, durante o Neogeno). A fase inicial é representada pela Formação Portobelo, composta por carbonatos e depósitos siliciclásticos em um contexto de plataforma mista, os quais são lateralmente interdigitados aos arenitos da Formação Tramandaí, em direção ao continente. Com o início do ciclo transgressivo, ocorre a deposição de carbonatos, folhelhos e margas da Formação Atlântida sobre os anteriores, elevando progressivamente o nível de base na bacia. Esses depósitos de

carbonatos são sobrepostos pelos depósitos marinhos da Formação Imbé, que são interdigitados com os depósitos costeiros da Formação Cidreira. Juntas, essas duas últimas formações, compõem o principal preenchimento da Bacia de Pelotas. Finalmente, no Neogeno ocorre um ciclo regressivo e a Formação Cidreira prograda sobre a Formação Imbé.

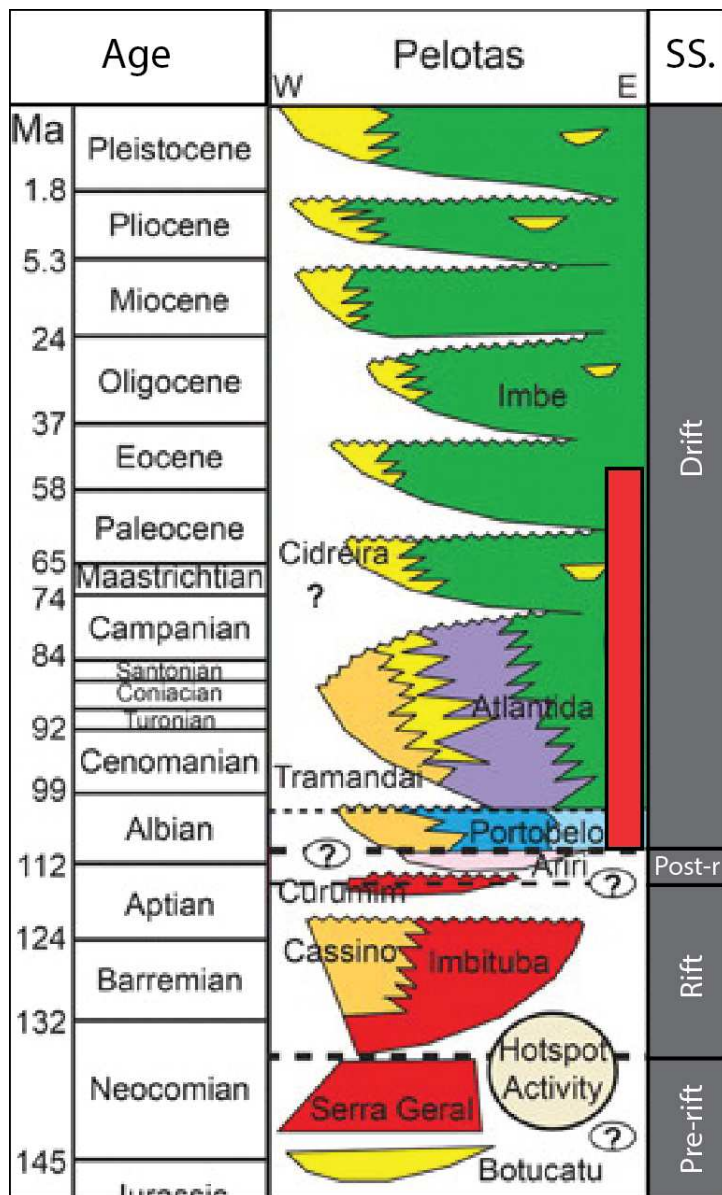


Figura 2.9: Carta estratigráfica da Bacia de Pelotas, com as Supersequências (SS.) indicadas. Modificado a partir de Dias et al. (2004), Bueno et al. (2007) e Beglinger et al. (2012).

Os esforços tectônicos associados à ruptura do Gondwana Ocidental e à abertura do Atlântico levaram à formação de outras duas bacias no Uruguai, denominadas bacias Santa Lucia e Laguna Merin (Bossi et al. 1998). Essas duas bacias formam um lineamento ENE-WSW conhecido como SaLAM, que é considerado um rifte abortado precursor da abertura do Atlântico Sul durante o

Jurássico-Cretáceo (Rossello *et al.* 2000). Apesar do vínculo genético, as bacias exibem preenchimentos vulcânicos-sedimentares bastante distintos e são separadas por um alto do embasamento representado pelo Terreno Nico Pérez (ver Capítulo 5), onde são encontrados apenas alguns remanescentes de depósitos vulcânicos (Rossello *et al.* 2000). O SaLAM foi desenvolvido durante a tectônica extensional relacionada ao rompimento do Gondwana Ocidental, com uma fase transtensiva dextral associada por Rossello *et al.* (2000, 2007) ao movimento que levou a abertura do Atlântico Sul. A Bacia de Santa Lucia corresponde à parte SW do SaLAM, apresenta um alto estrutural central de direção E-W e compreende principalmente depósitos siliciclásticos, atingindo uma espessura total de 2.500 m (Rossello *et al.* 2000; Veroslavsky *et al.* 2004). O NE do SaLAM é representado pela Bacia de Laguna Merin, composta principalmente por rochas vulcânicas com idades entre 134 e 127 Ma, e cobertas por rochas sedimentares cenozoicas (Cernuschi *et al.* 2015).

2.4.3 Outras coberturas volcano-sedimentares

Além das bacias acima mencionadas, registros de outras bacias Paleozoicas são encontrados em partes restritas dos escudos Sul-Rio-Grandense e Uruguaio. No Escudo Sul-Rio-Grandense ocorre a Bacia do Camaquã, enquanto que o Escudo uruguaio preservou registros do Grupo Arroyo del Soldado.

A Bacia do Camaquã cobre parte da porção oeste do Escudo Sul-Rio-Grandense e é composta por depósitos Ediacaranos a Cambrianos. Foi formada como resultado da sedimentação em sucessivos, mas independentes, depocentros na mesma região, e acumulou até 10.000 m de sedimentos e rochas vulcânicas (de Borba & Mizusaki 2003; Hasui 2012). Os depósitos sedimentares e vulcânicos sugerem uma evolução de ambientes tardi- a pós-orogênicos (Ciclo Brasiliano), com o contexto estrutural mudando da bacia de retroarco, para a bacia *strike-slip* e, por fim, um ambiente extensional (Hasui 2012; Paim *et al.* 2014). As sucessões sedimentares são comumente intercaladas com rochas vulcânicas e indicam uma evolução de estratos marinhos rasos na base, gradando para fácies lacustres, até depósitos eólicos e aluviais no topo da sucessão (de Borba & Mizusaki 2003; Maraschin *et al.* 2010; Paim *et al.* 2014). A unidade mais jovem preservada da Bacia do Camaquã é o Grupo Guaritas, com idade deposicional máxima de 540 ± 6 Ma e mínima de 473 ± 9 Ma (Maraschin *et al.* 2010; de Oliveira *et al.* 2014).

O Grupo Arroyo del Soldado ocorre na parte central do Escudo Uruguaio e foi depositado entre o Ediacarano e o Cambriano inferior. Ele representa uma espessa

(> 5.000 m) sequência de plataforma marinha depositada antes da aglutinação final de todos os terrenos Uruguaios (Blanco *et al.* 2009). O Grupo é composto de depósitos siliciclásticos alternados com unidades carbonáticas, sem registros vulcânicos (Gaucher *et al.* 2004). O registro sedimentar sugere que o Grupo Arroyo del Soldado foi depositado em uma plataforma estável do tipo Atlântico, afetada por sucessivas mudanças no nível do mar e com proveniência principalmente do Cráton Rio de La Plata (Gaucher *et al.* 2004; Blanco *et al.* 2009).

Capítulo 3 – Métodos

3.1 Introdução

A pesquisa apresentada nesta tese utilizou dois métodos analíticos principais: datação radioisotópica e análise sísmica. Como ambos são métodos amplamente aplicados nas geociências, este capítulo não tem o objetivo de fornecer uma revisão teórica completa, a qual está disponível em vários livros especializados. Em vez disso, são discutidos alguns dos conceitos teóricos básicos desses métodos, juntamente com sua aplicação na pesquisa, seus potenciais e limitações. A estratégia de modelagem térmica inversa também é apresentada neste capítulo.

Métodos radioisotópicos sensíveis a temperaturas abaixo de 300 °C, coletivamente denominados termocronômetros de baixa temperatura, foram utilizados para investigar a história térmica dos escudos. O resfriamento do embasamento atualmente exposto pode ser associado à exumação das rochas de condições mais profundas e quentes. As idades obtidas por diferentes termocronômetros, combinadas com outros parâmetros minerais (por exemplo, dimensões do cristal) e cinéticos, foram usadas para criar modelos inversos para a história de resfriamento/aquecimento de várias localidades nos dois escudos.

Dados de reflexão sísmica 2D foram utilizados para identificar superfícies-chave na Bacia de Pelotas, as quais representam variações nos padrões e espaço de acomodação da bacia. Essas variações podem estar relacionadas a movimentos tectônicos verticais (subsidiência e exumação) e, com o apoio de dados de poços, podem ser usadas para estimar os volumes sedimentares acumulados durante o desenvolvimento da bacia.

3.2 Termocronometria de baixa temperatura

A termocronometria de baixa temperatura diz respeito ao acúmulo de produtos radiogênicos no retículo cristalino de um mineral, mas que são perdidos pelo cristal através de diferentes processos quando a temperatura é muito elevada. Cada termocronômetro, isso é, mineral mais sistema isotópico (isótopo pai e produto do decaimento radioativo), tem sua própria temperatura de fechamento, abaixo da qual o produto radiogênico começa a se acumular no cristal (Fig. 3.1). Três termocronômetros de baixa temperatura foram utilizados para investigar a evolução térmica dos embasamentos Uruguaio e Sul-Rio-Grandense: traços de fissão de

apatita (AFT), (U-Th)/He em apatita (AHe) e (U-Th)/He em zircão (ZHe). Esses sistemas radioisotópicos têm temperaturas de retenção distintas, e juntos cobrem um intervalo entre c. 40 a 200 °C, ou seja, temperaturas correspondentes a parte superior da crosta. Cada método possui sua zona de retenção parcial específica (PRZ), que corresponde a um intervalo de temperaturas em que a acumulação e a perda dos produtos de decaimento radiogênico são simultâneas. Temperaturas inferiores à PRZ do termocronômetro analisado implicam uma retenção total dos produtos radiogênicos, enquanto temperaturas mais altas que a PRZ resultam em perda completa dos mesmos, resetando a idade do termocronômetro a zero.

TEMPERATURE RANGE OF THERMOCHRONOMETERS

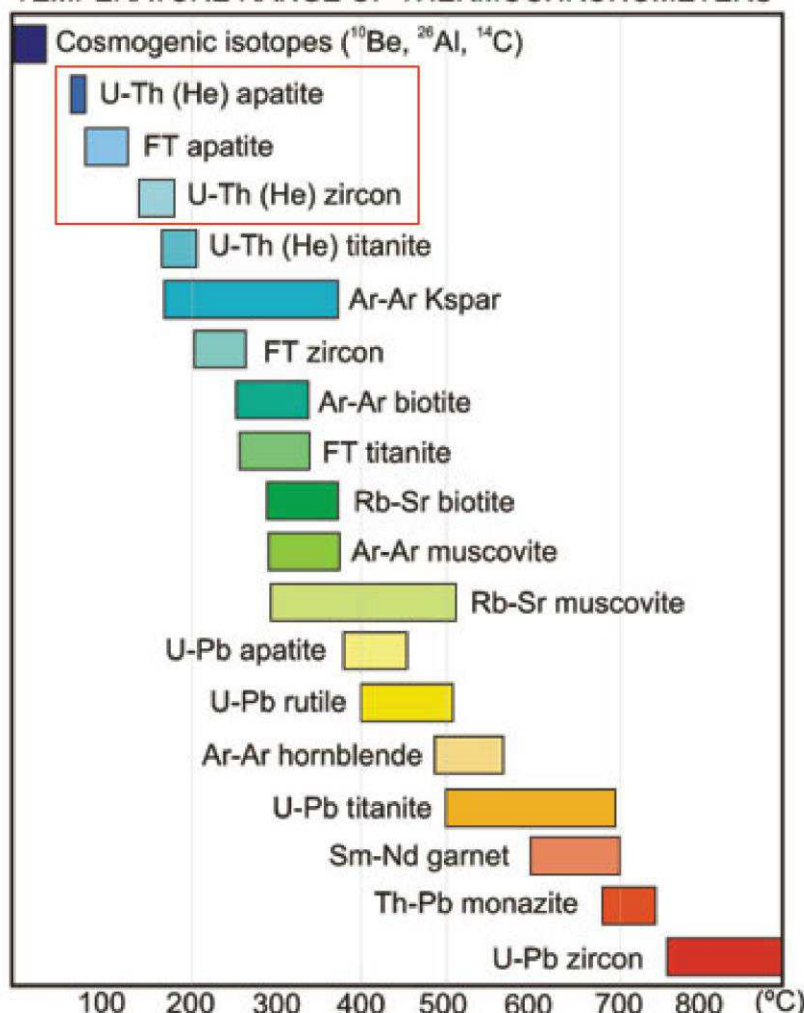


Figura 3.1: Intervalo de temperatura de detecção (ou zona de retenção parcial) de alguns sistemas isotópicos em diferentes minerais (termocronômetros). Os métodos usados aqui são indicados pela caixa vermelha e registram a passagem através de baixas temperaturas (< 200°C), que correspondem à profundidades superficiais da crosta. Extraído de Pollard (2003).

A idade obtida pelos métodos termocronométricos é uma idade de resfriamento, baseada no equilíbrio entre o isótopo pai e o produto do decaimento, e representa um ponto de tempo-temperatura ($t-T$) durante a passagem pela PRZ do termocronômetro. Fatores particulares de cada cristal, como suas dimensões ou composição química, podem afetar consideravelmente a PRZ do mineral e, consequentemente, a idade resultante. Assim, são feitas correções de idade para cada cristal com base em suas características singulares, e a datação por termocronometria é realizada em uma variedade de cristais dentro da mesma amostra, para que resultados individuais possam ser analisados no contexto da população da amostra. A equação fundamental da idade para qualquer datação radiogênica pode ser escrita como:

$$t = \frac{1}{\lambda} \ln \left(\frac{N_d}{N_p} + 1 \right)$$

onde t é a idade; λ é a constante de decaimento do sistema isotópico em questão; e N_d e N_p são os números de produtos do decaimento e isótopos pais do sistema, respectivamente. Essa equação é adaptada para cada termocronômetro analisado, o que é discutido abaixo.

3.2.1 Traços de fissão

Os traços de fissão são danos lineares na rede cristalina de um mineral, com comprimento inicial em torno de 16 μm (no caso da apatita) e sem uma orientação preferencial, sendo formados em consequência da fissão espontânea do ^{238}U (Price & Walker 1963; Fleischer *et al.* 1975; Galbraith *et al.* 1990). A principal diferença entre a datação por traços de fissão e outros métodos isotópicos convencionais é que o produto analisado em nessa datação é o dano ao retículo cristalino (os traços), e não a quantidade de isótopos presentes no mineral. Sendo assim, o fenômeno não é medido por espectrômetros de massa tal como outros métodos geocronológicos convencionais, mas sim através de uma determinação ótica, com a contagem dos traços de fissão, tratados quimicamente, a partir de um microscópio com aumento igual ou superior a 1000x. A densidade dos traços de fissão acumulados e a distribuição de seus comprimentos indicam o caminho térmico experimentado pelo mineral hospedeiro (Gleadow *et al.* 1986a, b; Galbraith *et al.* 1990).

Os traços formados pelo decaimento do urânio acumulam-se no cristal com o passar do tempo, desde que seja respeitada uma temperatura limite. A zona de retenção parcial dos traços de fissão em apatita (AFTPZ) corresponde a temperaturas entre c. 60 a 110 °C, em que os traços sofrem encurtamento lento e

gradual (*annealing*). Acima de c. 110 °C todos os AFT desaparecem rapidamente devido ao *annealing*, o que reseta a idade do termocronômetro a zero (Gleadow *et al.* 1986a; Green *et al.* 1986; Wagner *et al.* 1989; Gallagher *et al.* 1998). Abaixo de c. 60 °C o processo de *annealing* não é eficaz e os traços são preservados com o seu comprimento inicial. Embora a temperatura seja o principal fator de controle do *annealing*, esse processo também é afetado pelas variações na composição química da apatita e pela quantidade de dano radioativo acumulado no cristal (Gleadow *et al.* 1986a; Stockli 2005; Tagami & O'Sullivan 2005).

A datação AFT foi realizada usando o método do detector externo (Fig. 3.2) (Gleadow 1981; Hurford 1990). Para cada amostra, mais de 200 cristais de apatitas foram selecionados à mão e montadas em pastilhas de resina epóxi (Fig. 3.3), polidas até a porção central e atacadas com uma solução de HNO₃ 5,5M a 21 °C por 20 s para revelar os traços de fissão espontâneos (aqueles decorrentes do decaimento do ²³⁸U) (Carlson *et al.* 1999). Folhas de moscovita (detectores externos) foram acopladas às pastilhas, sendo então os conjuntos irradiados no reator IEA-R1/IPEN da Universidade de São Paulo, Brasil, juntamente com padrões geológicos de idade conhecida por outro método (Durango) e dosímetros com concentração de U conhecida e uniforme (Corning CN5). Posteriormente, as folhas de mica foram desacopladas e atacadas com 48% HF por 18 min a 20 °C para revelar os traços induzidos (aqueles decorrentes do decaimento do ²³⁵U no reator). As análises de AFT foram realizadas no Laboratório de Modelagem da Universidade Federal do Rio Grande do Sul, Brasil, utilizando um microscópio Leica DM 6000 M (1000x, seco). As idades foram calculadas com base em 20 cristais por amostra e no método de calibração ζ (Hurford & Green 1983; Hurford 1990), enquanto a homogeneidade das idades foi analisada pelo teste do chi-quadrado (χ^2) (Galbraith 1981; Galbraith & Green 1990) e dispersão das idades dos grãos individuais, utilizando o software RadialPlotter 9.0 (Vermeesch 2009).

Para serem usados durante a modelagem inversa, em cada amostra foram coletadas as medidas dos comprimentos de traços confinados e o ângulo que estes fazem com o eixo *c* do cristal de apatita. Buscou-se medir o comprimento e ângulo de 100 traços confinados do tipo TINT (*track-in-track*) (Lal *et al.* 1969), uma quantidade estatisticamente satisfatória para a modelagem do *annealing* sofrido pelos traços espontâneos no mineral. Além disso, foi medido o diâmetro do traço no plano polido (*etch pit*, ou Dpar) de cerca de 100 traços para cada amostra. O Dpar está correlacionado com o teor de Cl, OH e F nos cristais; valores baixos de Dpar ($\leq 1,75 \mu\text{m}$) são correlatos a alto teor de F e *annealing* mais rápido (Donelick 1993; Carlson

et al. 1999; Donelick *et al.* 2005). A distribuição de comprimentos de traços confinados (MTL) fornecem as restrições no caminho (variações no tempo e temperatura) experimentado pela amostra durante sua passagem pela PRZ, enquanto a idade AFT e a densidade dos traços posicionam esse caminho no tempo geológico.

Para o método do detector externo, a equação da idade é expressa como:

$$t = \frac{1}{\lambda_\alpha} \ln \left(1 + \frac{\rho_s}{\rho_i} \lambda_\alpha \rho_d \zeta \right)$$

onde t é a idade; ρ_s e ρ_i são as densidades de traços espontâneos e induzidos medidos durante a análise; λ_α é a constante de decaimento do ^{238}U ; ρ_d é a densidade de traços no dosímetro (material com concentração de urânio específica e usado para monitorar o fluxo neutrônico do reator); e ζ é a constante de calibração particular ao analista.

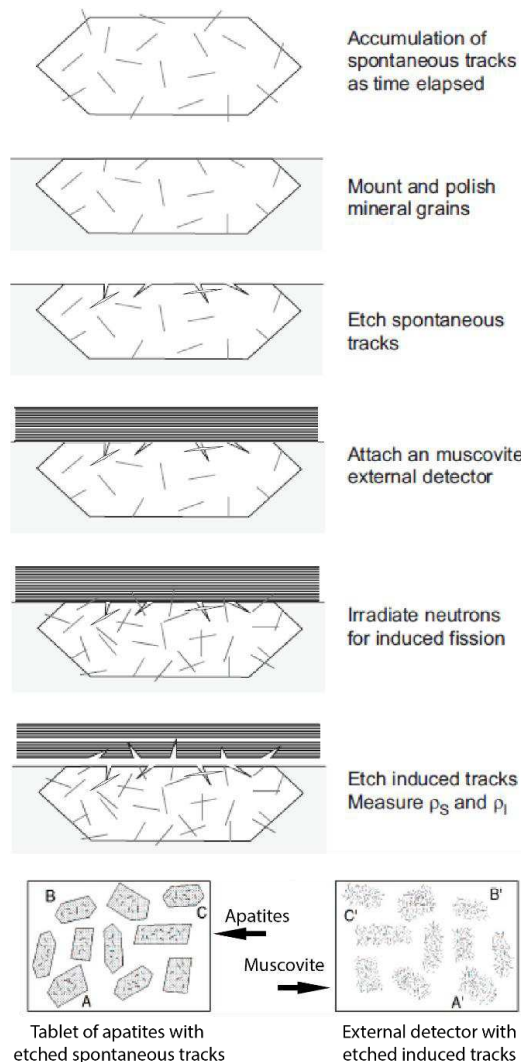


Figura 3.2: Etapas analíticas do método do detector externo. Após o ataque químico aos traços induzidas na moscovita, a densidade de traços de fissão é contada em áreas correspondentes entre pastilha com as apatitas e a moscovita. Modificado a partir de Tagami & O'Sullivan (2005).

3.2.2 (U-Th)/He

O método (U-Th)/He é baseado no acúmulo de partículas alfa (${}^4\text{He}$) na estrutura cristalina de um mineral após a cadeia de decaimento dos isótopos ${}^{238}\text{U}$, ${}^{235}\text{U}$ e ${}^{232}\text{Th}$ (com pequena contribuição do isótopo ${}^{147}\text{Sm}$). Sendo assim, nesse método as idades são calculadas a partir da acumulação de He radiogênico, formado durante a sequência em cadeia de decaimento dos elementos radioativos instáveis. Portanto, a equação da idade pode ser expressa como o equilíbrio entre os isótopos pai e o produto filho:

$${}^4\text{He}_{\text{all}} = 8{}^{238}\text{U}(e^{\lambda_{238}t} - 1) + 7{}^{235}\text{U}(e^{\lambda_{235}t} - 1) + 6{}^{232}\text{Th}(e^{\lambda_{232}t} - 1) + {}^{147}\text{Sm}(e^{\lambda_{147}t} - 1)$$

onde t é a idade; e λn é a constante de decaimento do isótopo em questão.

As partículas alfa se acumulam no mineral a baixas temperaturas, mas são expelidas da estrutura cristalina a altas temperaturas devido à difusão térmica. Na datação por (U-Th)/He em apatita, as partículas alfa são eficientemente expelidas a temperaturas acima de c. 70 °C, parcialmente retidas entre c. 40 e 70 °C (zona de retenção parcial da AHe - AHePRZ) e completamente retidas quando a temperatura estiver abaixo de c. 40 °C (Wolf *et al.* 1996, 1998; Farley 2002). No entanto, sabe-se que esses limites de temperatura variam com as dimensões do cristal, zonação química, concentração do teor total de urânio eU (eU = [U] + 0,235 × [Th]) e danos radioativos acumulados no retículo cristalino (e.g. Farley 2000; Reiners & Farley 2001; Shuster *et al.* 2006). Além disso, pequenas variações nesses fatores são ampliadas no caso de período prolongado na AHePRZ, resultando em AHe idades dispersas (Flowers & Kelley 2011).

Na datação (U-Th)/He em zircão, as partículas alfa são parcialmente retidas entre c. 150 e 190 °C (Zona de Retenção Parcial do ZHe - ZHePRZ) e expelidas quando os cristais se encontram a temperaturas superiores a c. de 190 °C (Reiners *et al.* 2018). De maneira semelhante à AHePRZ, a ZHePRZ é afetada por zonação química, concentração de eU, dano radioativo acumulado e residência prolongada a baixas temperaturas (Reiners *et al.* 2002, 2004; Nasdala *et al.* 2004; Reiners 2005). A influência desses fatores durante a determinação da idade, tanto em AHe quanto em ZHe, é discutida mais detalhadamente na avaliação das idades termocronométricas obtidas, nos Capítulos 5 e 6.

As análises (U-Th)/He foram realizadas no Arizona Radiogenic Helium Dating Laboratory (ARHDL), na University of Arizona, EUA. Apatitas e zircões foram criteriosamente escolhidos com base na morfologia, tamanho e clareza óptica, usando

um microscópio Leica MZ16. Como as apatitas tendem a acumular uma baixa quantidade de partículas alfa devido à baixa concentração de eU no mineral (geralmente eU <50 ppm), foi dada preferência às apatitas claras com ambas as terminações, com o objetivo de evitar cristais que eventualmente perderam ${}^4\text{He}$ por fraturas ou uma estrutura cristalina altamente danificada. Por outro lado, como o eU de zircões é geralmente uma ou duas ordens de magnitude mais alto, foram selecionados zircões com uma ampla gama de opacidade, que refletem a quantidade de dano acumulado da radiação e fornecem uma melhor visão da influência da eU sobre a idade ZHe.

Os cristais selecionados foram medidos e fotografados com o Leica Application Suite V3, para assim definir o domínio da difusão e permitir a correção da idade a partir da ejeção alfa (Farley *et al.* 1996), que contabiliza a ejeção de ${}^4\text{He}$ nas bordas do cristal durante o decaimento radioativo. Tubos de Nb foram usados para embalar os cristais para extração de hélio (Fig. 3.3), o qual foi liberado após o aquecimento do conjunto a laser (*laser ablation*) e medido com um espectrômetro de massa quadrupolo. Posteriormente, os cristais foram dissolvidos para as medições de U-Th, realizadas usando um ICP-MS Element2 de alta resolução. Os padrões Durango e Fish Canyon Tuff, além de tubos de Nb vazios, foram introduzidos sistematicamente entre as análises para garantir a confiabilidade das medições.



Figura 3.3: Materiais para análise de termocronometria. À esquerda, conjunto de pastilhas com aproximadamente 400 cristais cada para análise dos traços de fissão de apatita. À direita, dois cristais de apatita embalados individualmente em tubos de Nb para análise (U-Th)/He.

3.3 Modelagem térmica inversa

A história térmica de cada amostra foi modelada usando o programa QTQt 5.7 (Gallagher *et al.* 2009; Gallagher 2012), o qual simula pontos de tempo-temperatura (t-T) com o objetivo de reconstruir uma evolução térmica que melhor coincida com os dados termocronométricos obtidos. As simulações matemáticas da história térmica da amostra analisada são realizadas a partir de um método de inversão Bayesiana transdimensional, via uma abordagem *Markov chain Monte Carlo* (Gallagher *et al.* 2009; Gallagher 2012), na qual a complexidade da história é inferida a partir dos dados termocronométricos.

Os modelos inversos foram executados com um mínimo de restrições possíveis, para assim evitar o direcionamento a uma história térmica influenciada pelo usuário. Primeiramente, os modelos foram executados sem qualquer restrição exceto a de uma temperatura ambiente atual de 20 ± 10 °C, o que permitiu verificar qual o ponto de t-T mais antigo/mais alta que os dados poderiam determinar. Posteriormente, para definir um intervalo inicial para os modelos, uma grande caixa t-T foi inserida, com tempo variando de 500 ± 50 Ma e temperatura de 100 ± 100 °C, tempo correspondente ao final do Ciclo Brasiliense e com t-T maiores do que o que os modelos irrestritos podiam determinar. A restrição final com temperatura de 20 ± 10 °C no presente foi mantida. A história térmica entre as restrições inicial e final foi recriada livremente pelo QTQt 5.7, usando um intervalo de tempo definido pelo programa e correspondente a duas vezes o valor da idade mais antiga disponível na amostra, e uma faixa de temperatura de 70 ± 70 °C ao modelar apenas AFT e AHe e de 100 ± 100 °C quando a amostra tinha dados de ZHe disponíveis.

Como o atual entendimento do sistema AFT (e.g. cinética de *annealing* e suas variações com a composição química da apatita; formação dos traços) é melhor estabelecido do que o do sistema (U-Th)/He (e.g. difusão térmica e variações com a composição química do cristal; efeitos de residência por longo prazo na PRZ), os modelos foram executados inicialmente apenas com dados AFT. Foram realizados vários testes rápidos de 20.000 simulações para cada amostra para definir parâmetros apropriados durante a inversão (ver Gallagher 2012) e para testar a variabilidade dos modelos usando diferentes taxas de $\partial T/\partial t$. Os modelos executados apenas com dados AFT resultaram em uma boa concordância entre as idades e MTLs observadas nas análises e previstas nos modelos, enquanto que os modelos baseados apenas em dados (U-Th)/He não forneceram uma concordância satisfatória. Além disso, a

inclusão de dados AHe nos modelos contendo os dados de AFT geralmente levava a uma incompatibilidade considerável dos dados AFT observados e previstos. Esses modelos combinados previram idades AFT mais antigas do que as observadas e uma incompatibilidade nas distribuições dos traços (MTLs), enquanto tentavam (geralmente sem sucesso) encaixar todas as idades AHe, mas sem melhorar a história térmica de baixa temperatura (<60 °C). Para resolver esse conflito e manter um bom ajuste dos dados de AFT, foi utilizado um recurso do QTQt 5.7 que reanalisa o erro nas idades AHe para aceitar um maior grau de incompatibilidade entre os dados AHe obtidos e previstos. Por outro lado, a inclusão de dados de ZHe geralmente melhorou a determinação da época de resfriamento de temperaturas mais altas (> 150 °C) nos modelos.

Os modelos finais utilizaram todos os dados de termocronometria disponíveis para cada amostra, foram executados por 200.000 simulações ou mais e usaram um gradiente geotérmico ($\partial T/\partial t$) máximo de 10 °C/Ma, compatível com uma região cratônica de baixo relevo e topografia. Essa configuração final de modelagem permitiu que os caminhos de temperatura e tempo propostos nos modelos fossem bem definidos, mas não muito limitados pelas restrições do usuário ou pelas idades antigas e dispersas do AHe (consulte os Capítulos 5 e 6 e os Apêndices). Durante a modelagem, para a cinética do sistema AFT, foram utilizados os valores de Dpar e os comprimentos de traços projetados no eixo c (Donelick 1993; Donelick *et al.* 1999) e o modelo de *annealing* de Ketcham *et al.* (2007), enquanto para os sistemas (U-Th)/He foi utilizado o modelo de dano radioativo de Flowers *et al.* (2009) para AHe e de Guenthner *et al.* (2013) para ZHe.

Capítulo 4 – Síntese integradora

4.1 Introdução

A margem passiva da América do Sul apresenta uma grande variedade geológica ao longo da costa, e uma área importante de mudança substancial na estrutura da margem está localizada perto da cidade de Florianópolis (BR). Embora a região ao norte dessa fronteira tenha sido objeto de uma vasta quantidade de estudos, incentivada pelas volumosas reservas de petróleo e gás nas bacias de Santos e Campos, e outras menores no nordeste do Brasil, a evolução da região ao sul de Florianópolis é ainda mal compreendida. Uma melhor caracterização desta última deve aprimorar nossos modelos do rifte do Atlântico Sul e fornecer uma melhor medida da influência da pluma mantélica Tristão da Cunha durante a ruptura continental. Os resultados obtidos nesta tese não puderam responder todas as questões relacionadas ao desenvolvimento do rifte do Atlântico Sul, mas acrescentam informações significativas à discussão, elucidando a geodinâmica da crosta rasa durante o processo ruptura do Gondwana Ocidental. Este capítulo resume as principais conclusões deste projeto de doutorado e levanta outras questões para investigação.

4.2 Termocronologia dos escudos Uruguai e Sul-Rio-Grandense

Os resultados da termocronometria obtidos nos embasamentos Uruguai e Sul-Rio-Grandense mostram um comportamento muito semelhante em ambos escudos. A análise (U-Th)/He em zircão (ZHe) apresenta idades fortemente controladas pelo teor total de urânio (eU) dos cristais, nas quais os cristais com baixo eU têm idades do início do Paleozoico, enquanto que o aumento do eU resulta em idades mais jovens. Tal comportamento está relacionado ao acúmulo de danos cristalinos causados por radiação nos zircões: como os cristais com alto eU têm suas redes cristalinas danificadas mais rapidamente devido ao decaimento radioativo, essas imperfeições radiogênicas facilitam o escape das partículas alfa dos zircões, resultando em idades mais jovens (Shuster *et al.* 2006; Reiners *et al.* 2018). Sendo ZHe um termocronômetro que registra o resfriamento abaixo de c. 190 °C, os resultados sugerem que toda a região estava a temperaturas próximas ou abaixo desse limite no início do Paleozoico, o que favorece o acúmulo de danos radioativos em alguns cristais a longo prazo.

A análise dos traços de fissão de apatita (AFT) resultou em idades Mesozoicas, predominantemente Jurássicas, o que precede a abertura do Atlântico Sul na região. As idades da AFT sugerem temperaturas abaixo de 110 °C durante a transição Paleozoico-Mesozoico, e que os eventos magmáticos na região durante o Cretáceo, relacionados ao rifte do Atlântico Sul, não foram suficientemente potentes a ponto de aumentar a temperatura do embasamento acima de 110 °C e resetar as idades AFT durante a ruptura. Considerando trabalhos publicados sobre a região, há uma tendência de idades AFT mais antigas no interior do continente, o que sugere que a parte ocidental dos escudos resfriou mais cedo que a parte oriental (Fig 4.1).

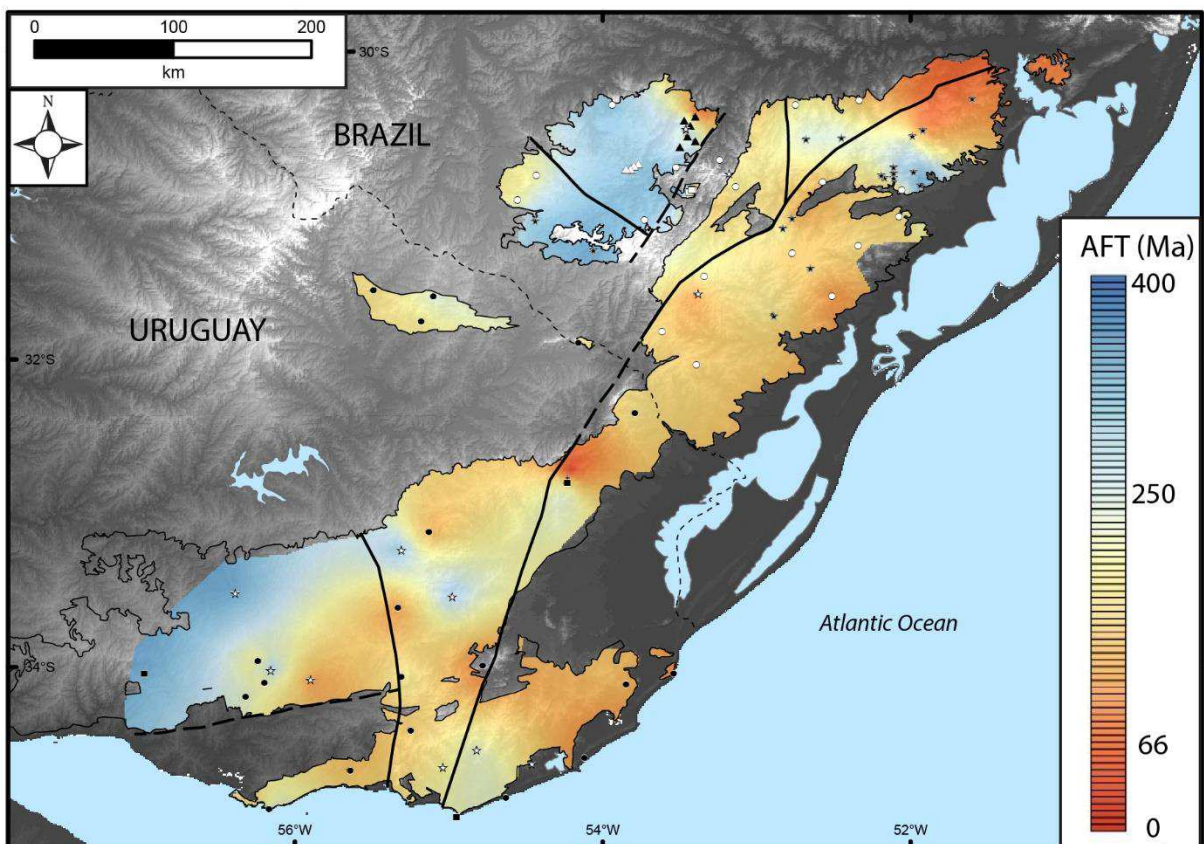


Figura 4.1: Interpolação por krigagem de todas as idades centrais de AFT disponíveis para a região. A porção oeste concentra as idades mais antigas, indicando um período mais longo de estabilidade a baixas temperaturas (<110 °C) quando comparado ao restante dos escudos. Dados deste trabalho e de Borba et al. (2002, 2003), Bicca et al. (2013), Kollenz (2015), de Oliveira et al. (2016) e Gomes & Almeida (2019).

As idades de (U-Th)/He em apatita (AHe) obtidas são muito dispersas, com uma leve concentração de idades Mesozoicas, e não exibem uma correlação direta com o teor de eU ou o tamanho dos cristais. Além disso, as idades AHe geralmente são mais antigas do que as AFT, apesar da menor temperatura de fechamento do primeiro termocronômetro. Todavia, recentes avanços no método (U-Th)/He mostraram que as

idades AHe podem ser maiores que as idades de AFT da mesma amostra quando as apatitas têm eU relativamente alto e/ou residem por prolongado período a temperaturas entre 30 e 60 °C. Essa inversão das idades também pode ser favorecida por histórias térmicas complexas, nas quais ocorre uma fase de reaquecimento dos cristais. Se as temperaturas subirem, mas permanecerem abaixo de 80-100 °C, as idades AFT podem ser mais jovens que as AHe, mesmo para cristais com teores de eU moderados a baixos (Reiners *et al.* 2018). Por fim, as idades do AHe corroboram que o rifteamento não aumentou as temperaturas o suficiente para resetar esse termocronômetro, já que praticamente nenhuma idade AHe é menor do que idade da ruptura.

As idades termocronométricas e outros parâmetros dos cristais foram utilizados para recriar a história térmica dos escudos Uruguai e Sul-Rio-Grandense. Apesar de diferenças locais, os modelos inversos obtidos revelam um padrão de resfriamento semelhante em ambos escudos (Figs. 5.10 e 6.9). O comportamento geral sugere um resfriamento prolongado de temperaturas acima de 150 °C no Carbonífero a temperaturas próximas da superfície (<60 °C) no início do Cretáceo. Essa fase contínua de resfriamento pode estar relacionada ao soerguimento e exumação dos escudos, causados por dois eventos tectônicos na região: as orogenias no SW de Gondwana, especialmente o ciclo Gondwanico, e a ruptura do Gondwana Ocidental.

O início de resfriamento regional é temporalmente correlacionado com o Ciclo Gondwanico, um evento colisional durante o Paleozoico tardio na margem SW do Gondwana Ocidental (Trouw & De Wit 1999; Milani & De Wit 2008). O ciclo Gondwanico envolve acréscimos de terrenos e subducção do oceano Panthalassa na margem SW do megacontinente. As colisões provavelmente foram caracterizadas, pelo menos durante algum período, pela subducção em baixo ângulo da crosta oceânica sob o continente, conforme sugerido pelos padrões de sedimentação na Argentina, Uruguai e no sul do Brasil (Zerfass *et al.* 2004). Esse ciclo colisional pode ter causado o soerguimento da região estudada, devido à propagação de tensões e esforços na placa continental, iniciando assim o resfriamento regional.

O segundo, e provavelmente mais importante evento tectônico, é a abertura do Atlântico Sul, no Mesozoico. Este evento está associado à pluma mantélica Tristão da Cunha e a volumoso magmatismo. É possível que o empuxo da pluma mantélica e o acúmulo de magma sob a litosfera antes da ruptura aumentaram a flutuabilidade da placa continental, causando soerguimento e uma topografia elevada durante o rifteamento (White & McKenzie, 1989; Quirk & Rüpke 2018). Esse soerguimento

regional causaria o resfriamento do embasamento devido à exumação, como sugerido pelos modelos aqui expostos. Além disso, o acúmulo de magma sob a região e a sua subsequente extrusão podem ter um efeito positivo posterior no geotermo regional. Ambos os embasamentos estão localizados entre dois grandes corpos ígneos (Fig. 4.2): o magmatismo da Paraná-Etendeka LIP (134-132 Ma) antes do rifte, e os SDRs na bacia de Pelotas (133-113 Ma). Além disso, ambos escudos registram magmatismo até cerca de 70 Ma. Os modelos inversos sugerem um pequeno reaquecimento do embasamento entre c. 140 e 60 Ma, o que pode ser uma consequência da intensa e contínua atividade magmática na região durante o Cretáceo.

O resfriamento final até temperaturas da superfície ocorreu no Cenozoico, mas os modelos inversos não permitem uma definição exata do mesmo. Essa fase de resfriamento corresponde a temperaturas abaixo das registradas pelo sistema AFT, e os dados AHe são muito complexos e dispersos para fornecer uma solução indiscutível para o tempo e a taxa de resfriamento/exumação final. No entanto, a análise sísmica da Bacia de Pelotas forneceu algumas informações úteis quanto às taxas de sedimentação e volume dos depósitos acumulados durante o Cenozoico, os quais podem ser correlacionados com a exumação/erosão continental.

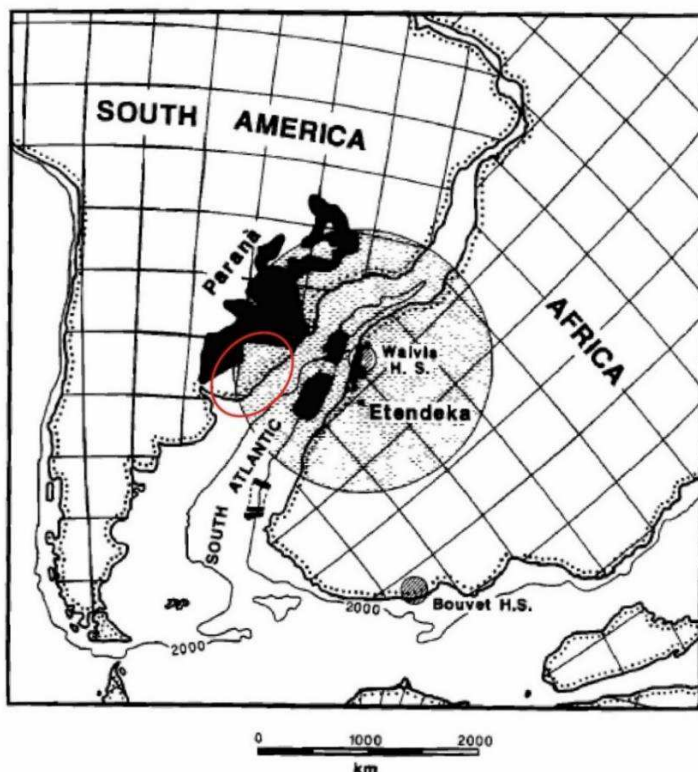


Figura 4.2: Reconstrução do Atlântico Sul durante o rifte (c. 120 Ma). A elipse vermelha marca a área de estudo, as áreas pretas sólidas representam o magmatismo extrusivo dos SDRs da Bacia de Pelotas e da Paraná-Etendeka LIP; o círculo sombreado indica a extensão da cabeça da pluma Tristão da Cunha. Extraído de White and McKenzie (1989).

4.3 Integração, conclusões e limitações

O presente estudo foi inicialmente planejado para quantificar o equilíbrio entre a exumação/erosão dos escudos Uruguai e Sul-Rio-Grandense e o preenchimento da Bacia de Pelotas, em trabalho *source to sink*. Entretanto, os resultados termocronométricos forneceram informações essencialmente sobre o período pré-rifte, antes da formação da Bacia de Pelotas. Além disso, a limitação dos dados da Bacia de Pelotas e de estudos publicados impuseram barreiras para definir com precisão os volumes e tendências deposicionais na bacia. Portanto, uma correlação indiscutível entre a erosão continental e o preenchimento da bacia não foi possível. Todavia, como é comum no meio científico, os produtos obtidos durante o desenvolvimento do projeto fomentaram novas questões e permitiram avanços importantes no conhecimento sobre a dinâmica do rifteamento. De maneira geral, os resultados aqui expostos fornecem inéditas informações sobre a ruptura do Gondwana Ocidental, o início do rifte e o desenvolvimento da Bacia de Pelotas.

O resfriamento regional observado nos modelos pode ter sido influenciado por forças relacionadas à subducção do oceano Panthalassa sob a margem SW do Gondwana, o que teria causado o soerguimento do embasamento no Uruguai e no sul do Brasil. Durante o final do Paleozoico essa região era um alto topográfico (Fig. 4.3), enquanto que no Mesozoico a pluma mantélica Tristão da Cunha colidiu com a base da litosfera, provavelmente causando um domo topográfico antes do rifte do Atlântico Sul. Zonas de fraqueza da litosfera favoreceram a exumação e o deslocamento vertical ao longo das estruturas do Ciclo Brasiliano (Will & Frimmel, 2018). A separação continental propagou-se de sul para norte e também de oeste para leste, avançando além do Terraço de Rio Grande e do Alto de Florianópolis somente após o Aptiano e resultando na segmentação do rifte (Stica *et al.* 2014). A cidade de Florianópolis, um limite importante no processo de rifteamento da margem continental, estava potencialmente sobre a pluma mantélica durante a separação (Salomon *et al.* 2017). O empurrão da pluma Tristão da Cunha, somado ao afinamento e extensão da crosta, parece ter mantido o sistema em uma posição elevada até a ruptura total (Aslanian *et al.* 2009; Beglinger *et al.* 2012), o que corrobora as idades da termocronometria anteriores ao rifte e os resultados da modelagem inversa. A alta topografia da região durante a abertura do Atlântico Sul também é sugerida pelos depósitos nas bacias adjacentes (Fig. 4.3) e pelo limitado registro sedimentar siliciclástico da Bacia de Pelotas durante o rifte (ver Apêndices). Os processos térmicos

ligados à exumação do manto/crosta inferior mantiveram a margem elevada ao longo da costa brasileira, o que favoreceu a deposição de carbonatos em ambiente de águas rasas, especialmente nas bacias do sudeste brasileiro (Aslanian *et al.* 2009). Basaltos e conglomerados oxidados foram observados em poços da Bacia de Pelotas e indicam exposição subaérea da Sequência Rift (formações Imbituba e Cassino) (Barboza *et al.* 2008); portanto, a bacia era provavelmente um planalto vulcânico elevado acima do nível do mar durante este período (Beglinger *et al.* 2012). Os primeiros depósitos na Bacia de Pelotas após o rifte são compostos principalmente de carbonatos e margas, e suas características sugerem um ambiente marinho raso durante a transição rifte-drifte.

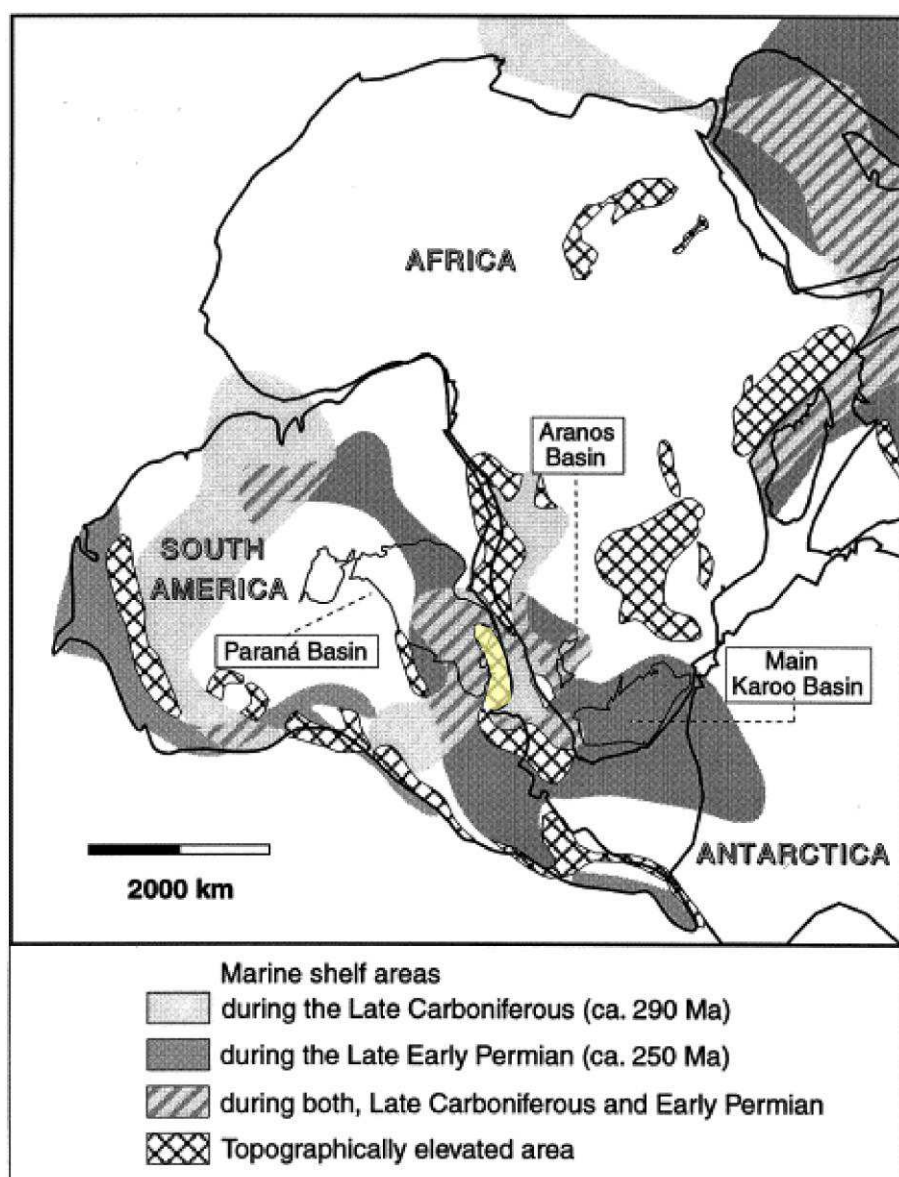


Figura 4.3: Reconstrução paleogeográfica do Gondwana Ocidental no final do Paleozoico. Estudos nas bacias adjacentes à área de estudo (destacada em amarelo) sustentam que o Uruguai e o sul do Brasil foram altos topográficos durante o Permiano. Isso corrobora um resfriamento (exumação) contínuo do embasamento desde o final do Paleozoico. Extraído de Stollhofen (2000).

Uma fase de reaquecimento, temporalmente correlacionada com a abertura do Atlântico Sul na região, foi sugerida pelos modelos inversos e, embora esteja no limite de detecção do método AFT e seja pouco definida pelos dados AHe, é geologicamente suportada pelas evidências de intenso magmatismo na região no Cretáceo. Durante a ruptura, uma rotação no sentido horário da parte sul da América do Sul, incluindo a região do Uruguai e sul do Brasil, formou estruturas perpendiculares à margem, como grabens e caminhos para a ascensão do magma, enquanto a parte norte era mais estável e conectada à África (Salomon *et al.* 2017). Esse comportamento reológico contrastante pode ter favorecido a colocação do volumoso magmatismo cretáceo na região, como os diques de alimentação da Paraná-Etendeka LIP no escudo Sul-Rio-Grandense e região mais ao norte, o intenso vulcanismo da bacia do Laguna Merin no nordeste do Uruguai, e a formação dos SDRs ao longo da margem. Além disso, ambos os escudos registram magmatismo até a transição Cretáceo-Paleógeno. Ademais, os SDRs aparecem aumentar sua largura e espessura do sul (UY), onde a espessura máxima é de cerca de 4 km, para o norte (BR), onde excedem 12 km (McDermott *et al.* 2019). Consequentemente, o gradiente geotérmico da área estudada foi potencialmente afetado durante o Cretáceo, considerando que a região estudada era uma “ilha” situada entre grandes unidades magmáticas. Infelizmente, os dados disponíveis não determinam de maneira precisa a duração dessa fase de reaquecimento.

No início da aparente fase de reaquecimento, após a ruptura, a taxa de sedimentação na Bacia de Pelotas parece ter atingido um pico (Fig. 4.4), o que sugere amplo aporte sedimentar e espaço de acomodação para sedimentação. Esse período é concomitante a uma época de nível de mar alto globalmente (Haq *et al.* 1987) e também pode estar ligado a uma subsidência significativa da bacia pós-rifte. Aslanian *et al.* (2009) sugerem, para as bacias do sudeste brasileiro, que o manto se movia horizontalmente de maneira rápida abaixo dessas bacias durante a ruptura continental, o que favoreceria um colapso quase que vertical de parte das bacias nos estágios iniciais pós-rifte. Um mecanismo de subsidência semelhante pode ter atuado na Bacia de Pelotas durante os estágios iniciais da deriva, o que, acompanhado pela subsidência térmica, criaria um substancial espaço de acomodação na bacia e sustentaria a perturbação do geotermo.

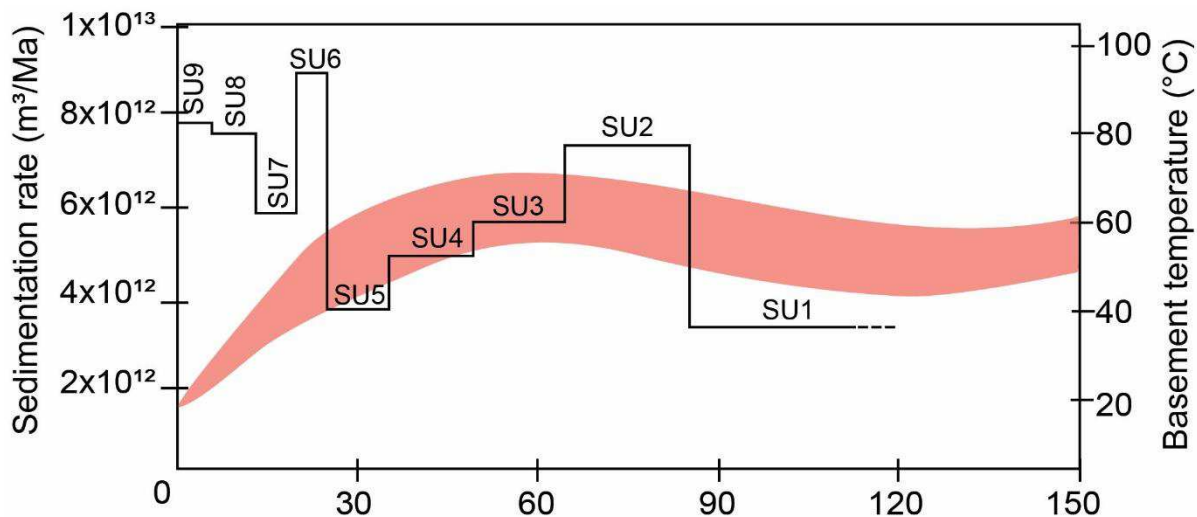


Figura 4.4: Correlação entre as taxas de sedimentação na Bacia de Pelotas (linhas pretas), de acordo com as unidades sísmicas definidas no Apêndice A1, e o padrão médio de resfriamento (curva vermelha) observado no Batólito de Pelotas (Fig. 6.7), adjacente à área da análise sísmica. O resfriamento final do embasamento próximo à margem começou entre 60 e 40 Ma, enquanto que um aumento substancial na taxa de sedimentação ocorreu em torno de 30 Ma. A aparente discrepância entre essas idades pode ser causada pelo tempo necessário entre a exumação, erosão, transporte e deposição dos sedimentos na bacia marginal.

O resfriamento final dos escudos às temperaturas da superfície começou no Paleogeno, entre c. 60 e 40 Ma. As estimativas volumétricas das sucessões da Bacia de Pelotas indicam um aumento abrupto nas taxas de sedimentação em torno de c. 30 Ma, o que pode estar ligado a uma aceleração no resfriamento/exumação do embasamento continental e maior disponibilidade de sedimentos para a bacia (Fig. 4.4). Considerando o tempo necessário entre exumação, erosão, transporte e deposição, é plausível que tal aumento esteja ligado, pelo menos em parte, ao resfriamento e soerguimento final dos escudos. Como sugerido por Salomon *et al.* (2015), a América do Sul está sob compressão devido à subducção no lado oeste do continente e a um fluxo astenosférico para oeste no lado leste do continente, a partir da dorsal Mesoatlântica. Desde a abertura do Atlântico Sul, a margem SE/S brasileira sofreu tensões de compressão associadas a movimentações em falhas transcorrentes. Isso pode ser uma consequência da flexão da margem combinada com a transmissão de tensões em toda a placa, relacionada à subducção da placa de Nazca sob a América do Sul durante o Paleogeno. Esse regime de tensão compressiva continuou durante o Neogeno, em função do soerguimento dos Andes e subducção em baixo ângulo da placa oceânica (Contreras *et al.* 2010; Salomon *et al.* 2015). Essa compressão pode ser o fator responsável pela exumação final do embasamento na região.

Estudos das formas de relevo costeiras na Argentina, a cerca de 2.000 km ao sul da Bacia de Pelotas, relacionam o desenvolvimento de terraços marinhos e barreiras costeiras nos últimos 0,4 Ma a ciclos do nível do mar e soerguimento tectônico com taxas entre 0,016 e 0,067 m/kyr (Pappalardo *et al.* 2015). Os sistemas laguna-barreira atualmente expostos da Bacia de Pelotas foram desenvolvidos no mesmo período de tempo (Rosa *et al.* 2017), e o resfriamento/soerguimento da parte leste do Escudo Sul-Rio-Grandense aqui estimados mostram taxas similares no Cenozoico (0,026 e 0,040 m/kyr). Embora essa coincidência sugira que a constante elevação continental nos últimos 40 Ma possa estar contribuindo para o desenvolvimento da morfologia costeira (e.g. Cone do Rio Grande, sistemas laguna-barreira da Bacia de Pelotas), a resolução dos modelos de termocronometria não é adequada para uma correlação indiscutível. Além disso, variações glacioeustáticas de alta frequência e processos autigênicos parecem ser dominantes na margem da Bacia de Pelotas (Rosa *et al.* 2017).

Em resumo, a história termotectônica da região estudada pode ser sintetizada da seguinte forma: 1) Resfriamento no Paleozoico tardio dos escudos Uruguai e Sul-Rio-Grandense, possivelmente causado pela exumação do embasamento devido aos efeitos das orogêneses na margem SW de Gondwana, 2) continuidade do resfriamento e exumação até temperatura próxima à superficial (< 60°C) no Mesozoico médio, provavelmente causada por soerguimento devido ao impacto da pluma mantélica Tristão da Cunha na região, anterior à abertura do Atlântico Sul; 3) no início do Cretáceo, volumoso magmatismo da Paraná-Etendeka LIP no norte e oeste dos escudos, seguido do rifteamento no leste e magmatismo na Bacia de Pelotas; 4) perturbação geotérmica positiva na região, causada pela contínua atividade ígnea, com um aumento discreto das temperaturas do embasamento durante o final do Cretáceo, 5) resfriamento Cenozoico dos escudos, com aumento da exumação do embasamento no Eoceno, possivelmente correlacionado a um aumento das taxas de sedimentação da Bacia de Pelotas a partir do Oligoceno, levando ao desenvolvimento de depósitos siliciclásticos espessos na margem.

4.4 Sugestões para pesquisas futuras

Como comumente ocorre em pesquisas científicas, a tentativa de responder a um questionamento levou à formulação de outros mais. Os resultados obtidos nesta pesquisa sugerem que o resfriamento e a elevação margem passiva da América do Sul ao longo do Uruguai e sul do Brasil começaram muito antes do rifteamento. Esse

segmento de margem mostra uma história termotectônica complexa, cujo início pode ser resultado de propagação de tensões ao longo da placa Sul-Americana devido à compressão na margem SW no final do Paleozoico, mas cuja a continuidade e clímax são prováveis consequências da dinâmica do manto relacionada à ruptura do Gondwana Ocidental no Mesozoico.

Para melhorar a compreensão da geodinâmica da região, são feitas algumas sugestões:

- Para determinar melhor a fase inicial de resfriamento do embasamento continental, termocronômetros de mais alta temperatura (e.g. traços de fissão em zircão) podem ser usados. Isso deve permitir uma determinação mais precisa da influência do ciclo Gondwanico na exumação do embasamento do Uruguai e do sul do Brasil durante o final do Paleozoico;
- Para refinar a história térmica recente, a datação por isótopos cosmogênicos pode ser aplicada ao embasamento continental. Estes representam o método de datação termocronométrica de menor temperatura e, como os dados aqui considerados sugerem temperaturas abaixo de 60 °C durante o Cenozoico, tal método pode fornecer importantes restrições para a exumação recente dos escudos, assim como sobre a contribuição sedimentar da erosão dos escudos no desenvolvimento da Bacia de Pelotas. Mais análises AHe provavelmente não aperfeiçoariam a história térmica recente;
- A aquisição de perfis sísmicos profundos que cortam os escudos das bacias de Pelotas e do Paraná, na direção E-W, tem o potencial de definir a espessura da crosta e a profundidade de Moho na região, auxiliando a determinar a exumação total da crosta durante e o seu estiramento durante o rifte;
- A perfuração de novos poços na Bacia de Pelotas pode melhorar a determinação da idade de cada unidade sísmica dentro da bacia. Se perfurados com profundidade suficiente, tais poços teriam o potencial para definir o embasamento econômico da Bacia de Pelotas e ajudar a distinguir entre o magmatismo das bacias do Paraná e Pelotas;
- O uso de informações dos *logs* de todos os poços da Bacia de Pelotas pode ajudar a estimar a variabilidade da porosidade, o que pode ser utilizado para restringir melhor os volumes e taxas de deposição de cada unidade sísmica.

Referências

- Amante, C., & Eakins, B. W. (2009).ETOPO1 arc-minute global relief model: procedures, data sources and analysis.
- Aslanian, D., Moulin, M., Olivet, J. L., Unternehr, P., Matias, L., Bache, F., ... & Labails, C. (2009). Brazilian and African passive margins of the Central Segment of the South Atlantic Ocean: Kinematic constraints. *Tectonophysics*, 468(1-4), 98-112.
- Basei, M.A.S., Neves, B. B. B., Junior, O. S., Babinski, M., Pimentel, M. M., Tassinari, C. C. G., ... & Cordani, U. G. (2010). Contribution of SHRIMP U-Pb zircon geochronology to unravelling the evolution of Brazilian Neoproterozoic fold belts. *Precambrian Research*, 183(1), 112-144.
- Barbieri, M., Beccaluva, L. et al. (1987). The phonolite suite from Piratini, RS. *Geochimica Brasiliensis*, 1, 109–138.
- Barboza, E. G., Rosa, M. L. C. C., & Ayup-Zouain, R. N. (2008). Cronoestratigrafia da Bacia de Pelotas: uma revisão das seqüências deposicionais. *Gravel*, 6(1), 125-138.
- Beglinger, S. E., Doust, H., & Cloetingh, S. (2012). Relating petroleum system and play development to basin evolution: West African South Atlantic basins. *Marine and Petroleum Geology*, 30(1), 1-25.
- Beri, Á., Gutiérrez, P. & Balarino, L. (2011). Palynostratigraphy of the late palaeozoic of Uruguay, paraná basin. *Review of Palaeobotany and Palynology*, 167, 16–29, <https://doi.org/10.1016/j.revpalbo.2011.05.004>.
- Bicca, M.M., Chemale, F., Jelinek, A.R., de Oliveira, C.H.E., Guadagnin, F. & Armstrong, R. (2013). Tectonic evolution and provenance of the Santa Bárbara Group, Camaquã Mines region, Rio Grande do Sul, Brazil. *Journal of South American Earth Sciences*, 48, 173–192, <https://doi.org/10.1016/j.jsames.2013.09.006>
- Blanco, G., Rajesh, H.M., Gaucher, C., Germs, G.J.B. & Chemale, F. (2009). Provenance of the Arroyo del Soldado Group (Ediacaran to Cambrian, Uruguay): Implications for the paleogeographic evolution of southwestern Gondwana. *Precambrian Research*, 171, 57–73, <https://doi.org/10.1016/j.precamres.2009.03.003>
- Bossi, J., Ferrando, L., Montaña, J., Campal, N., Morales, H., Gancio, F., Schipilov, A., Piñeyro, D., Sprechmann, P., (1998). Carta geológica del Uruguay. Escala 1:500.000. Geoeditores, Montevideo.
- Brown, R. W., Gallagher, K., Gleadow, A. J., & Summerfield, M.A. (2000). Morphotectonic evolution of the South Atlantic margins of Africa and South America. *Geomorphology and global tectonics*, 255-281.
- Brune, S., Williams, S.E., Butterworth, N.P. & Müller, R.D. (2016). Abrupt plate accelerations shape rifted continental margins. *Nature*, 536, 201–204, <https://doi.org/10.1038/nature18319>.
- Bueno, G.V., Zacharias, A.A., Oreiro, S.G., Cupertino, J.A., Falkenhein, F.U.H. & Martins Neto, M.A. (2007). Bacia de Pelotas. *Boletim de Geociencias da Petrobras*, 15, 551–559.
- Buiter, S. J., & Torsvik, T. H. (2014). A review of Wilson Cycle plate margins: A role for mantle plumes in continental break-up along sutures?. *Gondwana Research*, 26(2), 627-653.
- Carlson, W.D., Donelick, R.A. & Ketcham, R.A. (1999). Variability of apatite fission-track annealing kinetics; I, Experimental results. *American Mineralogist*, 84, 1213–1223, <https://doi.org/10.2138/am-1999-0901>

- Carneiro, C.D.R., de Almeida, F.F.M., Hasui, Y., Zalán, P.V. & Teixeira, J.B.G. (2012). Estágios evolutivos do Brasil no Fanerozoico. In: Hasui, Y., Carneiro, C.D.R., de Almeida, F.F.M. & Bartorelli, A. (eds) *Geologia do Brasil*. Beca, São Paulo, 131–137.
- Ceolin, D., Fauth, G., & Coimbra, J. C. (2011). Cretaceous–Lower Paleogene ostracods from the Pelotas Basin, Brazil. *Palaeobiodiversity and Palaeoenvironments*, 91(2), 111-128.
- Cernuschi, F., Dilles, J.H., Kent, A.J.R., Schroer, G., Raab, A.K., Conti, B. & Muzio, R. (2015). Geology, geochemistry and geochronology of the Cretaceous Lascano East intrusive complex and magmatic evolution of the Laguna Merín basin, Uruguay. *Gondwana Research*, 28, 837–857, <https://doi.org/10.1016/j.gr.2014.07.007>.
- Chang, H.K., Kowsmann, R.O., Figueiredo, A.M.F. & Bender, A.A. (1992). Tectonics and stratigraphy of the East Brazil Rift system: an overview. *Tectonophysics*, 213, 97–138, [https://doi.org/10.1016/0040-1951\(92\)90253-3](https://doi.org/10.1016/0040-1951(92)90253-3)
- Chemale, F. (2000). Evolução geológica do Escudo Sul-rio-grandense. In: Holz, M. & De Ros, L.F. (eds) *Geologia do Rio Grande do Sul*. Universidade Federal do Rio Grande do Sul, Porto Alegre, 13–52.
- Cogné, N., Gallagher, K. & Cobbold, P.R. (2011). Post-rift reactivation of the onshore margin of southeast Brazil: Evidence from apatite (U–Th)/He and fission-track data. *Earth and Planetary Science Letters*, 309, 118–130, <https://doi.org/10.1016/j.epsl.2011.06.025>
- Cogné, N., Gallagher, K., Cobbold, P.R., Riccomini, C. & Gautheron, C. (2012). Post-breakup tectonics in southeast Brazil from thermochronological data and combined inverse–forward thermal history modeling. *Journal of Geophysical Research B: Solid Earth*, 117, 1–16, <https://doi.org/10.1029/2012JB009340>
- Colli, L., Stotz, I., Bunge, H. P., Smethurst, M., Clark, S., Iaffaldano, G., ... & Bianchi, M. C. (2014). Rapid South Atlantic spreading changes and coeval vertical motion in surrounding continents: Evidence for temporal changes of pressure-driven upper mantle flow. *Tectonics*, 33(7), 1304-1321.
- Comin-Chiaromonti, P., Gomes, C. B., Censi, P., Gasparon, M., & Velázquez, V. F. (2005). Alkaline complexes from the Alto Paraguay province at the border of Brazil (Mato Grosso do Sul State) and Paraguay. *Mesozoic to Cenozoic alkaline magmatism in the Brazilian Platform*. São Paulo: Edusp/Fapesp, 71-148.
- Contreras, J., Zühlke, R., Bowman, S., & Bechstädt, T. (2010). Seismic stratigraphy and subsidence analysis of the southern Brazilian margin (Campos, Santos and Pelotas basins). *Marine and Petroleum Geology*, 27(9), 1952-1980.
- Cordani, U. G., Melcher, G. C., & Almeida, F. D. (1968). Outline of the Precambrian geochronology of South America. *Canadian Journal of Earth Sciences*, 5(3), 629-632.
- CPRM. (2010). *Projeto Aerogeofísico Escudo do Rio Grande do Sul*, CPRM– Serviço Geológico do Brasil, Brasília, <http://rigeo.cprm.gov.br/jspui/handle/doc/10948>
- de Almeida, F. F. M., Hasui, Y., de Brito Neves, B. B., & Fuck, R. A. (1981). Brazilian structural provinces: an introduction. *Earth-Science Reviews*, 17(1-2), 1-29.
- de Almeida, F. F. M., & Hasui, Y. (1984). *O pré-cambriano do Brasil*. Editora Edgard Blücher.
- de Almeida, F. F. M., Carneiro, C. D. R., & Bartorelli, A. (2012). Magmatismo pós-paleozoico no Brasil. *Geologia do Brasil*. São Paulo: Beca, 430-452.
- de Borba, A.W., Vignol-Lelarge, M.L.M. & Mizusaki, A.M.P. (2002). Uplift and denudation of the Caçapava do Sul granitoids (southern Brazil) during Late Paleozoic and Mesozoic: constraints from

- apatite fission-track data. *Journal of South American Earth Sciences*, 15, 683–692, [https://doi.org/10.1016/S0895-9811\(02\)00086-X](https://doi.org/10.1016/S0895-9811(02)00086-X)
- de Borba, A.W. & Mizusaki, A.M.P. (2003). Santa Bárbara Formation (Caçapava do Sul, southern Brazil): depositional sequences and evolution of an Early Paleozoic postcollisional basin. *Journal of South American Earth Sciences*, 16, 365–380, [https://doi.org/10.1016/S0895-9811\(03\)00102-0](https://doi.org/10.1016/S0895-9811(03)00102-0)
- de Borba, A.W., De Lima, E.F., Vignol-Lelarge, M.L.M., Mizusaki, A.M.P., Sparrenberg, I.&de Barros, C.E. (2003). Significance of Late Paleozoic fissiontrack ages in volcanic rocks from the Lavras do Sul Region, southernmost Brazil. *Gondwana Research*, 6, 79–88, [https://doi.org/10.1016/S1342-937X\(05\)70645-6](https://doi.org/10.1016/S1342-937X(05)70645-6)
- de Brito Neves, B. B., & Fuck, R. A. (2014). The basement of the South American platform: Half Laurentian (N-NW)+ half Gondwanan (E-SE) domains. *Precambrian Research*, 244, 75–86.
- de Oliveira, C.H.E., Jelinek, A.R., Chemale, F. & Bernet, M. (2016). Evidence of post-Gondwana breakup in Southern Brazilian Shield: Insights from apatite and zircon fission track thermochronology. *Tectonophysics*, 666, 173–187, <https://doi.org/10.1016/j.tecto.2015.11.005>
- de Oliveira, C.H.E., Chemale, F., Jelinek, A.R., Bicca, M.M. & Philipp, R.P. (2014). U–Pb and Lu–Hf isotopes applied to the evolution of the late to postorogenic transtensional basins of the Dom Feliciano belt, Brazil. *Precambrian Research*, 246, 240–255, <https://doi.org/10.1016/j.precamres.2014.03.008>
- de Oliveira, C.H.E., Jelinek, A.R., Chemale, F. & Bernet, M. (2016). Evidence of post-Gondwana breakup in Southern Brazilian Shield: Insights from apatite and zircon fission track thermochronology. *Tectonophysics*, 666, 173–187, <https://doi.org/10.1016/j.tecto.2015.11.005>
- de Santa Ana, H., Veroslavsky, G., Fúlfaro, V., Rossello, E. (2006). Cuenca Norte: evolución tectónica y sedimentaria del Carbonífero-Pérmino. En: Veroslavsky, G., Ubilla, M., Martínez, S. (Eds.): *Cuencas sedimentarias de Uruguay. Paleozoico*. Facultad de Ciencias, Montevideo, pp. 209–244.
- Dias, J. L., Sad, A. R., Fontana, R. L., & Feijó, F. J. (1994). Bacia de Pelotas. Boletim de Geociências da PETROBRAS, 8(1), 235–245.
- Donelick, R.A. (1993). Method of fission track analysis utilizing bulk chemical etching of apatite, U.S. Patent No. 5,267,274. 30 Nov. 1993.
- Donelick, R.A., Ketcham, R.A. & Carlson, W.D. (1999). Variability of apatite fission-track annealing kinetics; II, Crystallographic orientation effects. *American Mineralogist*, 84, 1213–1223, <https://doi.org/10.2138/am-1999-0901>
- Donelick, R.A., O'Sullivan, P.B. & Ketcham, R.A. (2005). Apatite fission-track analysis. In: Reiners, P.W. & Ehlers, T.A. (eds) *Low-Temperature Thermochronology: Techniques, Interpretations, and Applications*. Mineralogical Society of America and Geochemical Society, Reviews in Mineralogy and Geochemistry, 58, 49–94.
- Farley, K.A., Wolf, R.A. & Silver, L.T. (1996). The effects of long alpha-stopping distances on (U–Th)/He ages. *Geochimica et Cosmochimica Acta*, 60, 4223–4229, [https://doi.org/10.1016/S0016-7037\(96\)00193-7](https://doi.org/10.1016/S0016-7037(96)00193-7)
- Farley, K.A. (2000). Helium diffusion from apatite: General behavior as illustrated by Durango fluorapatite. *Journal of Geophysical Research: Solid Earth*, 105, 2903–2914, <https://doi.org/10.1029/1999JB900348>

- Farley, K.A. (2002). (U-Th)/He Dating: Techniques, Calibrations, and Applications. *Reviews in Mineralogy and Geochemistry*, 47, 819–844, <https://doi.org/10.2138/rmg.2002.47.18>.
- Fleischer, R.L., Price, P.B. & Walker, R.M. (1975). Nuclear Tracks in Solids: Principles and Applications. University of California. Press, Berkeley.
- Florisbal, L.M., Heaman, L.M., de Janasi, V.A. & de Bitencourt, M.F. (2014). Tectonic significance of the Florianópolis Dyke Swarm, Paraná–Etendeka Magmatic Province: A reappraisal based on precise U–Pb dating. *Journal of Volcanology and Geothermal Research*, 289, 140–150, <https://doi.org/10.1016/j.jvolgeores.2014.11.007>
- Flowers, R.M., Ketcham, R.A., Shuster, D.L. & Farley, K.A. (2009). Apatite (U–Th)/He thermochronometry using a radiation damage accumulation and annealing model. *Geochimica et Cosmochimica Acta*, 73, 2347–2365, <https://doi.org/10.1016/j.gca.2009.01.015>
- Flowers, R.M. & Kelley, S.A. (2011). Interpreting data dispersion and ‘inverted’ dates in apatite (U–Th)/He and fission-track datasets: An example from the US midcontinent. *Geochimica et Cosmochimica Acta*, 75, 5169–5186, <https://doi.org/10.1016/j.gca.2011.06.016>
- Galbraith, R.F. (1981). On statistical models for fission track counts. *Journal of the International Association for Mathematical Geology*, 13, 471–478, <https://doi.org/10.1007/BF01034498>
- Galbraith, R.F. & Green, P.F. (1990). Estimating the component ages in a finite mixture. *International Journal of Radiation Applications and Instrumentation, Part D*, 17, 197–206, [https://doi.org/10.1016/1359-0189\(90\)90035-V](https://doi.org/10.1016/1359-0189(90)90035-V)
- Galbraith, R.F., Laslett, G.M., Green, P.F. & Duddy, I.R. (1990). Apatite fission track analysis: geological thermal history analysis based on a three-dimensional random process of linear radiation damage. *Philosophical Transactions of the Royal Society of London, Series A*, 332, 419–438, <https://doi.org/10.1098/rsta.1990.0124>
- Gallagher, K., Hawkesworth, C.J. & Mantovani, M.S.M. (1994). The denudation history of the onshore continental margin of SE Brazil inferred from apatite fission track data. *Journal of Geophysical Research: Solid Earth*, 99, 18117–18145, <https://doi.org/10.1029/94JB00661>
- Gallagher, K., Hawkesworth, C. & Mantovani, M.S. (1995). Denudation, fission track analysis and the long-term evolution of passive margin topography: application to the southeast Brazilian margin. *Journal of South American Earth Sciences*, 8, 65–77, [https://doi.org/10.1016/0895-9811\(94\)00042-Z](https://doi.org/10.1016/0895-9811(94)00042-Z)
- Gallagher, K., Brown, R. & Johnson, C. (1998). Fission track analysis and its applications to geological problems. *Annual Review of Earth and Planetary Science*, 26, 519–572, <https://doi.org/10.1146/annurev.earth.26.1.519>
- Gallagher, K., Charvin, K., Nielsen, S., Sambridge, M. & Stephenson, J. (2009). Markov chain Monte Carlo (MCMC) sampling methods to determine optimal models, model resolution and model choice for Earth Science problems. *Marine and Petroleum Geology*, 26, 525–535, <https://doi.org/10.1016/j.marpetgeo.2009.01.003>
- Gallagher, K. (2012). Transdimensional inverse thermal history modeling for quantitative thermochronology. *Journal of Geophysical Research: Solid Earth*, 117, 1–16, <https://doi.org/10.1029/2011JB008825>
- Gaucher, C., Nóbrega Sial, A., Blanco, G. & Sprechmann, P. (2004). Chemostratigraphy of the lower Arroyo del soldado group (Vendian, Uruguay) and palaeoclimatic implications. *Gondwana Research*, 7, 715–730, [https://doi.org/10.1016/S1342-937X\(05\)71058-3](https://doi.org/10.1016/S1342-937X(05)71058-3).

- Gaucher, C., Babinski, M., Blanco, G. (2016). Riolitas del Cretácico Superior (Campaniense); el magmatismo más joven de Uruguay. In: *VIII Congreso Uruguayo de Geología, Actas*, pp. 160-161, Montevideo.
- Gladczenko, T. P., Hinz, K., Eldholm, O., Meyer, H., Neben, S., & Skogseid, J. (1997). South Atlantic volcanic margins. *Journal of the Geological Society*, 154(3), 465-470.
- Gleadow, A.J.W. (1981). Fission-track dating methods: What are the real alternatives? *Nuclear Tracks*, 5, 3–14, [https://doi.org/10.1016/0191-278X\(81\)90021-4](https://doi.org/10.1016/0191-278X(81)90021-4)
- Gleadow, A.J.W., Duddy, I.R., Green, P.F. & Hegarty, K.A. (1986a). Fission track lengths in the apatite annealing zone and the interpretation of mixed ages. *Earth and Planetary Science Letters*, 78, 245–254, [https://doi.org/10.1016/0012-821X\(86\)90065-8](https://doi.org/10.1016/0012-821X(86)90065-8)
- Gleadow, A.J.W., Duddy, I.R., Green, P.F. & Lovering, J.F. (1986b). Confined fission track lengths in apatite: a diagnostic tool for thermal history analysis. *Contributions to Mineralogy and Petrology*, 94, 405–415, <https://doi.org/10.1007/BF00376334>
- Green, P.F. (1986). On the thermo-tectonic evolution of Northern England: Evidence from fission track analysis. *Geological Magazine*, 123, 493–506, <https://doi.org/10.1017/S0016756800035081>
- Gomes, C.H. & Almeida, D. (2019). New insights into the Gondwana breakup at the Southern South America by apatite fission-track analyses. *Advances in Geosciences*, 47, 1–15, <https://doi.org/10.5194/adgeo-47-1-2019>.
- Graça, M. C., Kusznir, N., & Stanton, N. S. G. (2019). Crustal thickness mapping of the central South Atlantic and the geodynamic development of the Rio Grande Rise and Walvis Ridge. *Marine and Petroleum Geology*, 101, 230-242.
- Granot, R., & Dymant, J. (2015). The Cretaceous opening of the South Atlantic Ocean. *Earth and Planetary Science Letters*, 414, 156-163.
- Guenther, W.R., Reiners, P.W., Ketcham, R.A., Nasdala, L. & Giester, G. (2013). Helium diffusion in natural zircon: radiation damage, anisotropy, and the interpretation of zircon (U-Th)/He thermochronology. *American Journal of Science*, 313, 145–198, <https://doi.org/10.2475/03.2013.01>
- Hackspacher, P.C., Ribeiro, L.F.B., Ribeiro, M.C.S., Fetter, A.H., Hadler Neto, J.C., Tello, C.E.S. & Dantas, E.L. (2004). Consolidation and break-up of the South American Platform in southeastern Brazil: Tectonothermal and denudation histories. *Gondwana Research*, 7, 91–101, [https://doi.org/10.1016/S1342-937X\(05\)70308-7](https://doi.org/10.1016/S1342-937X(05)70308-7)
- Hackspacher, P.C., Godoy, D., Ribeiro, L.F.B., Hadler Neto, J.C. & Franco, A.O.B. (2007). Modelagem térmica e geomorfologia da borda sul do Cráton do São Francisco: termocronologia por traços de fissão em apatita. *Revista Brasileira de Geociências*, 37, 76–86.
- Haq, B. U., Hardenbol, J. A. N., & Vail, P. R. (1987). Chronology of fluctuating sea levels since the Triassic. *Science*, 235(4793), 1156-1167.
- Hartmann, L.A., Campal, N., Santos, J.O.S., McNaughton, N.J., Bossi, J., Schipilov, A. & Lafon, J.M. (2001). Archean crust in the Rio de la Plata Craton, Uruguay – SHRIMP U–Pb zircon reconnaissance geochronology. *Journal of South American Earth Sciences*, 14, 557–570, [https://doi.org/10.1016/S0895-9811\(01\)00055-4](https://doi.org/10.1016/S0895-9811(01)00055-4)
- Hartmann, L.A., Lopes, W.R. & Savian, J.F. (2016). Integrated evaluation of the geology, aerogammaspectrometry and aeromagnetometry of the Sul-Riograndense Shield, southernmost

- Brazil. *Anais da Academia Brasileira de Ciências*, 88, 75–92, <https://doi.org/10.1590/0001-3765201520140495>
- Hasui, Y. (2010). A grande colisão Pré-Cambrian do sudeste brasileiro e a estruturação regional. *Geociências – UNESP*, 29, 141–169.
- Hasui, Y. (2012). Sistema Orogenico Mantiqueira. In: Hasui, Y., Carneiro, C.D.R., de Almeida, F.F.M. & Bartorelli, A. (eds) *Geologia Do Brasil*. Beca, São Paulo, 331–373.
- Heilbron, M., Pedrosa-Soares, A. C., Campos Neto, M. C., Silva, L. C., & Trouw, R. A. J., Janasi V. (2004). A Província Mantiqueira. *Geologia do Continente Sul-Americanano: Evolução da Obra de Fernando Flávio Marques de Almeida*. São Paulo, Beca, 203-234.
- Hiruma, S.T., Riccomini, C., Modenesi-Gauttieri, M.C., Hackspacher, P.C., Neto, J.C.H. & Franco-Magalhães, A.O.B. (2010). Denudation history of the Bocaina Plateau, Serra do Mar, southeastern Brazil: Relationships to Gondwana breakup and passive margin development. *Gondwana Research*, 18, 674–687, <https://doi.org/10.1016/j.gr.2010.03.001>
- Hueck, M., Oriolo, S. et al. (2017). Phanerozoic low-temperature evolution of the Uruguayan Shield along the South American passive margin. *Journal of the Geological Society*, London, 174, 609–626, <https://doi.org/10.1144/jgs2016-101>
- Hurford, A.J. & Green, P.F. (1983). The zeta age calibration of fission-track dating. *Chemical Geology*, 41, 285–317, [https://doi.org/10.1016/S0009-2541\(83\)80026-6](https://doi.org/10.1016/S0009-2541(83)80026-6)
- Hurford, A.J. (1990). Standardization of fission-track dating calibration – recommendation by the Fission-Track Working Group of the IUGS Subcommission on Geochronology. *Chemical Geology*, 80, 171–178, [https://doi.org/10.1016/0168-9622\(90\)90025-8](https://doi.org/10.1016/0168-9622(90)90025-8)
- Jelinek, A.R., Cezar, A., Neto, B. & Poupeau, G. (2003). Análise por traços de fissão em apatitas do distrito fluorítico de Santa Catarina: relações entre hidrotermalismo e evolução da margem continental. *Revista Brasileira de Geociências*, 33, 289–298.
- Karl, M., Glasmacher, U.A., Kollenz, S., Franco-Magalhaes, A.O.B., Stockli, D.F. & Hackspacher, P.C. (2013). Evolution of the South Atlantic passive continental margin in southern Brazil derived from zircon and apatite (U-Th- Sm)/He and fission-track data. *Tectonophysics*, 604, 224–244, <https://doi.org/10.1016/j.tecto.2013.06.017>
- Ketcham, R.A., Carter, A., Donelick, R.A., Barbarand, J. & Hurford, A.J. (2007). Improved modeling of fission-track annealing in apatite. *American Mineralogist*, 92, 799–810, <https://doi.org/10.2138/am.2007.2281>
- Kollenz, S. (2015). Long-Term Landscape Evolution, Cooling and Exhumation History of the South American Passive Continental Margin in NE Argentina & SW Uruguay. *Dissertation zur Erlangung der Doktorwürde der Naturwissenschaftlich-Mathematischen*, Gesamtfakultät der Ruprecht-Karls-Universität, Heidelberg.
- Kollenz, S., Glasmacher, U.A., Rossello, E.A., Stockli, D.F., Schad, S. & Pereyra, R.E. (2017). Thermochronological constraints on the Cambrian to recent geological evolution of the Argentina passive continental margin. *Tectonophysics*, 716, 182–203, <https://doi.org/10.1016/j.tecto.2016.11.019>.
- Lal, D., Rajan, R.S. & Tamhane, A.S. (1969). Chemical composition of nuclei of $z>22$ in cosmic rays using meteoritic minerals as detectors. *Nature*, 211, 33–37, <https://doi.org/10.1038/221033a0>

- Maraschin, A.J., Mizusaki, A.M., Zwingmann, H., de Borba, A.W. & Sbrissa, G.F. (2010). Illite authigenesis in sandstones of the Guaritas Allogroup (Early Paleozoic): Implications for the depositional age, stratigraphy and evolution of the Camaquã Basin (Southern Brazil). *Journal of South American Earth Sciences*, 29, 400–411, <https://doi.org/10.1016/j.jsames.2009.07.007>
- McDermott, C., Collier, J. S., Lonergan, L., Fruehn, J., & Bellingham, P. (2019). Seismic velocity structure of seaward-dipping reflectors on the South American continental margin. *Earth and Planetary Science Letters*, 521, 14-24.
- Milani, E.J. (1997). Evolução Tectono-Estratigráfica da Bacia do Paraná e Seu Relacionamento com a Geodinâmica Fanerozóica do Gondwana Sul- Ocidental. *Tese de doutorado*. Universidade Federal do Rio Grande do Sul, Porto Alegre.
- Milani, E. J. & Ramos, V. A. (1998). Orogenias paleozóicas no domínio sul-ocidental do Gondwana e os ciclos de subsidência da Bacia do Paraná. *Revista Brasileira de Geociências*, 28(4), 473-484.
- Milani, E.J., de Melo, J.H.G., De Souza, P.A., Fernandes, L.A. & França, A.B. (2007). Bacia do Paraná. *Boletim de Geociências da Petrobras*, 8, 265–287.
- Milani, E.J. & De Wit, M.J. (2008). Correlations between the classic Paraná and Cape-Karoo sequences of South America and southern Africa and their basin infills flanking the Gondwanides: du Toit revisited. In: Pankhurst, R.J., Trouw, R.A.J., de Brito Neves, B.B. & de Wit, M.J. (eds) *West Gondwana: Pre- Cenozoic Correlations across the South Atlantic Region*. Geological Society, London, Special Publications, 294, 319–342, <https://doi.org/10.1144/SP294.17>
- Miller, D.J., Ketzer, J.M. et al. (2015). Natural gas hydrates in the Rio Grande Cone (Brazil): A new province in the western South Atlantic. *Marine and Petroleum Geology*, 67, 187–196, <https://doi.org/10.1016/j.marpetgeo.2015.05.012>
- Mizusaki, A. M. P., Thomaz filho, A., & De Cesero, P. (1998). Ages of the magmatism and the opening of the South Atlantic Ocean. *Pesquisas em Geociências*, 25(2), 47-57.
- Mohriak, W., Nemčok, M., & Enciso, G. (2008). South Atlantic divergent margin evolution: rift-border uplift and salt tectonics in the basins of SE Brazil. *Geological Society, London, Special Publications*, 294(1), 365-398.
- Mohriak, W. U., Nóbrega, M., Odegard, M. E., Gomes, B. S., & Dickson, W. G. (2010). Geological and geophysical interpretation of the Rio Grande Rise, south-eastern Brazilian margin: extensional tectonics and rifting of continental and oceanic crusts. *Petroleum Geoscience*, 16 (3): 231-245.
- Mohriak, W. (2012). Bacias da Margem Continental Divergente. *Geologia do Brasil*. São Paulo, Beca, 466-480.
- Morales, E., Chang, H.K., et al. (2017). Tectonic and stratigraphic evolution of the Punta del Este and Pelotas basins (offshore Uruguay). *Petroleum Geoscience*, 23, 415–426, <https://doi.org/10.1144/petgeo2016-059>.
- Nasdala, L., Reiners, P.W., Garver, J.I., Kennedy, A.K., Stern, R.A., Balan, E. & Wirth, R. (2004). Incomplete retention of radiation damage in zircon from Sri Lanka. *American Mineralogist*, 89, 219–231, <https://doi.org/10.2138/am-2004-0126>.
- Nürnberg, D., & Müller, R. D. (1991). The tectonic evolution of the South Atlantic from Late Jurassic to present. *Tectonophysics*, 191(1-2), 27-53.

- Oriolo, S., Oyhantçabal, P., Wemmer, K., & Siegesmund, S. (2017). Contemporaneous assembly of Western Gondwana and final Rodinia break-up: Implications for the supercontinent cycle. *Geoscience Frontiers*, 8(6), 1431-1445.
- Paim, P.S.G., Chemale, F. & Wildner, W. (2014). Estágios evolutivos da Bacia do Camaquã (RS). *Ciência e Natura*, 36, 1–11, <https://doi.org/10.5902/2179460X13748>
- Pappalardo, M., Aguirre, M., Bini, M., Consoloni, I., Fucks, E., Hellstrom, J., ... & Zanchetta, G. (2015). Coastal landscape evolution and sea-level change: a case study from Central Patagonia (Argentina). *Zeitschrift für Geomorphologie*, 59(2), 145-172.
- Pereira, E., Carneiro, C. D. R., Bergamaschi, S., & Almeida, F. D. (2012). Evolução das Sinéclises Paleozoicas: Províncias Solimões, Amazonas, Parnaíba e Paraná. *Geologia do Brasil*, 374-394.
- Pérez-Díaz, L., & Eagles, G. (2014). Constraining South Atlantic growth with seafloor spreading data. *Tectonics*, 33(9), 1848-1873.
- Philipp, R.P., Massonne, H.J. & de Campos, R.S. (2013). Peraluminous leucogranites of the Cordilheira Suite: A record of Neoproterozoic collision and the generation of the Pelotas Batholith, Dom Feliciano Belt, Southern Brazil. *Journal of South American Earth Sciences*, 43, 8–24, <https://doi.org/10.1016/j.jsames.2012.10.006>
- Pollard, D. D., Allmendinger, R., & Brandon, M. T. (2003). New departures in structural geology and tectonics. <http://pangea.stanford.edu/~dpollard/NSF/main.html>
- Ponte, F. C., & Asmus, H. E. (2004). As bacias marginais brasileiras: estágio atual de conhecimento. *Boletim de Geociências da Petrobras*, 12(2), 385-420.
- Price, P.B. & Walker, R.M. (1963). Fossil tracks of charged particles in mica and the age of minerals. *Journal of Geophysical Research*, 68, 4847–4862, <https://doi.org/10.1029/JZ068i016p04847>
- Quirk, D.G. & Rüpke, L.H. (2018). Melt-induced buoyancy may explain the elevated rift-rapid sag paradox during breakup of continental plates. *Scientific Reports*, 8, 9985, <https://doi.org/10.1038/s41598-018-27981-2>
- Reiners, P.W. & Farley, K.A. (2001). Influence of crystal size on apatite (U–Th)/He thermochronology: An example from the Bighorn Mountains, Wyoming. *Earth and Planetary Science Letters*, 188, 413–420, [https://doi.org/10.1016/S0012-821X\(01\)00341-7](https://doi.org/10.1016/S0012-821X(01)00341-7)
- Reiners, P.W., Farley, K.A. & Hickes, H.J. (2002). He diffusion and (U–Th)/He thermochronometry of zircon: Initial results from Fish Canyon Tuff and Gold Butte. *Tectonophysics*, 349, 297–308, [https://doi.org/10.1016/S0040-1951\(02\)00058-6](https://doi.org/10.1016/S0040-1951(02)00058-6)
- Reiners, P.W., Spell, T.L., Nicolescu, S. & Zanetti, K.A. (2004). Zircon (U–Th)/He thermochronometry: He diffusion and comparisons with 40Ar/39Ar dating. *Geochimica et Cosmochimica Acta*, 68, 1857–1887, <https://doi.org/10.1016/j.gca.2003.10.021>
- Reiners, P.W. (2005). Zircon (U–Th)/He thermochronometry. In: Reiners, P.W. & Ehlers, T.A. (eds) *Low-temperature Thermochronology: Techniques, Interpretations, and Applications*. Mineralogical Society of America and Geochemical Society, Reviews in Mineralogy and Geochemistry, 58, 151–179, <https://doi.org/10.2138/rmg.2005.58.6>
- Reiners, P. W., Carlson, R. W., Renne, P. R., Cooper, K. M., Granger, D. E., McLean, N. M., & Schoene, B. (2018). *Geochronology and thermochronology*. John Wiley & Sons.

- Renne, P.R., Deckart, K., Ernesto, M., Fe'raud, G. & Piccirillo, E.M. (1996). Age of the Ponta Grossa dike swarm (Brazil), and implications to Paraná flood volcanism. *Earth and Planetary Science Letters*, 144, 199–211, [https://doi.org/10.1016/0012-821X\(96\)00155-0](https://doi.org/10.1016/0012-821X(96)00155-0)
- Rosa, M. L. C. D. C., Barboza, E. G., Abreu, V. D. S., Tomazelli, L. J., & Dillenburg, S. R. (2017). High-Frequency Sequences in the Quaternary of Pelotas Basin (coastal plain): a record of degradational stacking as a function of longer-term base-level fall. *Brazilian Journal of Geology*, 47(2), 183-207.
- Rossello, E.A., De Santa Ana, H. & Veroslavsky, G. (2000). El lineamiento Santa Lucia-Aigua-Merín (Uruguay): un corredor tectónico extensivo y transcurrente dextral precuros de la apertura atlantica. *Revista Brasileira de Geociências*, 30, 749–756.
- Rossello, E.A., Veroslavsky, G., Masquelin, H. & De Santa Ana, H. (2007). El corredor juro-cretácico Santa Lucía-Aiguá-Merín (Uruguay): Evidencias cinemática transcurrente dextral y controles preexistentes. *Revista de la Asociacion Geologica Argentina*, 62, 92–104.
- Rossetti, L.M., Lima, E.F., Waichel, B.L., Scherer, C.M. & Barreto, C.J. (2014). Stratigraphical framework of basaltic lavas in Torres Syncline main valley, southern Parana-Etendeka Volcanic Province. *Journal of South American Earth Sciences*, 56, 409–421, <https://doi.org/10.1016/j.jsames.2014.09.025>
- Rossetti, L.M., (2018). Lithostratigraphy and Geochemistry of the Paraná-Etendeka Large Igneous Province and Constraints on the Petrophysical Properties of Volcano-sedimentary Sequences. *PhD Thesis*. University of Aberdeen.
- Sprechmann, P., Montaña, J., Gaucher, C. (1993). Devónico. In: Bossi, J. (Ed.): *Geología y Recursos Minerales del Departamento de Durazno*. Intendencia Municipal de Durazno y Cátedra de Geología de la Facultad de Agonomía, Montevideo, pp. 25-55.
- Saenz, C.A.T., Hackspacher, P.C., Hadler Neto, J.C., Iunes, P.J., Guedes, S., Ribeiro, L.F.B. & Paulo, S.R. (2003). Recognition of Cretaceous, Paleocene, and Neogene tectonic reactivation through apatite fission-track analysis in Precambrian areas of southeast Brazil: association with the opening of the South Atlantic Ocean. *Journal of South American Earth Sciences*, 15, 765–774, [https://doi.org/10.1016/S0895-9811\(02\)00131-1](https://doi.org/10.1016/S0895-9811(02)00131-1)
- Salomon, E., Passchier, C., & Koehn, D. (2017). Asymmetric continental deformation during South Atlantic rifting along southern Brazil and Namibia. *Gondwana Research*, 51, 170-176.
- Santos, J. O., Chernicoff, C. J., Zappettini, E. O., McNaughton, N. J., Greau, Y. (2017). U-Pb geochronology of Martín García, Sola, and Dos Hermanas Islands (Argentina and Uruguay): Unveiling Rhyacian, Statherian, Ectasian, and Stenian of a forgotten area of the Río de la Plata Craton. *Journal of South American Earth Sciences*, 80, 207-228.
- Scherer, C.M. (2000). Eolian dunes of the Botucatu Formation (Cretaceous) in southernmost Brazil: morphology and origin. *Sedimentary Geology*, 137, 63–84, [https://doi.org/10.1016/S0037-0738\(00\)00135-4](https://doi.org/10.1016/S0037-0738(00)00135-4)
- Shuster, D.L., Flowers, R.M. & Farley, K.A. (2006). The influence of natural radiation damage on helium diffusion kinetics in apatite. *Earth and Planetary Science Letters*, 249, 148–161, <https://doi.org/10.1016/j.epsl.2006.07.028>
- Soares, C.J., Guedes, S., Jonckheere, R., Hadler, J.C., Passarella, S.M. & Dias, A.N.C. (2016). Apatite fission-track analysis of Cretaceous alkaline rocks of Ponta Grossa and Alto Paranaíba Arches, Brazil. *Geological Journal*, 51, 805–810, <https://doi.org/10.1002/gj.2694>

- Soto, M., Morales, E., Veroslavsky, G., de Santa Ana, H., Ucha, N. & Rodríguez, P. (2011). The continental margin of uruguay: Crustal architecture and segmentation. *Marine and Petroleum Geology*, 28, 1676–1689, <https://doi.org/10.1016/j.marpetgeo.2011.07.001>.
- Sprechmann, P., Bossi, J., Da Silva, J. (1981). Cuencas del Jurásico y Cretácico del Uruguay. In: Volkheimer, W., Musacchio (Eds.) *Cuencas sedimentarias del Jurásico y Cretácico de América del Sur*, 1, pp. 239-270, Buenos Aires.
- Stica, J.M., Zalán, P.V. & Ferrari, A.L. (2014). The evolution of rifting on the volcanic margin of the Pelotas Basin and the contextualization of the Paraná–Etendeka LIP in the separation of Gondwana in the South Atlantic. *Marine and Petroleum Geology*, 50, 1–21, <https://doi.org/10.1016/j.marpetgeo.2013.10.015>
- Stockli, D.F. (2005). Application of low-temperature thermochronometry to extensional tectonic settings. In: Reiners, P.W. & Ehlers, T.A. (eds) *Low-Temperature Thermochronology: Techniques, Interpretations, and Applications*. Mineralogical Society of America and Geochemical Society, Reviews in Mineralogy and Geochemistry, 58, 411–448.
- Stollhofen, H., Stanistreet, I. G., Bangert, B., & Grill, H. (2000). Tuffs, tectonism and glacially related sea-level changes, Carboniferous–Permian, southern Namibia. *Palaeogeography, Palaeoclimatology, Palaeoecology*, 161(1-2), 127-150.
- Tagami, T. & O'Sullivan, P.B. (2005). Fundamentals of fission-track thermochronology. In: Reiners, P.W. & Ehlers, T.A. (eds) *Low-Temperature Thermochronology: Techniques, Interpretations, and Applications*. Mineralogical Society of America and Geochemical Society, Reviews in Mineralogy and Geochemistry, 58, 19–48.
- Trouw, R. A., & De Wit, M. J. (1999). Relation between the Gondwanide Orogen and contemporaneous intracratonic deformation. *Journal of African Earth Sciences*, 28(1), 203-213.
- Turner, S., Regelous, M., Kelley, S., Hawkesworth, C. & Mantovani, M. (1994). Magmatism and continental break-up in the South Atlantic: high precision ^{40}Ar – ^{39}Ar geochronology. *Earth and Planetary Science Letters*, 121, 333–348, [https://doi.org/10.1016/0012-821X\(94\)90076-0](https://doi.org/10.1016/0012-821X(94)90076-0)
- Uriz, N.J., Cingolani, C.A., Basei, M.A.S., Blanco, G., Abre, P., Portillo, N.S. & Siccardi, A. (2016). Provenance and paleogeography of the Devonian Durazno Group, southern Parana Basin in Uruguay. *Journal of South American Earth Sciences*, 66, 248–267, <https://doi.org/10.1016/j.jsames.2016.01.002>.
- Vermeesch, P. (2009). RadialPlotter: a Java application for fission track, luminescence and other radial plots. *Radiation Measurements*, 409–410, <http://www.ucl.ac.uk/~ucfbpve/radialplotter/>, <https://doi.org/10.1016/j.radmeas.2009.05.003>
- Veroslavsky, G., De Santa Ana, H., Rossello, E. (2004). Depósitos del Jurásico y Cretácico temprano de la región meridional de Uruguay. In: Veroslavsky, G., Ubilla, M., Martínez, S. (Eds.): *Cuencas sedimentarias de Uruguay*. Mesozoico. Facultad de Ciencias, Montevideo, pp. 117-142.
- Wagner, G.A., Gleadow, A.J.W. & Fitzgerald, P.G. (1989). The significance of the partial annealing zone in apatite fission-track analysis: Projected track length measurements and uplift chronology of the Transantarctic Mountains. *Chemical Geology: Isotope Geoscience Section*, 79, 295–305, [https://doi.org/10.1016/0168-9622\(89\)90035-3](https://doi.org/10.1016/0168-9622(89)90035-3)
- White, R., & McKenzie, D. (1989). Magmatism at rift zones: the generation of volcanic continental margins and flood basalts. *Journal of Geophysical Research: Solid Earth*, 94(B6), 7685-7729.

- Will, T. M., & Frimmel, H. E. (2018). Where does a continent prefer to break up? Some lessons from the South Atlantic margins. *Gondwana Research*, 53, 9-19.
- Wolf, R.A., Farley, K.A. & Silver, L.T. (1996). Helium diffusion and lowtemperature thermochronometry of apatite. *Geochimica et Cosmochimica Acta*, 60, 4231–4240, [https://doi.org/10.1016/S0016-7037\(96\)00192-5](https://doi.org/10.1016/S0016-7037(96)00192-5)
- Wolf, R.A., Farley, K.A. & Kass, D.M. (1998). Modeling of the temperature sensitivity of the apatite (U–Th)/He thermochronometer. *Chemical Geology*, 148, 105–114, [https://doi.org/10.1016/S0009-2541\(98\)00024-2](https://doi.org/10.1016/S0009-2541(98)00024-2)
- Zerfass, H., Chemale, F., Leandro, C. & Lavina, E. (2004). Tectonics and sedimentation in southern South America during Triassic. *Sedimentary Geology*, 166, 265–292, <https://doi.org/10.1016/j.sedgeo.2003.12.008>

Capítulo 5 - Low-temperature thermochronology of the South Atlantic margin along Uruguay and its relation to tectonic events in West Gondwana

João Pacífico Silveira Luiz Machado^{1,2*}, Andréa Ritter Jelinek², Randell Stephenson¹, Claudio Gaucher³, Marcos Müller Bicca², Leticia Chiglino³, Frederico Antonio Genezini⁴

¹ School of Geosciences, University of Aberdeen, United Kingdom

² Instituto de Geociências, Universidade Federal do Rio Grande do Sul, Porto Alegre, Brazil

³ Facultad de Ciencias, Universidad de la República, Montevideo, Uruguay

⁴ Instituto de Pesquisas Energéticas e Nucleares, Centro do Reator de Pesquisas, São Paulo, Brazil

Nota explicativa

Este capítulo corresponde ao artigo que está em revisão pelo periódico *Tectonophysics*. Ao final do manuscrito encontra-se a carta de submissão do mesmo.

Abstract

The geodynamic forces acting during Jurassic-Cretaceous South Atlantic rifting provoked intense transformations in West Gondwana, such as the reactivation of ancient basement structures, broad magmatism and general uplift of the new continental margins. Low-temperature thermochronology records cooling associated with exhumation syn- and post-breakup along the Brazilian margin, while further south, in Uruguay, mostly pre-breakup uplift is identified. Thermochronometric data are scarce in Uruguay, but previous studies suggest that basement cooling and exhumation preceded West Gondwana breakup by hundreds of millions of years. To improve our knowledge of the evolution of rifting, we present 19 apatite fission track ages in this study, 42 apatite and 40 zircon (U-Th)/He single crystal ages for the Uruguayan shield (UYS), from which we modelled 19 inverse thermal histories. Our results suggest that the UYS temperatures were below 200 °C since the early Palaeozoic, and that cooling below 110 °C started during the Carboniferous, with continuous exhumation of the basement until Early Cretaceous. The onset of this long-

term uplift is correlated with orogenesis and terrane accretions in the SW margin of West Gondwana during the Palaeozoic. Lithosphere thinning and uplift preceding breakup contributed to the continuous Late Palaeozoic to middle Mesozoic exhumation, until the voluminous volcanism of the Paraná-Etendeka Large Igneous Province (c. 133 Ma). This magmatic event, combined with the thermal influence of the Tristan da Cunha mantle plume and rift spreading, likely raised the basement geotherm during the Late Cretaceous. Models suggest a slight increase in temperatures of the UYS from Late Cretaceous until the Oligocene, when a final cooling to surface temperatures took place. Our findings corroborate a long and complex thermal history for Uruguay, with crustal uplift occurring essentially before West Gondwana breakup.

Keywords: Thermochronometry; Fission-tracks; (U-Th)/He; West Gondwana; South Atlantic.

5.1 Introduction

The Atlantic passive margin in South America was established after Gondwana breakup in the Jurassic-Cretaceous, during which rifting propagated from southernmost Tierra del Fuego towards the NE, forming the eastern continental margins of Argentina, Uruguay and Brazil. Basement uplift and exhumation syn- and post-rift have been widely reported by low-temperature thermochronometry studies in SE Brazil (e.g. Gallagher *et al.* 1994, 1995; Gallagher & Brown 1999; Tello Saenz *et al.* 2003; Hackspacher *et al.* 2004; Cogné *et al.* 2011, 2012; Karl *et al.* 2013; Krob *et al.* 2019; Van Ranst *et al.* 2019), where the high escarpments (up to 2.000 m) from the Serra do Mar and Serra da Mantiqueira provide an ideal scenario for this research method. Cooling in the region is often associated with uplift and exhumation, related to the far-field effects of the Andean Orogeny and to structural reactivations in the passive margin during the development of the Atlantic Ocean. On the other hand, thermochronometry studies are scarcer towards the south of the Atlantic margin, where a subdued topography and low relief are dominant. Published data suggest that an important limit between pre- and post-rift cooling and exhumation is located in the Florianópolis region, southern Brazil (Fig. 5.1), where a very complex thermal history has been reported (Jelinek *et al.* 2003; Karl *et al.* 2013; Hueck *et al.* 2018a). Further south of this region, thermochronometry studies have reported mainly pre-rift Paleozoic cooling phases in southernmost Brazil (Borba *et al.* 2002, 2003; Oliveira *et al.* 2016; Machado *et al.* 2019), Uruguay (Kollenz 2015; Hueck *et al.* 2017; Gomes & Almeida 2019) and Argentina (Kollenz *et al.* 2017). These were generally linked to

Paleozoic orogenic cycles on the active SW margin of Gondwana and the geodynamics of Gondwana breakup.

Approximately 800 km south of Florianópolis, Uruguay has represented an area of increased interest for thermochronometry studies in recent years, but data are still very limited in the region. The Uruguayan shield (UYS) occupies almost half of the territory of Uruguay (Fig. 5.1 and 5.2) and includes exposures of the Archean to Paleoproterozoic Rio de La Plata Craton and of the Neoproterozoic Dom Feliciano Belt, associated with the formation of West Gondwana (Hartmann *et al.* 2001; Gaucher *et al.* 2011; Oyhantçabal *et al.* 2011). Although passive margins and cratons are often considered as characterized by long-term stability, the low-temperature thermochronology studies in Uruguay indicate basement cooling since the early Paleozoic, suggesting a lengthy and complex Phanerozoic thermotectonic history. Available data suggest that the main exhumation event in the region was initiated well before Gondwana breakup (Kollenz 2015; Hueck *et al.* 2017; Gomes & Almeida 2019). However, the current thermal histories modelled for the UYS by different authors and based on distinct thermochronometers suggest alternative phases of cooling and reheating of the basement, and imply conflicting geodynamic models for the regional tectonic evolution. The complex and scattered thermochronometry data in the region represent a restraint to our understanding of the tectonic activity preceding South Atlantic rifting and breakup.

A deeper comprehension of the cooling and exhumation history of the Uruguay basement can improve our models for the Gondwana breakup and tectonic activity in the early stages of rifting, including rift propagation northwards. Moreover, it is necessary to evaluate the somewhat conflicting models for exhumation of the UYS. Therefore, with the objective to enhance our knowledge of the thermal history of the region, here we combine the methods used individually in previous thermochronometry studies and generate new thermal models for the Uruguayan basement. We present a new dataset with 19 apatite fission track ages, 42 apatite and 40 zircon (U-Th)/He single crystal ages, from which we model 19 inverse thermal histories across the UYS. After integration with previously published data, we identify the main cooling/reheating phases of the shield and associate them to the collisional cycles in the SW margin of Gondwana, and to the opening of the South Atlantic. Our results support models of a complex long-lived thermal evolution for the Uruguayan shield, and a thermotectonic history that utilizes the thermochronometry data currently available for the region is suggested.

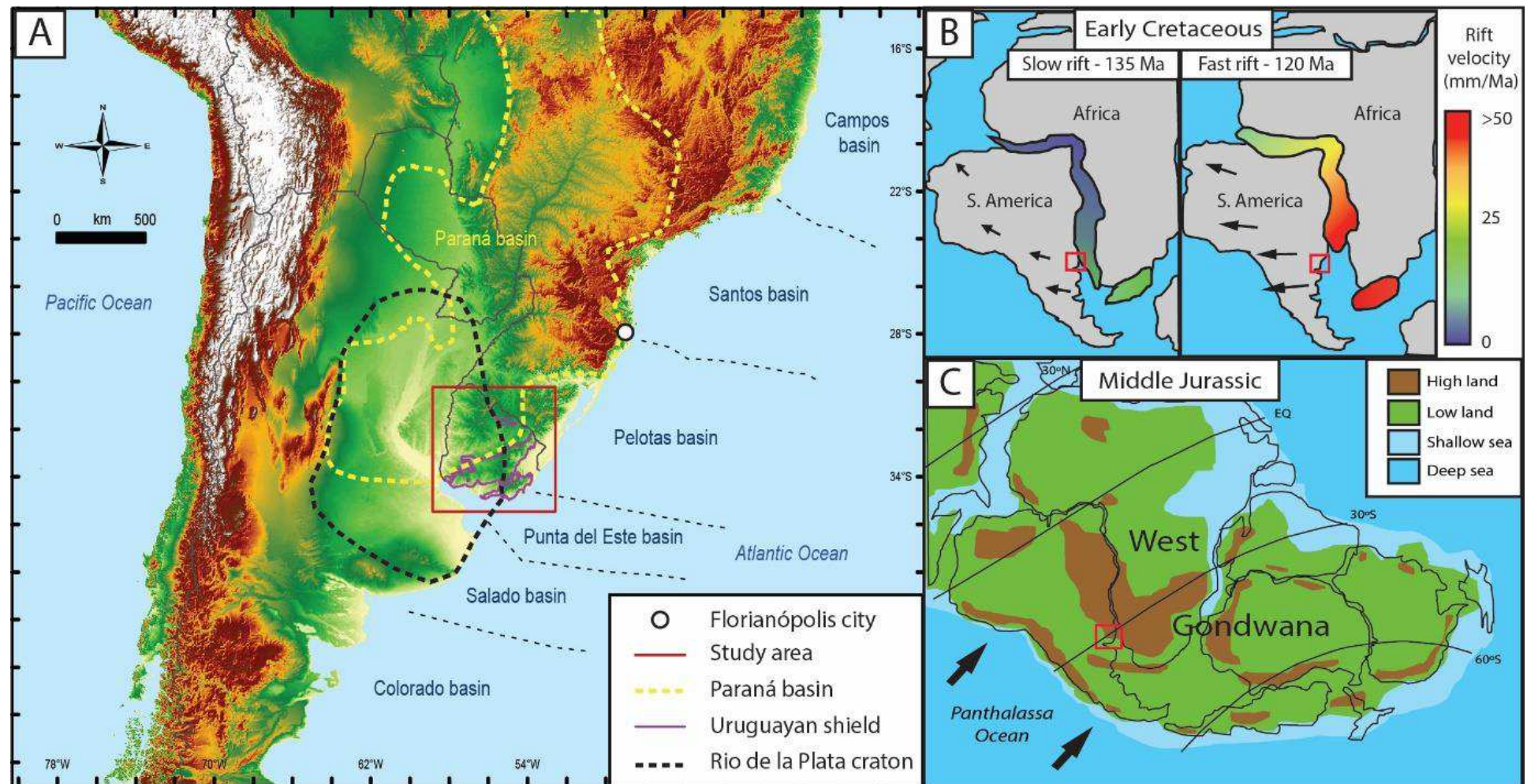


Figure 5.1: Panel with (A) DEM image of the study area in the South Atlantic margin, with schematic boundaries of the Paraná Basin and Rio de La Plata Craton indicated. The region of Florianópolis marks the limit between pre-rift cooling (south) and post-rift cooling (north); (B) study area location during the South Atlantic rift velocity increase (after Brune et al., 2016) and (C) before West Gondwana break-up, with subduction of the Panthalassa Ocean under West Gondwana (after Scotese et al., 1999).

5.2 The Uruguayan Shield

Uruguay is located at the eastern margin of South America and exhibits a surprising geological diversity considering its relatively small size (176.215 km²). Its Precambrian basement records geological events from the Archean, accessible to investigation by exposure across 44% of its territory (Bossi *et al.* 1998; Hartmann *et al.* 2001; Masquelin 2006). The country has low topography and subdued relief, with very few peaks over 500 m above sea level. The Uruguayan shield (UYS) crops out mainly in the southern and eastern part of the country, and is divided into four tectonostratigraphic terranes, while the remaining area is covered by Phanerozoic volcano-sedimentary deposits (Fig. 5.2).

The four UYS terranes are limited by regional shear zones and known, from W to E, as the: 1) Piedra Alta Terrane (PAT), 2) Tandilia Terrane (TT), 3) Nico Pérez Terrane (NPT), and 4) Cuchilla Dionisio Terrane (CDT) (Bossi *et al.* 1998; Bossi & Gaucher 2004, 2014a; Bossi & Cingolani 2009). Although this division is still a matter of debate, the westernmost PAT and TT are unanimously considered part of the Rio de La Plata Craton, a major tectonic feature in South America; the easternmost CDT represents the Dom Feliciano Belt and had been associated with the Kalahari Craton, of southern Africa; and the central and highly complex NPT has been considered part of the Rio de La Plata Craton or not, depending on author (see Basei *et al.* 2005; Bossi and Gaucher, 2004; Gaucher *et al.* 2011; Hartmann *et al.* 2001; Masquelin 2006; Oriolo *et al.* 2016a; Oyhantçabal *et al.* 2018; Philipp *et al.* 2016; Rapela *et al.* 2011; Santos *et al.* 2017). In any case, there is consensus that all terranes were finally assembled during the end of the Brasiliano/Pan-African Orogeny (Neoproterozoic), a multi-episodic collision between the Rio de La Plata, Congo and Kalahari cratons and several microcontinents and arc terranes (e.g. Arachania), which culminated with the consolidation of West Gondwana (Gaucher *et al.* 2009, 2011; Hueck *et al.* 2018b; Philipp *et al.* 2018; Schmitt *et al.* 2018).

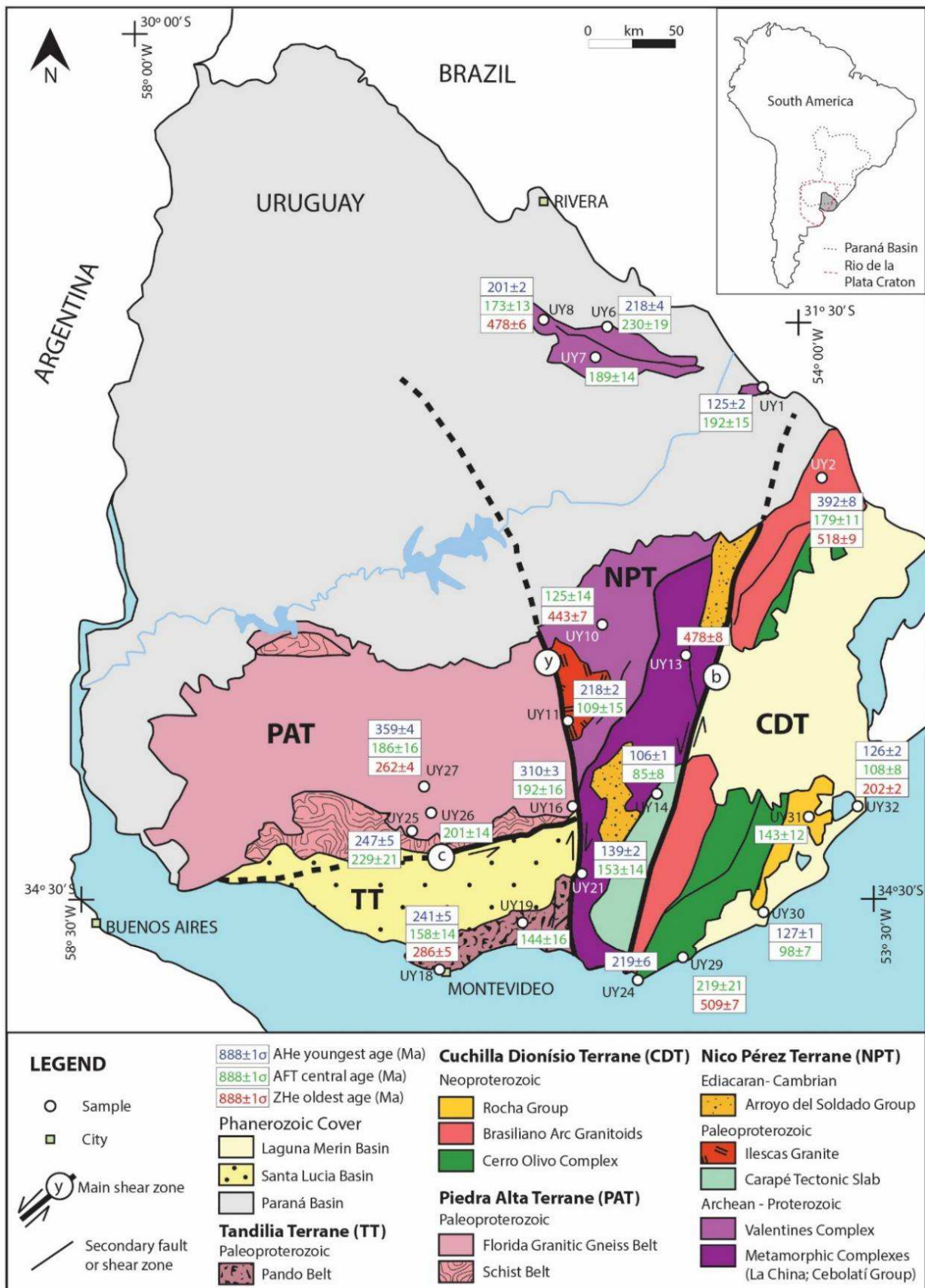


Figure 5.2: Simplified geological map of Uruguay with sample locations and new thermochronometry ages. Central AFT ages, oldest ZHe and youngest AHe single crystal ages are reported. Main shear zones: (c) Colonia, (y) Sarandí del Yí and (b) Sierra Ballena. Inset map indicates the approximated extension of the Paraná Basin and Rio de La Plata Craton.

Three major crustal-scale regional shear zones delimit the four UYS terranes, and several NE-trending smaller lineaments occur in the NPT and CDT. The oldest lineament is the Colonia Shear Zone, which separates the PAT from the TT (Bossi and Cingolani 2009). It comprises an E-W trending, several km-thick ultramylonite band showing abundant sinistral shear indicators (Ribot *et al.* 2005; Abre *et al.* 2014). The age of the shear zone has been determined by K-Ar ages of deformed granitoids as 1.75 Ga (Faraone 2018). Central in the shield, the Sarandí del Yí Shear Zone is a mylonitic belt with c. 2 km width and a NNW-SSE strike, which displays dextral shearing with sinistral reactivation and limits the western PAT and TT from the central NPT (Bossi & Gaucher 2014a; Oriolo *et al.* 2018). Ar-Ar ages of mafic dikes deformed by the main dextral shear yielded Mesoproterozoic ages of c. 1,200 Ma (Teixeira *et al.* 1999), that were related to the tangential collision between the TPA and TT with the NPT during the formation of the Rodinia supercontinent (Bossi & Cingolani 2009; Gaucher *et al.* 2011; Bossi & Gaucher 2014a). More recent publications have supported a Neoproterozoic onset of deformation (c. 630 Ma), linked to the collision of the Rio de La Plata and Congo cratons during West Gondwana formation (Rapela *et al.* 2011; Oriolo *et al.* 2016b, 2018), but the new ages do not rule out a Mesoproterozoic main event (Santos *et al.* 2017). This discussion is still ongoing and has important implications for the Precambrian evolution of Uruguay. Another major lineament is the Sierra Ballena Shear Zone, a c. 4 km-wide mylonitic belt with NNE-SSW direction that propagates to southernmost Brazil as the Dorsal do Canguçu Shear Zone (Fernandes *et al.* 1993; Fernandes & Koester 1999; Oriolo *et al.* 2018). In Uruguay this shear zone represents the suture between the central NPT and the coastal CDT, and displays sinistral shearing during the end of the Brasiliano/Pan-African Orogeny (latest Ediacaran-Cambrian) with brittle reactivation during the Mesozoic (Bossi & Gaucher 2004, 2014a; Hueck *et al.* 2017; Oriolo *et al.* 2018).

The PAT is a Paleoproterozoic (2.2 to 2.0 Ga) block composed of two supracrustal low-grade metamorphic belts (Arroyo Grande and San José belts), separated by the wide central Florida Belt, which comprises granitoids and gneiss (Hartmann *et al.* 2001; Oyhantçabal *et al.* 2011; Bossi & Piñeyro 2014). The southern San José Belt is cut by the E-W Colonia Shear Zone and partially covered by the Santa Lucía Basin. The central Florida Belt was intruded by thousands of mafic dikes with E-W direction around 1.79 Ga (Teixeira *et al.* 1999) which underwent a NW-SE flexure near the Sarandí del Yí Shear Zone, indicating dextral movement during the collision of the PAT and the NPT (Bossi and Campal 1992; Hartmann *et al.* 2001; Gaucher *et*

al. 2011; Bossi & Piñeyro 2014; Oriolo *et al.* 2016b; Oyhantçabal *et al.* 2018). The PAT yielded widespread positive ε Nd values and Nd model ages between 2.4 and 2.1 Ga, which shows its juvenile character and lack of an Archean basement (Pamoukaghlián *et al.* 2017).

The TT, to the south of the Colonia Shear Zone, comprises the Paleoproterozoic Montevideo Formation (Pando Belt) and several intrusive granitoids, such as the Soca rapakivi granite (2056 Ma) (Santos *et al.* 2003) and the La Tuna Granite, which yielded a U-Pb crystallization age of 2156 Ma (Pamoukaghlián *et al.* 2017). The terrane continues to the south beneath the Río de la Plata and into Argentina, cropping out again in its type area (Tandilia) in the southern Buenos Aires Province, Argentina (Bossi and Cingolani 2009). Apart from older ages for the metasediments and intrusive granitoids compared to the PAT, Nd model ages are in average 200 Myr older in the TT (Pamoukaghlián *et al.* 2017), matching comparable model ages in the type area in Argentina (Hartmann *et al.* 2002). Furthermore, Neoproterozoic anorogenic granitoids and sedimentary rocks occur in the TT in Argentina and Uruguay (Gaucher *et al.* 2008; Abre *et al.* 2014) but are so far unknown in the PAT.

The NPT (Bossi and Campal 1992; Bossi *et al.* 1998) is a complex terrane in Uruguay and a key element for understanding the formation of West Gondwana. It is usually considered part of the Rio de La Plata Craton since the Mesoproterozoic (Hartmann *et al.* 2001; Gaucher *et al.* 2008, 2009b; Bossi & Cingolani 2009; Santos *et al.* 2017), but other studies have related the NPT to the Congo Craton, suggesting it was amalgamated to the Rio de La Plata Craton only during the Ediacaran (Oyhantçabal *et al.* 2011; Rapela *et al.* 2011; Oriolo *et al.* 2016a). The NPT presents a highly complex geology and the oldest rocks in Uruguay, with major internal units limited by the NE-SW shear zones, a basement window (Isla Cristalina de Rivera) cropping out far north in the Paraná Basin (Fig. 5.2), and continuity to southernmost Brazil (Taquarembó Terrane) (Oyhantçabal *et al.* 2011, 2012; Bossi & Gaucher 2014b; Oriolo *et al.* 2016a, 2018). In a simplified way, the NPT is composed of the Valentines Granulitic Complex in the northwest, the La China Complex and the Cebolatí Group in the middle, and the Carapé Tectonic Slab and Mesoproterozoic volcano-sedimentary successions in the southeast. The Valentines Complex, which includes the Isla Cristalina de Rivera, comprises gneisses (felsic granulites), pyroxenites and banded iron formations (BIF) as well as intruding tonalites, trondhjemites and granites with ages between 2.6 and 2.2 Ga (Santos *et al.* 2003; Oyhantcabal *et al.* 2012). They are in turn intruded by the Illescas rapakivi granite, which yielded an U-Pb zircon age of

1.784 Ma (Bossi *et al.* 1998; Bossi & Cingolani 2009). The central domain includes the La China Complex, which comprises metatonalites of amphibolite facies, and the metasedimentary Cebollatí Group (formerly known under the informal term “Las Tetas complex”), both units with Archean ages between 3.4 and 2.7 Ga (Hartmann *et al.* 2001; Gaucher *et al.* 2010, 2011, 2014b). To the southeast of the Archean units, a NE-trending belt of Mesoproterozoic (1.5-1.3 Ga), low-grade meta-volcano-sedimentary rocks occurs, which includes the Parque UTE and Mina Verdún groups and the Tapes Complex (Chiglino *et al.* 2010; Gaucher *et al.* 2011, 2014a; Poiré *et al.* 2005). At the southeastern corner of the NPT, the Carapé Complex, sometimes referred to as the Campanero Unit, is a tectonic slab emplaced in the NPT in the latest Ediacaran-early Cambrian, and comprises mainly metagranitoids and metasediments juxtaposed by reverse and transcurrent faults (Hartmann *et al.* 2001; Mallmann *et al.* 2007; Chiglino *et al.* 2010, Bossi *et al.* 2014). Unconformably overlying parts of the NPT are remnants of the Arroyo del Soldado Group, a 5,000 m thick marine platform succession rich in carbonate deposits and with depositional age between 566 and 530 Ma (Gaucher 2000; Gaucher *et al.* 2004; Blanco *et al.* 2009).

The CDT, also known as Punta del Este Terrane (Oyhantçabal *et al.* 2011), is an allochthonous unit laterally accreted to the NPT during the Brasiliano/Pan-African Orogeny (Bossi & Gaucher 2004). This terrane is composed mainly of deformed calc-alkaline granitic (e.g. Aiguá and Cuchilla Dionisio batholiths) with ages between 615 and 530 Ma, and occupies most of the CDT and is known in Brazil as the Pelotas Batholith (Fernandes *et al.* 1995; Bossi & Gaucher 2004; Philipp *et al.* 2016). The Paleo-Mesoproterozoic Cerro Olivo Complex occurs further east; it is considered the basement of this terrane and includes high-grade metamorphic rocks with protolith ages between 1000 and 750 Ma, metamorphosed at c. 650 Ma (Bossi & Gaucher 2004; Basei *et al.* 2011; Oyhantçabal *et al.* 2011; Peel *et al.* 2018; Will *et al.* 2019). Finally, near the South Atlantic coast the metasediments of the Rocha Group, are exposed. These have ages between c. 600 to 550 Ma and affinity to units from the Kalahari Craton, being correlated to the Oranjemund Group of the Gariep Belt in Namibia (Bossi & Gaucher 2004; Basei *et al.* 2005).

Although the discussion is still ongoing on how and when the tectonostratigraphic terranes of the UYS were assembled, there is a consensus that the long lived Brasiliano/Pan-African Orogeny represents the final event for the consolidation of Uruguayan basement. The juxtaposition of UYS terranes, related to the diachronous collision of Uruguayan, Brazilian and African units, led to the formation of the West

Gondwana megacontinent by Cambrian times (Bossi & Gaucher 2004, 2014a). The successive collisions related to the Brasiliano/Pan-African Orogeny were responsible for establishing sutures that later played an important role during Pangea breakup and South Atlantic opening in the Mesozoic (Oriolo *et al.* 2018; Schmitt *et al.* 2018; Will & Frimmel 2018).

5.3 Previous thermochronometry studies in Uruguay

The first thermochronometry investigation in the UYS was made by Kollenz (2015), who obtained seven AFT ages in the shield. Five AFT central ages in the PAT and TT range between 325 ± 25 and 200 ± 20 Ma, with a mean of 260 Ma, and show a tendency to increase with the distance from the coast, although the youngest age is in the middle of the PAT. The remaining two ages, around 225 Ma, were obtained in the western part of the CDT. Track lengths were obtained from four samples from PAT, TT and CDT and display a unimodal distribution, with a range between 12.2 and 10.8 μm . Inverse thermal modeling made in these four samples using HeFTy (Ketcham 2005), show general cooling from the high limit of the AFTPRZ to surface temperature between the Carboniferous and Middle Jurassic, followed by a period of reheating until Late Cretaceous, when some samples reached temperatures up to 65 °C. A final cooling back to surface temperature was observed in all models during the Cenozoic. According to Kollenz (2015) the Paleozoic to Mesozoic cooling trend is linked to a regional exhumation, possibly related to compressional stress in the SW of Gondwana (e.g. Gondwanic cycle) and which has been also reported further south in Argentina and north in southernmost Brazil (de Borba *et al.* 2002, 2003; de Oliveira *et al.* 2016; Kollenz *et al.* 2017; Machado *et al.* 2019). They suggest that the late Mesozoic reheating phase is associated to the Paraná-Etendeka LIP, which lava flows would have buried the UYS and caused an increase in the bedrock temperature.

Gomes & Almeida (2019) published AFT ages for nine locations of the UYS. Their ages present a range from 326 ± 30 to 121 ± 19 Ma (if an outlier of 38 ± 2 Ma is ignored), suggest a positive correlation with altitude and are divided by the authors into a western domain of older ages and an eastern domain of younger ages. The MTL show a unimodal distribution and range from 12.5 to 10.0 μm . Inverse thermal modeling was made in eight samples using the outdated AFTSolve (Ketcham *et al.* 2000), a software without c-axis projected track lengths, and a limited number of confined tracks (usually < 45), so that the resulting models should be taken carefully. In any case, they suggest a general cooling trend until the Triassic, when samples

reached stability around the lower limit of the AFTPRZ (60 °C). Some of their samples in Uruguay and southernmost Brazil suggest reheating during Cretaceous. All models show a final cooling to surface temperature after the Paleogene.

Based on a dataset of AHe and ZHe ages, Hueck *et al.* (2017) suggested a distinct thermal evolution for the UYS. They obtained 33 ZHe ages from 11 locations, with average ages between 560 and 460 Ma and acquired within zircons mostly of eU < 500 ppm. ZHe ages do not show correlation with eU, crystal size, altitude or location. Their AHe ages were obtained from 27 crystals from nine locations and show considerable dispersion, with mean ages ranging from Permian to Cretaceous. No correlation was found between AHe ages and eU or crystal size, but it is suggested that samples from the southern UYS, closer to the coast, have the youngest values. From inverse thermal models made in HeFTy, the authors suggest that the UYS reached near-surface conditions by Silurian (c. 420 Ma), succeeded by cycles of burial (and minor reheating) and erosion, associated to Devonian and Permian Paraná Basin deposits. Their models imply a final Mesozoic exhumation of the UYS, with restricted sedimentation, and possibly related to the tectonic stress associated with Pangea breakup. According to the authors, by the end of Mesozoic the analyzed samples would have reached surface temperature, and a Cretaceous reheating is not supported.

In summary, Kollenz (2015) models based on AFT support cooling towards near-surface conditions ($T < 30^\circ\text{C}$) from Carboniferous to Jurassic, followed by reheating (up to 65 °C) in the Cretaceous and a final cooling to surface temperature during Cenozoic. Gomes & Almeida (2019) AFT models suggest a major cooling phase until the Triassic, without reaching near-surface conditions and followed by stability around 60 °C or minor reheating during the late Mesozoic, until a final cooling phase starting in the Miocene. On the other hand, Hueck *et al.* (2017) (U-Th)/He models suggest cooling to near-surface conditions by the Silurian, followed by shallow reburial (with reheat below 90 °C) and exhumation cycles until Permian and a final cooling to surface temperature during Mesozoic. Despite the temporal conflict, all authors support a complex thermal history for the region, with a main Paleo- Mesozoic cooling phase to temperatures close or below 60 °C, minor reheating episodes or protracted stability at this temperature, and a final Meso- Cenozoic cooling towards surface temperature. Remarkably, their models were made using different data and user constraints, and their cooling/heating phases imply distinct thermotectonic histories for the UYS.

5.4 Materials and methods

5.4.1 Sampling

A total of 32 basement samples were collected across Uruguay. Locations with published low-temperature thermochronometry data were avoided, as the project aimed to increase the coverage of thermochronometry data in the shield. Samples were collected from the margins and central parts of each tectonostratigraphic terrane. Standard crushing, magnetic and heavy liquids separation were processes applied to separate apatite and zircon crystals. Although mainly granitic rocks were sampled, which are usually rich in apatite and zircon, only 21 samples provided crystals suitable for the thermochronometry analysis (Fig. 5.2, Tab. 5.1).

Table 5.1: Details of each location and analysis made. Stratigraphic ages from Bossi & Gaucher (2004) and Masquelin (2006); coordinates in degrees and datum WGS84; (D. sea) = shortest distance to Atlantic Ocean.

Sample	Lithology	Age (Ma)	Lat (°)	Long (°)	Altitude (m)	D. sea (km)	Analysis
UY1	Granite	> 550	-31,89	-54,16	225	181	AFT, AHe
UY2	Granite	575 ± 14	-32,35	-53,79	110	133	AFT, AHe, ZHe
UY6	Granite	590 - 530	-31,59	-55,10	259	277	AFT, AHe
UY7	Granite	550 - 510	-31,75	-55,18	208	278	AFT
UY8	Granite	590 - 530	-31,55	-55,49	193	312	AFT, AHe, ZHe
UY10	Granite	> 1000	-33,12	-55,13	245	173	AFT, ZHe
UY11	Granite	1785 ± 9	-33,61	-55,33	235	161	AFT, AHe
UY13	Granite	> 1000	-33,28	-54,62	102	120	ZHe
UY14	Granite	590 - 530	-33,99	-54,78	131	89	AFT, AHe
UY16	Granite	c. 2200	-34,06	-55,31	266	104	AFT, AHe
UY18	Gnaisse	c. 2200	-34,92	-56,17	150	111	AFT, AHe, ZHe
UY19	Granite	2054 ± 11	-34,67	-55,64	55	69	AFT
UY21	Granite	574 ± 34	-34,41	-55,25	182	66	AFT, AHe
UY24	Gnaisse	1006 ± 37	-34,97	-54,95	9	0	AHe
UY25	Diorite	2065 ± 9	-34,19	-56,32	54	153	AFT, AHe
UY26	Granite	c. 2100	-34,10	-56,20	47	150	AFT
UY27	Granite	c. 2200	-33,96	-56,24	133	163	AFT, AHe, ZHe
UY29	Granite	> 550	-34,85	-54,63	7	0	AFT, ZHe
UY30	Schist	< 1540	-34,59	-54,12	3	0	AFT, AHe
UY31	Granite	556 ± 7	-34,11	-53,85	71	17	AFT
UY32	Granite	678 ± 14	-34,04	-53,54	4	0	AFT, AHe, ZHe

5.4.2 Low-temperature thermochronometry

We used three low-temperature thermochronometers to investigate the thermal evolution of the Uruguayan basement: apatite fission-tracks (AFT), apatite (U-Th)/He (AHe) and zircon (U-Th)/He (ZHe). These radio-isotopic systems have distinct retention temperatures, and together cover an interval between c. 40 to 190 °C, simply

put, shallow crust temperatures. Each method has its specific partial retention zone (PRZ), which corresponds to a temperature interval where accumulation and loss of the radiogenic decay product are coeval. Temperatures lower than the PRZ of the thermochronometer appraised imply total retention of the radiogenic products, while higher temperatures than the PRZ result in complete loss of them, resetting the age of the thermochronometer to zero. Therefore, the age obtained by thermochronometry methods is a cooling age, based on the balance between radiogenic parent and decay product, and represents a time-temperature point during the passage through the PRZ of the thermochronometer.

Apatite fission-tracks thermochronometry is based on the accumulation of linear defects (tracks) in the crystal lattice, formed by spontaneous fission of ^{238}U and which the quantity and variable lengths indicates the thermal path experienced by the crystal (Price & Walker 1963; Fleischer *et al.* 1975; Gleadow *et al.* 1986a, b; Galbraith *et al.* 1990). The apatite fission-track partial retention zone (AFTPRZ) corresponds to temperatures between c. 60 to 110°C, in which the tracks slowly shrink in a process known as annealing (Wagner *et al.* 1989). Below c. 60°C the annealing process is not effective, and tracks are preserved with their full initial length (c. 16 μm). Although temperature is the main factor controlling annealing, this process is also affected by variations in apatite chemical composition and the amount of accumulated radiation damage (Gleadow *et al.* 1986a; Stockli 2005; Tagami & O'Sullivan 2005).

We used the external detector method for AFT dating (Gleadow 1981; Hurford 1990). For each sample, more than 200 apatites were hand-picked and mounted in epoxy resin tablets, polished to the central portion, and etched in a 5.5M HNO₃ solution at 21°C for 20 s to reveal the spontaneous fission tracks (Carlson *et al.* 1999). Muscovite sheets were coupled to the tablets, which then were irradiated at the IEA-R1/IPEN-CNEN Reactor, São Paulo, Brazil, along with Durango age standards and Corning CN5 dosimeters. Afterwards, mica sheets were decoupled and etched in 48% HF for 18 min at 20°C to reveal the induced tracks. AFT analyses were performed at the Universidade Federal do Rio Grande do Sul, Brazil, using a Leica DM 6000 M Microscope (1000x, dry). Ages were calculated based on 20 crystals per sample and the ζ calibration method (Hurford & Green 1983; Hurford 1990), while ages homogeneity was analyzed through the chi-square test (Galbraith 1981; Galbraith & Green 1990) using the software RadialPlotter 9.0 (Vermeesch 2009). For thermal modeling we aimed to measure lengths and *c*-axis angles of 100 confined TINT tracks (Lal *et al.* 1969) in each sample, and used the mean etch pit diameter D_{par} from about

100 measurements as kinetic parameter (Donelick 1993; Carlson *et al.* 1999; Donelick *et al.* 2005).

The (U-Th)/He method is based in the accumulation of alpha particles (${}^4\text{He}$) in the crystal lattice after the decay chain of ${}^{238}\text{U}$, ${}^{235}\text{U}$ and ${}^{232}\text{Th}$ isotopes. The alpha particles are expelled from the mineral structure at high temperatures owing to thermal diffusion. In apatite (U-Th)/He dating, alpha particles are efficiently expelled at temperatures above c. 70°C, partially retained between c. 40 and 70°C (AHe Partial Retention Zone – AHePRZ), and completely retained when temperature is below c. 40°C (Wolf *et al.* 1996, 1998; Farley 2002). However, these temperature limits are known to vary with crystal dimensions, compositional zonation, eU concentration ($\text{eU} = [\text{U}] + 0.235 \times [\text{Th}]$) and accumulated radiation damage (Farley 2000; Reiners & Farley 2001; Shuster *et al.* 2006). Moreover, small fluctuations in these factors are magnified by extended residence in the AHePRZ, commonly resulting in dispersed AHe ages (Flowers & Kelley 2011). In zircon (U-Th)/He dating, alpha particles are partially retained between c. 150 and 190°C (ZHe Partial Retention Zone – ZHePRZ), and promptly expelled at temperatures higher than 190°C (Reiners *et al.* 2018 book). Similarly to AHePRZ, the ZHePRZ is affected by compositional zonation, eU concentration, accumulated radiation damage and protracted residence at low temperatures (Reiners *et al.* 2002, 2004; Nasdala *et al.* 2004; Reiners 2005).

The (U-Th)/He analyses were conducted in the Baja Arizona Radiogenic Helium Dating Laboratory (BARHDL), at the University of Arizona, US. Both apatites and zircons were handpicked based on morphology, size and optical clarity, using a Leica MZ16 microscope. Because apatites tend to accumulate low quantity of alpha particles due the low eU concentration ($\text{eU} < 50 \text{ ppm}$), preference was given to clear apatites with both terminations, aiming to avoid crystals that loss ${}^4\text{He}$ through fractures or a highly damaged crystal lattice. On the other hand, since zircon eU usually is one or two orders of magnitude higher, we picked zircons with a wide range of opacity, which ultimately reflect the amount of accumulated radiation damage, and provide a better view of the eU influence over the ZHe age. Crystals were measured and photographed with Leica Application Suite V3, to define the diffusion domain and allow the alpha-ejection age correction (Farley *et al.* 1996), which accounts for the ejection of ${}^4\text{He}$ in crystal rims during decay. Nb foil tubes were used to pack the crystals for helium extraction, made using long-wavelength laser heating and measured with a quadrupole mass spectrometer. Subsequently, crystals were dissolved for the U-Th measurements, performed using a high-resolution Element2 ICP-MS. Durango

standards and blank samples were systematically introduced in between analysis to guarantee reliability of the measurements.

5.4.3 Inverse thermal modeling

The thermal history of each sample was recreated using the program QTQt 5.7, which tests time-temperature points aiming to reconstruct a thermal history that predicts and reproduces the observed thermochronometric data (Gallagher *et al.* 2009; Gallagher 2012). We opted to run models with a minimum of user-imposed constraints, to avoid a biased thermal history. To initiate our models, a large t-T box was set with time ranging from 500 ± 50 Ma and temperature from $100 \pm 100^\circ\text{C}$, time corresponding to the end of the Brasiliano/Pan-African. A final constraint was set with temperature of $20 \pm 10^\circ\text{C}$ at the present time. The thermal history between initial and final constraints was recreated freely by QTQt 5.7, using a temperature range of $70 \pm 70^\circ\text{C}$ when modeling only AFT and AHe, and up to $100 \pm 100^\circ\text{C}$ when ZHe data were available.

Because our current understanding of the AFT system is arguably better established than the (U-Th)/He system, trial models were run only with AFT data at first, and (U-Th)/He data were included in posterior models. Several fast runs of 20,000 interactions were made initially for each sample to set appropriate parameters during inversion (see Gallagher, 2012), and to test the variability of models using different $\partial T/\partial t$ rates. Models run only with AFT data resulted in good fit between observed and predicted ages and MTL, but the inclusion of AHe data into the models led to a considerable mismatch of the AFT data. The later models predicted older AFT ages than the observed while attempting (and usually failing) to fit all AHe ages without improving the low temperature ($< 60^\circ\text{C}$) thermal history. To address this conflict and maintain a good fit of our AFT data, we used a feature from QTQt 5.7 that resamples the AHe age error in order to accept a larger degree of mismatch of AHe data. On the other hand, the inclusion of ZHe data usually better constrained the cooling time from higher temperatures ($> 150^\circ\text{C}$) in the models. Final models combined all thermochronometry data available for each sample, were run for 200,000 interactions or more, and used a maximum $\partial T/\partial t$ of 10°C/Ma , compatible with a cratonic region of subdued topography. This final modeling set up permitted the proposed time-temperature paths to be well defined but not tightly limited by our constraints or by the old and dispersed AHe ages (see Results and Interpretations). During modeling, for AFT we used the D_{par} values and c-axis projected tracks lengths (Donelick 1993; Donelick *et al.* 1999a), the AFT annealing model from Ketcham *et al.* (2007), and the

radiation damage model from Flowers *et al.* (2009) for AHe and from Guenthner *et al.* (2013) for ZHe.

5.5 Thermochronometry results

5.5.1 Apatite fission tracks

We obtained AFT ages from 19 samples (Table 5.2), all of which passed the homogeneity chi-square test ($P\chi^2 > 5\%$) and generally did not show single grain age dispersion, which means that the central ages obtained correspond to single populations. Three samples presented minor age dispersion (UY10 = 17%, UY19 = 18% and UY32 = 18%) that could indicate a mix of apatite populations, but because they passed the chi-square test and their central ages agree with neighborhood samples, we considered them as single population also. All obtained ages are Mesozoic, ranging from 230.9 ± 18.7 Ma to 85.8 ± 8.4 Ma (Late Triassic to Late Cretaceous), with the majority situated in the Jurassic Period. In general, the younger ages are near the coast or structural lineaments, while the older ones are hinterland, in a common distribution of ages of passive margins (Gallagher & Brown 1997). When including data from previous AFT studies in the region, a positive correlation between ages and elevation or distance to the Atlantic Ocean is observed (Fig. 5.3). The NPT presented simultaneously one of the oldest AFT age in our set (sample UY6 with c. 230 Ma, located in the north on the Isla Cristalina de Rivera) and also the youngest AFT age (UY14 with c. 85 Ma, in the southern-central portion of the terrane). This deviation can be related to the complexity of the NPT, composed of distinct rock associations and cut by several faults and shear zones, prone to variable exhumation within the terrane. Sample UY14 for example, the youngest one, is located near a major fault, and might reflect the last stage of tectonic reactivation of this structure at the time of Campanian rhyolitic volcanism (Gaucher *et al.* 2016).

Table 5.2: Apatite fission track data from the Uruguayan shield. Ages were calculated using $\zeta = 280.17$. N: number of grains analyzed; ps: spontaneous track density; Ns: number of spontaneous tracks counted; pi: induced track density; Ni: number of induced tracks counted; pd: dosimeter tracks density; Nd: number of tracks used to determine pd; χ^2 : chi-square probability of single population; U: estimated value of uranium content; Dpar: mean etch pit diameter; CT: confined tracks measured; MTL: mean track length; SD: standard deviation of mean track length distribution; cP.MTL: c-axis projected mean track length; cP. SD: standard deviation of c-axis mean track length; (-): data not available.

Apatite Fission Tracks analysis																		
Sample	N	ps	Ns	pi	Ni	pd	Nd	Central Age	$\pm 1\sigma$	χ^2	U	Dpar	CT	MTL	$\pm 1\sigma$	SD	cP. MTL	cP. SD
#	#	(x10 ⁵)	#	(x10 ⁵)	#	(x10 ⁵)	#	(Ma)	(Ma)	(%)	(ppm)	(μm)	#	(μm)	(μm)	(μm)	(μm)	(μm)
<i>Cuchilla Dionísio Terrane</i>																		
UY2	20	18,91	779	10,46	431	7,17	14341	179,0	10,8	88	18,5	1,87	100	11,46	0,15	1,48	13,31	0,90
UY29	20	9,16	338	4,12	152	7,17	14341	219,6	21,5	99	7,3	1,79	100	10,18	0,22	2,22	12,31	1,39
UY30	20	12,96	359	12,85	356	7,00	13999	98,1	7,4	69	23,3	2,18	100	12,57	0,18	1,83	13,89	1,43
UY31	20	15,5	369	10,76	256	7,17	14341	143,2	11,7	94	19,1	2,04	100	12,73	0,16	1,63	13,93	1,31
UY32	20	15,14	542	13,85	496	7,17	14341	108,3	8,1	11	24,5	1,91	100	12,71	0,17	1,65	14,08	1,07
<i>Nico Pérez Terrane</i>																		
UY1	20	19,25	460	9,92	237	7,17	14341	192,1	15,4	99	17,6	1,82	100	11,17	0,12	1,21	13,00	0,80
UY6	20	12,29	515	5,25	220	7,17	14341	230,9	18,7	95	9,3	1,88	100	11,52	0,14	1,44	13,31	0,88
UY7	20	17,97	532	9,19	272	7,00	13999	189,0	14,2	98	16,7	1,81	100	11,53	0,12	1,25	13,24	0,84
UY8	20	13,24	507	7,60	291	7,17	14341	172,7	12,8	99	13,5	1,90	100	11,56	0,13	1,34	13,30	0,83
UY10	20	4,06	204	3,17	159	7,00	13999	125,4	14,1	59	5,7	1,87	-	-	-	-	-	-
UY11	20	5,3	114	4,84	104	7,17	14341	109,2	14,8	100	8,6	1,79	30	12,68	0,29	1,61	13,87	1,23
UY14	20	3,47	191	4,05	223	7,17	14341	85,8	8,4	100	7,2	1,88	52	12,23	0,21	1,53	13,72	1,16
UY21	20	8,39	308	5,42	199	7,17	14341	153,6	14,0	94	9,6	1,87	42	12,43	0,23	1,49	13,84	1,04
<i>Piedra Alta Terrane</i>																		
UY16	20	10,71	422	5,38	212	7,00	13999	192,3	16,3	100	9,8	1,76	100	12,00	0,15	1,45	13,58	0,99
UY25	20	18,78	417	8,06	179	7,17	14341	229,9	20,6	82	14,3	1,99	100	12,05	0,14	1,45	13,54	1,10
UY26	20	22,09	612	10,87	301	7,17	14341	201,1	14,3	74	19,2	2,27	100	12,20	0,14	1,38	13,73	0,87
UY27	20	12,69	387	6,59	201	7,00	13999	186,1	16,2	99	12,0	2,03	100	11,50	0,15	1,46	13,18	1,04
<i>Tadilia Terrane</i>																		
UY18	20	13	360	7,94	220	7,00	13999	158,5	13,6	100	14,4	1,77	100	11,59	0,15	1,47	13,30	0,95
UY19	20	13,79	222	9,63	155	7,17	14341	144,0	16,2	53	17,1	1,86	38	11,25	0,29	1,78	13,08	1,11

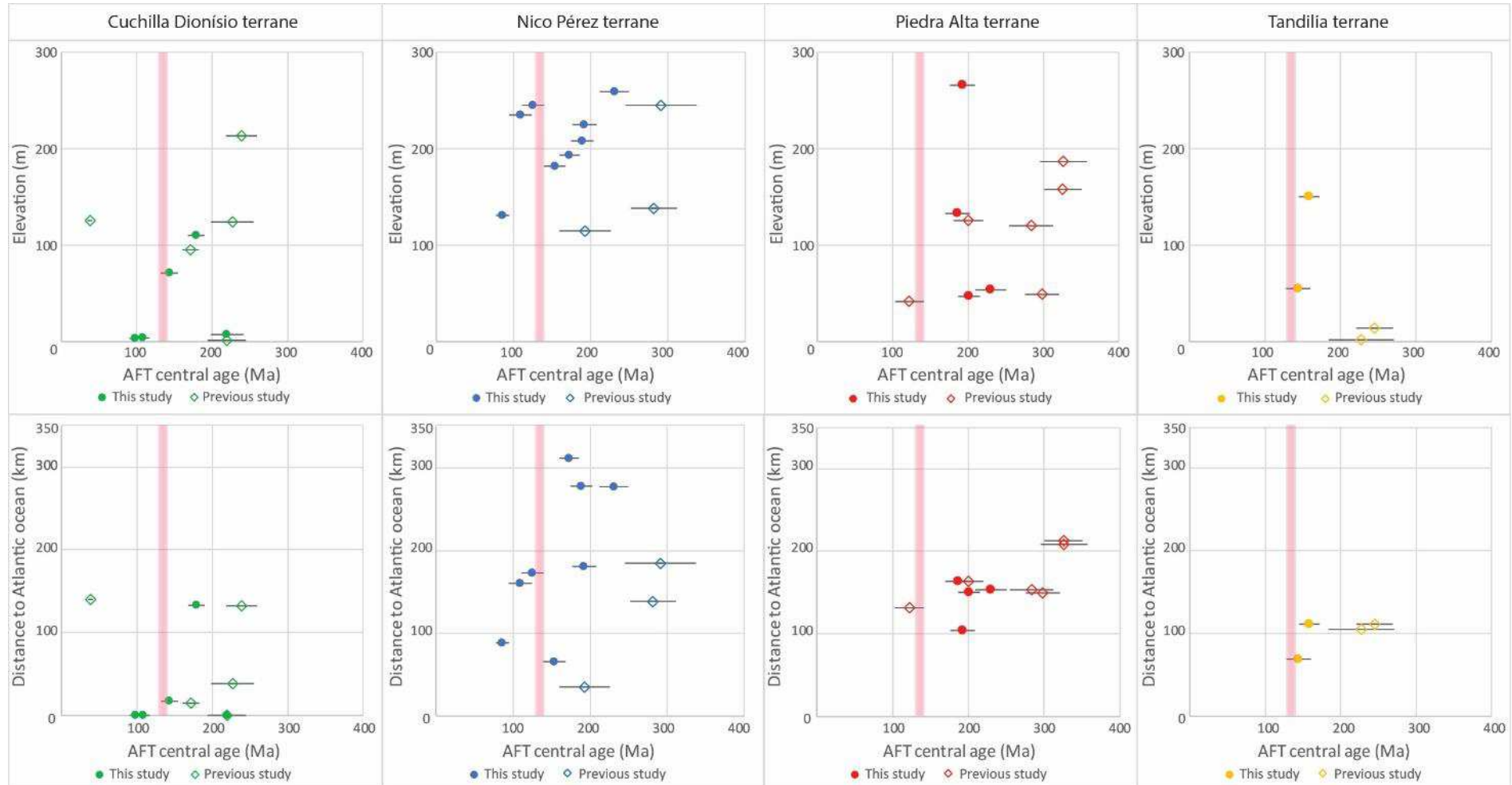


Figure 5.3: Compilation of AFT data available for the Uruguayan shield. Top row shows plots of AFT central ages against elevation, with a general positive correlation for the CDT, NPT and PAT. Bottom row shows AFT ages against the shortest distance to the Atlantic margin in the east, with positive correlation for the NPT and PAT as well. Vertical red bar indicates the Paraná-Etendeka LIP volcanism.

The non-projected mean track lengths (MTL) of all samples are rather medium to short, ranging from 12.7 ± 0.2 to 10.2 ± 0.2 μm (Table 5.2). After applying the c-axis projection (Donelick *et al.* 1999), the MTL range from 13.9 to 12.3 μm , with standard deviation between 1.4 and 0.8 μm . The lengths scattering tends to be unimodal for all samples but UY29, which displays a bimodal distribution and a distinct old AFT age in SSE coastal region (CDT). In most cases, the track lengths distribution is Gaussian around the mean value or negatively skewed, with a larger proportion of longer tracks (see Supplementary Material), which can be interpreted in terms of protracted cooling (Gallagher & Brown 1999). A plot of the MTLs against AFT central ages (Fig. 5.4), including published data (Kollenz 2015; Gomes & Almeida 2019), does not show a clear “boomerang” shape (Green 1986), which is characteristic of reheating with partial reset of AFT ages in a region. Instead it suggests that samples went through protracted cooling without a major reheating, and with distinct parts of the shield cooling below 110 °C at different times. Measurements of the D_{par} range between 2.27 and 1.76 μm , which indicates a predominance of chlorine rich apatites, with high resistance to annealing (Carlson *et al.* 1999; Donelick *et al.* 2005).

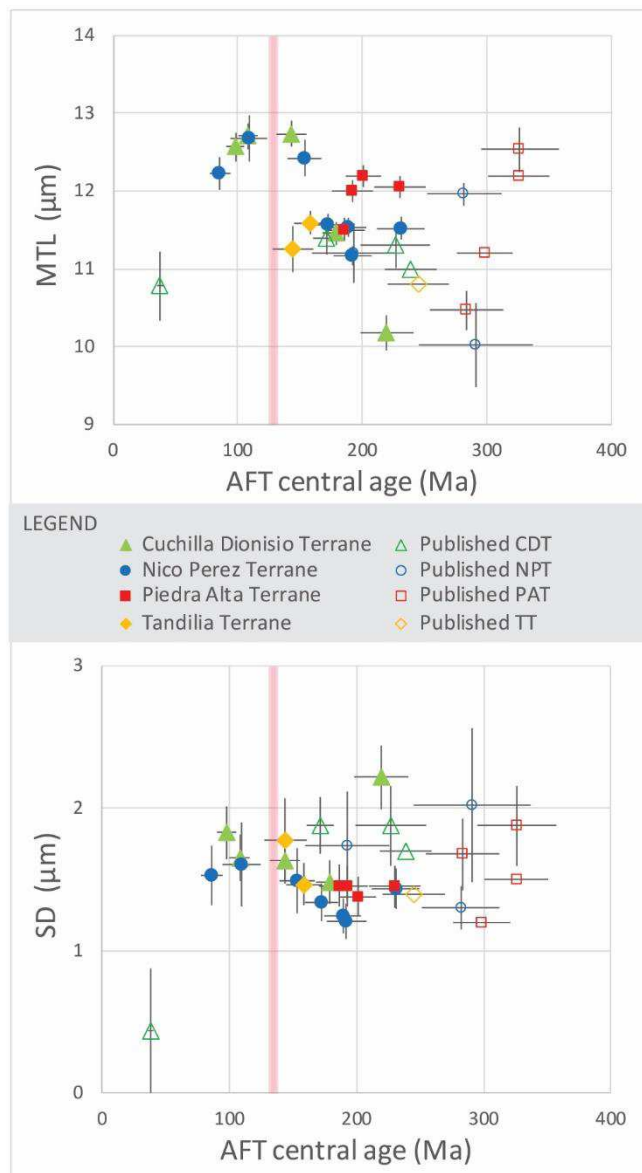


Figure 5.4: Compilation of AFT data available for the Uruguayan shield. Top, AFT central ages against MTLs uncorrected for their c-axis orientation, suggesting that samples went through protracted cooling without partial resetting during the Paraná-Etendeka LIP volcanism (vertical red bar), and with distinct parts of the shield cooling below 110 °C at different times. Bottom, plot of the AFT central ages against the standard deviation of the MTLs, which also does not show a “boomerang” shape. Error bars represent $\pm 1\sigma$ range.

5.5.2 Apatite (U-Th)/He

Apatites from 14 locations were selected for AHe analysis, in total representing 42 single crystal ages (Table 5.3). The obtained ages present are widely dispersed, not only between samples and terranes, but also among apatites from each sample, in a similar way as observed by Hueck *et al.* (2017).

Table 5.3: Summary of Apatite (U-Th)/He ages and parameters. Crystal dimensions were used to estimate an equivalent spherical radius. eU, total uranium content; Term, number of crystal terminations; Unc., uncorrected; Corr., corrected; SD, standard deviation; Ft, alpha ejection factor for age correction.

Apatite (U-Th)/He analysis																			
Sample	Crystal	U	Th	Sm	He	eU	Term.	Radius	Age Unc.	$\pm 1\sigma$	Ave. Unc.	SD	$\pm 1\sigma$	Ft	Age Corr.	$\pm 1\sigma$	Ave. Corr.	SD	$\pm 1\sigma$
#	#	(ppm)	(ppm)	(ppm)	(nmol/g)	(ppm)	#	(μm)	(Ma)	(Ma)	(Ma)	(Ma)	(Ma)	#	(Ma)	(Ma)	(Ma)	(Ma)	(Ma)
<i>Cuchilla Dionísio Terrane</i>																			
UY2	1	59,92	130,15	488,89	146,82	92,67	1	57,38	292,10	5,96	441,09	106,69	61,60	0,74	392,38	8,07	546,46	109,62	63,29
	2	21,79	61,86	368,63	101,75	37,99	1	79,51	494,97	10,11				0,81	608,67	12,54			
	3	8,78	24,84	305,88	45,05	16,03	2	92,53	536,20	11,07				0,84	638,33	13,27			
UY30	1	8,13	12,82	214,17	7,49	12,14	2	42,71	120,51	2,68	107,98	10,71	6,18	0,67	180,31	4,03	152,31	21,71	12,53
	2	24,29	19,84	478,29	15,14	31,18	2	55,35	94,34	1,31				0,74	127,41	1,77			
	3	9,85	8,15	18,56	7,00	11,85	1	53,89	109,09	1,69				0,73	149,21	2,33			
UY32	1	59,86	11,48	467,66	38,88	64,74	2	40,45	113,17	2,51	135,58	50,08	28,91	0,66	171,81	3,83	196,36	69,34	40,03
	2	45,55	5,08	421,35	22,73	48,72	1	46,78	88,60	1,97				0,70	126,41	2,83			
	3	46,53	4,36	447,24	54,10	49,65	1	46,86	204,97	4,58				0,70	290,85	6,54			
UY24	1	3,91	2,21	271,49	4,03	5,70	1	45,94	155,03	4,61	211,19	56,16	39,71	0,71	219,65	6,55	314,97	95,32	67,40
	2	2,22	1,89	469,70	4,75	4,87	1	34,84	267,35	10,79				0,65	410,29	16,33			
<i>Nico Pérez Terrane</i>																			
UY1	3	14,64	2,24	157,52	8,04	15,90	1	62,41	96,34	2,15	131,16	29,66	17,13	0,77	125,01	2,80	170,41	32,60	18,82
	4	19,69	54,24	222,63	22,89	33,42	1	47,23	128,32	1,81				0,69	186,17	2,65			
	5	26,26	25,87	124,55	30,01	32,90	2	95,87	168,83	2,52				0,84	200,06	3,00			
UY6	1	7,99	36,96	66,71	15,38	16,96	2	66,62	167,83	3,39	262,62	67,12	38,75	0,77	218,10	4,42	346,05	90,48	52,24
	2	9,03	43,73	74,69	32,68	19,61	2	59,49	305,66	6,20				0,75	409,89	8,37			
	3	5,90	24,48	68,68	20,36	11,95	2	64,67	314,37	6,41				0,77	410,17	8,42			
UY8	1	4,54	15,55	44,52	7,53	8,39	1	47,93	166,91	2,27	182,64	40,46	18,09	0,69	241,31	3,32	281,44	63,42	28,36
	2	21,50	41,04	72,27	21,49	31,45	2	38,08	126,17	1,46				0,63	201,46	2,37			
	3	11,28	50,36	358,19	30,32	24,75	2	41,09	234,61	3,28				0,65	362,35	5,08			
	4	11,46	44,23	88,01	24,41	22,22	1	39,51	202,88	2,86				0,63	320,65	4,56			

continues...

Sample	Crystal	U	Th	Sm	He	eU	Term.	Radius	Age Unc.	±1σ	Ave. Unc.	SD	±1σ	Ft	Age Corr.	±1σ	Ave. Corr.	SD	±1σ
#	#	(ppm)	(ppm)	(ppm)	(nmol/g)	(ppm)	#	(μm)	(Ma)	(Ma)	(Ma)	(Ma)	(Ma)	#	(Ma)	(Ma)	(Ma)	(Ma)	(Ma)
UY11	1	4,25	36,85	694,43	20,01	16,14	2	52,86	265,25	3,24	208,62	48,20	27,83	0,72	367,60	4,44	285,99	61,74	35,65
	2	6,21	43,76	359,92	13,63	18,14	1	45,83	147,43	1,89				0,68	218,29	2,79			
	3	8,34	74,17	621,66	30,96	28,61	1	71,44	213,17	2,59				0,78	272,07	3,29			
UY14	1	3,10	23,24	96,80	4,47	9,00	2	73,47	94,61	1,22	103,01	16,33	7,30	0,79	120,26	1,55	133,43	20,82	9,31
	2	3,92	24,81	91,44	6,31	10,16	2	62,63	117,32	1,33				0,75	155,65	1,76			
	3	5,86	22,81	69,82	4,94	11,53	2	62,61	80,37	0,90				0,76	106,26	1,19			
	5	2,84	20,74	85,27	5,10	8,09	2	74,51	119,73	1,42				0,79	151,57	1,79			
	UY21	1	18,58	52,98	716,38	15,92	97,71	1	41,89	91,78	1,90	105,94	14,16	8,18	0,68	139,63	2,90	152,94	13,31
<i>Piedra Alta Terrane</i>																			
UY16	1	6,08	24,39	164,32	14,82	12,56	2	54,18	224,94	2,63	250,26	18,01	10,40	0,73	310,02	3,64	328,44	23,04	13,30
	2	8,40	23,61	171,26	20,68	14,73	2	55,50	265,35	2,98				0,74	360,93	4,09			
	3	10,39	8,93	103,22	18,10	12,96	2	85,64	260,49	3,26				0,83	314,37	3,96			
UY25	1	56,87	38,42	271,62	64,15	67,13	1	49,97	176,95	3,78	258,83	59,84	34,55	0,72	247,45	5,32	368,18	85,42	49,32
	2	25,50	24,77	219,10	55,67	32,33	1	56,98	318,28	6,78				0,75	424,81	9,15			
	3	27,21	24,40	212,86	51,57	33,92	2	39,58	281,27	6,07				0,65	432,29	9,47			
UY27	1	13,43	16,16	314,13	30,29	18,69	2	46,35	311,03	3,97	263,80	34,10	19,69	0,70	445,54	5,76	388,25	40,51	23,39
	2	23,25	42,01	431,60	42,83	35,11	2	39,54	231,74	2,76				0,64	359,42	4,34			
	3	19,50	36,16	468,71	39,06	30,16	2	46,06	248,63	2,92				0,69	359,80	4,27			
<i>Tandilia Terrane</i>																			
UY18	1	9,44	2,74	129,44	12,50	10,69	2	49,67	222,16	6,50	201,68	21,16	10,58	0,72	308,79	9,10	289,96	34,86	17,43
	2	16,26	12,18	136,90	18,21	19,75	2	50,06	172,54	3,98				0,72	241,10	5,60			
	3	12,28	4,32	108,17	15,50	13,79	2	40,05	210,33	5,11				0,66	320,01	7,86			

The AHe uncorrected ages range throughout the Phanerozoic, but the majority of them are Mesozoic. No reduction in the age dispersion is observed after applying the Ft correction (Farley *et al.* 1996). Furthermore, the AHe ages obtained are mostly older than the AFT ages from the same location, portraying an inverse pattern that is often observed in cratonic regions (Flowers & Kelley 2011).

A common approach to investigate AHe ages dispersion is to evaluate the influence of the crystal radius and integrity (Reiners & Farley 2001; Brown *et al.* 2013), and of the effective uranium (eU) content of crystals (Flowers *et al.* 2007), factors that commonly affect AHe ages. Our samples do not show a clear correlation between ages and these parameters, suggesting that other factors are responsible for the AHe ages dispersion. Several variables can influence AHe ages, including U and Th zonation (Farley *et al.* 1996; Flowers & Kelley 2011), U-rich inclusions (Stockli *et al.* 2000), ${}^4\text{He}$ implantation from U-rich neighbor minerals and phases (Murray *et al.* 2014), accumulated radiation damage on the crystal lattice (Green & Duddy 2006; Shuster *et al.* 2006), among others – see Wildman *et al.* (2016) for a summary of the influence of these and others factors. These variables can be used to explain the dispersion in some samples, as in sample UY2, collected from a region of eU rich granites and that present old AHe ages and high values of ${}^4\text{He}$ for its eU content, making ${}^4\text{He}$ implantation or U-rich inclusions likely occurrences. Figure 5.5 shows apatites from samples UY8, UY27 and UY32 that were subjected of AFT analysis and exhibits zonation and inclusions. Although the images are not from crystals used for AHe dating, they represent common features in these samples that potentially affected our AHe ages. Considering this, we opted to report in Figure 5.2 the youngest AHe age for each location, which potentially represents the age least affected by factors such as implantation and inclusions. As such, these would be closer to the actual cooling age of the sample and correspond to the standard closure temperature (Dodson 1973) of the AHe system. The presence of inclusions, zonation or defects in the crystal lattice can lead to the highly dispersed ages and mask the common correlations between ages and eU or crystal radius. However, because dispersion is observed in most of our samples, a more general approach is desired to explain our results, as suggested later in the Discussion section.

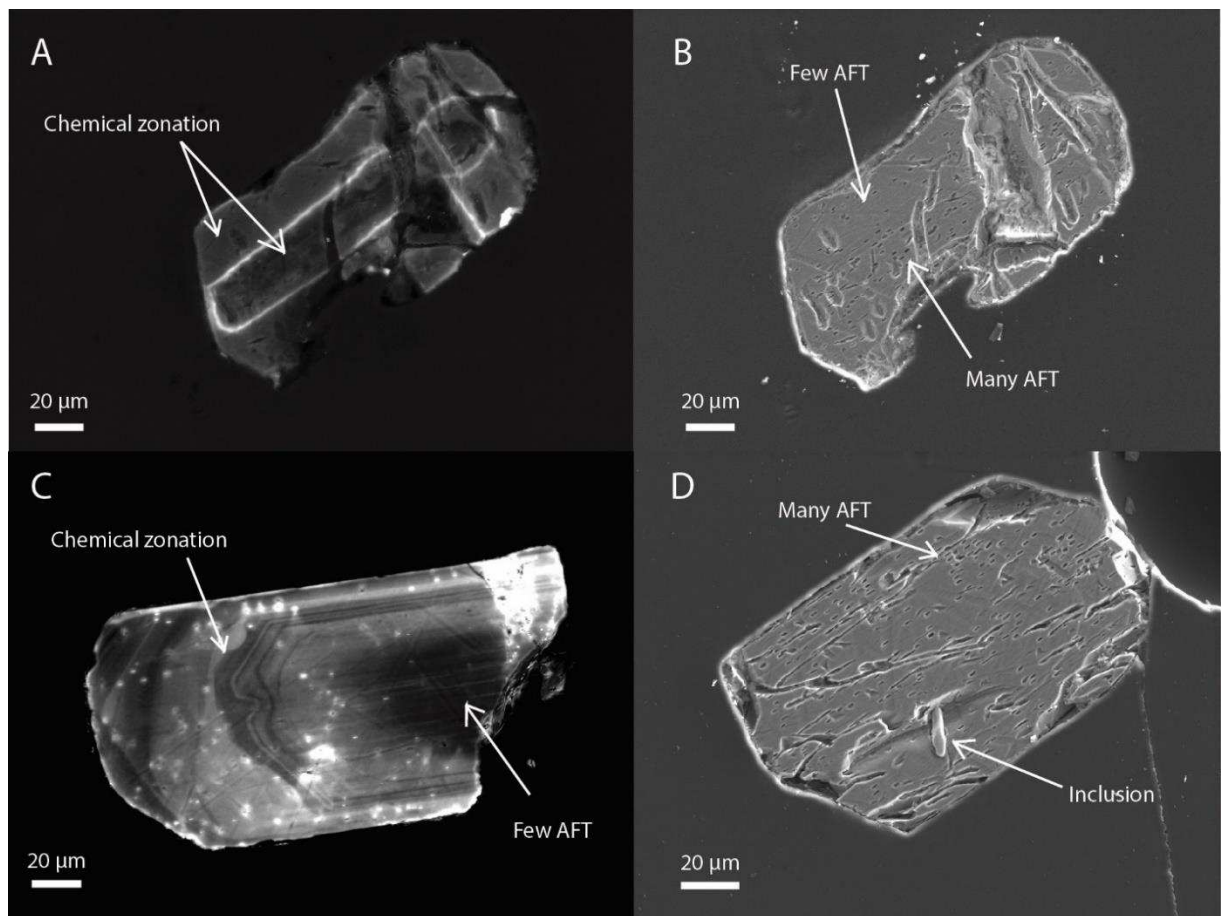


Figure 5.5: Photomicrographs of apatites showing factors that can affect the (U-Th/He) analysis and cause significant age inaccuracies. (A,B) Cathodoluminescence and secondary electron images from the same apatite from UY32 showing a brightly marked chemical zonation coincident with a fission-track density zonation. (C) Cathodoluminescence from apatite from UY8 showing chemical zonation and a low density of tracks in the centre. (D) Secondary electron image from apatite from UY27 showing inclusion and a higher density of tracks in the rims.

5.5.3 Zircon (U-Th)/He

A total of 40 zircons were dated from eight locations across the UYS (Tab. 5.4). Single crystal ZHe ages range through the entire Paleozoic and show a strong negative correlation with eU, unlike our AHe ages (Fig. 5.6). Such negative correlation is common in Cratonic regions and usually is attributed to long-term accumulation of radiation damage in the crystals. Zircons with high eU and long low-temperature histories are prone to develop a damage net within the crystalline lattice, which increases the diffusivity and loss of alpha particles, thus resulting in younger ages (Reiners 2005; Guenthner *et al.* 2013). Considering this, we opted to show in the map (Fig. 5.2) the oldest single grain ZHe age for each location, usually Cambrian/Ordovician for the NPT and CDT samples, and Permian for the PAT. The oldest ZHe age potentially represents the cooling age of the least damaged zircon

analyzed, likely closer to the beginning of the ${}^4\text{He}$ accumulation within the sample and to the standard closure temperature of the ZHe system. No correlation between ZHe ages and crystal radius, location or altitude was observed in our samples.

Table 5.4: Summary of Zircon (U-Th)/He ages and parameters. Crystal dimensions were used to estimate an equivalent spherical radius. eU, total uranium content; Unc., uncorrected; Corr., corrected; SD, standard deviation; Ft, alpha ejection factor for age correction.

Zircon (U-Th)/He analysis																		
Sample	Crystal	U	Th	He	eU	Radius	Age Unc.	±1σ	Ave. Unc.	SD	±1σ	Ft	Age Corr	±1σ	Ave. Corr.	SD	±1σ	
#	#	(ppm)	(ppm)	(nmol/g)	(ppm)	(μm)	(Ma)	(Ma)	(Ma)	(Ma)	(Ma)	#	(Ma)	(Ma)	(Ma)	(Ma)	(Ma)	
<i>Cuchilla Dionísio Terrane</i>																		
UY2	1	1216,02	636,19	1592,79	1365,52	36,94	212,40	3,02	273,11	68,31	30,55	0,68	311,46	4,49	371,45	86,13	38,52	
	2	773,03	215,67	1214,88	823,71	39,61	267,17	5,04				0,70	379,04	7,24				
	3	741,36	175,63	1292,37	782,64	52,87	298,24	5,68				0,77	385,10	7,41				
	4	395,44	195,09	957,90	441,28	47,41	389,04	7,28				0,75	518,30	9,84				
	7	1267,26	388,53	1480,69	1358,56	48,81	198,68	3,71				0,75	263,37	4,96				
UY29	1	543,50	270,19	1130,77	606,99	61,94	335,50	4,39	299,50	80,16	35,85	0,80	417,01	5,52	395,12	94,15	42,11	
	2	293,29	213,03	693,26	343,35	50,85	362,95	4,57				0,76	475,00	6,09				
	3	1963,03	622,64	2228,84	2109,35	42,73	192,73	2,84				0,72	266,84	3,97				
	4	298,36	167,44	736,46	337,71	50,99	390,86	5,61				0,77	509,99	7,43				
	5	704,82	281,30	912,64	770,93	39,63	215,49	3,13				0,70	306,73	4,52				
UY32	1	2844,44	1344,08	1280,10	3160,30	94,20	74,66	1,03	121,47	29,46	13,18	0,87	86,22	1,20	152,75	40,98	18,33	
	2	1943,91	245,54	1307,62	2001,62	59,78	119,95	1,73				0,80	150,63	2,18				
	3	1857,49	725,71	1768,94	2028,03	57,63	159,57	2,22				0,79	202,44	2,83				
	4	1138,28	3274,83	1505,60	1907,87	55,28	144,52	1,60				0,77	187,89	2,09				
	5	1542,94	344,60	960,09	1623,92	59,83	108,67	1,50				0,80	136,58	1,90				
<i>Nico Pérez Terrane</i>																		
UY8	1	438,83	158,79	1033,20	476,15	77,94	388,74	6,15	377,98	21,07	9,42	0,84	460,49	7,35	456,99	16,15	7,22	
	2	281,82	94,67	569,75	304,06	55,21	337,27	5,32				0,78	430,51	6,87				
	3	280,84	77,47	647,22	299,04	88,50	387,67	6,27				0,86	449,53	7,32				
	4	350,88	76,05	817,60	368,75	70,52	396,72	5,74				0,83	478,21	6,98				
	5	281,90	113,49	653,05	308,57	64,82	379,52	5,32				0,81	466,22	6,61				

continues...

Sample	Crystal	U	Th	He	eU	Radius	Age Unc.	$\pm 1\sigma$	Ave. Unc.	SD	$\pm 1\sigma$	Ft	Age Corr	$\pm 1\sigma$	Ave. Corr.	SD	$\pm 1\sigma$
#	#	(ppm)	(ppm)	(nmol/g)	(ppm)	(μ m)	(Ma)	(Ma)	(Ma)	(Ma)	(Ma)	#	(Ma)	(Ma)	(Ma)	(Ma)	(Ma)
UY10	2	1519,54	1104,20	1203,76	1779,03	32,76	124,16	1,53	213,19	89,58	40,06	0,64	193,48	2,43	297,42	109,43	48,94
	3	1821,40	1769,65	1672,24	2237,27	37,42	137,00	1,65				0,68	201,41	2,47			
	4	758,05	703,75	812,20	923,43	39,14	160,89	1,98				0,69	231,92	2,90			
	6	415,63	219,89	836,49	467,30	43,53	322,77	5,21				0,73	443,12	7,25			
	7	489,04	235,10	969,29	544,29	52,03	321,12	5,19				0,77	417,14	6,82			
UY13	1	646,57	326,51	1441,94	723,30	54,84	358,30	6,20	365,08	12,08	5,40	0,78	458,57	8,03	469,36	8,45	3,78
	2	628,19	257,97	1467,16	688,81	60,34	381,89	6,69				0,80	476,73	8,45			
	3	491,98	235,19	1140,75	547,25	54,63	374,08	6,54				0,78	478,93	8,48			
	4	770,65	247,05	1600,27	828,70	44,30	347,24	5,86				0,73	472,45	8,09			
	5	560,25	224,84	1242,32	613,09	57,29	363,90	6,07				0,79	460,11	7,76			
<i>Piedra Alta Terrane</i>																	
UY27	1	851,37	116,24	755,00	878,69	90,84	157,22	2,19	170,76	40,11	17,94	0,86	182,07	2,54	206,24	46,65	20,86
	2	1102,95	316,03	1163,28	1177,22	60,71	180,43	2,46				0,80	225,73	3,10			
	3	1629,90	301,28	945,84	1700,71	60,34	102,28	1,44				0,80	128,27	1,81			
	4	483,89	69,39	525,97	500,19	68,89	191,79	3,14				0,82	233,07	3,84			
	5	670,02	204,32	876,64	718,04	80,79	222,08	3,49				0,85	262,08	4,14			
<i>Tandilia Terrane</i>																	
UY18	1	2012,46	328,91	1106,92	2089,76	59,72	97,46	1,61	154,81	42,01	18,79	0,80	122,52	2,03	207,89	59,07	26,42
	2	1670,14	299,44	1299,07	1740,51	47,60	136,83	1,86				0,75	182,88	2,51			
	4	1771,17	383,20	1365,69	1861,22	43,11	134,55	1,81				0,72	185,87	2,52			
	5	1105,25	334,62	1245,33	1183,88	44,39	191,87	2,58				0,73	262,18	3,56			
	6	784,68	167,61	965,85	824,07	46,85	213,35	3,77				0,75	286,00	5,10			

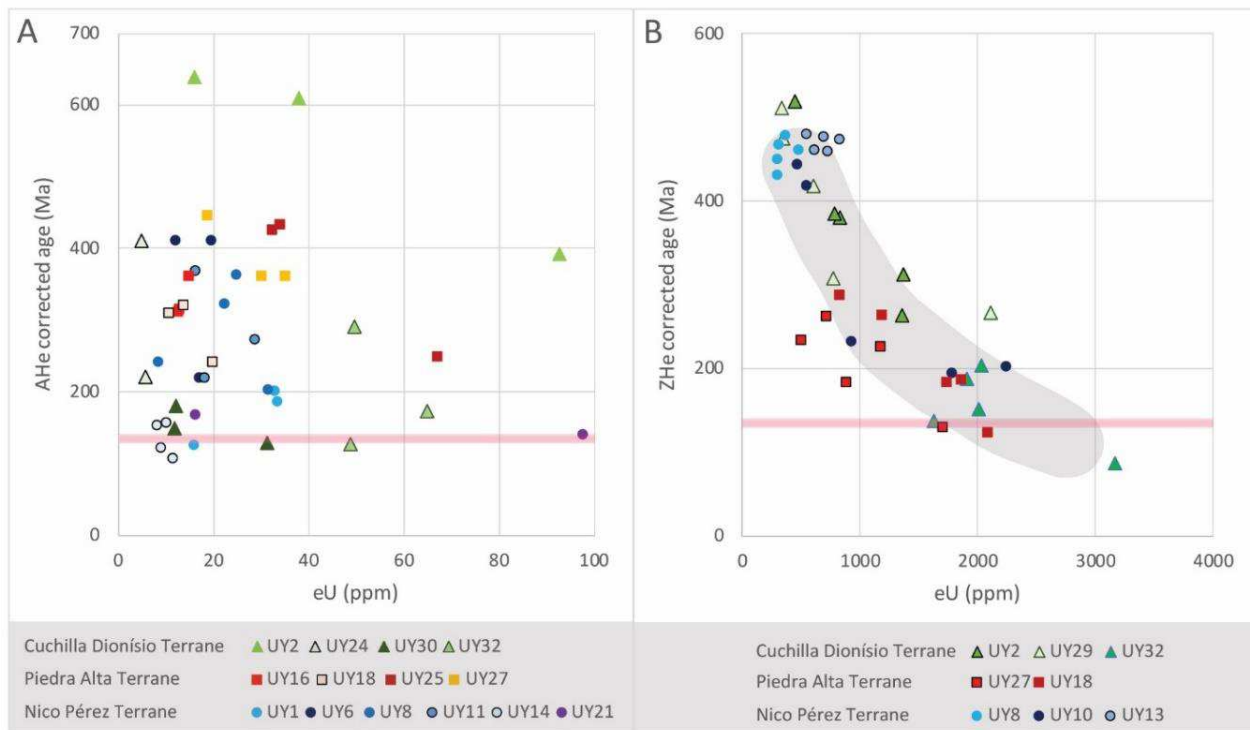


Figure 5.6. Plots of ($\text{U-Th}/\text{He}$) corrected ages against effective uranium content ($\text{eU} = [\text{U}] + 0.235 \times [\text{Th}]$). (A) AHe ages showing variable intrasample behavior and no apparent general trend. (B) ZHe ages clustered or showing a negative correlation intrasample and as general trend. Horizontal bar indicates the Paraná-Etendeka LIP volcanism.

5.6 Inverse thermal history modelling

The thermal history of 19 locations was computed by inverse modeling and the results can be divided into two main groups with distinct cooling patterns. All models use AFT data as baseline, thermochronometer with the most consistent regional results and those physical proprieties that are better understood in the scientific community, but most of the models include ($\text{U-Th}/\text{He}$) data as well. Final models display a good fit between observed and predicted AFT ages and MTL, a good fit of ZHe ages and usually a poor fit of AHe ages. Representative models are shown in Figure 5.7 and the final models of each sample can be found in the Supplementary Material.

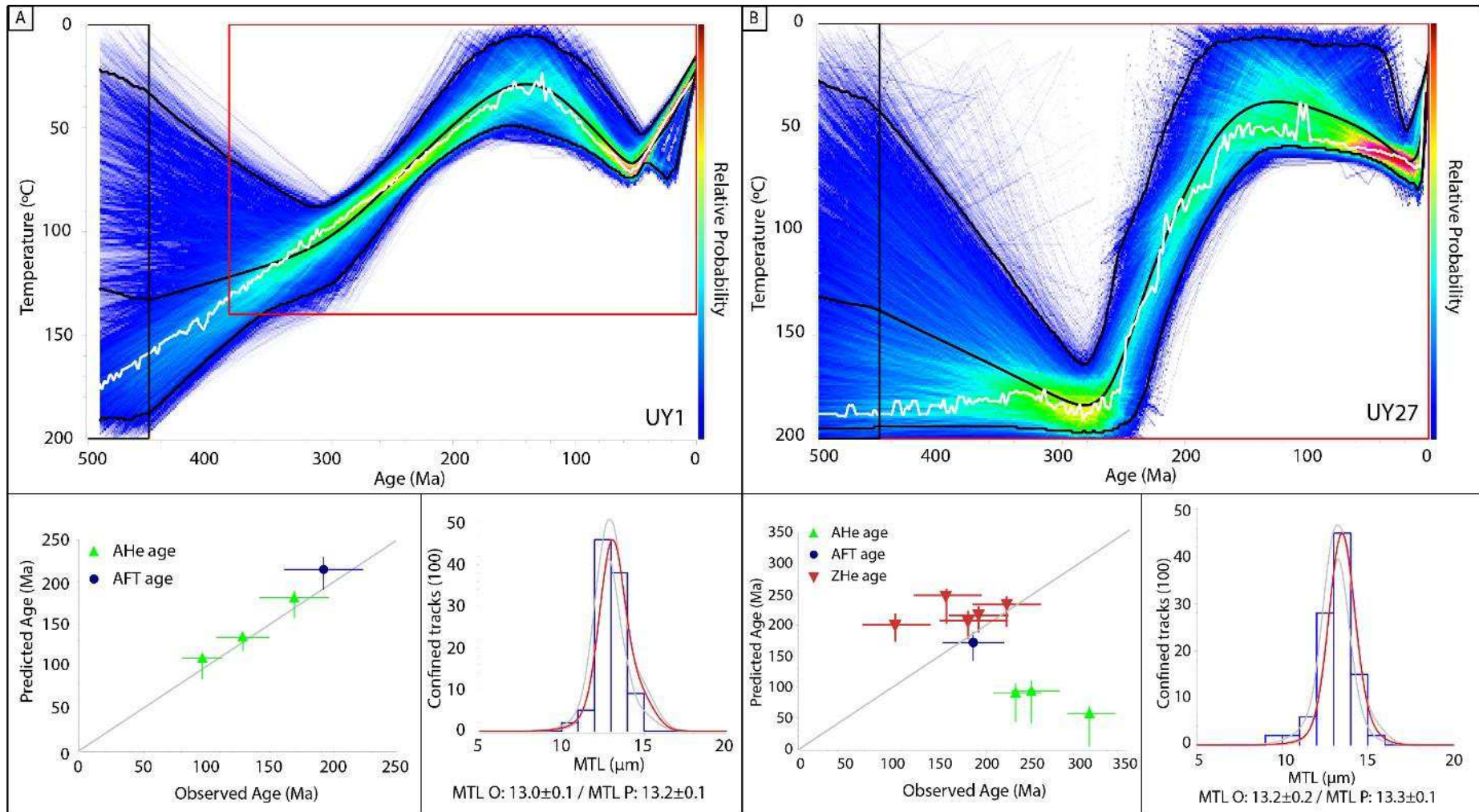


Figure 5.7: Panel of representative inverse thermal models from Group 1. (A) On the top: Model for sample UY1. Black line represents the mean cooling trajectory, white line the maximum mode and colored pathway the 95% confidence interval with relative probability scale. Black rectangle is the start constraint box for the model, red box the prior to test thermal paths (see Gallagher, 2012). Bottom left: fit between observed ages and predicted ages by the model, including $\pm 1\sigma$ range. Bottom right: track length distribution with values of MTL observed and predicted by the model. (B): Same as in (A) but for sample UY27, with ZHe data.

Group 1 is composed by ten samples (UY1, UY2, UY6, UY7, UY8, UY16, UY18, UY25, UY26 and UY27) located essentially in the west and NW of the shield (PAT, TT and northern part of the NPT). Models from these samples show passage through the AFTPRZ between c. 300 and 180 Ma (Fig. 5.8), with cooling rates varying between 0.60 and 0.32 °C/Ma. In most cases, entrance in the AFTPRZ (c. 110 °C) occurs in the Carboniferous-Permian transition, while cooling out from the zone (c. 60°C) occurs by Late Jurassic-Early Jurassic. Samples UY18 and UY27, which present relatively young ZHe ages, went through the AFTPRZ slightly later and faster (c. 0.90 °C/Ma) than the general trend. Models from Group 1 suggest that in Early Cretaceous all these samples might have reached surface temperatures, although it cannot be precisely constrained by our AHe data (Fig. 5.7). Afterwards, all models support a subtle reheating phase, that possibly lasted until the end of the Paleogene and raised temperatures slightly over 60 °C in some samples. This reheating is at the limit of the AFT method resolution, and possibly a modelling artefact (Jonckheere 2003), a reflection of the considerably short length of the confined tracks of these samples, usually below 12 µm, which would require a prolonged time in the AFTPRZ. A final cooling towards surface temperature takes place by the Miocene. Sample UY29 resulted in a thermal history similar to Group 1 but with earlier and faster passage through the AFTPRZ, at a rate of 0.88 °C/Ma. Cooling into the AFTPRZ occurs by the Devonian-Carboniferous transition with an exit by the Permian. The model from this sample shows stability at temperatures around 30 to 50 °C until the Cretaceous, when a reheating phase occurred raising the temperature to 75 °C. A final cooling towards surface conditions is observed after the Paleocene. Sample UY29 is located in the extreme SE of the shield, where most samples present thermal histories belonging to Group 2.

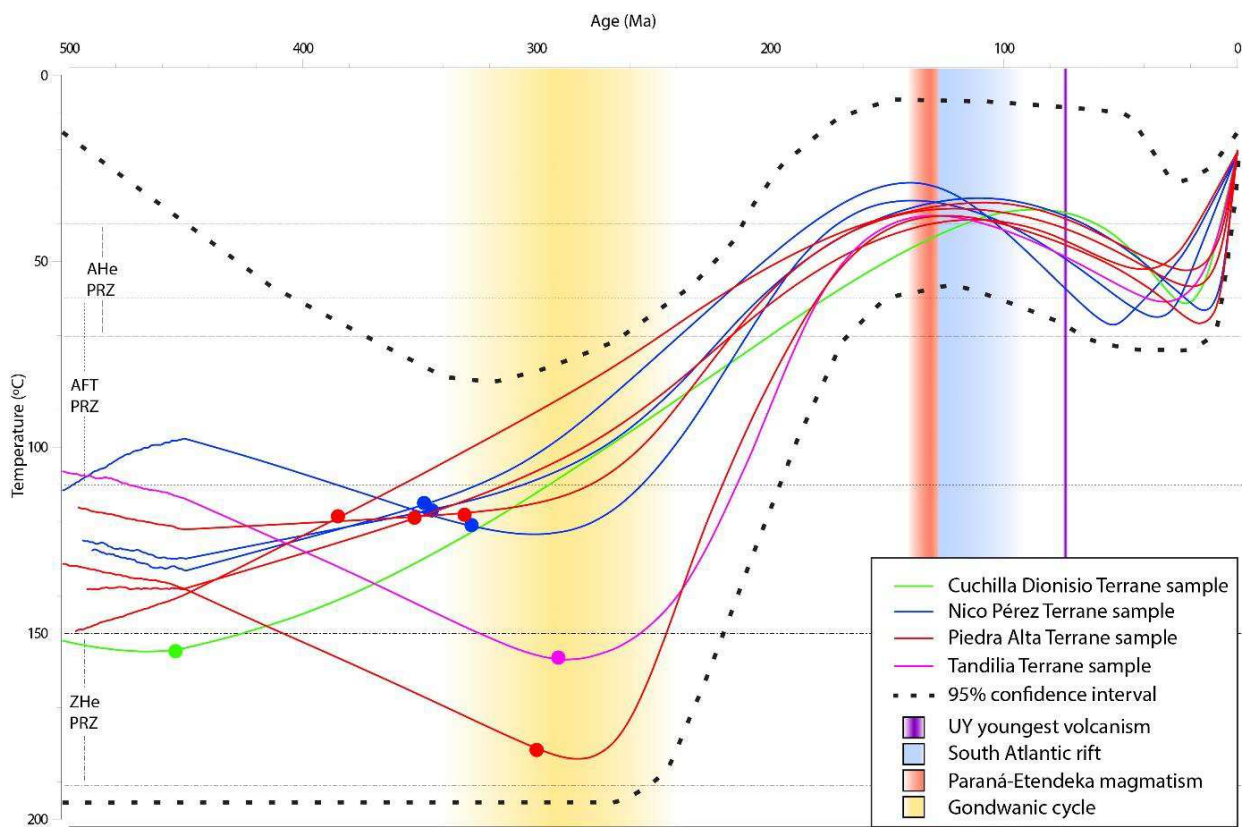


Figure 5.8: Mean cooling trajectories of inverse models for samples from Group 1. Dashed bold lines represent the superposition of the 95% confidence interval of individual models. Dots indicate point after which trajectory relative probability is over 50 % inside the confidence interval, i.e. model curve before the dot is poorly constrained. Approximate interval of PRZ of each thermochronometer indicated with dashed horizontal lines. Main thermotectonic events in the region are indicated as shaded bars: Gondwanic cycle (c. 340 to 250 Ma) (Milani & De Wit, 2008), Paraná-Etendeka LIP (138 to 125 Ma) (Rossetti et al. 2014) and Atlantic Ocean opening (130 to 113 Ma) (Stica et al. 2014).

Group 2 comprises eight samples UY10, UY11, UY14, UY19, UY21, UY30, UY31 and UY32. These samples are located mostly in the centre and SE of the shield (NPT and CDT), and are often near shear zones. Unlike Group 1, the models for these samples lack a Late Cretaceous reheating phase, and show a monotonic cooling towards surface since early Mesozoic. The time of cooling into the AFTPRZ occurs later than Group 1 and is variable among the samples, ranging between the Permian and Jurassic (Fig. 5.9). Cooling occurs at rates between 0.30 and 0.71 °C/Ma, and during the Cretaceous all samples reached temperatures below 60 °C. Although Group 2 corresponds to protracted and monotonic thermal histories, it should be considered that some of these samples have a limited number (< 50) of confined tracks to be used during modelling, thus their models are less robust. Nonetheless, all of them have younger AFT ages and higher track length values (MTL) than Group 1, with lengths usually above 12.2 µm, even when 100 confined tracks were measured. Therefore,

their monotonic thermal histories can represent Mesozoic tectonic activity in faults/shear zones or at the margins of the shield, especially near the Atlantic Ocean, but can also reflect their long and often limited number of confined tracks, which do not require a protracted period in the AFTPRZ or a reheating phase to shorten them as in Group 1.

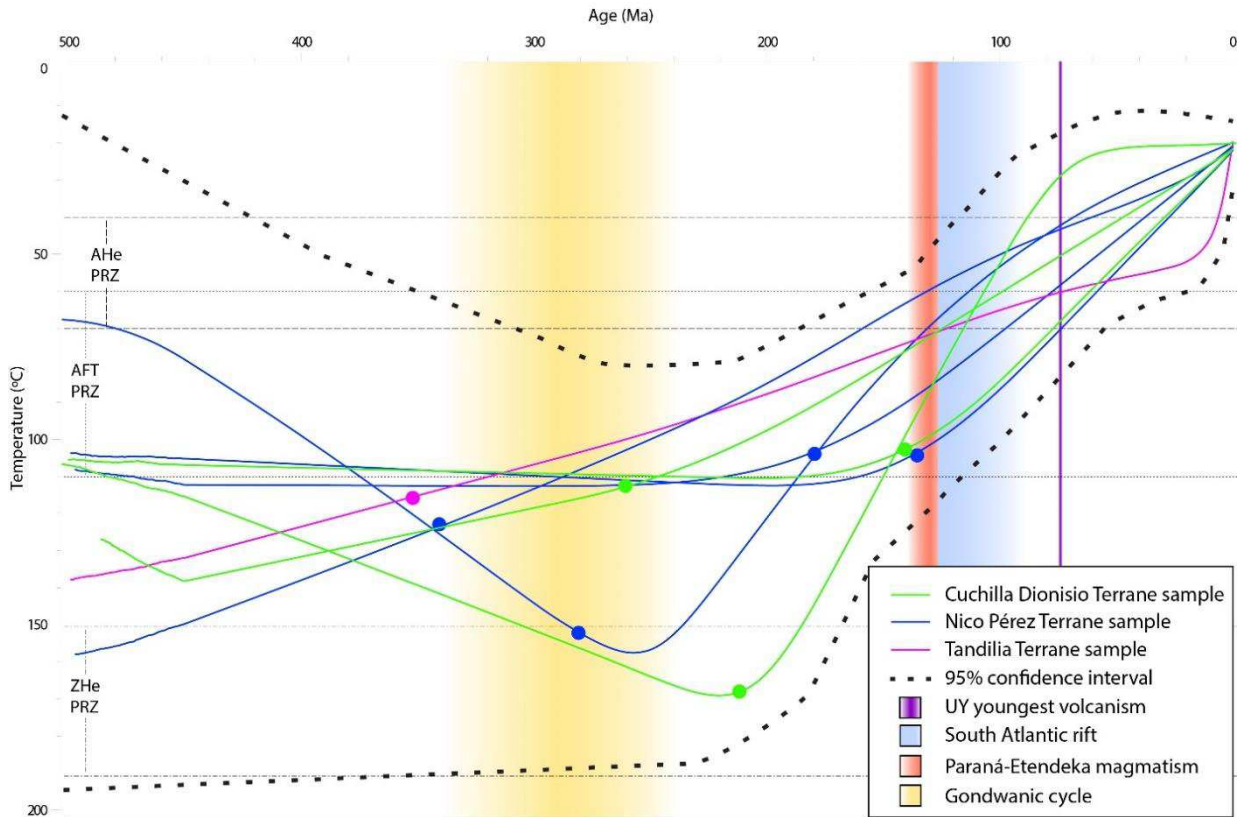


Figure 5.9: Mean cooling trajectories of inverse models for samples from Group 2. Dashed bold lines represent the superposition of the 95% confidence interval of individual models. Dots indicate point after which trajectory relative probability is over 50 % inside the confidence interval. i.e. model curve before the dot is poorly constrained. Approximate interval of PRZ of each thermochronometer indicated with dashed horizontal lines. Main thermotectonic events in the region are indicated as shaded bars: Gondwanic cycle (c. 340 to 250 Ma) (Milani & De Wit, 2008), Paraná-Etendeka LIP (138 to 125 Ma) (Rossetti et al. 2014) and Atlantic Ocean opening (130 to 113 Ma) (Stica et al. 2014).

5.7 Discussion and integration

In this study we combined three thermochronometers to investigate the cooling history of the Uruguayan shield. We presented a new dataset with 19 AFT, 42 AHe and 40 ZHe ages, plus the inverse thermal histories modeled for 19 locations. This dataset, combined with information from previous works (Kollenz 2015; Hueck et al. 2017; Gomes & Almeida 2019) provides an extensive coverage of the low-temperature history of the UYS. Based on the integration of these data, we characterized the

thermal evolution of the shield during the Phanerozoic and discuss the exhumation of the basement, taking into account the apparent disparities between previous models.

5.7.1 Thermochronometry ages

All AFT ages obtained in this work are much younger than the host rock stratigraphic age and the last orogenic cycle that affected the region (Gondwana assembly during the Brasiliano/Pan-African cycle, late Neoproterozoic-Cambrian). Thus, we interpret our AFT ages as cooling ages that represent exhumation of the basement due to denudational events. There is good agreement between our AFT ages and those obtained by Kollenz (2015) and Gomes & Almeida (2019), totalling a combined dataset of 36 AFT ages across the UYS. Although the shield does not have significant topographic variations, a plot of the AFT central ages against sample elevation, including the works aforementioned, presents clear positive correlations for the CDT, NPT and PAT (Fig. 5.3). Ages also tend to increase with the distance from the South Atlantic Ocean, a common pattern observed in continental passive margins (Gallagher & Brown 1997). The PAT, representative of the Rio de La Plata Craton, and the northern part of the NPT, arguably part of the Craton as well, concentrates the older AFT ages in Uruguay. Remarkable is the similarity between the confined track lengths in the three works, both in values and distributions, which reveal MTL of short to medium values, independently of the location in the shield. This pattern of tracks with reduced lengths implies that the samples went through a long period at temperatures close or inside the AFTPRZ, allowing continuous annealing of the tracks. The medium-high Dpar values of our samples, indicative of a fairly high resistance to annealing (Carlson *et al.* 1999; Donelick *et al.* 2005), reinforce this interpretation.

Regarding the (U-Th/He) data, our AHe ages tend to be slightly older and present higher dispersion when compared to those obtained by Hueck *et al.* (2017), who reported mainly Permian to mid-Cretaceous ages, but discarded several older crystals. Although the AHe represents a lower temperature thermochronometer than the AFT system, our AHe ages are usually older than AFT ages from the same sample, in an inverse pattern common in Cratonic regions (Flowers & Kelley 2011). This inverted behavior is characteristic for apatites with $eU > 15$ ppm subject to prolonged residence at temperatures below 70 °C, and augmented by reheating episodes that do not reset the AHe ages (Shuster *et al.* 2006; Reiners *et al.* 2018). The wide dispersion of AHe ages within a sample can be attributed to internal factors, such as chemical zonation and alpha implantation, among others, that affect single aliquots. However, because

inversion of AHe and AFT ages is a pattern in our dataset, and considerable dispersion of AHe ages is observed in almost every sample, this behavior must be attributed to a more embracing mechanism. Considering that our samples are of Precambrian rocks, and that our models and AFT data indicate residence at low temperatures (<110 °C) since the middle Mesozoic, it is likely that the analyzed apatites have accumulated a relatively high degree of radiation in the last 200 Ma. The damaged crystal lattice affects the diffusivity of the alpha particles within the apatites, initially increasing the retentivity of He, and resulting in abnormally old ages for the AHe system (Green & Duddy 2006; Shuster *et al.* 2006). Furthermore, Shuster *et al.* (2006) claims that apatite with variable eU content and subject to a reheating episode after significant accumulation of radiation damage might present a large span of AHe ages, being most extreme when the reheating increase temperatures close to 60 °C. Therefore, it is likely that some of our AHe ages are affected by intrasample factors, but it is plausible that the general behavior observed in the UYS is a consequence of accumulation of radiation damage in the apatites since the early Mesozoic, with dispersion augmented by an episode of subtle reheat in the region.

The accumulation of radiation damage plays a major role in our ZHe ages as well. If the density of damage sites overcome a threshold, they can become interconnected and decrease the retentivity of He, resulting in young ages owing to rapid He escape. Because a zircon's eU is usually one or two orders of magnitude higher than an apatite's eU, the connection between radioactive defects within the crystal lattice after long-term residence at shallow temperatures is very likely. Therefore, although our ZHe ages tend to be younger than the ones obtained by Hueck *et al.* (2017), this can be attributed to the difference in the eU of the zircons analyzed in each work. While we found that our dispersed ages have a clear negative correlation with eU, which varies between 299 and 3160 ppm (Fig. 5.6), Hueck *et al.* (2017) presented mostly zircons with eU below 500 ppm and whose ZHe ages clustered in the Cambrian. Our low eU samples present very similar ages to those from their work, indicating that most of the UYS reached temperatures within the ZHePRZ in the early Paleozoic. Additionally, the age dispersion observed by us indicates that samples passed through a protracted period of low temperatures (< 150 °C), favoring the accumulation of radiation damage that when interconnected became escape paths for the alpha particles generated within the zircons (Shuster *et al.* 2006; Reiners *et al.* 2018).

The evaluation of the thermochronometry ages alone, obtained from the three thermochronometers used in this work and integrated with ages previously published,

gives important insights into the thermal behaviour of the Uruguayan Shield. The higher temperature thermochronometer ZHe ages suggest that most of the shield rocks currently exposed were at temperatures below 200 °C since the early Paleozoic. The AFT data, of intermediate temperature, indicate that samples passed through temperatures between 100 and 60 °C from the late Paleozoic to the middle Mesozoic. Finally, the lower temperature thermochronometer AHe suggests that our samples have been accumulating considerable amounts of radiation damage since the late Paleozoic, and that magmatic events in the region, such as the Paraná-Etendeka LIP and the South Atlantic rift, did not raise basement temperatures to the point of resetting AHe ages (> 70 °C). Nonetheless, AHe ages dispersion and inverse modeling of the thermal history of our samples suggest that these plate-wide events might have increased UYS temperature during Late Cretaceous, as discussed below.

5.7.2 Thermotectonic evolution of Uruguay

Previous thermotectonic models proposed for the UYS all infer a complex thermal history for the now exposed basement rocks, but are not consistent regarding the timing of cooling/reheating phases and exhumation/burial events. Based on ZHe and AHe data, Hueck *et al.* (2017) argued that the shield reached near-surface conditions (< 60 °C) in the Silurian and went through subsidence and exhumation cycles during the Paleozoic, related to deposition of Devonian and Permian Paraná Basin sequences over the UYS. According to the authors, these depositional cycles of shallow burial and erosion did not increase basement temperatures over 90 °C. However, models based on AFT data by Kollenz (2015) and Gomes & Almeida (2019), as well as the multi-thermochronometers models presented here, suggest that most of the shield cooled from the high end of the AFTPRZ (110 °C) only after the Devonian. Therefore, if the UYS rocks were exposed to near surface conditions during the Silurian, a reheating to temperatures above the 110 °C is necessary to reset the AFT thermochronometer during the Devonian.

Deposits of the Durazno Group, part of the Devonian Paraná Supersequence, are exposed in the shield NNE and overlie the eastern PAT and western NPT. Provenance studies by Uriz *et al.* (2016) support the CDT as the main source for the Durazno Group sediments, which corroborates the early onset of cooling and exhumation observed in our models for CDT samples UY2 and UY29. These models, which include ZHe, suggest temperatures above 150 °C during the Silurian, followed by continuous cooling and exhumation of the samples towards the surface. Thus, the

exposure of the CDT to near surface conditions during the Silurian followed by reburial to reset the AFT thermochronometer seems unlikely. The Durazno Group would have been deposited on a rather narrow and N-S oriented depression over the PAT and NPT terranes, which also acted as secondary and proximal detrital sources. In our models, the onset of cooling for these terranes occurs only around the Devonian-Carboniferous boundary, so they could have been exposed to near surface conditions during the Silurian and buried by the Durazno Group to temperatures over 100 °C to reset their AFT ages during the Devonian. However, our models for these terranes favor a simpler cooling history, fitting Mesozoic AFT ages with ZHe ages as old as Ordovician in the NPT or young as Permian in the PAT, without the need of exposure to the surface during the Silurian and burial in the Devonian. Moreover, palynomorphs and organic matter in the Durazno Group show little thermal overprint, mostly below 60 °C. All things considered and adopting an Occam's razor principle, exposure of our samples to near surface conditions in the Silurian followed by reset of AFT ages in Devonian seems unlikely, and a continuous protracted cooling of the shield since early to middle Paleozoic until the Mesozoic provide a satisfactory fit to the available data, with onset of cooling occurring earlier in the CDT than in the NPT and PAT.

The main cooling phase that led most of the shield rocks to near surface conditions seems to have started during the Carboniferous-Permian transition (Fig. 5.10). This denudation-induced cooling is characteristic of models from Group 1 (Fig. 5.8), in which most samples pass through the AFTPZ (between 110 and 60 °C) from c. 300 Ma until the Jurassic. This behavior is consistent over the PAT, TT and NPT, but less constrained on the CDT, where samples went through cooling since early Paleozoic (UY2 and UY29) or later in the Mesozoic (UY30, UY31 and UY32). Continuous cooling from late Paleozoic to middle Mesozoic is also dominant in AFT models from Kollenz (2015) and Gomes & Almeida (2019), although some samples from the latter suggest subtle reheating in this period. The onset of this cooling phase is correlated to the Gondwanic cycle, characterized by subduction of the Panthalassa Ocean and accretion of exotic terranes on the SW margin of Gondwana (Fig 5.1) (Scotese *et al.* 1999; Milani & Wit 2008). Intraplate stress transmission linked to these collisions reactivated basement structures below the Paraná Basin and surrounding areas (Milani & Wit 2008), with deformation and exhumation inferred from NE Argentina to southern Brazil until the Triassic (Zambrano & Urien 1970; Zerfass *et al.* 2004; Pankhurst *et al.* 2006; de Oliveira *et al.* 2016; Machado *et al.* 2019). Therefore, the onset of this major cooling phase in the UYS is likely related to far field propagation

stress and deformation caused by the Gondwanic cycle. Furthermore, during the Permian the Gondwana I Supersequence was deposited in the Paraná Basin, with its thickness increasing towards NW Uruguay (de Santa Ana *et al.* 2006). Paleocurrents of the lower part of this supersequence are preferentially towards the west and NW, and the alluvial, coarse syn-orogenic deposits from the upper part suggest that the Uruguayan shield was a basement high and possibly a limit for deposition (de Santa Ana 2004). However, restricted sedimentation and burial of parts of the UYS might have occurred as well and could explain local reheating observed in some models from Gomes & Almeida (2019).

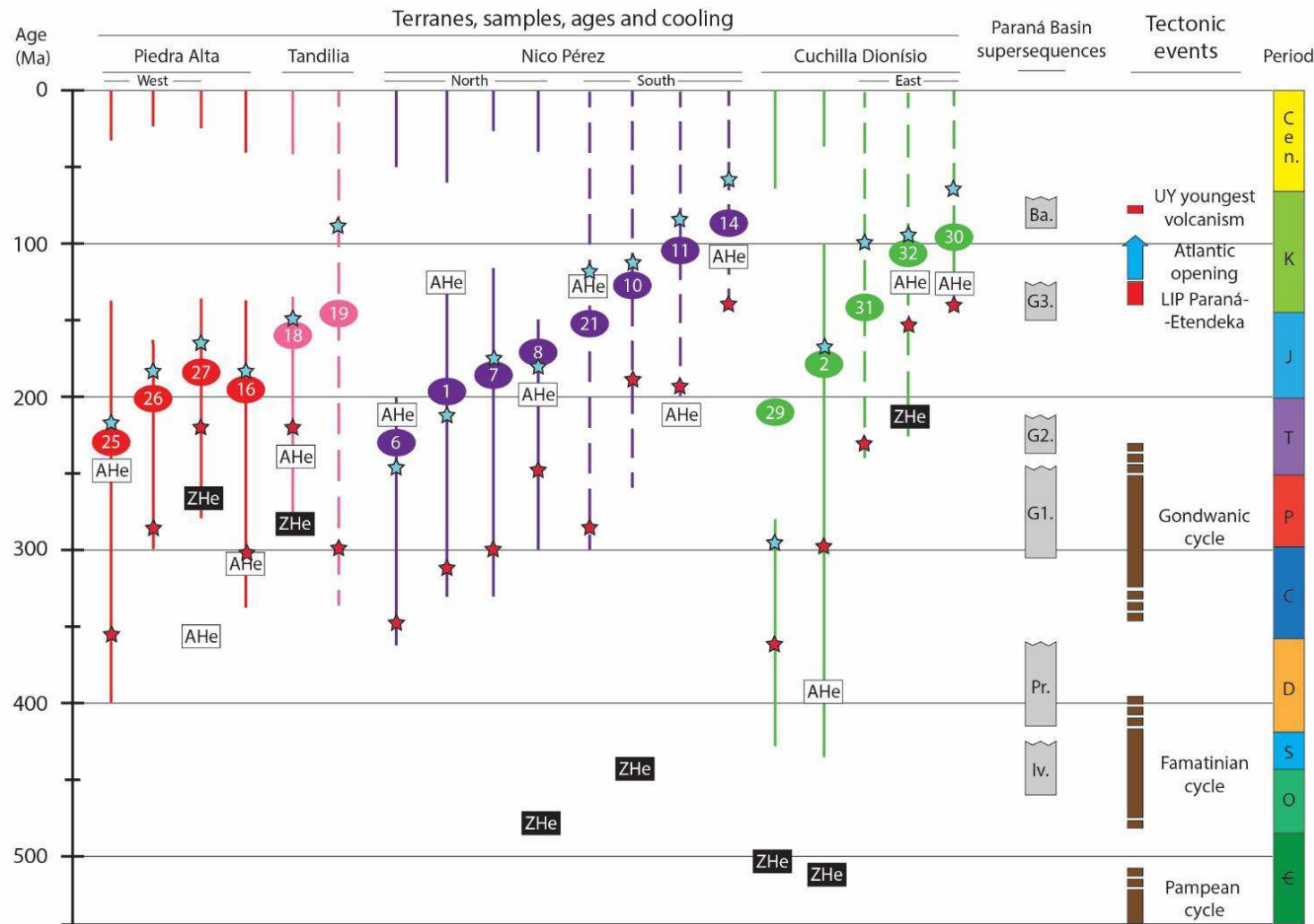


Figure 5.10: Chronological chart of cooling phases in the Uruguayan Shield observed in inverse thermal models. Solid lines represent cooling of samples from Group 1, dashed lines from Group 2. Sample ID placed according to its AFT central age, while the oldest ZHe and youngest AHe corrected ages are reported when available. Red and blue stars indicate the approximated time of passage through temperatures of 110 and 60 °C, respectively. Boxes on the right represent tectonic and magmatic regional events in the vicinity of the UYS, and the sedimentary record of the Paraná Basin (supergroups Rio Ivaí - Iv., Paraná - Pr., Gondwana I - G1, Gondwana II - G2, Gondwana III - G3, and Bauru - Ba.).

This main cooling phase of the UYS seems to have persisted until the Late Jurassic, when models suggest that our samples reached near surface temperatures (<60 °C). In NW Uruguay, fluvial and aeolian sandstones from the Gondwana III Supersequence (Sprechmann *et al.* 1981) indicate exposed areas of the Rio de La Plata Craton during the Early Cretaceous (Bossi *et al.* 1998; de Santa Ana 2004). The continuous and protracted cooling of the UYS, the beginning of which is likely related to intraplate deformation caused by the Gondwanic cycle, might have continued by uplift of the lithosphere preceding the South Atlantic opening (Early Cretaceous). During the Mesozoic the Brazilian margin went through broad epeirogenic uplift, proposed to be related to lithosphere thinning before Gondwana breakup (Tello Saenz *et al.* 2003; Zalán 2004; Carneiro *et al.* 2012). Cooling contemporaneous to that found in the UYS was observed in southernmost Brazil (de Oliveira *et al.* 2016; Machado *et al.* 2019) and can be attributed to increased buoyancy of the lithosphere before rifting, possibly caused by the accumulation of melt in the asthenosphere underneath (Quirk & Rüpke 2018). Remarkably, in the Early Cretaceous the voluminous extrusive magmatism of the Paraná-Etendeka Large Igneous Province covered most of the Paraná Basin, with lava flows extending from NE Argentina to central Brazil and Paraguay, and correlative units in southern Africa (Zambrano & Urien 1970; Turner *et al.* 1994; Gibson *et al.* 2006). This magmatism is often associated with the presence of the Tristan da Cunha mantle plume under the region and had its peak at c. 133 Ma, closely preceding the opening of the South Atlantic Ocean (Turner *et al.* 1994; Meisling *et al.* 2001; Gibson *et al.* 2006; Rossetti *et al.* 2014).

Rifting in the Atlantic Ocean propagated from SW to NE and is characterized by intense volcanic activity around the UYS. Besides the Paraná-Etendeka LIP magmatism that covered northern Uruguay, the eastern Uruguayan continental margin possesses broad wedges of magmatic seaward-dipping reflectors, which thicknesses might reach more than a dozen kilometers and width up to one hundred (Soto *et al.* 2011; Morales *et al.* 2017; Reuber *et al.* 2019). Moreover, the spreading rates between South America and Africa increased continuously from 20 mm/yr at c. 125 Ma to a peak of 77 mm/yr at c. 80 Ma (Granot & Dyment 2015; Brune *et al.* 2016), implying in intense magmatic activity at the east of Uruguay. Furthermore, the tectonic stresses related to rifting are thought to have provoked the development of the SaLAM basins, a SW-NE oriented corridor within the shield considered to be an aborted rift precursor to the South Atlantic opening (Rossello *et al.* 2007). The Laguna Merín Basin, NE sector of the SaLAM, is filled with igneous rocks dated between 134 and 127 Ma

(Cernuschi *et al.* 2015). Therefore, during the Cretaceous, the shield was surrounded by active magmatism and likely lying above the Tristan da Cunha plume influence area. It is plausible that this magmatic context had a thermal effect on the UYS, probably increasing the regional geothermal gradient, and possibly causing partial and shallow burial of the shield by lava flows (Kollenz 2015). A reheating episode starting around 140 Ma is suggested by our models from Group 1, with temperatures increasing from surface conditions to about 60 °C during Paleogene. It has been argued that such a reheating phase is a modelling artefact caused by problems related to annealing of fission tracks on temperatures below 60 °C on geological timescales (Jonckheere 2003), and because it is at the limit of resolution of the AFT system, thus poorly constrained. However, the coincidence in time between the beginning of this reheating phase suggested by the models and the magmatic events surrounding the UYS is notable. Moreover, our set of disperse and old AHe ages argue in favor of a slight reheat to temperatures < 70 °C (Shuster *et al.* 2006). Therefore, the subtle reheating of the UYS during the Late Cretaceous suggested by the inverse models is supported by evidence of contemporaneous magmatism in the vicinity of the shield. The duration and magnitude of such reheating cannot be constrained by our data, but the models suggest there was regional cooling Neogene.

Finally, although our models from Group 2 are in general less robust than Group 1 due to the limited number of confined fission tracks, they concur with cooling to temperatures below 60 °C in the Late Cretaceous, possibly reflecting tectonic adjustments during the final stages of the South Atlantic Oceanic opening, including acid volcanism dated at 77 ± 1 Ma in the southern NPT (Gaucher *et al.*, 2016). Samples from Group 2 are located in the eastern margin of the shield or near ancient faults and shear zones, structures that played an important role during the rifting along the South American coast (Schmitt *et al.* 2018). K-Ar ages on fault gouge also revealed tectonic activity in the Sierra Ballena Shear Zone during Late Cretaceous, related to breakup (Hueck *et al.* 2017). Therefore, the Gondwana breakup represents a period of intense transformations on the UYS, with movement across old basement structures, intense magmatic events surrounding the shield, and possibly a subtle reheating of the region during the Late Cretaceous. Unfortunately, the precise timing of such reheating and of the final cooling to surface temperature cannot be well defined by our AHe data, but it likely occurred during the Cenozoic.

5.8 Conclusions

In this work we analysed the thermal behaviour of the Uruguayan shield based on information derived from apatite fission tracks and apatite and zircon (U-Th)/He thermochronometry. We provided an integrated view of the thermotectonic evolution of the shield, combining 19 new AFT ages, 42 new AHe and 40 new ZHe single crystal ages with data from previous thermochronometry studies. We modelled thermal histories for 19 locations across the UYS and compared the results with previously proposed models. Our main conclusions can be summarized as follows:

- 1) Most of the shield reached temperatures below 200 °C in the early Paleozoic;
- 2) Denudation-induced cooling was first observed in samples from the Cuchilla Dionísio Terrane, which provided a major sedimentary source for the Devonian deposits of the Paraná Basin;
- 3) The main cooling event of the Uruguayan shield began around the Carboniferous-Permian boundary, cooling our samples from temperatures above 100 °C to near surface conditions (< 60 °C) by the Jurassic;
- 4) The onset of this cooling phase is likely related to far field propagation of tectonic stress associated with the Gondwanan cycle on the SW margin of Gondwana;
- 5) Lithospheric uplift linked to South Atlantic rifting contributed to the continuity of this cooling phase until the Mesozoic;
- 6) The magmatic events related to Atlantic Ocean opening likely had a positive thermal effect on the Uruguayan shield, subtly increasing temperatures of the basement rocks during the Late Cretaceous; and
- 7) Final cooling to surface temperatures occurred in the Cenozoic, but the rates and timing cannot be precisely constrained by the available thermochronometry data.

5.9. Acknowledgments

The authors gratefully acknowledge the support from Shell Brasil through the “BG05: UoA-UFRGS-SWB Sedimentary Systems” project at UFRGS and the strategic importance of the support given by ANP through the R&D levy regulation. The first author thanks the CNPq scholarship (SWE 204254/2017-5) during the exchange period at the University of Aberdeen. A.R. Jelinek also thanks the support from CNPq (Project 303184/2017-5). We thank Peter W. Reiners and his team at the Baja Arizona Radiogenic Helium Dating Laboratory (US) for the (U-Th)/He analyses and support during the data evaluation.

5.10 References

- Angelo, M., Basei, S., Frimmel, H.E., Campos, C., Eduardo, C. & Araujo, G. De. 2018. *Geology of Southwest Gondwana*. Springer International Publishing, <https://doi.org/10.1007/978-3-319-68920-3>.
- Basei, M.A.S., Frimmel, H.E., Nutman, A.P., Preciozzi, F. & Jacob, J. 2005. A connection between the Neoproterozoic Dom Feliciano (Brazil/Uruguay) and Gariep (Namibia/South Africa) orogenic belts - Evidence from a reconnaissance provenance study. *Precambrian Research*, **139**, 195–221, <https://doi.org/10.1016/j.precamres.2005.06.005>.
- Basei, M.A.S., Peel, E., Sánchez Bettucci, L., Preciozzi, F., Nutman, A.P., 2011. The basement of the Punta del Este Terrane (Uruguay): an African Mesoproterozoic fragment at the eastern border of the South American Río de la Plata Craton. *International Journal of Earth Sciences* **100**, 289–304.
- Beri, Á., Gutiérrez, P. & Balarino, L. 2011. Palynostratigraphy of the late palaeozoic of Uruguay, paraná basin. *Review of Palaeobotany and Palynology*, **167**, 16–29, <https://doi.org/10.1016/j.revpalbo.2011.05.004>.
- Blanco, G., Rajesh, H.M., Gaucher, C., Germs, G.J.B. & Chemale, F. 2009. Provenance of the Arroyo del Soldado Group (Ediacaran to Cambrian, Uruguay): Implications for the paleogeographic evolution of southwestern Gondwana. *Precambrian Research*, **171**, 57–73, <https://doi.org/10.1016/j.precamres.2009.03.003>.
- Borba, A.W. de, Vignol-Lelarge, M.L.M. & Mizusaki, A.M.P. 2002. Uplift and denudation of the Caçapava do Sul granitoids (southern Brazil) during Late Paleozoic and Mesozoic: constraints from apatite fission-track data. *Journal of South American Earth Sciences*, **15**, 683–692, [https://doi.org/10.1016/S0895-9811\(02\)00086-X](https://doi.org/10.1016/S0895-9811(02)00086-X).
- Borba, A.W. de, Lima, E.F. De, Vignol-Lelarge, M.L.M., Mizusaki, A.M.P., Sparrenberg, I. & Barros, C.E. de. 2003. Significance of Late Paleozoic Fission-track Ages in Volcanic Rocks from the Lavras Do Sul Region, Southernmost Brazil. *Gondwana Research*, **6**, 79–88, [https://doi.org/10.1016/S1342-937X\(05\)70645-6](https://doi.org/10.1016/S1342-937X(05)70645-6).
- Bossi, J., Campal, N., 1992. Magmatismo y tectónica transcurrente durante el Paleozoico Inferior en Uruguay. In: Gutierrez- Marco, J. G., Saavedra, J., Rabano, I. (Eds.): *Paleozoico Inferior de Iberoamérica*. Mérida, pp 343- 356.
- Bossi, J., Ferrando, L., Montaña, J., Campal, N., Morales, H., Gancio, F., Schipilov, A., Piñeyro, D., Sprechmann, P., 1998. Carta geológica del Uruguay. Escala 1:500.000. Geoeditores, Montevideo.
- Bossi, J. & Cingolani, C. 2009. Extension and General Evolution of the Río de la Plata Craton. *Developments in Precambrian Geology*, [https://doi.org/10.1016/S0166-2635\(09\)01604-1](https://doi.org/10.1016/S0166-2635(09)01604-1).
- Bossi, J. & Gaucher, C. 2004. The cuchilla dionisio terrane, Uruguay: An allochthonous block accreted in the Cambrian to SW-Gondwana. *Gondwana Research*, **7**, 661–674, [https://doi.org/10.1016/S1342-937X\(05\)71054-6](https://doi.org/10.1016/S1342-937X(05)71054-6).
- Bossi, J. & Gaucher, C. 2014a. Estratigrafia del Predevónico del Uruguay. In: Bossi, J. & Gaucher, C. (eds) *Geología Del Uruguay - Tomo 1: Predevónico*. Montevideo, 19–42.
- Bossi, J. & Gaucher, C. 2014b. Formacion Valentines. In: Bossi, J. & Gaucher, C. (eds) *Geología Del Uruguay - Tomo 1: Predevónico*. 171–189.

- Bossi, J. & Piñeyro, D. 2014. Terreno Piedra Alta. In: Bossi, J. & Gaucher, C. (eds) *Geología Del Uruguay - Tomo 1: Predevónico*. Montevideo, 43–86.
- Bossi, J., Ferrando, L., et al. 1998. Carta geológica del Uruguay. Escala 1:500.000.
- Bossi, J., Gaucher, C., Chiglino, L., Navarro, R. & Piñeyro, D. 2014. Escama Tectonica Carape. In: Bossi, J. & Gaucher, C. (eds) *Geología Del Uruguay - Tomo 1: Predevónico*. 265–282.
- Brown, R.W., Beucher, R., Roper, S., Persano, C., Stuart, F. & Fitzgerald, P. 2013. Natural age dispersion arising from the analysis of broken crystals. Part I: Theoretical basis and implications for the apatite (U-Th)/He thermochronometer. *Geochimica et Cosmochimica Acta*, **122**, 478–497, <https://doi.org/10.1016/j.gca.2013.05.041>.
- Brune, S., Williams, S.E., Butterworth, N.P. & Müller, R.D. 2016. Abrupt plate accelerations shape rifted continental margins. *Nature*, **536**, 201–204, <https://doi.org/10.1038/nature18319>.
- Carlson, W.D., Donelick, R.A. & Ketcham, R.A. 1999. Variability of apatite fission-track annealing kinetics: I. Experimental results. *American Mineralogist*, **84**, 1213–1223, <https://doi.org/10.2138/am-1999-0901>.
- Carneiro, C.D.R., Almeida, F.F.M. de, Hasui, Y., Zalán, P. V. & Teixeira, J.B.G. 2012. Estagios Evolutivos do Brasil no Fanerozoico. In: Hasui, Y., Carneiro, C. D. R., Almeida, F. F. M. de & Bartorelli, A. (eds) *Geologia Do Brasil*. São Paulo, Editora Beca, 131–137.
- Cernuschi, F., Dilles, J.H., Kent, A.J.R., Schroer, G., Raab, A.K., Conti, B. & Muzio, R. 2015. Geology, geochemistry and geochronology of the Cretaceous Lascano East intrusive complex and magmatic evolution of the Laguna Merín basin, Uruguay. *Gondwana Research*, **28**, 837–857, <https://doi.org/10.1016/j.gr.2014.07.007>.
- Chiglino, L., Gaucher, C., Sial, A.N., Bossi, J., Ferreira, V.P., Pimentel, M.M., 2010. Chemostratigraphy of Mesoproterozoic and Neoproterozoic carbonates of the Nico Pérez Terrane, Río de la Plata Craton, Uruguay. *Precambrian Research* 182, 313-336.
- Cogné, N., Gallagher, K. & Cobbold, P.R. 2011. Post-rift reactivation of the onshore margin of southeast Brazil: Evidence from apatite (U-Th)/He and fission-track data. *Earth and Planetary Science Letters*, **309**, 118–130, <https://doi.org/10.1016/j.epsl.2011.06.025>.
- Cogné, N., Gallagher, K., Cobbold, P.R., Riccomini, C. & Gautheron, C. 2012. Post-breakup tectonics in southeast Brazil from thermochronological data and combined inverse-forward thermal history modeling. *Journal of Geophysical Research B: Solid Earth*, **117**, 1–16, <https://doi.org/10.1029/2012JB009340>.
- De Santa Ana, H., Veroslavsky, G., Fúlfaro, V., Rossello, E. 2006. Cuenca Norte: evolución tectónica y sedimentaria del Carbonífero-Pérmino. En: Veroslavsky, G., Ubilla, M., Martínez, S. (Eds.): Cuencas sedimentarias de Uruguay. Paleozoico. Facultad de Ciencias, Montevideo, pp. 209-244.
- de Santa Ana, H. 2004. *Análise Tectono-Estratigráfica Das Seqüências Chacoparanense Uruguaias (“Cuenca Norte”)*. Universidade Estadual Paulista.
- Dodson, M.H. 1973. Closure temperature in cooling geochronological and petrological systems. *Contributions to Mineralogy and Petrology*, **40**, 259–274, <https://doi.org/10.1007/BF00373790>.
- Donelick, R.A. 1993. Method of Fission Track Analysis Utilizing Bulk Chemical Etching of Apatite. 35.
- Donelick, R.A., Ketcham, R.A. & Carlson, W.D. 1999a. Variability of apatite fission-track annealing kinetics: II. Crystallographic orientation effects. *American Mineralogist*, **84**, 1224–1234, <https://doi.org/10.2138/am-1999-0902>.

- Donelick, R.A., Ketcham, R.A. & Carlson, W.D. 1999b. Variability of apatite fission-track annealing kinetics: II. Crystallographic orientation effects. *American Mineralogist*, **84**, 1224–1234, <https://doi.org/10.2138/am-1999-0901>.
- Donelick, R.A., O'Sullivan, P.B. & Ketcham, R.A. 2005. Apatite Fission-Track Analysis. In: Reiners, P. W. & Ehlers, T. A. (eds) *Low-Temperature Thermochronology: Techniques, Interpretations, and Applications*. Mineralogical Society of America, 49–94.
- Faraone, M., 2018. Geología, petrografía y aspectos estructurales del extremo sur-occidental de la Zona de Cizalla Sarandí del Yí (área SW de Solís de Mataojo). Degree Thesis, Facultad de Ciencias, Montevideo.
- Farley, K.A. 2000. Helium diffusion from apatite: General behavior as illustrated by Durango fluorapatite. *Journal of Geophysical Research: Solid Earth*, **105**, 2903–2914, <https://doi.org/10.1029/1999JB900348>.
- Farley, K.A. 2002. (U-Th)/He Dating: Techniques, Calibrations, and Applications. *Reviews in Mineralogy and Geochemistry*, **47**, 819–844, <https://doi.org/10.2138/rmg.2002.47.18>.
- Farley, K.A., Wolf, R.A. & Silver, L.T. 1996. The effects of long alpha-stopping distances on (U-Th)/He ages. *Geochimica et Cosmochimica Acta*, **60**, 4223–4229, [https://doi.org/10.1016/S0016-7037\(96\)00193-7](https://doi.org/10.1016/S0016-7037(96)00193-7).
- Fernandes, L.A.D.A. & Koester, E. 1999. The Neoproterozoic Dorsal de Canguru strike-slip shear zone: Its nature and role in the tectonic evolution of southern Brazil. *Journal of African Earth Sciences*, **29**, 3–24, [https://doi.org/10.1016/S0899-5362\(99\)00076-7](https://doi.org/10.1016/S0899-5362(99)00076-7).
- Fernandes, L.A.D.A., TOMMASI, A., VAUCHEZ, A., PORCHER, C.C., MENEGAT, R. & KOESTER, E. 1993. Zona De Cisalhamento Transcorrente Dorsal De Canguçu: Caracterização E Importância Na Compartimentação Tectônica Do Cinturão Dom Feliciano. *Revista Brasileira de Geociências*, **23**, 224–233, <https://doi.org/10.25249/0375-7536.1993233224233>.
- Fernandes, L.A.D.A., MENEGAT, R., et al. 1995. EVOLUÇÃO TECTÔNICA DO CINTURÃO DOM FELICIANO NO ESCUDO SUL-RIO-GRANDENSE: PARTE L - UMA CONTRIBUIÇÃO A PARTIR DO REGISTRO GEOLÓGICO. *Revista Brasileira de Geociências*, **25**, 351–374, <https://doi.org/10.25249/0375-7536.1995351374>.
- Fleischer, R.L., Price, P.B. & Walker, R.M. 1975. *Nuclear Tracks in Solids: Principles and Applications*. California, University of California Press.
- Flowers, R.M. & Kelley, S.A. 2011. Interpreting data dispersion and ‘inverted’ dates in apatite (U-Th)/He and fission-track datasets: An example from the US midcontinent. *Geochimica et Cosmochimica Acta*, **75**, 5169–5186, <https://doi.org/10.1016/j.gca.2011.06.016>.
- Flowers, R.M., Shuster, D.L., Wernicke, B.P. & Farley, K.A. 2007. Radiation damage control on apatite (U-Th)/He dates from the Grand Canyon region, Colorado Plateau. *Geology*, **35**, 447, <https://doi.org/10.1130/G23471A.1>.
- Flowers, R.M., Ketcham, R.A., Shuster, D.L. & Farley, K.A. 2009. Apatite (U-Th)/He thermochronometry using a radiation damage accumulation and annealing model. *Geochimica et Cosmochimica Acta*, **73**, 2347–2365, <https://doi.org/10.1016/j.gca.2009.01.015>.
- Galbraith, R.F. 1981. On statistical models for fission track counts. *Journal of the International Association for Mathematical Geology*, **13**, 471–478, <https://doi.org/10.1007/BF01034498>.

- Galbraith, R.F. & Green, P.F. 1990. Estimating the component ages in a finite mixture. *International Journal of Radiation Applications and Instrumentation. Part D. Nuclear Tracks and Radiation Measurements*, **17**, 197–206, [https://doi.org/10.1016/1359-0189\(90\)90035-V](https://doi.org/10.1016/1359-0189(90)90035-V).
- Galbraith, R.F., Laslett, G.M., Green, P.F. & Duddy, I.R. 1990. Apatite fission track analysis: geological thermal history analysis based on a three-dimensional random process of linear radiation damage. *Philosophical Transactions of the Royal Society of London. Series A: Physical and Engineering Sciences*, **332**, 419–438, <https://doi.org/10.1098/rsta.1990.0124>.
- Gallagher, K. 2012. Transdimensional inverse thermal history modeling for quantitative thermochronology. *Journal of Geophysical Research: Solid Earth*, **117**, 1–16, <https://doi.org/10.1029/2011JB008825>.
- Gallagher, K. & Brown, R. 1997. The onshore record of passive margin evolution. *Journal of the Geological Society*, **154**, 451–457, <https://doi.org/10.1144/gsjgs.154.3.0451>.
- Gallagher, K. & Brown, R.W. 1999. The Mesozoic denudation history of the Atlantic margins of southern Africa and southeast Brazil and the relationship to offshore sedimentation. *Geological Society, London, Special Publications*, **153**, 41–53, <https://doi.org/10.1144/GSL.SP.1999.153.01.03>.
- Gallagher, K., Hawkesworth, C.J. & Mantovani, M.S.M. 1994. The denudation history of the onshore continental margin of SE Brazil inferred from apatite fission track data. *Journal of Geophysical Research: Solid Earth*, **99**, 18117–18145, <https://doi.org/10.1029/94JB00661>.
- Gallagher, K., Hawkesworth, C.J. & Mantovani, M.S.M. 1995. Denudation, fission track analysis and the long-term evolution of passive margin topography: application to the southeast Brazilian margin. *Journal of South American Earth Sciences*, **8**, 65–77, [https://doi.org/10.1016/0895-9811\(94\)00042-Z](https://doi.org/10.1016/0895-9811(94)00042-Z).
- Gallagher, K., Charvin, K., Nielsen, S., Sambridge, M. & Stephenson, J. 2009. Markov chain Monte Carlo (MCMC) sampling methods to determine optimal models, model resolution and model choice for Earth Science problems. *Marine and Petroleum Geology*, **26**, 525–535, <https://doi.org/10.1016/j.marpetgeo.2009.01.003>.
- Gaucher, C., 2000. Sedimentology, palaeontology and stratigraphy of the Arroyo del Soldado Group (Vendian to Cambrian, Uruguay). *Beringeria* 26, 1-120.
- Gaucher, C., Babinski, M., Blanco, G. 2016. Riolitas del Cretácico Superior (Campaniense); el magmatismo más joven de Uruguay. In: VIII Congreso Uruguayo de Geología, Actas, pp. 160-161, Montevideo.
- Gaucher, C., Bossi, J., Blanco, G., 2009a. Palaeogeography. Neoproterozoic-Cambrian evolution of the Río de la Plata Palaeocontinent. In: Gaucher, C., Sial, A.N., Halverson, G.P., Frimmel, H.E. (Eds.): *Neoproterozoic-Cambrian Tectonics, Global Change and Evolution: a focus on southwestern Gondwana. Developments in Precambrian Geology*, 16, Elsevier, pp. 131-141 .
- Gaucher, C., Bossi, J., Samaniego, L., Frei, R., 2014a. Complejo Tapes. In: Bossi, J., Gaucher, C. (Eds.) *Geología del Uruguay. Tomo 1: Predevónico*. Polo, Montevideo, pp. 253-264.
- Gaucher, C., Finney, S.C., Poiré, D.G., Valencia, V.A., Grove, M., Blanco, G., Pamoukaghlián, K., Gómez Peral, L., 2008. Detrital zircon ages of Neoproterozoic sedimentary successions in Uruguay and Argentina: insights into the geological evolution of the Río de la Plata Craton. *Precambrian Research* 167, 150-170.

- Gaucher, C., Frei, R., Sial, A.N., Castiglioni, E., Ferreira, V.P., 2014b. Grupo Cebollatí. In: Bossi, J., Gaucher, C. (Eds.) *Geología del Uruguay. Tomo 1: Predevónico. Polo, Montevideo*, pp. 155-169.
- Gaucher, C.; Frimmel, H.E., Germs, G.J.B. 2009b. Tectonic events and palaeogeographic evolution of southwestern Gondwana in the Neoproterozoic and Cambrian. In: Gaucher, C., Sial, A.N., Halverson, G.P., Frimmel, H.E. (Eds): *Neoproterozoic-Cambrian Tectonics, Global Change and Evolution: a focus on southwestern Gondwana. Developments in Precambrian Geology*, 16, Elsevier, pp. 295-316.
- Gaucher, C., Nóbrega Sial, A., Blanco, G. & Sprechmann, P. 2004. Chemostratigraphy of the lower Arroyo del soldado group (Vendian, Uruguay) and palaeoclimatic implications. *Gondwana Research*, 7, 715–730, [https://doi.org/10.1016/S1342-937X\(05\)71058-3](https://doi.org/10.1016/S1342-937X(05)71058-3).
- Gaucher, C., Chemale, F., Bossi, J. & Castiglioni, E.A. 2010. Grupo Cebollatti, Terreno Nico Perez: definición y edad. *VI Congreso Uruguayo de Geología, Minas*.
- Gaucher, C., Frei, R., et al. 2011. Mesoproterozoic evolution of the Río de la Plata Craton in Uruguay: At the heart of Rodinia? *International Journal of Earth Sciences*, 100, 273–288, <https://doi.org/10.1007/s00531-010-0562-x>.
- Gibson, S.A., Thompson, R.N. & Day, J.A. 2006. Timescales and mechanisms of plume-lithosphere interactions: $^{40}\text{Ar}/^{39}\text{Ar}$ geochronology and geochemistry of alkaline igneous rocks from the Paraná-Etendeka large igneous province. *Earth and Planetary Science Letters*, 251, 1–17, <https://doi.org/10.1016/j.epsl.2006.08.004>.
- Gleadow, A.J.W. 1981. Fission-track dating methods: What are the real alternatives? *Nuclear Tracks*, 5, 3–14, [https://doi.org/10.1016/0191-278X\(81\)90021-4](https://doi.org/10.1016/0191-278X(81)90021-4).
- Gleadow, A.J.W., Duddy, I.R., Green, P.F. & Lovering, J.F. 1986a. Confined fission track lengths in apatite: a diagnostic tool for thermal history analysis. *Contributions to Mineralogy and Petrology*, 94, 405–415, <https://doi.org/10.1007/BF00376334>.
- Gleadow, A.J.W., Duddy, I.R., Green, P.F. & Hegarty, K.A. 1986b. Fission track lengths in the apatite annealing zone and the interpretation of mixed ages. *Earth and Planetary Science Letters*, 78, 245–254, [https://doi.org/10.1016/0012-821X\(86\)90065-8](https://doi.org/10.1016/0012-821X(86)90065-8).
- Gomes, C.H. & Almeida, D. 2019. New insights into the Gondwana breakup at the Southern South America by apatite fission-track analyses. *Advances in Geosciences*, 47, 1–15, <https://doi.org/10.5194/adgeo-47-1-2019>.
- Granot, R. & Dyment, J. 2015. The Cretaceous opening of the South Atlantic Ocean. *Earth and Planetary Science Letters*, 414, 156–163, <https://doi.org/10.1016/j.epsl.2015.01.015>.
- Green, P.F. 1986. On the thermo-tectonic evolution of Northern England: Evidence from fission track analysis. *Geological Magazine*, 123, 493–506, <https://doi.org/10.1017/S0016756800035081>.
- Green, P.F. & Duddy, I.R. 2006. Interpretation of apatite (U-Th)/He ages and fission track ages from cratons. *Earth and Planetary Science Letters*, 244, 541–547, <https://doi.org/10.1016/j.epsl.2006.02.024>.
- Guenthner, W.R., Reiners, P.W., Ketcham, R.A., Nasdala, L. & Giester, G. 2013. Helium diffusion in natural zircon: radiation damage, anisotropy, and the interpretation of zircon (U-Th)/He thermochronology. *American Journal of Science*, 313, 145–198, <https://doi.org/10.2475/03.2013.01>.
- Hackspacher, P.C., Ribeiro, L.F.B., Ribeiro, M.C.S., Fetter, A.H., Hadler Neto, J.C., Tello, C.E.S. & Dantas, E.L. 2004. Consolidation and break-up of the South American Platform in southeastern

- Brazil: Tectonothermal and denudation histories. *Gondwana Research*, **7**, 91–101, [https://doi.org/10.1016/S1342-937X\(05\)70308-7](https://doi.org/10.1016/S1342-937X(05)70308-7).
- Hartmann, L.A., Campal, N., Santos, J.O.S., McNaughton, N.J., Bossi, J., Schipilov, A. & Lafon, J.M. 2001. Archean crust in the Rio de la Plata Craton, Uruguay - SHRIMP U-Pb zircon reconnaissance geochronology. *Journal of South American Earth Sciences*, **14**, 557–570, [https://doi.org/10.1016/S0895-9811\(01\)00055-4](https://doi.org/10.1016/S0895-9811(01)00055-4).
- Hartmann, L.A., Santos, J.O.S., Cingolani, C.A., McNaughton, N.J. 2002. Two Paleoproterozoic Orogenies in the Evolution of the Tandilia Belt, Buenos Aires, as evidenced by zircon U-Pb SHRIMP geochronology. *International Geology Review*, **44**: 528-543.
- Hueck, M., Oriolo, S., et al. 2017. Phanerozoic low-temperature evolution of the Uruguayan Shield along the South American passive margin. *Journal of the Geological Society of London*, <https://doi.org/10.1144/jgs2016-101>.
- Hueck, M., Dunkl, I., Heller, B., Angelo, M., Basei, S. & Siegesmund, S. 2018a. (U-Th) / He Thermochronology and Zircon Radiation Damage in the South American Passive Margin : Thermal Overprint of the Paraná LIP ? 1–18, <https://doi.org/10.1029/2018TC005041>.
- Hueck, M., Oyhantçabal, P., Philipp, R.P., Angelo, M., Basei, S. & Siegesmund, S. 2018b. *The Dom Feliciano Belt in Southern Brazil and Uruguay*. Siegesmund, S., Basei, M. A. S., Oyhantçabal, P. & Oriolo, S. (eds). Cham, Springer International Publishing, Regional Geology Reviews, <https://doi.org/10.1007/978-3-319-68920-3>.
- Hurford, A.J. 1990. Standardization of Fission-Track Dating Calibration - Recommendation by the Fission-Track Working Group of the IUGS Subcommission on Geochronology. *Chemical Geology*, **80**, 171-178 ST-Standardization of Fission-Track Dat.
- Hurford, A.J. & Green, P.F. 1983. The zeta age calibration of fission-track dating. *Chemical Geology*, **41**, 285–317, [https://doi.org/10.1016/S0009-2541\(83\)80026-6](https://doi.org/10.1016/S0009-2541(83)80026-6).
- Jelinek, A.R., Cezar, A., Neto, B. & Poupeau, G. 2003. Análise Por Traços De Fissão Em Apatitas Do Distrito Fluorítico De Santa Catarina : Relações Entre Hidrotermalismo E Evolução Da Margem Continental. *Recherche*, **33**, 289–298.
- Jonckheere, R. 2003. On methodical problems in estimating geological temperature and time from measurements of fission tracks in apatite. *Radiation Measurements*, **36**, 43–55, [https://doi.org/10.1016/S1350-4487\(03\)00096-9](https://doi.org/10.1016/S1350-4487(03)00096-9).
- Karl, M., Glasmacher, U.A., Kollenz, S., Franco-Magalhaes, A.O.B., Stockli, D.F. & Hackspacher, P.C. 2013. Evolution of the South Atlantic passive continental margin in southern Brazil derived from zircon and apatite (U-Th-Sm)/He and fission-track data. *Tectonophysics*, **604**, 224–244, <https://doi.org/10.1016/j.tecto.2013.06.017>.
- Ketcham, R.A. 2005. Forward and Inverse Modeling of Low-Temperature Thermochronometry Data. *Reviews in Mineralogy and Geochemistry*, **58**, 275–314, <https://doi.org/10.2138/rmg.2005.58.11>.
- Ketcham, R.A., Donelick, R.A. & Donelick, M.B. 2000. AFTSolve: A program for multi-kinetic modeling of apatite fission-track data. *American Mineralogist*, **88**, 929.
- Ketcham, R.A., Carter, A., Donelick, R.A., Barbarand, J. & Hurford, A.J. 2007. Improved modeling of fission-track annealing in apatite. *American Mineralogist*, **92**, 799–810, <https://doi.org/10.2138/am.2007.2281>.

- Kollenz, S. 2015. *Long-Term Landscape Evolution, Cooling and Exhumation History of the South American Passive Continental Margin in NE Argentina & SW Uruguay.*
- Kollenz, S., Glasmacher, U.A., Rossello, E.A., Stockli, D.F., Schad, S. & Pereyra, R.E. 2017. Thermochronological constraints on the Cambrian to recent geological evolution of the Argentina passive continental margin. *Tectonophysics*, **716**, 182–203, <https://doi.org/10.1016/j.tecto.2016.11.019>.
- Krob, F.C., Glasmacher, U.A., Karl, M., Perner, M., Hackspacher, P.C. & Stockli, D.F. 2019. Multi-chronometer thermochronological modelling of the Late Neoproterozoic to recent t-T-evolution of the SE coastal region of Brazil. *Journal of South American Earth Sciences*, **92**, 77–94, <https://doi.org/10.1016/j.jsames.2019.02.012>.
- Lal, D., Rajan, R.S. & Tamhane, A.S. 1969. Chemical Composition of Nuclei of $Z > 22$ in Cosmic Rays using Meteoritic Minerals as Detectors. *Nature*, **211**, 33–37, <https://doi.org/10.1038/221033a0>.
- Machado, J.P.S.L., Jelinek, A.R., Bicca, M.M., Stephenson, R. & Genezini, F.A. 2019. West Gondwana orogenies and Pangaea breakup: thermotectonic effects on the southernmost Mantiqueira Province, Brazil. *Journal of the Geological Society*, *jgs2019-018*, <https://doi.org/10.1144/jgs2019-018>.
- Mallmann, G., Chemale, F., Ávila, J.N., Kawashita, K. & Armstrong, R.A. 2007. Isotope geochemistry and geochronology of the Nico Pérez Terrane, Rio de la Plata Craton, Uruguay. *Gondwana Research*, **12**, 489–508, <https://doi.org/10.1016/j.gr.2007.01.002>.
- Masquelin, H. 2006. El Escudo Uruguayo. In: *Cuencas Sedimentarias Del Uruguay*. DIRAC Facultad de Ciencias, 37–106.
- Meisling, K.E., Cobbold, P.R. & Mount, V.S. 2001. Segmentation of an obliquely rifted margin, Campos and Santos basins, southeastern Brazil. *AAPG Bulletin*, **85**, 1903–1924, <https://doi.org/10.1306/8626D0B3-173B-11D7-8645000102C1865D>.
- Milani, E.J. 1997. *Evolução Tectono-Estratigráfica Da Bacia Do Paraná e Seu Relacionamento Com a Geodinâmica Fanerozóica Do Gondwana Sul-Oeste.* Universidade Federal do Rio Grande do Sul.
- Milani, E.J. & Wit, M.J. De. 2008. Correlations between the classic Paraná and Cape – Karoo sequences of South America and southern Africa and their basin infills flanking the Gondwanides : du Toit revisited and Cape – Karoo Correlations between the classic Parana sequences of South Amer, <https://doi.org/10.1144/SP294.17>.
- Milani, E.J., Melo, J.H.G. de, Souza, P.A. De, Fernandes, L.A. & França, A.B. 2007. Bacia do Paraná. *Boletim de Geociências da Petrobras*, **8**, 265–287.
- Morales, E., Chang, H.K., et al. 2017. Tectonic and stratigraphic evolution of the Punta del Este and Pelotas basins (offshore Uruguay). *Petroleum Geoscience*, **23**, 415–426, <https://doi.org/10.1144/petgeo2016-059>.
- Murray, K.E., Orme, D.A. & Reiners, P.W. 2014. Effects of U–Th-rich grain boundary phases on apatite helium ages. *Chemical Geology*, **390**, 135–151, <https://doi.org/10.1016/j.chemgeo.2014.09.023>.
- Nasdala, L., Reiners, P.W., Garver, J.I., Kennedy, A.K., Stern, R.A., Balan, E. & Wirth, R. 2004. Incomplete retention of radiation damage in zircon from Sri Lanka. *American Mineralogist*, **89**, 219–231, <https://doi.org/10.2138/am-2004-0126>.

- Oliveira, C.H.E. de, Jelinek, A.R., Chemale, F. & Bernet, M. 2016. Evidence of post-Gondwana breakup in Southern Brazilian Shield: Insights from apatite and zircon fission track thermochronology. *Tectonophysics*, **666**, 173–187, <https://doi.org/10.1016/j.tecto.2015.11.005>.
- Oriolo, S., Oyhantçabal, P., Basei, M.A.S., Wemmer, K. & Siegesmund, S. 2016a. The Nico Pérez Terrane (Uruguay): From Archean crustal growth and connections with the Congo Craton to late Neoproterozoic accretion to the Río de la Plata Craton. *Precambrian Research*, **280**, 147–160, <https://doi.org/10.1016/j.precamres.2016.04.014>.
- Oriolo, S., Oyhantçabal, P., et al. 2016b. Timing of deformation in the Sarandí del Yí Shear Zone, Uruguay: Implications for the amalgamation of western Gondwana during the Neoproterozoic Brasiliano-Pan-African Orogeny. *Tectonics*, **35**, 754–771, <https://doi.org/10.1002/2015TC004052>.
- Oriolo, S., Hueck, M., Oyhantçabal, P., Goscombe, B., Wemmer, K. & Siegesmund, S. 2018. Shear Zones in Brasiliano-Pan-African Belts and Their Role in the Amalgamation and Break-Up of Southwest Gondwana. In: *Geology of Southwest Gondwana*. Springer International Publishing, 593–613., <https://doi.org/10.1007/978-3-319-68920-3>.
- Oyhantçabal, P., Siegesmund, S. & Wemmer, K. 2011. The Río de la Plata Craton: A review of units, boundaries, ages and isotopic signature. *International Journal of Earth Sciences*, **100**, 201–220, <https://doi.org/10.1007/s00531-010-0580-8>.
- Oyhantçabal, P.B., Wagner-Eimer, M., Wemmer, K., Schulz, B., Frei, R., Siegesmund, S., 2012. Paleo- and Neoproterozoic magmatic and tectonometamorphic evolution of the Isla Cristalina de Rivera (Nico Pérez Terrane, Uruguay). *International Journal of Earth Sciences* 101, 1745–1762.
- Oyhantçabal, P., Cingolani, C.A. & Wemmer, K. 2018. *The Río de La Plata Craton of Argentina and Uruguay*. Springer International Publishing, <https://doi.org/10.1007/978-3-319-68920-3>.
- Pamoukaghlián, K., Gaucher, C., Frei, R., Poiré, D. G., Chemale, F., Frei, D., Will, T. M., 2017. U-Pb age constraints for the La Tuna Granite and Montevideo Formation (Paleoproterozoic, Uruguay): Unravelling the structure of the Río de la Plata Craton. *Journal of South American Earth Sciences* 79, 443–458.
- Panario, D., Gutierrez, O., Bettucci, L.S., Peel, E., Oyhantçabal, P. & Raba. 2014. Ancient Landscapes of Uruguay. In: *Gondwana Landscapes in Southern South America: Argentina, Uruguay and Southern Brazil*. 1–545., <https://doi.org/10.1007/978-94-007-7702-6>.
- Pankhurst, R.J., Rapela, C.W., Fanning, C.M. & Márquez, M. 2006. Gondwanide continental collision and the origin of Patagonia. *Earth-Science Reviews*, **76**, 235–257, <https://doi.org/10.1016/j.earscirev.2006.02.001>.
- Peel, E., Sánchez Bettucci, L., Basei, M.A.S., 2018. Geology and geochronology of Paso del Dragón Complex (northeastern Uruguay): implications on the evolution of the Dom Feliciano Belt (Western Gondwana). *J. South Amer. Earth Sci.* 85, 250–262.
- Philipp, R.P., Pimentel, M.M. & Chemale, F. 2016. Tectonic evolution of the Dom Feliciano Belt in Southern Brazil: Geological relationships and U-Pb geochronology. *Brazilian Journal of Geology*, **46**, 83–104, <https://doi.org/10.1590/2317-4889201620150016>.
- Philipp, R.P., Pimentel, M.M. & Basei, M.A.S. 2018. The Tectonic Evolution of the São Gabriel Terrane, Dom Feliciano Belt, Southern Brazil: The Closure of the Charrua Ocean. In: *Geology of Southwest Gondwana*. Springer International Publishing, 243–265., <https://doi.org/10.1007/978-3-319-68920-3>.

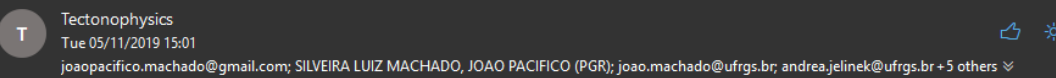
- Price, P.B. & Walker, R.M. 1963. Fossil tracks of charged particles in mica and the age of minerals. *Journal of Geophysical Research*, **68**, 4847–4862, <https://doi.org/10.1029/JZ068i016p04847>.
- Quirk, D.G. & Rüpke, L.H. 2018. Melt-induced buoyancy may explain the elevated rift-rapid sag paradox during breakup of continental plates. *Scientific Reports*, **8**, 1–13, <https://doi.org/10.1038/s41598-018-27981-2>.
- Rapela, C.W., Fanning, C.M., Casquet, C., Pankhurst, R.J., Spalletti, L., Poiré, D. & Baldo, E.G. 2011. The Rio de la Plata craton and the adjoining Pan-African/brasiliano terranes: Their origins and incorporation into south-west Gondwana. *Gondwana Research*, **20**, 673–690, <https://doi.org/10.1016/j.gr.2011.05.001>.
- Reiners, P.W. 2005. Zircon (U-Th)/He Thermochronometry. In: *Reviews in Mineralogy and Geochemistry*. 151–179., <https://doi.org/10.2138/rmg.2005.58.6>.
- Reiners, P.W. & Farley, K.A. 2001. Influence of crystal size on apatite (U-Th)/He thermochronology: An example from the Bighorn Mountains, Wyoming. *Earth and Planetary Science Letters*, **188**, 413–420, [https://doi.org/10.1016/S0012-821X\(01\)00341-7](https://doi.org/10.1016/S0012-821X(01)00341-7).
- Reiners, P.W., Farley, K.A. & Hickes, H.J. 2002. He diffusion and (U-Th)/He thermochronometry of zircon: Initial results from Fish Canyon Tuff and Gold Butte. *Tectonophysics*, **349**, 297–308, [https://doi.org/10.1016/S0040-1951\(02\)00058-6](https://doi.org/10.1016/S0040-1951(02)00058-6).
- Reiners, P.W., Spell, T.L., Nicolescu, S. & Zanetti, K.A. 2004. Zircon (U-Th)/He thermochronometry: He diffusion and comparisons with 40Ar/39Ar dating. *Geochimica et Cosmochimica Acta*, **68**, 1857–1887, <https://doi.org/10.1016/j.gca.2003.10.021>.
- Reiners, P.W., Carlson, R.W., Renne, P.R., Cooper, K.M., Granger, D.E., McLean, N.M. & Schoene, B. 2018. The (U-Th)He system. In: *Geochronology and Thermochronology*. John Wiley & Sons Ltd., 291–363.
- Ribot, A., Bossi, J., Cingolani, C.A., Piñeyro, D. 2005. Caracterización petrográfica de la faja milonítica Colonia-Arroyo Pavón en el Sur del Terreno Piedra Alta, Uruguay: Zona de cizalla principal en basamento precámbrico? Actas 16º Congreso Geológico Argentino, 789, La Plata.
- Reuber, K., Mann, P. & Pindell, J. 2019. Hotspot Origin for Asymmetrical Conjugate Volcanic Margins of the Austral South Atlantic Ocean As Imaged on Deeply-Penetrating Seismic Reflection Images. *Interpretation*, 1–88, <https://doi.org/10.1190/int-2018-0256.1>.
- Rossello, E.A., De Santa Ana, H. & Veroslavsky, G. 2000. El lineamiento Santa Lucia-Aigua-Merín (Uruguay): un corredor tectónico extensivo y transcurrente dextral precuros de la apertura atlantica. *Revista Brasileira de Geociências*, **30**, 749–756.
- Rossello, E.A., Veroslavsky, G., Masquelin, H. & De Santa Ana, H. 2007. El corredor juro-cretácico Santa Lucía-Aiguá-Merín (Uruguay): Evidencias cinemática transcurrente dextral y controles preexistentes. *Revista de la Asociacion Geologica Argentina*, **62**, 92–104.
- Rossetti, L.M., Lima, E.F., Waichel, B.L., Scherer, C.M. & Barreto, C.J. 2014. Stratigraphical framework of basaltic lavas in Torres Syncline main valley, southern Parana-Etendeka Volcanic Province. *Journal of South American Earth Sciences*, **56**, 409–421, <https://doi.org/10.1016/j.jsames.2014.09.025>.
- Santos, J.OS., Hartmann, L.A., Bossi, J., Campal, N., Schipilov, A., Piñeyro, D., McNaughton, N.J., 2003. Duration of the Transamazonian and its correlation within South America based on U-Pb SHRIMP geochronology of the la Plata Craton, Uruguay. *International Geology Review* 45, 27-48.

- Santos, J. O., Chernicoff, C. J., Zappettini, E. O., McNaughton, N. J., Greau, Y. 2017. U-Pb geochronology of Martín García, Sola, and Dos Hermanas Islands (Argentina and Uruguay): Unveiling Rhyacian, Statherian, Ectasian, and Stenian of a forgotten area of the Río de la Plata Craton. *Journal of South American Earth Sciences*, **80**, 207-228.
- Schmitt, R. da S., Fragoso, R.D.A. & Collins, A.S. 2018. Suturing Gondwana in the Cambrian: The Orogenic Events of the Final Amalgamation. In: *Geology of Southwest Gondwana*. Springer International Publishing, 411–432., https://doi.org/10.1007/978-3-319-68920-3_15.
- Scotese, C.R., Boucot, A.J. & McKerrow, W.S. 1999. Gondwanan palaeogeography and palaeoclimatology. *Journal of African Earth Sciences*, **28**, 99–114.
- Shuster, D.L., Flowers, R.M. & Farley, K.A. 2006. The influence of natural radiation damage on helium diffusion kinetics in apatite. *Earth and Planetary Science Letters*, **249**, 148–161, <https://doi.org/10.1016/j.epsl.2006.07.028>.
- Soto, M., Morales, E., Veroslavsky, G., de Santa Ana, H., Ucha, N. & Rodríguez, P. 2011. The continental margin of uruguay: Crustal architecture and segmentation. *Marine and Petroleum Geology*, **28**, 1676–1689, <https://doi.org/10.1016/j.marpetgeo.2011.07.001>.
- Sprechmann, P., Bossi, J., Da Silva, J. 1981. Cuencas del Jurásico y Cretácico del Uruguay. In: Volkheimer, W., Musacchio (Eds.) Cuencas sedimentarias del Jurásico y Cretácico de América del Sur, 1, pp. 239-270, Buenos Aires.
- Sprechmann, P., Montaña, J., Gaucher, C. 1993. Devónico. In: Bossi, J. (Ed.): Geología y Recursos Minerales del Departamento de Durazno. Intendencia Municipal de Durazno y Cátedra de Geología de la Facultad de Agonomía, Montevideo, pp. 25-55.
- Stockli, D.F. 2005. Application of low-temperature thermochronometry to extensional tectonic settings. In: Reiners, P. W. & Ehlers, T. A. (eds) *Low-Temperature Thermochronology: Techniques, Interpretations, and Applications*. Mineralogical Society of America, 411–448.
- Stockli, D.F., Farley, K.A. & Dumitru, T.A. 2000. Calibration of the apatite (U-Th)/ He thermochronometer on an exhumed fault block , White Mountains , California. *Geology*, **28**, 983–986, [https://doi.org/10.1130/0091-7613\(2000\)28<983](https://doi.org/10.1130/0091-7613(2000)28<983).
- Tagami, T. & O'Sullivan, P.B. 2005. Fundamentals of fission-track thermochronology. In: Reiners, P. W. & Ehlers, T. A. (eds) *Low-Temperature Thermochronology: Techniques, Interpretations, and Applications*. Mineralogical Society of America, 19–48.
- Teixeira W., Renne, P., Bossi. J., Campal, N., D'Aguella, F., 1999. $^{40}\text{Ar}/^{39}\text{Ar}$ and Rb/Sr geochronology of the Uruguayan dike swarm, Río de la Plata Craton and implications for Proterozoic intraplate activity in western Gondwana. *Precambrian Research*, **93**, 153-180.
- Tello Saenz, C.A., Hackspacher, P.C., et al. 2003. Recognition of Cretaceous, Paleocene, and Neogene tectonic reactivation through apatite fission-track analysis in Precambrian areas of southeast Brazil: association with the opening of the south Atlantic Ocean. *Journal of South American Earth Sciences*, **15**, 765–774, [https://doi.org/10.1016/S0895-9811\(02\)00131-1](https://doi.org/10.1016/S0895-9811(02)00131-1).
- Turner, S., Regelous, M., et al. 1994. Magmatism and Continental Break-Up in the South Atlantic. *Earth. Planet. Sci. Lett.*, **121**, 333–348, [https://doi.org/10.1016/0012-821X\(94\)90076-0](https://doi.org/10.1016/0012-821X(94)90076-0).
- Uriz, N.J., Cingolani, C.A., Basei, M.A.S., Blanco, G., Abre, P., Portillo, N.S. & Siccardi, A. 2016. Provenance and paleogeography of the Devonian Durazno Group, southern Parana Basin in

- Uruguay. *Journal of South American Earth Sciences*, **66**, 248–267, <https://doi.org/10.1016/j.jsames.2016.01.002>.
- Van Ranst, G., Pedrosa-Soares, A.C., Novo, T., Vermeesch, P. & De Grave, J. 2019. New insights from low-temperature thermochronology into the tectonic and geomorphologic evolution of the south-eastern Brazilian highlands and passive margin. *Geoscience Frontiers*, <https://doi.org/10.1016/j.gsf.2019.05.011>.
- Vermeesch, P. 2009. RadialPlotter: a Java application for fission track, luminescence and other radial plots. *Radiation Measurementes*, 409–410<http://www.ucl.ac.uk/~ucfbpve/radialplotter/>.
- Veroslavsky, G., De Santa Ana, H., Rossello, E. 2004. Depósitos del Jurásico y Cretácico temprano de la región meridional de Uruguay. In: Veroslavsky, G., Ubilla, M., Martínez, S. (Eds.): Cuencas sedimentarias de Uruguay. Mesozoico. Facultad de Ciencias, Montevideo, pp. 117-142.
- Wagner, G.A., Gleadow, A.J.W. & Fitzgerald, P.G. 1989. The significance of the partial annealing zone in apatite fission-track analysis: Projected track length measurements and uplift chronology of the transantarctic mountains. *Chemical Geology: Isotope Geoscience section*, **79**, 295–305, [https://doi.org/10.1016/0168-9622\(89\)90035-3](https://doi.org/10.1016/0168-9622(89)90035-3).
- Will, T.M. & Frimmel, H.E. 2018. Where does a continent prefer to break up? Some lessons from the South Atlantic margins. *Gondwana Research*, **53**, 9–19, <https://doi.org/10.1016/j.gr.2017.04.014>.
- Will, T. , Gaucher, C., Ling, X.X. , Li, X.H. , Li, Q.L. , Frimmel, H.E. 2019 Neoproterozoic magmatic and metamorphic events in the Cuchilla Dionisio Terrane, Uruguay, and possible correlations across the South Atlantic. *Precambrian Research* 320, 303-322.
- Wolf, R.A., Farley, K.A. & Silver, L.T. 1996. Helium diffusion and low-temperature thermochronometry of apatite. *Geochimica et Cosmochimica Acta*, **60**, 4231–4240, [https://doi.org/10.1016/S0016-7037\(96\)00192-5](https://doi.org/10.1016/S0016-7037(96)00192-5).
- Wolf, R.A., Farley, K.A. & Kass, D.M. 1998. Modeling of the temperature sensitivity of the apatite (U-Th)/He thermochronometer. *Chemical Geology*, **148**, 105–114, [https://doi.org/10.1016/S0009-2541\(98\)00024-2](https://doi.org/10.1016/S0009-2541(98)00024-2).
- Zalán, P. V. 2004. Evolução Fanerozóica das Bacias Sedimentares Brasileiras. In: Mantesso-Neto, V., Bartorelli, A., Carneiro, C. D. R. & Neves, B. B. de B. (eds) *Geologia Do Continente Sul-Americano: Evolução Da Obra de Fernando Flávio Marques de Almeida*. Beca Produções Culturais Ltda, 595–612.
- Zambrano, J.J. & Urien, C.M. 1970. Geological outline of the basins in southern Argentina and their continuation off the Atlantic shore. *Journal of Geophysical Research*, **75**, 1363–1396, <https://doi.org/10.1029/JB075i008p01363>.
- Zerfass, H., Chemale, F., Leandro, C. & Lavina, E. 2004. Tectonics and sedimentation in Southern South America during Triassic. **166**, 265–292, <https://doi.org/10.1016/j.sedgeo.2003.12.008>.

5.11 Email de submissão

Segue abaixo a confirmação de submissão do manuscrito ao periódico *Tectonophysics*. Atualmente (fevereiro/2020) o manuscrito está sendo modificado após as sugestões dos revisores, e sua versão atualizada deve ser resubmetida em breve.

 CAUTION: This email contains web links. Do NOT click on these links unless you recognise the sender and know the content is safe.

*** Automated email sent by the system ***

Dear Mr. Machado,

Your submission entitled "Low-temperature thermochronology of the South Atlantic margin along Uruguay and its relation to tectonic events in West Gondwana" has been received by *Tectonophysics* for the article type Research Paper.

Please note that submission of an article is understood to imply that the article is original and is not being considered for publication elsewhere. Submission also implies that all authors have approved the paper for release and are in agreement with its content.

You will be able to check on the progress of your paper by logging on to <https://ees.elsevier.com/tecto/>

Elsevier Editorial System™

Full-Function Web-Enabled Manuscript Submission and Tracking System for Peer Review

ees.elsevier.com

as Author.

Your manuscript will be given a reference number in due course.

Thank you for submitting your work to this journal.

Kind regards,

Journal Management
Tectonophysics

Capítulo 6 - West Gondwana orogenies and Pangaea breakup: thermotectonic effects on the southernmost Mantiqueira Province, Brazil

João Pacífico S. L. Machado^{1,2*}, Andréa R. Jelinek¹, Marcos M. Bicca¹, Randell Stephenson², Frederico A. Genezini³

¹ Instituto de Geociências, Universidade Federal do Rio Grande do Sul, Brazil

² School of Geosciences, University of Aberdeen, United Kingdom

³ Instituto de Pesquisas Energéticas e Nucleares, Centro do Reator de Pesquisas, Brazil

Nota explicativa

Este capítulo corresponde ao artigo publicado pelo periódico *Journal of the Geological Society*. Ao final do manuscrito encontra-se a carta de aceite do mesmo. Para conferência online da publicação, pesquisar pelo doi [10.1144/jgs2019-018](https://doi.org/10.1144/jgs2019-018).

Abstract

Through the joint use of apatite fission tracks (AFT) and (U-Th)/He analysis in apatite (AHe) and zircon (ZHe), we evaluate the thermotectonic evolution of the Sul-Rio-Grandense Shield (SRGS), southernmost Mantiqueira Province, Brazil. Formed during the assembly of West Gondwana (Neoproterozoic), the shield comprises four tectonostratigraphic terranes separated by regional faults and shear zones. The central and eastern terranes present Mesozoic AFT ages, while the western mostly late Palaeozoic. AHe ages show considerable dispersion, although most are Mesozoic. ZHe ages from the east are early Permian, while the west presents Devonian ages. Inverse thermal modelling indicates a Devonian to Carboniferous cooling phase in the west, time correlated with orogenies occurring at the SW margin of Gondwana, which affected the regional geodynamics and are possibly linked to limited uplift of the shield. From Permian to Jurassic a major cooling phase took place in the SRGS, likely related to lithosphere thinning and uplift preceding the South Atlantic rifting. Samples closer to the Atlantic coast suggest a subtle reheating after this event, provisionally linked to a geothermal disturbance related to ocean opening and associated magmatism. A final post-Palaeocene cooling phase towards surface conditions affected the entire SRGS.

6.1 Introduction

Thermochronometry studies of the Brazilian passive margin have traditionally focused on the development of the southeastern coastal escarpments. This region is part of the Mantiqueira Province (Fig. 6.1a), formed during the Brasiliano/Pan-African Orogeny (Neoproterozoic) as a result of the assembly of West Gondwana (de Almeida & Hasui 1984). The southeastern region of the Mantiqueira Province attracts interest due to its distinct high topography, an uncommon feature along the Brazilian coast, and the proximity of the Campos and Santos marginal basins, both large offshore hydrocarbon reservoirs. Thermochronometry studies in this area were able to link cooling and exhumation phases to South Atlantic rifting, the development of the marginal basins, and to the far-field effects of the Andean Orogeny (Gallagher *et al.* 1994, 1995; Saenz *et al.* 2003; Hackspacher *et al.* 2007; Hiruma *et al.* 2010; Cogné *et al.* 2011, 2012; Karl *et al.* 2013; Soares *et al.* 2016). Only a few studies were made in the southern part of the Mantiqueira Province (de Borba *et al.* 2002, 2003; Bicca *et al.* 2013; de Oliveira *et al.* 2016), where the Sul-Rio-Grandense Shield (SRGS) is located (Fig. 6.1a). The SRGS corresponds to approximately 50,000 km² of subdued topography in southernmost Brazil and is adjacent to the offshore Pelotas Basin, a promising province for gas hydrates (Miller *et al.* 2015). Although the existing thermochronometry studies provide a record of pre-rift exhumation in the shield, their limited number leaves a gap in our comprehension of the evolution of Pangaea and Atlantic rifting in the southernmost Mantiqueira Province.

In this study, we apply three low-temperature thermochronometers to basement rocks from the SRGS to better understand its tectonic behaviour since assembly in the Neoproterozoic. We aim to constrain the thermotectonic effects on the shield during the Palaeozoic orogenic cycles occurring on the SW Gondwana margin, the Mesozoic South Atlantic rifting and the Pelotas Basin development. We utilize a dataset with 18 apatite fission track ages, 43 apatite and 30 zircon (U-Th)/He single crystal ages, from which we model 17 inverse thermotectonic histories across the SRGS. From these, we estimate the exhumation and erosion rates of each terrane during distinct inferred cooling periods. Our results, combined with previous results, evince three distinct cooling phases during the Phanerozoic, indicate an earlier thermotectonic stability of the shield's western region, and suggest a subtle reheating of its eastern part following Pangaea breakup.

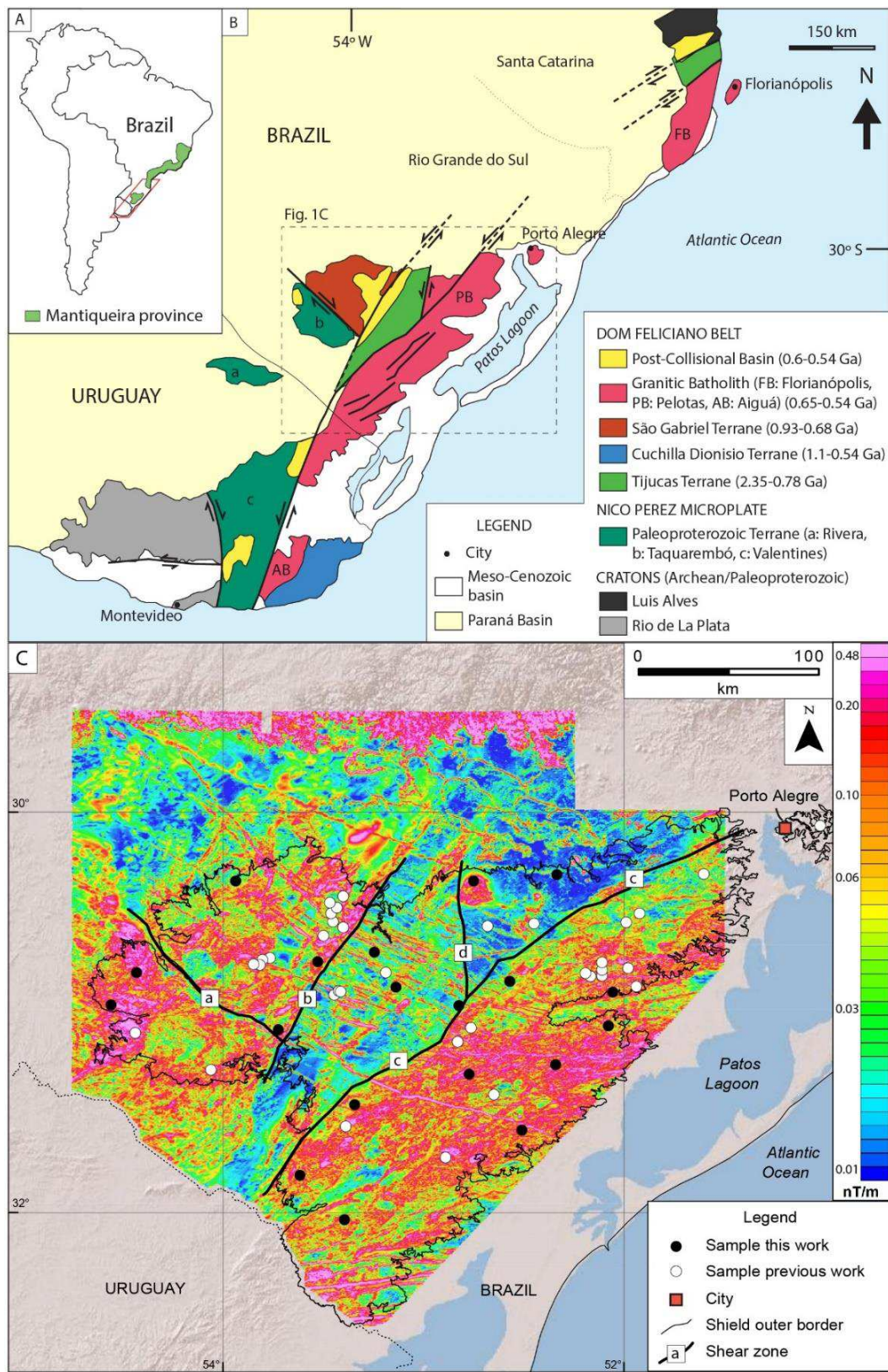


Figure 6.1: (a) Geotectonic map of the study region. Inset map indicates location of the Mantiqueira Province. Dashed square marks the Sul-Rio-Grandense Shield (modified after Philipp et al. 2013). (b) Analytic signal of the aeromagnetic anomaly, with shield outlined. Black circles represent samples from this work, white circles samples from de Borba et al. (2002, 2003), Bicca et al. (2013) and de Oliveira et al. (2016). Main faults and shear zones: a) Ibaré, b) Caçapava do Sul, c) Dorsal de Canguçu and d) Passo do Marinheiro (modified after CPRM 2010).

6.2 Geological Setting

The Mantiqueira Province is a major tectonic feature in Brazil, composed of three mobile belts and having a length of 3,000 km along the coast (Fig. 6.1a). The Province comprises mainly pre-Silurian high-grade metamorphic and igneous rocks, which record the processes and evolution of the region from the Archaean to the Brasiliano/Pan-African Orogeny (Neoproterozoic Era) (Hasui 2012). Our study area is the known as the Sul-Rio-Grandense Shield (SRGS), partially covered to the north and west by the Paraná Basin, and to the east and SE by the Pelotas Basin (Figs. 6.1a and 6.2).

6.2.1 The Sul-Rio-Grandense Shield

The SRGS represents the basement in southernmost Brazil and mostly comprises Proterozoic tectonostratigraphic terranes, consisting of rocks from the Rio de La Plata Craton and Dom Feliciano belt (Figs. 6.1a and 6.2) (Fernandes *et al.* 1995; Chemale 2000; Hartmann *et al.* 2000, 2007; Hasui 2012). The SRGS was consolidated after the multi-episodic collision between the Rio de La Plata, Congo and Kalahari cratons, during the Brasiliano/Pan-African Orogeny, and is characterized by subdued topography below 500 m. There is an ongoing debate about the provenance of the terranes within the shield and how they were assembled to form West Gondwana, with authors suggesting different subduction orientations and block origins (Fernandes *et al.* 1995; Chemale 2000; Saalmann *et al.* 2005; Philipp *et al.* 2016; Schmitt *et al.* 2018). The SRGS is traditionally divided into four main tectonostratigraphic terranes: 1) Taquarembó Terrane in the SW, 2) São Gabriel Terrane in the NW, 3) Tijucas Terrane in the centre and 4) Pelotas Batholith in the east (Figs. 6.1a and 6.2). The first is interpreted as part of the Nico Pérez Microplate, a terrane of controversial origin, usually associated with the Rio de La Plata Craton, but which has also been related to the Congo Craton (Hartmann *et al.* 2001; Gaucher *et al.* 2011; Oriolo *et al.* 2016). The other three terranes comprise rocks from orogenic belts formed during the diachronous collision between the Rio de La Plata, Congo and Kalahari cratons (Chemale 2000; Hartmann *et al.* 2007).

The four SRGS terranes are limited by crustal-scale transcurrent fault and shear zones (Fig. 6.1b and 6.2) that formed during the Brasiliano/Pan-African Orogeny, which had three main collisional phases between 870 and 540 Ma and peaked from c. 640 to 600 Ma (Hasui 2010; Philipp *et al.* 2016; Basei *et al.* 2018; Hueck *et al.* 2018b; Oriolo *et al.* 2018; Schmitt *et al.* 2018). The Dorsal do Canguçu Shear Zone is the most

notable limiting structure; it's a NE-SW lineament of sinistral shear sense, characterized by the intrusion of synkinematic granitic bodies with ages between c. 650 and 600 Ma (Philipp *et al.* 2003, 2013; Oriolo *et al.* 2018). The Passo do Marinheiro Shear Zone, a N-S brittle fault system of sinistral displacement, partially crosscuts the Dorsal do Canguçu Shear Zone and has a maximum age of 595 Ma (Philipp *et al.* 2016; Oriolo *et al.* 2018). Both the Dorsal do Canguçu and Passo do Marinheiro shear zones separate the easternmost Pelotas Batholith from the central Tijucas Terrane. The NE-SW orientated Caçapava Lineament is the western limit of the Tijucas Terrane. It is completely covered by the Camaquã Basin, but recognized on aeromagnetic data (Fig. 6.1b) and interpreted as a suture zone between the Tijucas Terrane and the northwestern São Gabriel Terrane (Hartmann *et al.* 2016; Oriolo *et al.* 2018). Last, the NW-SE Ibaré Shear Zone limits the two western terranes of the shield, the São Gabriel and Taquarambó terranes. It presents indicators of dextral movement and sinistral reactivation, but the deformation age is unresolved (Fernandes *et al.* 1995; Oriolo *et al.* 2018).

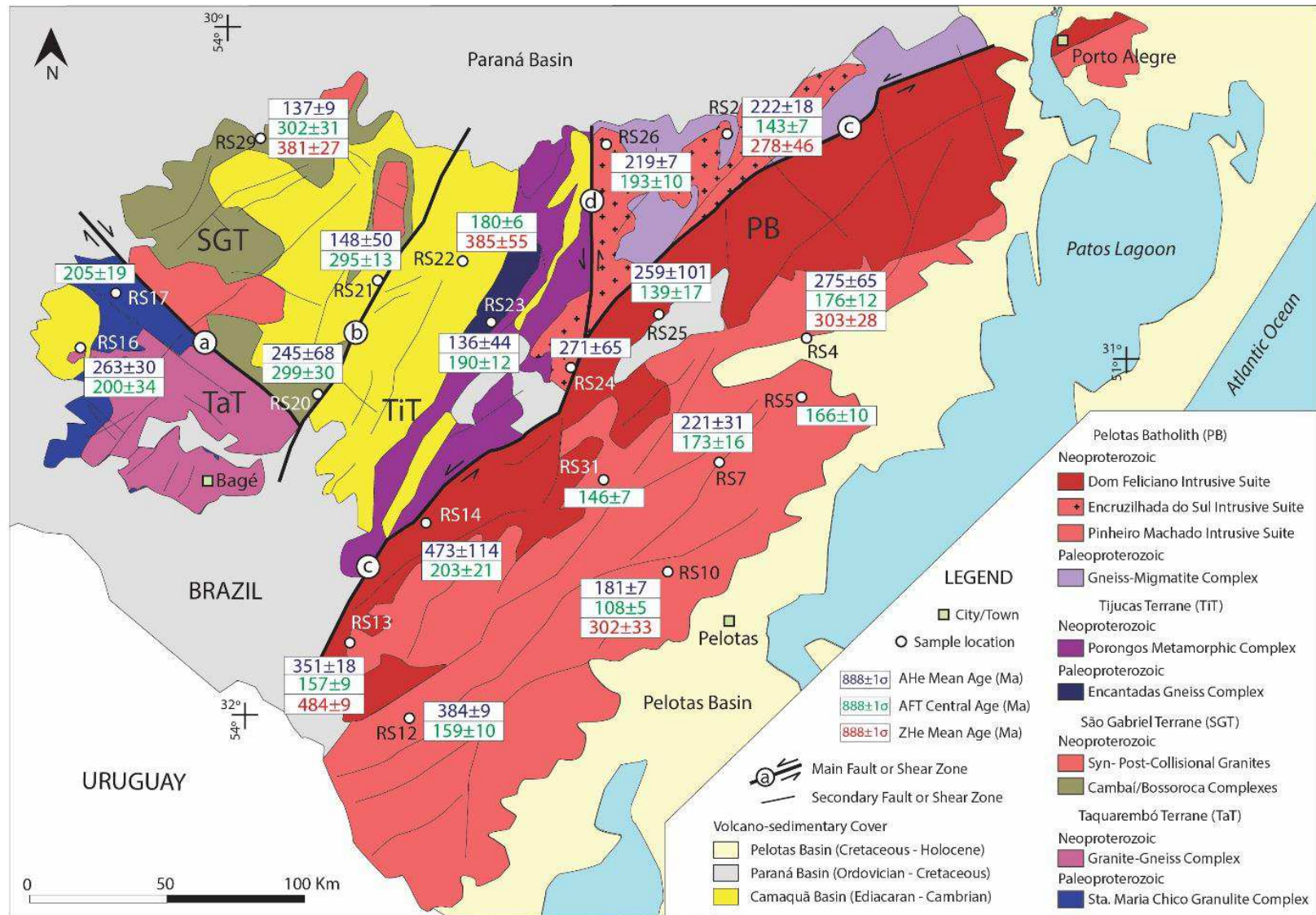


Figure 6.2: Geotectonic map of the SRGS with sample location and thermochronometry ages. Mean values of (U-Th)/He corrected ages reported. Main faults and shear zones: a) Ibaré, b) Caçapava do Sul, c) Dorsal de Canguçu, and d) Passo do Marinheiro (modified after Wildner et al. 2008).

The Taquarembó Terrane (TaT) is located in the SW of the shield (Fig. 6.2) and comprises high-grade metamorphic rocks from the Santa Maria Chico Granulite Complex (2.5 to 2.0 Ga), intruded by granitoids between 650 and 550 Ma and covered by volcano-sedimentary rocks from the Camaquã Basin (Chemale 2000; Wildner *et al.* 2002; Gastal *et al.* 2005; Hartmann *et al.* 2007, 2008; Philipp *et al.* 2016). The São Gabriel Terrane (SGT) is located in the NW of the shield and comprises Neoproterozoic rocks tectonically juxtaposed during the first phase of the Brasiliano cycle, as gneisses and ophiolite slabs of the Cambaí Complex, passive margin associations, and three magmatic arc-related rocks (Vacacaí/Bossoiroca Group). The SGT units are controlled by NE trending shear zones, were intruded by post-orogenic granites and later covered by the Camaquã Basin (Chemale 2000; Saalmann *et al.* 2005; Hartmann *et al.* 2007; Philipp *et al.* 2016). The Tijucas Terrane (TiT), in the central portion of the SRGS, is characterized by the Encantadas Complex, a gneiss-amphibolite basement inlier of 2.2 to 2 Ga, and the Porongos Complex, composed of supracrustal metavolcano-sedimentary sequences with age c. 780 Ma. These units were intruded by granites during the Brasiliano Orogeny and small plugs of phonolites (Late Cretaceous), and covered by the Camaquã Basin (Barbieri *et al.* 1987; Chemale 2000; Hartmann *et al.* 2007; Philipp *et al.* 2008, 2016). The Pelotas Batholith (PB), easternmost terrane of the shield, is composed predominantly of intrusive suites, most of them formed c. 600 Ma with emplacement controlled by high angle shear zones of NE-SW orientation, such as the Dorsal de Canguçu Shear Zone and related structures (Chemale 2000; Philipp *et al.* 2003, 2016; Hueck *et al.* 2018b). Aeromagnetometry from the Brazilian Geological Survey (CPRM 2010) helped to define the geotectonic units and subsurface features of the SRGS. Although this survey highlights the terranes limits and the pervasiveness of a WNW-ESE dyke swarm (Fig. 6.1b), it is not yet possible to establish a unique division of the SRGS that satisfactory incorporates all methods and data available (Hartmann *et al.* 2016).

After assembly, the SRGS went through a long period of tectonic quiescence. Indeed, the whole South American Platform (continental portion of the South American plate not affected by the Caribbean and Andean orogenic zones), passed through a stable stage that lasted from the Ordovician until the Triassic (de Almeida *et al.* 2000; Zalán 2004). During the early Mesozoic the Platform was uplifted, causing reactivation of basement structures formed during the Brasiliano Orogeny (de Matos 1999; Zalán 2004; Carneiro *et al.* 2012; Schmitt *et al.* 2018). The SRGS was the locus of active

tectonic events during the opening of the South Atlantic Ocean (Jurassic-Cretaceous) (Nürnberg & Müller 1991; Milani 1997; Stica *et al.* 2014; Oriolo *et al.* 2018).

6.2.2 Surrounding basins

The TaT, SGT and TiT are partly covered by remnants of the Camaquã Basin, but no record is found in the PB (Fig. 6.2). The Camaquã Basin, composed of late Ediacaran to Cambrian strata, was formed as result of sedimentation in independent but successive depocenters in the same region, accumulating up to 10,000 m of sediments and volcanic rocks (Borba & Mizusaki 2003; Hasui 2012). Deposits encompass evolution from late- to post-orogenic settings, with structural framework changing from back-arc basin, to strike-slip basin and a final rift environment (Hasui 2012; Paim *et al.* 2014). Sedimentary successions, commonly intercalated with volcanic rocks, evolved from shallow marine strata at the base, through lacustrine facies, to final aeolian and alluvial deposits (Borba & Mizusaki 2003; Maraschin *et al.* 2010; Paim *et al.* 2014). The youngest preserved unit of the Camaquã Basin is the Guaritas Group, with a maximum depositional age of 540 ± 6 Ma and minimum of 473 ± 9 Ma (Maraschin *et al.* 2010; Oliveira *et al.* 2014).

Limiting the SRGS to the north and west is the Paraná Basin (Fig. 6.2), a broad continental basin developed in the interior of West Gondwana, with deposits of Palaeozoic and Mesozoic age. Milani (1997) defined six supersequences in the Paraná Basin, separated by interregional unconformities: Rio Ivaí (Ordovician to Silurian), Paraná (Devonian), Gondwana I (Upper Carboniferous to Lower Triassic), Gondwana II (Middle to Upper Triassic), Gondwana III (Jurassic to Lower Cretaceous), and Bauru (Upper Cretaceous). The first three supersequences are related to transgressive-regressive cycles, while the last three comprise continental volcano-sedimentary deposits (Milani *et al.* 2007). In the vicinity of the SRGS, units from the supersequences Gondwana I, II and III are exposed, with prominence in the north, where thick (up to 500 m) volcanic deposits from the Paraná-Etendeka Large Igneous Province (LIP) (*c.* 130 Ma) are situated (Turner *et al.* 1994; Renne *et al.* 1996; Florisbal *et al.* 2014; Rossetti *et al.* 2014). Aeromagnetic data (CPRM 2010) reveal a WNW-ESE dyke system feeding the Paraná-Etendeka LIP throughout the shield (Fig. 6.1b), indicating that the SRGS was directly affected by the Early Cretaceous magmatism of the Gondwana III supersequence (Hartmann *et al.* 2016).

The offshore Pelotas Basin (Meso-Cenozoic eras) occurs to the east of the SRGS (Fig. 6.2) as a passive marginal basin developed during the Atlantic Ocean opening.

The basement of the Pelotas Basin constitutes deposits of the Paraná Basin, especially the volcanic rocks from the Paraná-Etendeka LIP, as well as the Pelotas Batholith rocks (Stica *et al.* 2014). Unlike other marginal basins towards the NE Brazilian coast, the Pelotas Basin presents abundant siliciclastic sediments and lacks evaporitic deposits (Bueno *et al.* 2007). Hydrocarbon reserves have not been found in the basin, but there is growing interest in the development of the Pelotas Basin for gas hydrate resources (Miller *et al.* 2015).

6.4 Material and methods

6.4.1 Sampling

Samples with crystals suitable for thermochronometry analysis were collected from 19 selected locations in the SRGS (Figs. 6.1b and 6.2, Tab. 6.1), in an array covering the four tectonostratigraphic terranes and avoiding locations subject to previous studies. Preference was given to sites with outcropping granite and gneiss, lithologies usually rich in apatites and zircons, but two sedimentary samples from Camaquã Basin were also collected for a better coverage of the area. Standard crushing, magnetic and heavy liquid separation were applied to concentrate apatite and zircon.

Table 6.1: Details of each location and analysis made. Stratigraphic ages from Wildner *et al.* (2008) and de Oliveira *et al.* (2014); coordinates in degrees and datum WGS84; (D. sea) = shortest distance to seashore.

Sample	Lithology	Strat. Age (Ma)	Lat (°)	Long (°)	Altitude (m)	D. sea (km)	Analysis
RS2	Granite	594±5	-30,31	-52,33	118	170	AFT, AHe, ZHe
RS4	Granite	572±10	-30,90	-52,06	107	105	AFT, AHe, ZHe
RS5	Granite	609±17	-31,07	-52,08	61	90	AFT
RS7	Granite	609±17	-31,26	-52,34	284	90	AFT, AHe
RS10	Diorite	609±17	-31,59	-52,51	190	70	AFT, AHe, ZHe
RS12	Granite	572±10	-32,03	-53,39	285	110	AFT, AHe
RS13	Granite	609±17	-31,81	-53,62	321	135	AFT, AHe, ZHe
RS14	Granite	572±10	-31,46	-53,34	426	135	AFT, AHe
RS16	Syenite	566±44	-30,96	-54,56	248	265	AFT, AHe
RS17	Granite	640±52	-30,80	-54,43	186	265	AFT
RS20	Granite	605±8	-31,09	-53,73	304	190	AFT, AHe
RS21	Sandstone	535±10	-30,75	-53,53	299	205	AFT, AHe
RS22	Sandstone	535±10	-30,70	-53,24	170	190	AFT, ZHe
RS23	Schist	2263±18	-30,87	-53,14	324	170	AFT, AHe
RS24	Granite	594±5	-31,00	-52,86	192	140	AHe
RS25	Granite	550±6	-30,84	-52,57	114	140	AFT, AHe
RS26	Syenite	611±3	-30,35	-52,75	280	195	AFT, AHe
RS29	Gneiss	750±16	-30,34	-53,94	89	265	AFT, AHe, ZHe
RS31	Granite	609±17	-31,31	-52,77	412	110	AFT

6.4.2 Low-Temperature Thermochronometry

Low-temperature thermochronometry accounts for the accumulation of radiogenic products in a mineral, but which are lost by the crystal through different processes at elevated temperatures. Each thermochronometer (mineral plus radiogenic parent and product) has its own closure temperature, below which the radiogenic product begins to accumulate. Ages obtained by thermochronometry analysis represent a time-temperature point during the passage through the partial retention zone (PRZ) of the given thermochronometer, a temperature zone where production and loss of radiogenic products are concurrent.

6.4.2.1 Apatite fission-track analysis

Fission tracks are linear defects in the crystal lattice, with initial length around 16 µm, formed by spontaneous fission of ^{238}U (Price & Walker 1963; Fleischer *et al.* 1975; Galbraith *et al.* 1990). The density of accumulated fission tracks and its variable lengths distribution indicate the thermal path experienced by the host mineral (Gleadow *et al.* 1986b, a; Galbraith *et al.* 1990). The apatite fission tracks partial retention zone (AFTPRZ) corresponds to temperatures between c. 60 to 110 °C, in which apatite fission tracks (AFT) undergo slow and gradual shortening (annealing). Above c. 110 °C all AFT disappear due annealing, resetting the thermochronometer age to zero (Gleadow *et al.* 1986a; Green *et al.* 1986; Wagner *et al.* 1989; Gallagher *et al.* 1998). Besides temperature, annealing of AFT is also influenced by compositional variability, crystallographic anisotropy and radiation damage (Green *et al.* 1986; Stockli 2005; Tagami & O'Sullivan 2005).

For AFT dating, we use the external detector method from Gleadow (1981). For each sample, between 150 to 400 apatite crystals were hand-picked and mounted in epoxy resin, polished to expose their central portion, and etched for 20 s in a 5.5M HNO_3 solution at 21 °C to reveal spontaneous fission tracks (Carlson *et al.* 1999). Muscovite sheets were coupled to the apatite mounts, and the sets were irradiated at the IEA-R1/IPEN-CNEN Reactor, São Paulo, Brazil, along with Durango age standards and Corning CN5 dosimeters. Afterwards, mica sheets were decoupled from samples and etched in 48% HF for 18 min at 20 °C to reveal the induced tracks. AFT analysis was performed at the Universidade Federal do Rio Grande do Sul, Brazil, using a Leica DM 6000 M Microscope (1000x, dry). For bedrock samples, 20 crystals per sample were dated, while 50 grains were analysed for the sedimentary samples from Camaquã Basin. Ages were calculated using the ζ calibration method (Hurford & Green

1983; Hurford 1990), while dispersion and homogeneity were analysed through the chi-square test (Galbraith 1981; Galbraith & Green 1990) with the program RadialPlotter 9.0 (Vermeesch 2009). When possible, lengths of 100 confined tracks of the TINT type (Lal *et al.* 1969) and *c*-axis angles were measured. As kinetic parameter for thermal modelling, we use the mean etch pit diameter D_{par} (Donelick 1993) from about 100 measurements, which is correlated to the Cl, OH and F crystal content; low D_{par} values ($\leq 1.75 \mu\text{m}$) correlates with high F content and fast annealing (Carlson *et al.* 1999; Donelick *et al.* 2005).

6.4.2.2 Apatite and Zircon (U-Th)/He analysis

The decay chain of ^{238}U , ^{235}U and ^{232}Th isotopes produces alpha particles (^4He) that are retained in the crystal lattice at low temperatures, while at high temperatures diffusion expels ^4He from the mineral. In apatite (U-Th)/He thermochronometry (AHe) the partial retention zone (AHePRZ) lies between c. 40 to 70 °C and corresponds to the temperature interval where ^4He accumulation and diffusion are simultaneous. At temperatures higher than c. 70 °C, alpha particles are readily expelled and thermochronometer age is reset to zero (Wolf *et al.* 1996, 1998; Farley 2000). However, ^4He diffusion is substantially influenced by crystal dimension, accumulated radiation damage and compositional zonation of the crystal (Farley 2000; Reiners & Farley 2001; Shuster *et al.* 2006). Variations in these factors are magnified by thermal histories with extended residence in the AHePRZ, commonly resulting in dispersed AHe ages (Flowers & Kelley 2011). Zircon (U-Th)/He thermochronometry (ZHe) retain ^4He at considerable higher temperature than apatite. ZHe partial retention zone (ZHePRZ) range between c. 170 to 200 °C, and can be affected by radiation damage, eU concentration, long-term residence at low temperatures, and zonation of U and Th (Reiners *et al.* 2002, 2004; Reiners 2005).

AHe and ZHe analyses were performed at the Baja Arizona Radiogenic Helium Dating Laboratory, at the University of Arizona, US. Between three to five crystals of each sample were handpicked for analysis, based on morphology, size and optical clarity, using a Leica MZ16 microscope. Selected apatites had between 60 to 200 µm width, were no longer than 360 µm, and in most cases had two terminations. In turn, picked zircons had between 60 to 165 µm width and in vast majority were no longer than 500 µm. Selected crystals were photographed and their dimensions measured with Leica Application Suite V3, later used for the alpha-ejection age corrections (Farley *et al.* 1996), which accounts for the ejection of alpha particles in the borders of the crystals during decay. Subsequently, picked crystals were individually packed into

Nb foil tubes for degassing. Helium was extracted from apatites and zircons using long-wavelength laser heating and measured with a quadrupole mass spectrometer. Afterwards, crystals were retrieved and dissolved for U-Th measurements, using a high-resolution Element2 ICP-MS. During all procedures, Durango standards and blank samples were analysed to guarantee reliability of measurements.

6.4.3 Thermal History Modelling

Inverse modelling was done using QTQt 5.7 (Gallagher 2012), a program that employs a Bayesian transdimensional Markov Chain Monte Carlo approach (Gallagher *et al.* 2009), where time-temperature points are tested to construct a continuous thermal history consistent with the input data from thermochronometers. A temperature range of 70 ± 70 °C was set when modelling only AFT or AHe, and of 100 ± 100 °C when ZHe data were available. A large initial T-t box was set for our models, corresponding to the end of the Brasiliano/Pan-African Orogeny, with time ranging from 500 ± 50 Ma and temperature from 100 ± 100 °C. To represent current conditions, a final constraint was set with surface temperature of 20 ± 10 °C on present time. For the sedimentary samples (RS21 and RS22), the initial constraint was set at 535 ± 10 Ma with temperature of 20 ± 20 °C, corresponding to the maximum deposition age of Guaritas Group (Oliveira *et al.* 2014). An additional constraint was set at 474 ± 9 Ma and 90 ± 30 °C, corresponding to illite authigenesis formation, which cemented the sandstones of this group and represents their minimum depositional age (Maraschin *et al.* 2010).

Initially, fast runs of 20,000 iterations were made to set proper search parameters before longer runs, and to test variability of the resulting models when imposing different $\partial T/\partial t$ rates. Final models were run with a maximum $\partial T/\partial t$ of 10 °C/Ma, compatible with a cratonic region of subdued topography, and which resulted in less noisy thermal histories, with thermal paths of higher probability better constrained. We ran models of each thermochronometer individually to investigate consistency between models of each method. Final models were run with at least 200,000 iterations, up to 1 million, and when available, AFT, AHe and ZHe data were used together during final modelling to better constrain time-temperature paths. Other parameters set during modelling included, for AFT, c-axis projected tracks lengths from Donelick *et al.* (1999) and the annealing model from Ketcham *et al.* (2007), while for AHe we used the radiation damage model from Flowers *et al.* (2009) and for ZHe from Guenthner *et al.* (2013).

6.5 Thermochronometry results

6.5.1 Apatite fission tracks

We obtained 18 AFT ages in the SRGS (Tab. 6.2, Fig. 6.2), which all passed the chi-square test ($P\chi^2 > 5\%$), meaning that the central ages obtained for each sample correspond to single populations, even the sedimentary samples (RS21 and RS22). Reinforcing this result, single crystal age dispersion is low (< 5%) for all samples, but for RS23 and RS29, with 7% and 24% of dispersion, respectively.

Table 6.2: Apatite fission track data from the Sul-Rio-Grandense Shield. Ages were calculated using $\zeta = 280.17$. N: number of grains analyzed; ps: spontaneous track density; Ns: number of spontaneous tracks counted; pi: induced track density; Ni: number of induced tracks counted; pd: dosimeter tracks density; Nd: number of tracks used to determine pd; χ^2 : chi-square probability of single population; U: estimated value of uranium content; Dpar: mean etch pit diameter; CT: confined tracks measured; MTL: mean track length; SD: standard deviation of measured track length distribution; cP.MTL: c-axis projected mean track length; cP. SD: c-axis projected standard deviation of measured track length distribution; (-): data not available.

Sample	N	ps	Ns	pi	Ni	pd	Nd	Central Age	$\pm 1\sigma$	χ^2	U	Dpar	CT	MTL	$\pm 1\sigma$	SD	cP. MTL	cP. SD
#	#	(x10 ⁵)	#	(x10 ⁵)	#	(x10 ⁵)	#	(Ma)	(Ma)	(%)	(ppm)	(μm)	#	(μm)	(μm)	(μm)	(μm)	(μm)
<i>Pelotas Batholith</i>																		
RS2	20	16,73	875	15,51	602	7,0	13999	143,7	7,7	35	20,9	-	-	-	-	-	-	-
RS4	20	12,83	607	7,02	332	7,0	13999	176,8	12,1	99	12,7	2,00	100	11,72	0,18	1,77	13,23	1,30
RS5	20	18,82	702	11,21	418	7,17	14341	166,5	10,4	90	19,8	2,17	100	11,01	0,16	1,63	12,93	1,11
RS7	20	11,83	330	6,59	184	7,0	13999	173,5	16,0	100	12,0	2,12	45	10,78	0,27	1,82	12,71	1,18
RS10	20	21,39	783	19,64	719	7,17	14341	108,5	5,7	98	34,8	2,11	100	12,85	0,16	1,59	14,08	1,18
RS12	20	17,57	608	10,69	370	7,0	13999	159,1	10,6	87	19,4	1,81	100	12,06	0,16	1,61	13,56	1,04
RS13	20	23,82	774	14,62	475	7,0	13999	157,8	9,3	76	26,5	1,98	100	12,09	0,16	1,58	13,64	1,05
RS14	20	13,7	285	6,49	135	7,0	13999	203,7	21,4	91	11,8	2,60	100	11,52	0,17	1,68	13,20	1,15
RS25	20	7,84	163	5,43	113	7,0	13999	139,9	17,2	87	9,9	1,84	24	10,88	0,41	1,99	12,43	1,68
RS26	20	20,7	1087	10,59	556	7,17	14341	193,4	10,2	88	18,8	2,22	100	12,12	0,16	1,59	13,59	1,11
RS31	20	30,83	1853	25,66	1542	8,14	16276	146,6	7,4	38	35,5	-	-	-	-	-	-	-
<i>Taquarembo Terrane</i>																		
RS16	20	5,23	102	2,53	49	7,0	13999	200,9	34,9	100	4,6	1,82	21	11,33	0,41	1,87	12,98	1,25
RS17	20	9,36	334	4,51	161	7,17	14341	205,1	19,7	95	8,0	2,46	94	12,83	0,12	1,21	14,09	0,98
<i>Tijucas Terrane</i>																		
RS23	20	15,74	773	8,19	402	7,17	14341	190,3	12,1	34	14,5	2,18	100	11,94	0,15	1,50	13,44	1,02
<i>São Gabriel Terrane</i>																		
RS20	20	18,74	403	6,0	129	7,0	13999	299,3	30,4	100	10,9	1,82	100	11,58	0,16	1,57	13,17	1,23
RS29	20	19,69	567	6,08	175	7,0	13999	302,9	31,2	12	11,0	2,22	59	11,23	0,28	2,12	13,06	1,41
<i>Camaquã Basin</i>																		
RS21	50	19,61	1965	6,52	653	7,17	14341	295,4	13,6	82	11,5	2,09	100	11,59	0,15	1,51	13,23	1,08
RS22	50	25,59	2185	13,75	1174	7,0	13999	180,0	6,5	88	24,9	1,55	100	10,73	0,19	1,93	12,59	1,53

Thirteen samples from the PB, TiT and TaT have Jurassic AFT central ages, ranging from 139.9 ± 17.2 to 205.1 ± 19.7 Ma, of which PB samples have the younger ages and TaT the older ones. Sample RS10, from PB, yielded the youngest AFT age among analysed samples, with an age of 108 ± 5.7 Ma (Early Cretaceous). Otherwise, the AFT ages obtained for SGT (RS20 and RS29) are the oldest in the shield, with ages of 299.3 ± 30.4 Ma and 302.9 ± 31.2 Ma (Carboniferous - Permian transition). The two sedimentary samples from the Guaritas Group, collected above different terranes (RS21 in SGT and RS22 in TiT), yield AFT ages 100 Ma apart (RS21 = 295.4 ± 13.6 Ma; RS22 = 180 ± 6.5 Ma). Both samples passed the chi-square test (RS21 $P\chi^2 = 82\%$; RS22 $P\chi^2 = 88\%$), and both have unimodal tracks length distribution, which indicates complete annealing and age resetting during burial. Thus, the dissonant AFT ages obtained from these two sedimentary samples suggest that they went through the AFTPRZ at different times.

The non-projected Mean Track Lengths (MTL) of all samples range from 10.7 ± 0.2 to 12.8 ± 0.2 μm (Tab. 6.2). After c-axis projection (Donelick *et al.* 1999), the MTL ranges from 12.43 to 14.09 μm , with standard deviation between 0.9 and 1.68 μm . The lengths scattering of our samples tends to be unimodal, and in most cases presents either normal distribution around the mean value or is negatively skewed, with a larger proportion of long tracks. Plot of MTLs against AFT central ages, including previously published data, do not show a clear “half boomerang” shape (Fig. 6.3a) (Green 1986). The kinetic parameter Dpar ranges from 1.55 (sample RS22) to 2.60 μm (sample RS14), with most of the samples (81%) lying in the interval between 1.8 and 2.2 μm , indicating intermediate to low fluorine content and medium-high resistance to annealing. Considering the shortest distance from sample location to the coast, independent of direction, AFT ages tend to show positive correlation with distance (Fig. 6.3b), with samples from the coastal PB presenting younger ages, while hinterland samples from SGT and TaT present older ages. The correlation between ages and elevation is unclear, most likely due to the low relief topography.

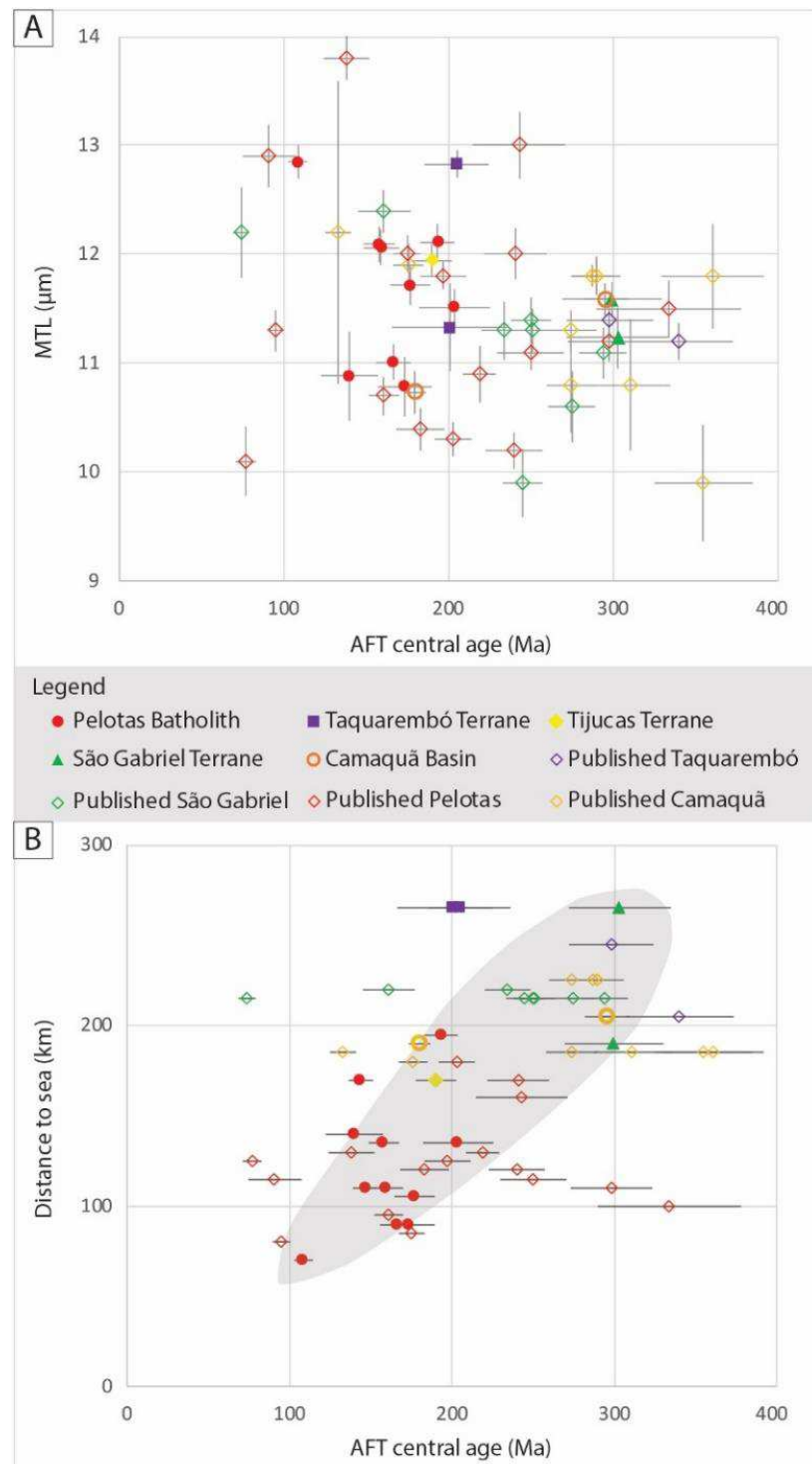


Figure 6.3: (a) Plot of AFT central ages against MTLs uncorrected for their c-axis orientation, suggesting a “half-boomerang” shape, indicative of protracted cooling through AFT PRZ with a considerable amount of annealing in older samples. (b) Plot of AFT central ages against distance to the coast, showing a tendency of increase in ages with continentality. Error bars represent $\pm 1\sigma$ range. Published data from de Borba et al. (2002, 2003), Bicca et al. (2013) and de Oliveira et al. (2016).

6.5.2 Apatite (U-Th)/He

Single crystal apatite (U-Th)/He analysis resulted in 43 AHe ages from 15 locations. Considerable dispersion is observed in our data set, not only between different samples, but also between crystals from each sample. The AHe uncorrected single crystal ages range over the Phanerozoic, although 86% are Meso- Cenozoic. After applying the Ft correction (Farley *et al.* 1996), AHe corrected ages became slightly more dispersed, with 70% post-Palaeozoic (Tab. 6.3, Fig. 6.4). Despite being a lower temperature thermochronometer, the mean AHe corrected ages are in general older than the AFT central ages obtained from same location, presenting an “inverse” pattern compared to other cratonic regions (Green & Duddy 2006; Flowers & Kelley 2011; Wildman *et al.* 2016).

The correlation between AHe corrected ages and effective uranium content of crystals ($eU = [U] + 0.235 \times [Th]$) is variable amongst our samples, but there is a tendency to reach stability below 250 Ma for crystals with $eU > 50$ ppm (Fig. 6.4). The expected positive correlation, caused by the trapping of alpha particles in samples with high eU and damaged crystal lattice (Flowers *et al.* 2007), is better defined for samples from the TiT, SGT and Camaquã Basin. Crystals from the PB, especially those with $eU < 50$ ppm, present a wide age dispersion, but ages tend to stabilize below 250 Ma for apatites with higher eU content. Plot of AHe corrected ages against crystals radius are more complex and the correlation is unclear.

Table 6.3: Summary of AHe ages and parameters. Crystal dimensions were used to estimate an equivalent spherical radius. eU: total uranium content; Term: number of crystal terminations; SD: standard deviation; Ft: alpha ejection factor for age correction.

Apatite He analyses																			
Sample	Crystal	U	Th	Sm	He	eU	Term.	Radius	Age Unc.	±1σ	Ave. Unc.	±1σ	SD	Ft	Age Corr	±1σ	Ave. Corr.	±1σ	SD
#	#	(ppm)	(ppm)	(ppm)	(nmol/g)	(ppm)	#	(μm)	(Ma)	(Ma)	(Ma)	(Ma)	(Ma)	#	(Ma)	(Ma)	(Ma)	(Ma)	
<i>Pelotas Batholith</i>																			
RS2	1	44,24	102,64	573,29	57,70	70,95	2	57,11	152,95	1,67	157,12	16,76	29,02	0,74	206,48	2,27	222,92	18,89	32,73
	2	31,52	159,66	1180,00	50,13	74,43	2	41,39	130,40	1,40					0,65	201,68	2,16		
	3	24,31	88,74	896,08	47,59	49,29	2	52,97	188,00	1,95					0,72	260,61	2,70		
RS4	1	11,10	19,46	494,84	20,68	17,98	2	43,48	231,40	2,75	191,62	39,78	56,26	0,68	341,10	4,09	275,46	65,64	92,83
	2	9,22	15,91	531,17	11,27	15,44	2	51,31	151,83	1,79					0,72	209,82	2,48		
RS7	1	15,25	75,38	230,83	28,00	33,97	2	37,19	154,17	1,78	147,28	21,31	42,62	0,61	252,96	2,93	221,60	31,61	63,22
	2	6,45	32,95	90,35	12,48	14,58	1	44,56	159,67	1,98					0,67	239,53	2,97		
	3	13,76	73,50	216,36	17,12	31,98	1	43,66	100,41	1,23					0,66	152,36	1,86		
	4	8,46	45,08	238,05	22,09	20,12	1	48,35	208,45	2,29					0,69	301,19	3,31		
	5	7,58	32,23	76,03	9,45	15,48	2	50,38	113,72	1,46					0,70	161,98	2,08		
RS10	1	57,89	160,24	125,20	69,84	95,97	2	54,69	133,75	1,44	128,27	5,39	9,33	0,73	184,02	1,99	181,00	7,89	13,66
	2	179,90	462,78	223,47	210,55	289,24	2	47,90	133,56	1,43					0,69	192,90	2,08		
	3	89,27	258,71	141,02	96,22	150,47	2	50,89	117,50	1,24					0,71	166,08	1,76		
RS12	1	20,55	17,41	438,14	37,13	26,68	2	49,45	267,57	3,90	271,03	2,83	4,89	0,72	373,49	5,50	384,75	9,20	15,93
	3	32,76	30,89	609,20	61,72	42,85	2	45,50	274,49	4,02					0,69	396,01	5,87		
RS13	1	30,93	23,13	319,79	55,73	37,84	2	55,20	274,78	5,85	276,05	1,27	1,79	0,74	370,05	7,96	351,60	18,45	26,09
	3	41,73	43,35	289,26	79,99	53,23	1	88,12	277,31	5,80					0,83	333,15	7,01		
RS14	1	16,02	56,69	374,54	60,80	31,05	1	37,92	368,49	4,96	299,54	68,95	97,51	0,63	587,59	8,03	473,05	114,54	161,99
	2	14,30	54,11	346,20	34,72	28,59	1	40,39	230,58	3,12					0,64	358,51	4,89		
RS24	2	13,73	21,45	473,84	14,02	20,98	2	35,76	132,89	1,64	171,38	38,88	67,34	0,61	216,28	2,69	271,44	65,23	112,99
	4	11,28	15,52	436,13	11,13	16,96	2	42,65	132,11	1,66					0,67	196,63	2,48		
	5	8,04	19,40	411,44	17,94	14,52	2	36,36	249,13	3,18					0,62	401,42	5,17		
RS25	1	38,29	138,69	2363,29	111,27	81,85	2	34,05	274,28	5,63	149,34	62,49	108,24	0,59	461,58	9,71	259,28	101,19	175,27
	4	36,88	191,57	2385,01	41,49	92,92	2	31,11	89,92	1,02					0,55	163,27	1,83		
	5	23,07	96,15	2053,31	21,95	55,22	2	30,22	83,82	0,99					0,55	152,98	1,79		

continues...

Sample	Crystal	U	Th	Sm	He	eU	Term.	Radius	Age Unc.	±1σ	Ave. Unc.	±1σ	SD	Ft	Age Corr	±1σ	Ave. Corr.	±1σ	SD
#	#	(ppm)	(ppm)	(ppm)	(nmol/g)	(ppm)	#	(μm)	(Ma)	(Ma)	(Ma)	(Ma)	(Ma)	#	(Ma)	(Ma)	(Ma)	(Ma)	(Ma)
RS26	1	14,21	93,28	775,56	38,04	39,69	2	80,19	187,52	2,40	178,23	4,90	8,49	0,81	232,39	2,97	219,78	7,44	12,88
	2	21,85	109,10	825,94	45,30	51,26	2	89,53	170,87	2,16				0,83	206,65	2,61			
	3	26,20	117,82	354,81	52,39	55,44	2	77,35	176,29	2,24				0,80	220,29	2,80			
<i>Taquarémbó Terrane</i>																			
RS16	1	2,18	8,75	671,00	4,09	7,39	1	39,43	148,63	3,22	173,17	22,58	39,12	0,67	222,03	4,75	263,72	30,27	52,44
	2	3,48	12,62	872,97	8,97	10,54	1	40,82	218,28	3,75				0,68	322,59	5,49			
	3	2,86	15,74	959,47	6,42	11,05	2	34,15	152,60	2,93				0,62	246,54	4,67			
<i>Tijucas Terrane</i>																			
RS23	1	2,11	2,72	38,34	0,57	2,92	2	69,55	37,49	0,60	96,59	29,64	51,35	0,79	47,65	0,77	136,13	44,28	76,70
	2	15,51	1,42	118,96	11,35	16,40	2	47,98	130,19	2,05				0,71	183,72	2,90			
	3	12,09	0,79	108,18	8,25	12,78	2	44,72	122,10	1,85				0,69	177,01	2,70			
<i>São Gabriel Terrane</i>																			
RS20	1	33,16	14,94	485,42	46,26	38,94	2	35,16	225,89	3,54	153,01	41,16	71,28	0,62	366,28	5,83	245,93	68,14	118,03
	2	3,30	10,33	339,79	2,78	7,32	2	38,54	83,44	1,68				0,64	130,36	2,62			
	3	21,78	9,74	413,40	20,08	26,01	2	35,73	149,70	2,40				0,62	241,15	3,90			
RS29	1	32,73	3,36	62,48	20,43	33,81	2	52,48	111,77	1,78	99,27	7,74	13,40	0,73	153,16	2,45	137,07	9,14	15,84
	2	33,80	14,26	69,62	17,21	37,46	2	47,48	85,12	1,35				0,70	121,50	1,94			
	3	27,16	2,07	66,35	15,21	27,95	2	54,51	100,92	1,65				0,74	136,54	2,25			
<i>Camaquã Basin</i>																			
RS21	1	92,73	10,76	524,52	88,67	97,71	2	43,06	169,03	2,52	99,66	34,69	60,09	0,68	248,92	3,75	148,21	50,42	87,34
	2	5,66	22,85	94,06	3,88	11,45	2	38,75	63,97	0,92				0,62	102,52	1,48			
	3	10,03	24,46	102,14	5,70	16,23	2	50,62	65,98	0,95				0,71	93,20	1,35			

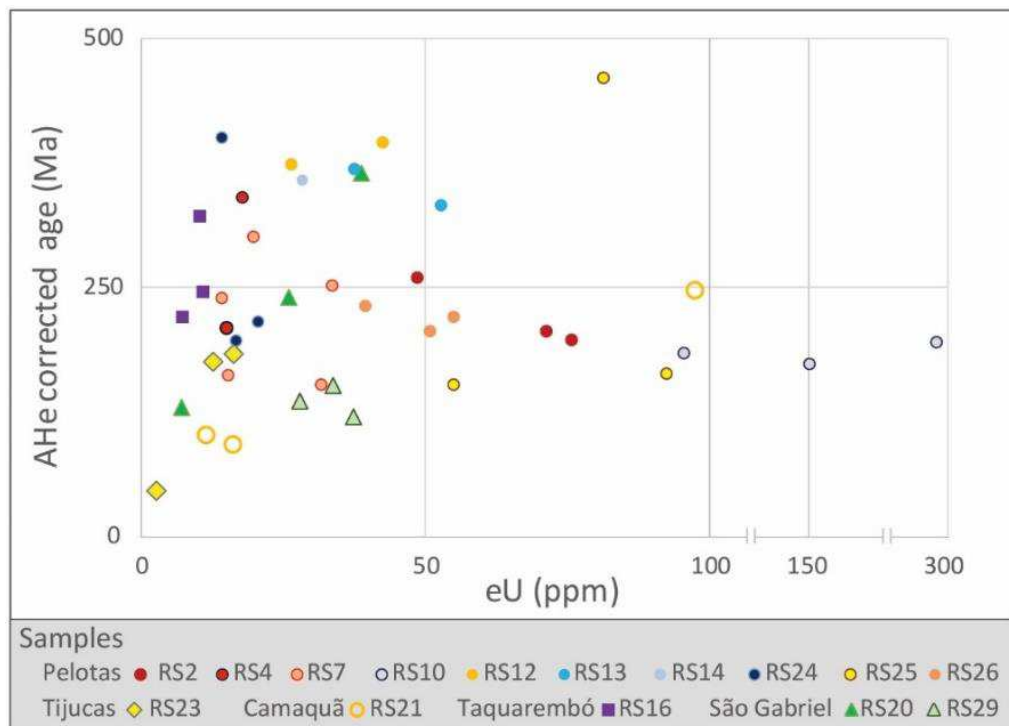


Figure 6.4: Plot of single crystal AHe corrected ages against eU. Few samples present the expected positive correlation between these parameters; samples with crystals with eU < 50 ppm tend to present larger age dispersion, while those with eU > 50 ppm tend to remain below 250 Ma.

6.5.3 Zircon (U-Th)/He

We performed ZHe analysis on 30 crystals from six samples, whose results and crystal parameters are given in Table 6.4. As expected, the ZHe ages are systematically the oldest in our dataset, attributed to the higher closure temperature of this thermochronometer. Three samples from the PB present Triassic average uncorrected ZHe ages (209 to 254 Ma), while sample RS13 from the PB, which zircons have the lowest eU in our set (<550 ppm), have a distinct Carboniferous average uncorrected ZHe age (349 Ma). Samples from the Camaquã Basin and SGT present early Permian average uncorrected ages (290 and 294 Ma, respectively). After applying the Ft correction, samples from PB present early Permian ZHe ages (278 to 303 Ma), besides the outlier sample RS14, of Early Ordovician age (484 Ma), whereas the Camaquã Basin and SGT ages are Devonian (385 and 381 Ma, respectively).

Table 6.4: Summary of ZHe ages and parameters. Crystal dimensions were used to estimate an equivalent spherical radius. eU: total uranium content; SD: standard deviation; Ft: alpha ejection factor for age correction.

Zircon He analyses																	
Sample	Crystal	U	Th	He	eU	Radius	Age Unc.	±1σ	Ave. Unc.	±1σ	SD	Ft	Age Corr	±1σ	Ave. Corr.	±1σ	SD
#	#	(ppm)	(ppm)	(nmol/g)	(ppm)	(µm)	(Ma)	(Ma)	(Ma)	(Ma)	(Ma)	#	(Ma)	(Ma)	(Ma)	(Ma)	(Ma)
<i>Pelotas Batholith</i>																	
RS2	1	2092,42	528,50	1979,08	2216,62	38,96	163,28	3,81	209,09	38,62	86,35	0,70	234,00	5,51	278,38	46,21	103,33
	2	3391,22	799,08	2477,65	3579,01	39,12	127,02	1,77				0,70	181,97	2,56			
	3	1447,40	385,07	1540,06	1537,89	48,57	182,81	2,56				0,75	242,71	3,44			
	4	1766,54	649,23	2334,46	1919,11	56,93	221,30	3,05				0,79	281,16	3,91			
	5	725,63	124,71	1474,93	754,94	53,00	351,04	5,07				0,78	452,05	6,61			
RS4	1	1118,45	115,86	1171,69	1145,67	70,19	186,62	2,71	210,98	17,12	38,29	0,83	225,90	3,30	303,26	28,34	63,37
	2	571,53	161,09	840,48	609,39	35,91	250,23	3,51				0,68	369,53	5,27			
	3	657,63	280,06	1013,65	723,44	38,12	254,17	4,07				0,69	366,88	5,96			
	4	618,71	237,44	707,76	674,51	34,63	191,41	3,06				0,66	288,38	4,68			
	5	465,03	100,44	461,24	488,64	32,91	172,48	2,82				0,65	265,62	4,40			
RS10	1	893,41	522,19	1629,08	1016,12	73,67	289,96	3,92	254,69	25,97	58,07	0,83	348,11	4,75	302,88	33,07	73,95
	2	1670,54	456,43	1597,32	1777,80	84,03	164,30	2,43				0,85	192,75	2,86			
	3	557,20	327,90	1107,47	634,26	65,06	315,10	4,31				0,81	387,80	5,36			
	4	1193,40	1466,81	2011,25	1538,10	82,19	237,73	3,12				0,85	280,88	3,71			
	5	794,55	364,99	1293,95	880,33	98,47	266,35	3,89				0,87	304,86	4,47			
RS13	1	403,63	169,38	832,03	443,43	47,60	337,79	6,46	349,156275	8,89	19,88048649	0,75	449,85	8,71	484,73	9,25	20,67
	2	349,68	214,46	752,18	400,08	37,83	338,59	6,37				0,69	489,72	9,37			
	3	297,98	366,67	700,95	384,15	35,36	329,29	5,97				0,67	493,55	9,12			
	4	417,06	166,10	956,09	456,10	52,55	376,03	7,24				0,77	486,07	9,48			
	5	491,93	214,57	1099,46	542,35	42,09	364,09	4,72				0,72	504,43	6,66			
<i>São Gabriel Terrane</i>																	
RS29	1	426,01	112,98	628,10	452,55	63,64	251,76	4,35	294,86	21,18	47,35	0,81	311,06	5,42	381,30	27,95	62,49
	2	348,07	80,92	578,89	367,09	41,61	285,16	5,00				0,72	396,85	7,05			
	3	193,05	29,70	281,78	200,03	48,91	255,41	4,68				0,76	337,27	6,24			
	4	482,34	130,98	1045,02	513,12	52,06	365,54	5,26				0,77	473,29	6,91			
	5	365,41	166,72	709,69	404,59	65,89	316,42	4,37				0,82	388,00	5,41			
<i>Camaquã Basin</i>																	
RS22	1	555,23	594,77	1485,65	695,00	49,13	383,89	5,86	290,80	40,11	89,70	0,75	508,58	7,88	385,15	55,03	123,04
	2	344,04	392,25	777,47	436,22	44,13	321,78	4,16				0,73	442,22	5,82			
	3	955,23	787,99	1118,24	1140,41	51,40	179,09	2,20				0,76	235,00	2,93			
	4	492,21	331,11	669,60	570,02	56,99	213,90	2,72				0,79	272,36	3,50			
	5	872,53	349,62	1887,47	954,69	49,41	355,33	4,82				0,76	467,61	6,43			

Plot of ZHe corrected ages against eU indicate a negative correlation for the PB, especially for crystals with eU >1000 ppm, but correlation is inconclusive for the SGT and Camaquã Basin zircons (Fig. 6.5). Sample RS14 has the oldest ages in PB and the lowest eU values, while RS2 has relatively young ZHe ages and the highest eU values. This negative correlation is common in Cratonic regions, where crystals accumulate high amount of radiation damage at low temperature over a long time, which then can be interconnected and act as “escape paths” for the alpha particles, resulting in younger ages for crystals with high eU content (Reiners 2005; Guenthner *et al.* 2013). Plot of ZHe ages against crystal radius do not show correlation.

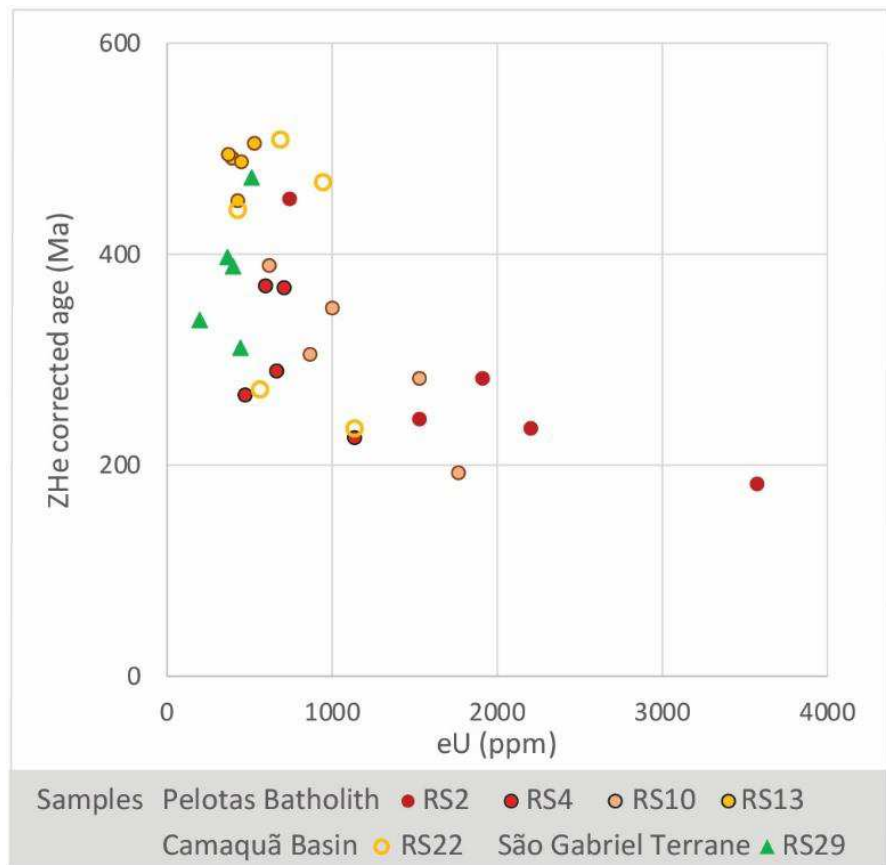


Figure 6.5: Plot of ZHe corrected ages against eU, showing negative correlation for the Pelotas Batholith zircons, pattern commonly found in old crustal environment, where crystals with high eU accumulate high amounts of radiation damage and display younger ages, owing to ${}^4\text{He}$ escape. Correlation in the São Gabriel Terrane and Camaquã Basin samples is unclear.

6.6 Thermal modelling results

Inverse thermal modelling was first performed with input data from each individual thermochronometer, and final models were run with all data available for the sample. Models exclusively from AFT data were the most consistent, with a good fit between observed and predicted ages and lengths. In most of the cases, models obtained only

from (U-Th)/He data did not fit all obtained ages, due to the wide dispersion of ages amongst crystals from a single sample. In an attempt to fit AHe ages, we allowed errors of AHe ages to be resampled by QTQt. Regardless, models obtained exclusively with AHe data did not result in geologically reasonable thermal histories, being unable to resolve the time of cooling, or presenting a cooling phase prior to that of the AFT models, followed by stability at surface temperature since middle Palaeozoic. ZHe models also showed difficulty to fit all obtained ages, but in general they were successful in constraining the epoch of cooling from higher temperatures. In any case, the combination of AFT, AHe and ZHe data in the long run usually resulted in better constrained time-temperature paths, with the thermal path obtained from AFT models predominant and a poor fit of AHe ages. Final models of each sample can be found in the supplementary material. The resulting mean paths of the models for each sample are given in Figures 6.6 and 6.7, together with models from representative samples.

Considering that the palaeogeothermal gradient for the SRGS is unknown, exhumation rates were calculated using a hypothetical constant value of 25 °C/km, obtained in the adjacent Paraná Basin (Hurter & Pollack 1996), and used in previous thermochronometry studies in the SRGS (de Borba *et al.* 2003; de Oliveira *et al.* 2016). Assuming that the cooling phases observed in our models are the result of rock exhumation from deeper crustal levels, mainly by erosive processes, we were able to estimate the total denudation from different locations across the SRGS.

6.6.1 São Gabriel Terrane

Samples from this terrane display the oldest AFT ages in our set, and this pattern is observed in the models as an earlier cooling phase since the Devonian and protracted (> 100 Ma) period of cooling through the AFTPZ (Fig. 6.6). After the first cooling phase, that lasted until the early Permian, the samples went through a long period of relative thermal stability, followed by final cooling towards surface temperature starting in the Palaeocene. The total denudation reached 6,600 m since Early Devonian (RS29).

The inverse model from RS29 (AFT, AHe, ZHe) shows two main cooling phases. The first one was a fast cooling period between 420 and 300 Ma, with temperature decreasing from c. 180 °C to 95 °C, which corresponds to an exhumation rate of 29 m/Ma and denudation of 3,800 m. Afterwards, a very slow cooling persisted until c. 60 Ma, when the sample reached temperature around 60 °C. Finally, a Cenozoic cooling phase linked to an exhumation rate of 28 m/Ma and denudation of 1400 m brought the

rock to the surface. Inverse models from sample RS20 (AFT, AHe) were not able to solve the thermal history above c. 80 °C; in any case, they indicate cooling since the Devonian, with a long period (> 200 Ma) of relative stability, similar to RS29, but at lower temperature (c. 50 °C), culminating in a final rapid cooling phase in the Paleogene.

6.6.2 Taquarembó Terrane

Two samples modelled in this terrane indicate residence at temperatures around 50 °C between the Jurassic and Cretaceous (Fig. 6.6), and a total denudation of 2,000 to 3,400 m since the Permian. The model obtained for sample RS17 (AFT), shows entry to the AFTPRZ during the Permian, at an exhumation rate of 15 m/Ma and with denudation of 2,400 m until the Cretaceous. This sample reached stability in the Early Cretaceous with temperature close to 50 °C, and went through a final cooling phase after the Eocene, with exhumation of 22 m/Ma and denudation of 1,000 m. Models from sample RS16 (AFT, AHe) provided unsatisfactory results, probably a consequence of the low number (21) of confined tracks. The thermal history before 250 Ma is poorly constrained although the model suggests that between the Jurassic and Early Cretaceous the sample was held at temperature around 60 °C, followed by protracted cooling towards surface temperature in the last 100 Ma, and a total denudation of 2,000 m.

6.6.3 Tijucas Terrane

The thermal history model of sample RS23 (AFT, AHe) indicates cooling through the AFTPRZ between the Permian and Early Jurassic (Fig. 6.6), at an exhumation rate of 15 m/Ma and denudation of 1,800 m. This cooling phase was followed by a steady-state period at temperatures of c. 60 °C until a final phase of cooling that started around 70 Ma, with exhumation rates of 23 m/Ma and denudation of 1,600 m.

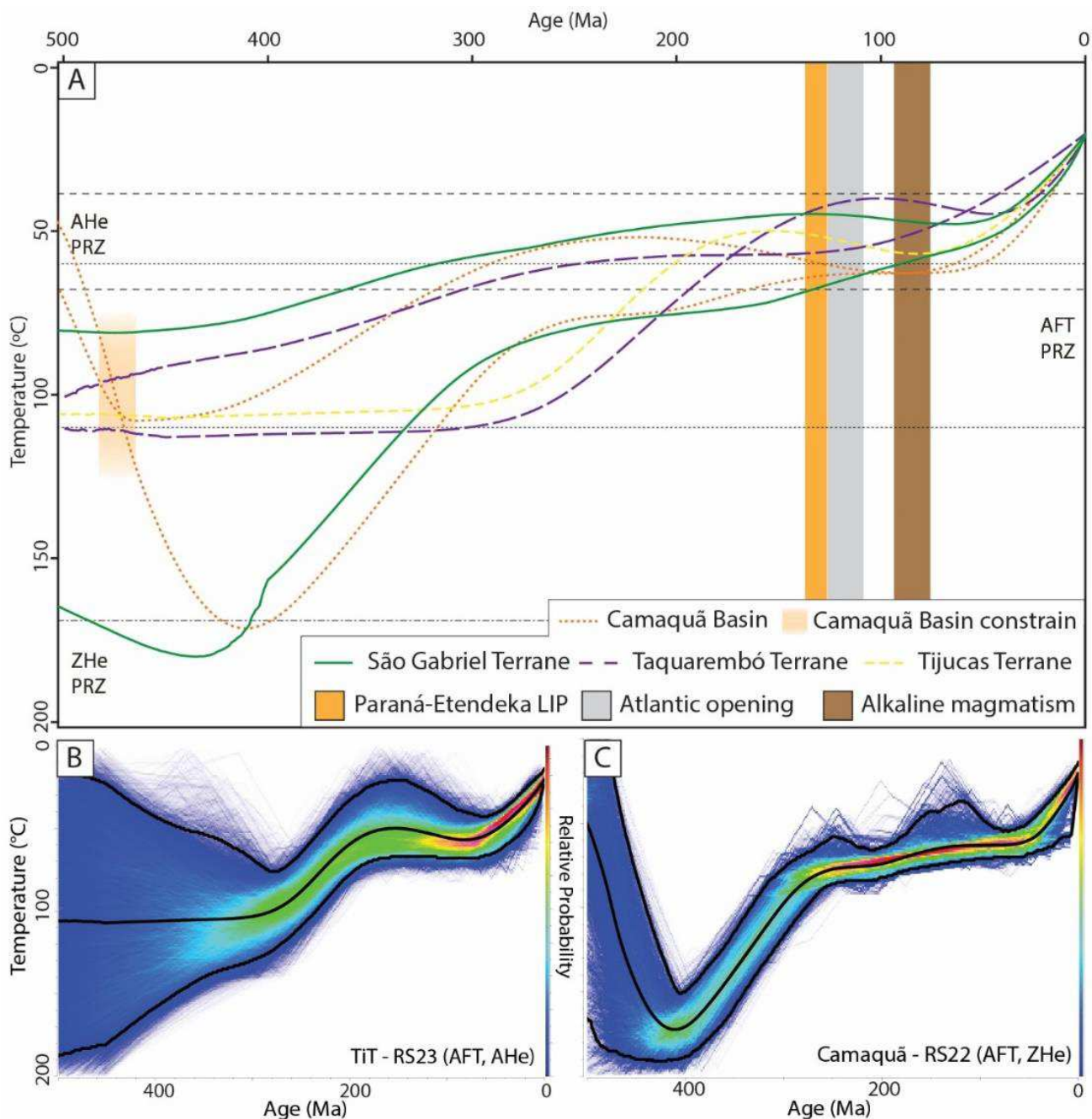


Figure 6.6. (a) Mean cooling trajectory of inverse models for samples from Camaquā Basin, São Gabriel, Taquarembó and Tijucas Terranes. Main thermotectonic events in the region are indicated as shaded bars: Paraná-Etendeka LIP (138 to 125 Ma) (Rossetti et al. 2014), Atlantic Ocean opening (130 to 113 Ma) (Stica et al. 2014), and alkaline magmatism (99 to 76 Ma) (Barbieri et al. 1987). Approximate interval of PRZ of each thermochronometer indicated with dashed horizontal lines. At the bottom, two representative samples are shown: (b) RS23 from Tijucas Terrane, that displays a similar thermal path to the Pelotas Batholith, but without significant reheating; (c) RS22 from the Camaquā Basin, which presents fast cooling between c. 400 and 300 Ma, similar to the São Gabriel Terrane, followed by protracted cooling through AFTPRZ. Black line represents the mean cooling trajectory, with coloured pathways within the 95% confidence interval.

6.6.4 Pelotas Batholith

We modelled the thermal history of ten locations in the PB, which were clustered in three groups (Fig. 6.7). Most of the models include both AFT and AHe data, while three locations also have ZHe data. Overall, models indicate cooling through the AFTPRZ between Triassic and Jurassic, followed by a subtle reheating during the Cretaceous, and a final cooling phase towards the present-day surface temperature since the Palaeocene. Samples RS2 and RS4, with ZHe data, indicate total denudation around 6000 m from the Carboniferous to the present.

Group 1 is composed of samples RS2 (AFT, AHe, ZHe), RS4 (AFT, AHe, ZHe), RS5 (AFT), RS12 (AFT, AHe), RS13 (AFT, AHe, ZHe) and RS26 (AFT, AHe), which show virtually identical thermal histories, although they can be more than 200 km apart. Their models show a cooling phase through the AFTPRZ between Triassic and Jurassic, reaching stability at temperature around 50 and 60 °C in the Middle/Late Jurassic, and in some cases possibly achieving near surface temperature around c. 140 Ma, although the models cannot precisely constrain it. ZHe data from samples RS2 and RS4 indicate that this cooling phase started during the Carboniferous, when both samples cooled from temperatures above 160 °C. Although most samples referred to do not have ZHe data, we assume that all have experienced a very similar thermal history since the Carboniferous, based on the resemblance of their thermal paths revealed by AFT data after the Triassic, and on the similarity of the ZHe ages from RS2 and RS4, despite the distance between them (75 km), thus suggesting that the PB cooled as a single block. Exhumation rates for this cooling phase range between 18 and 32 m/Ma and correspond to 1800 to 2400 m denudation between the Triassic and Jurassic. The late Palaeozoic-early Mesozoic cooling phase was followed by a subtle reheating (c. 15 °C) during Cretaceous, which lasted until c. 60 Ma, when a final cooling phase accompanied samples to surface conditions. This final Palaeocene cooling corresponds to exhumation rates of 7 to 40 m/Ma and denudation of 1000 to 2000 m of overburden.

Group 2 is composed of samples RS7 (AFT, AHe) and RS14 (AFT, AHe), which present thermal histories slightly different from Group 1, with slower cooling through the AFTPRZ between the Carboniferous and Jurassic, exhumation rates of 10 m/Ma and denudation of 1000 to 1800 m. However, like the samples above, this cooling phase was followed by a heating episode to temperatures of c. 70 °C that lasted until 60 Ma, when final cooling towards surface conditions took place. This final cooling

corresponds to exhumation rates of 26 to 33 m/Ma and denudation of 1800 to 2000 m. Group 3 is composed by two samples with distinct thermal histories: RS10 (AFT, AHe, ZHe), which display fast and monotonic cooling towards surface temperature since the Early Triassic, at a rate of 22 m/Ma and a total denudation of 5600 m of overburden; and RS25 (AFT), which gives a poorly constrained model, most likely due to the limited quantity (24) of confined tracks available. Inverse model of RS25 presents protracted cooling throughout the AFTPRZ, better defined after the Triassic, until c. 60 Ma, when a final cooling took place.

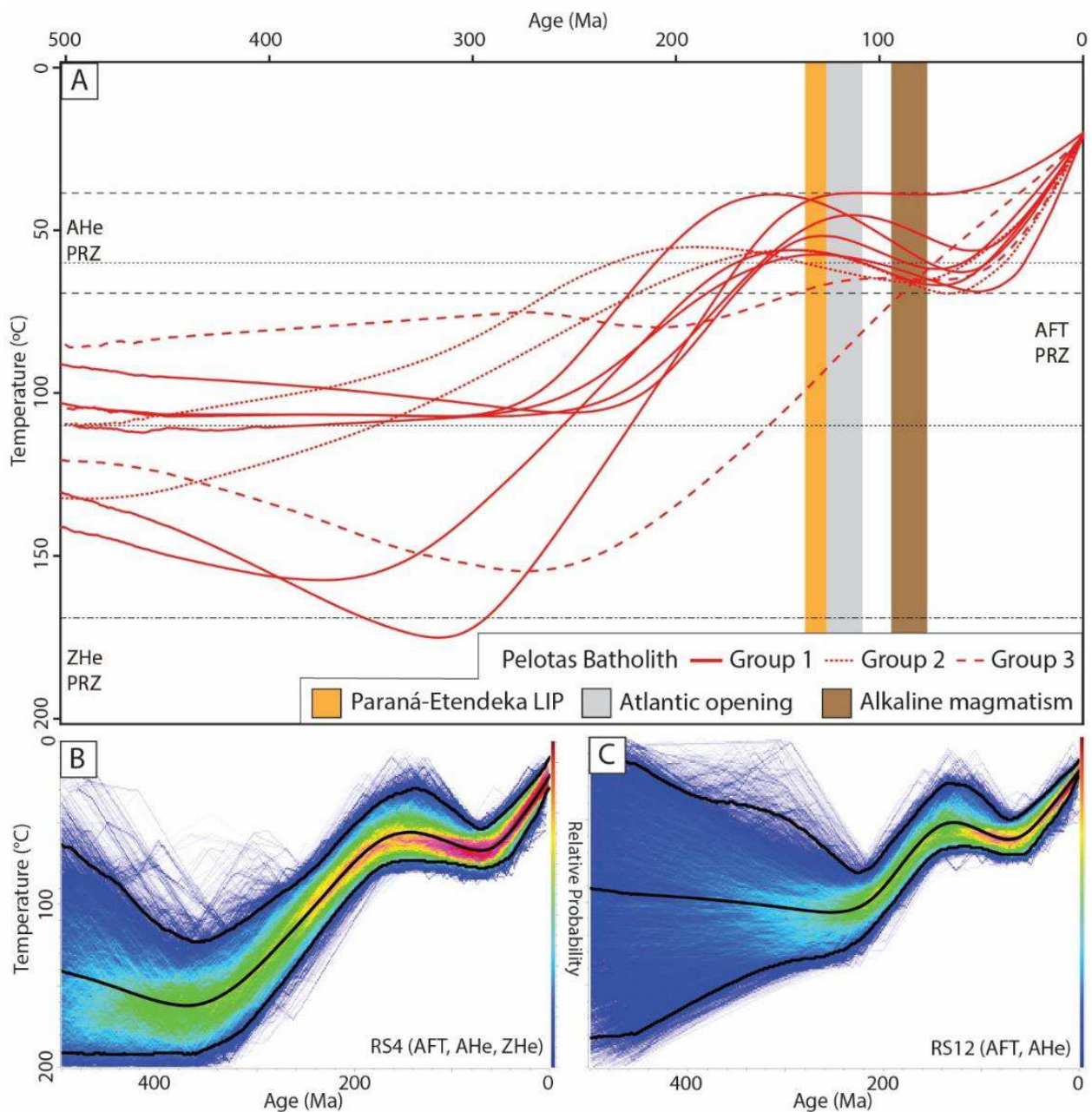


Figure 6.7: (a) Mean cooling trajectory of inverse models from each of Pelotas Batholith samples. Main thermotectonic events in the region are indicated as shaded bars: Paraná-Etendeka LIP (138 to 125 Ma) (Rossetti et al. 2014), Atlantic Ocean opening (130 to 113 Ma) (Stica et al. 2014), and alkaline magmatism (99 to 76 Ma) (Barbieri et al. 1987). Approximate interval of the PRZ of each thermochronometer indicated with dashed horizontal lines. At the bottom, two representative samples are shown: (b) RS4, which contains ZHe data that constrain the model at higher temperatures and older times; (c) RS12, without ZHe data, but with the same cooling pattern observed after c. 220 Ma, defined by AFT data. Black line represents the mean cooling trajectory, with coloured pathways within the 95% confidence interval

6.6.4 Camaquã Basin

Two models were obtained for the Camaquã Basin, from samples collected from different basement terranes. Both models indicate exhumation from the Devonian to early Permian, followed by a long period of relative thermal stability, until a final Cenozoic phase of exhumation towards surface temperature (Fig. 6.6). Sample RS21 (AFT, AHe), situated over the SGT, records cooling through the AFTPRZ from the Devonian to the Permian, with an exhumation rate of 18 m/Ma and denudation of 1600 m. This cooling phase was followed by residence at temperature close to 60 °C until c. 80 Ma, when the final cooling phase occurs, at a rate of 23 m/Ma and an additional erosion of 1600 m. Models from sample RS22 (AFT, ZHe), situated over the west of TiT, indicate burial peak prior to the Devonian as well, when an exhumation phase takes place and cools the rock from temperatures above 160 °C to the AFTPRZ in the late Carboniferous. This exhumation phase occurred at a rate of 29 m/Ma and represents the denudation of 3800 m of sedimentary overburden. Afterwards this sample went through a protracted slow cooling phase (6 m/Ma) within the AFTPRZ until the Palaeocene, when fast cooling is observed at a rate of 32 m/Ma and denudation of 1600 m.

6.7 Discussion

In our study we used a multi-thermochronometer approach to investigate the exhumation history of the SRGS. On the basis of 18 AFT, 43 AHe and 30 ZHe ages presented here and the thermal histories inverse modelled for 17 locations, along with data from previous work (de Borba *et al.* 2002, 2003; Bicca *et al.* 2013; de Oliveira *et al.* 2016), we were able to characterize the thermal behaviour of the SRGS in the Phanerozoic. Four main thermal events were revealed, which affected different parts of the shield. First, a Devonian to Carboniferous cooling phase occurred in the NW of the SRGS, followed by a broader event that cooled almost the entire shield from Permian to Early Cretaceous time. During the Cretaceous a subtle reheating was registered in samples from the PB, along the Atlantic margin. A final cooling phase that began around the Paleogene is observed in all models.

6.7.1 Evaluation of Thermochronometry Ages

AFT ages are at least 200 Ma younger than the host rock emplacement/stratigraphic age or the last orogenic event in the region (Brasiliano/Pan-African Orogeny) and, therefore, we interpret our AFT ages as cooling ages that

represent gradual exhumation of the rocks from deeper crustal levels due to denudational events. The correlation between AFT ages and MTLs in Figure 6.3a, along with the short lengths of the AFT and their unimodal normal or negatively skewed distribution, indicate a protracted cooling of our samples through the AFTPRZ, with different parts of the shield reaching the closure temperature of AFT (c. 110 °C) at different times. Figure 6.8 presents the kriging interpolation of all AFT central ages available for the SRGS, in which a good match between our data and the published data is observed. AFT ages tend to increase towards the west part of the shield, where the SGT and TaT concentrate Palaeozoic ages. An exception to this pattern is observed in the ENE of the PB, where de Oliveira *et al.* (2016) obtained two late Carboniferous ages and associated them to a local uplift caused by the Gondwanic Orogeny, in contrast to surrounding Mesozoic ages. Overall, the integrated database indicates that the west of the SRGS reached relative stability at temperatures below 110 °C during the late Palaeozoic, earlier than the central-eastern regions, which record mostly middle Mesozoic AFT ages.

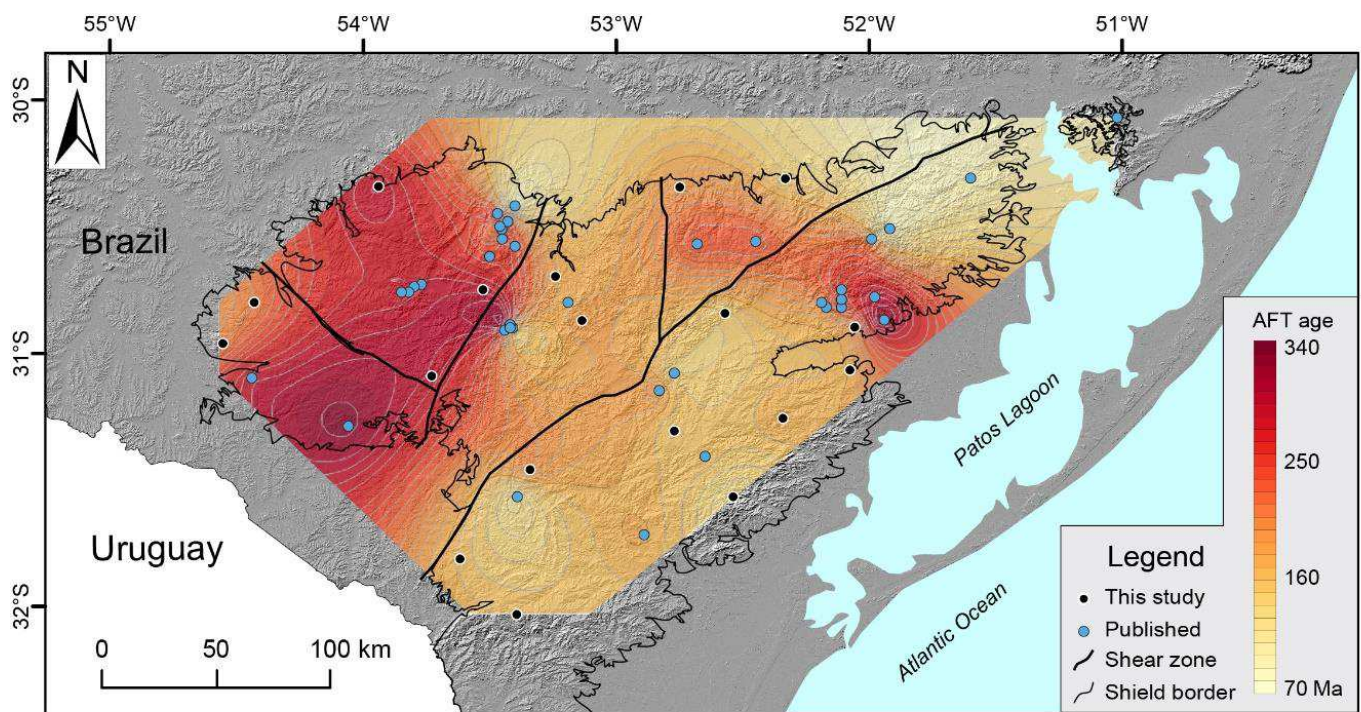


Figure 6.8. Kriging interpolation of the dataset of all AFT central ages available for the SRGS. The west portion concentrates the oldest AFT central ages, indicating a longer period of stability at low temperature (<110 °C) when compared to the rest of the shield. Published data from de Borba *et al.* (2002, 2003), Bicca *et al.* (2013) and de Oliveira *et al.* (2016).

Regarding (U-Th)/He analysis, the ZHe oldest single crystal ages of our samples indicate that this thermochronometer was partially closed and accumulating ${}^4\text{He}$ and radiation damage from the early Palaeozoic. The negative correlation between ZHe ages and eU shows that age dispersion within samples is controlled by the amount of radiation damage accumulated in each crystal; therefore, the apparent ages do not represent a specific thermotectonic event, but reflect the variability of the closure temperature of each crystal exposed to a similar thermal history (Guenthner *et al.* 2013; Hueck *et al.* 2018a). Overall, inverse modelling was able to fit the ZHe age dispersion and constrain the cooling time of our samples to temperatures below c. 160 °C, suggesting that the SGT and Camaquã Basin reached lower temperatures earlier than the PB (Figs. 6.6 and 6.7).

On the other hand, our AHe ages are too dispersed and do not constrain the samples' thermal histories while passing through the shallower levels of the crust (< 60 °C). Similar dispersion was observed in other studies that applied AHe analysis in Palaeozoic or older rocks (Green & Duddy 2018). Flowers & Kelly (2011) argued that, because small differences in apatite ${}^4\text{He}$ diffusivity are amplified during slow cooling, a range of AHe ages is expected in Cratonic regions; they presented an approach to interpret such dispersion through evaluation of age-eU and age-crystal size correlations. Our AHe ages do not show a clear correlation with crystal size, but do exhibit a tendency towards stability under 250 Ma when $\text{eU} > 50 \text{ ppm}$, which could be an indication that the AHe Palaeozoic ages in crystals with low eU content were influenced by factors poorly understood or improperly weighted during the age calculations. Several other works have investigated additional factors that might cause AHe age dispersion in cratons. Murray *et al.* (2014) demonstrated that U-Th-Fe-rich grain boundary phases, usually observed as coats of red/orange colour around apatite, can produce large effects in AHe ages. Recanati *et al.* (2017) showed the influence of accumulated radiation damage in ${}^4\text{He}$ accumulation and diffusion, as well as Shuster *et al.* (2006), who argued that samples subjected to reheating after substantial accumulation of radiation damage are more ${}^4\text{He}$ retentive, resulting in abnormal older ages. Wildman *et al.* (2016) summarized six other factors, from previous work, that can cause AHe age dispersion, for instance eU crystal zonation and ${}^4\text{He}$ injection from neighbouring minerals. Therefore, the high amount of radiation damage accumulated in the apatites and a short-duration reheating term can result in age dispersion and an inverse pattern between AFT and AHe ages, as observed in our samples (Shuster *et al.* 2006; Flowers 2009; Flowers *et al.* 2009). Furthermore, orange coats were

observed in some of our crystals, and eU zonation was indirectly observed in many of our samples. The latter was inferred by the spatially variable density of fission tracks in crystals selected for AFT, usually with a greater number of tracks in the core of the apatites relative to their rims.

Although several publications successfully applied AHe analysis in Meso-Cenozoic settings with fast monotonic exhumation, there are limitations when using this methodology in older environments with more complex thermal history. The work cited above as well as our own observations and AHe ages reinforce the current drawbacks of the method. Our thermochronometry data do provide relevant information about the exhumation of the SRGS, with AHe age dispersion indicating a complex and protracted period of cooling in the AHePRZ, and a possible reheating phase, as also indicated by independent AFT models. However, due to our limited knowledge of ${}^4\text{He}$ diffusion in protracted cooling environments, this information was not fully accessed, and we were unable to constrain the Cenozoic thermotectonic evolution of the SRGS.

6.7.2 Thermotectonic evolution of the Sul-Rio-Grandense Shield

Inverse modelling reveals three distinct cooling phases affecting the SRGS back to the Devonian, and a discrete heating episode during the Cretaceous, acting mostly in the east of the shield. Moreover, our models indicate distinct thermal history of samples collected in the São Gabriel Terrane, which attained relative stability at temperatures earlier than the other shield terranes. Timing of the cooling episodes for each location are given in Figure 6.9, in the context of established regional tectonic and magmatic events.

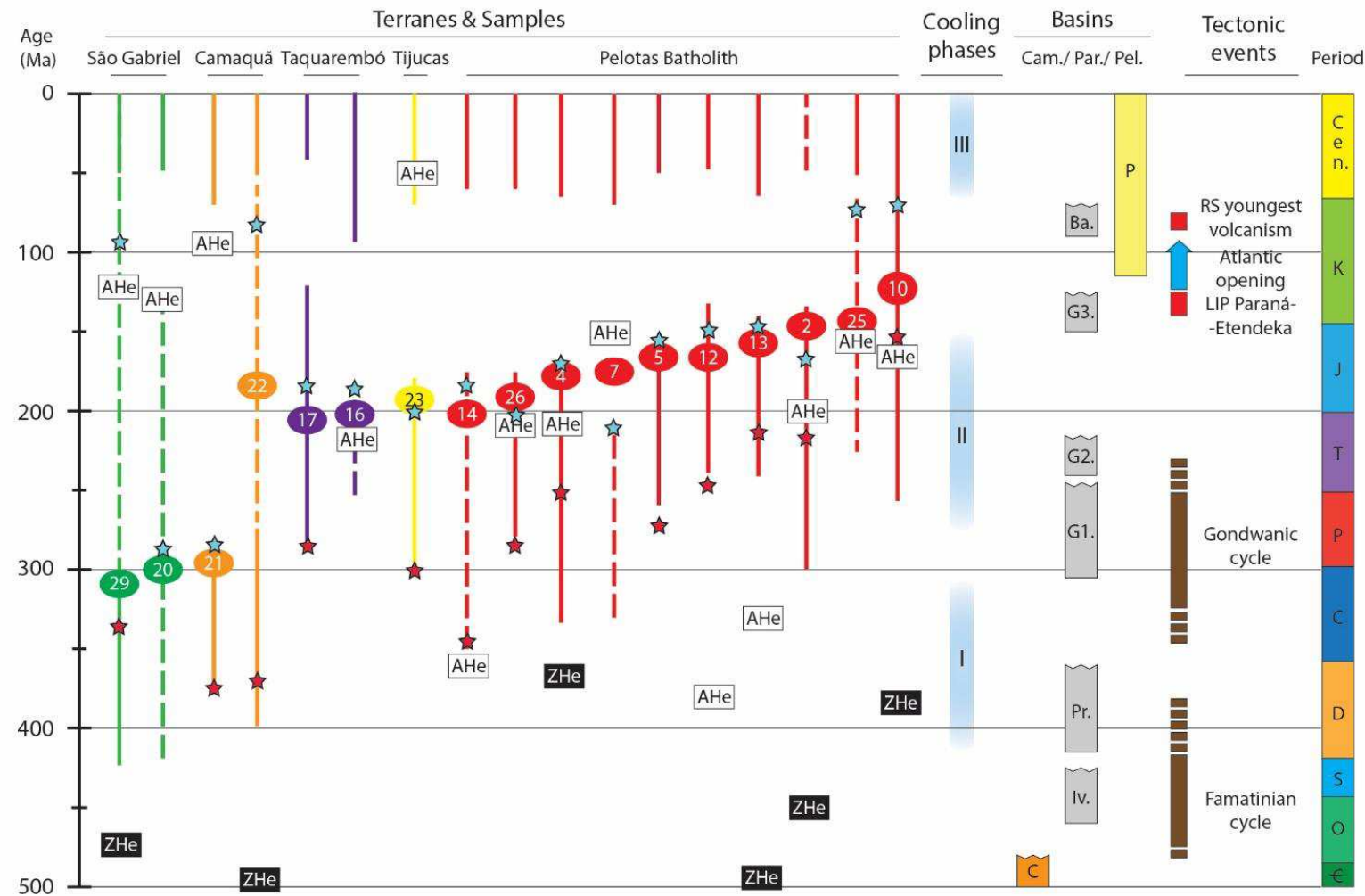


Figure 6.9. Chronological chart of cooling phases in the SRGS observed in inverse thermal models. Solid lines represent fast exhumation (>15 m/Ma), dashed lines slow exhumation (≤ 15 m/Ma), and gaps steady state or reheating. Sample ID placed according to its AFT central age, while the oldest ZHe and youngest AHe corrected ages are reported when available. Red and blue stars indicate the approximated time of passage through temperatures of 110 and 60 °C, respectively. Boxes on the right represent cooling phases, tectonic and magmatic regional events in the vicinity of the SRGS, and the sedimentary record in Camaquá (C), Paraná (supergroups Rio Ivaí - Iv., Paraná - Pr., Gondwana I - G1, Gondwana II - G2, Gondwana III - G3, and Bauru - Ba.) and Pelotas (P) basins.

The first cooling phase (phase I) in the SRGS is observed in samples from the SGT and Camaquã Basin. The former presents the oldest AFT ages in our dataset, and inverse models from both regions reveal a fast exhumation episode, at rates up to 30 m/Ma, from the Devonian to late Carboniferous. de Oliveira *et al.* (2016) and de Borba *et al.* (2002, 2003) recognized a similar cooling in samples from the SGT and TaT, and related it to collisional events in the SW portion of Gondwana, when compressive stress propagation led to reactivation of basement structures and local uplift. During the entire Palaeozoic, West Gondwana was built by a succession of accretionary cycles on its SW margin, the main ones known as the Famatinian and Gondwanan orogenies. Although the timing of each phase of these collisional events remains controversial, most authors concur that the Famatinian Orogeny was active between the Ordovician and Devonian and the Gondwanan Orogeny between the Carboniferous and Permian (see Zalán 1991, 2004; Cawood 2005; Pankhurst *et al.* 2006; Charrier *et al.* 2007; Ramos 2009; Milani & Wit 2008; de Luchi *et al.* 2018). Our data support the hypothesis that the Devonian to Carboniferous cooling episode, observed by us essentially in the NW of the SRGS, is related to these collisional cycles. As such, the west portion of the SRGS was uplifted in response to intraplate stress, caused by the continuous subduction of oceanic crust and accretionary processes on the SW Gondwana margin. This uplift phase is also marked in the adjacent Paraná Basin, NW of the shield, as an interregional unconformity and absence of sedimentary deposits of Late Devonian to Carboniferous age (Milani 1997). This cooling phase on the west of the SRGS lost intensity in the late Carboniferous, as indicated by a change to slow exhumation rates (<10 m/Ma) or stability in our models from the SGT and Camaquã Basin (Figs. 6.6 and 6.9).

A regional cooling phase (phase II) took place in the SRGS from the Permian to Early Cretaceous, corresponding to exhumation rates between 10 and 25 m/Ma and triggering passage through the AFTPZ for most of our samples, which was also observed in many PB models from de Oliveira *et al.* (2016). Conversely, samples from the SGT and Camaquã Basin, affected by the previous cooling phase, do not show an increase in exhumation rate during Permian to Mesozoic times, which indicates that the SRGS west portion was more stable compared to the rest of the shield at that time. The beginning of this regional cooling episode was contemporaneous with Gondwana deglaciation and southward migration of the ice cap, which exposed the shield bedrock to conditions of more intense weathering and erosion (de Borba *et al.* 2003; Montañez & Poulsen 2013; Goddérus *et al.* 2017). Ice cap retreat records are found in close

vicinity of the SRGS, as tills and striated pavements from the early Permian Itararé Group (Paraná Basin, Gondwana I supergroup) (de Borba *et al.* 2002; Milani *et al.* 2007). Additionally, the late stages of the Gondwanic Cycle (San Rafaelic phase) took place during the late Permian, and led to exhumation of the shield with reactivation of basement structures in the SRGS and Paraná Basin, related to intraplate stress transmission (Zerfass *et al.* 2004; Milani & Wit 2008; de Oliveira *et al.* 2016). The deposition of the Gondwana II Supersequence (Milani 1997), mostly restricted to a few grabens in the SRGS, indicates tectonic stress in the shield during the Early Triassic (Zerfass *et al.* 2004; Milani *et al.* 2007; Borsa *et al.* 2017).

Although the end of the Palaeozoic ice age and the final stages of Gondwanan Orogeny may have contributed to this Permian to Mesozoic exhumation of the SRGS, we suggest that doming and uplift, associated with Pangaea breakup, may have been the main drivers of this cooling phase. During the Mesozoic the Brazilian Platform went through broad epeirogenic uplift, related to the South Atlantic opening (Zalán 2004; Carneiro *et al.* 2012) and associated with lithosphere thinning and density decrease (Saenz *et al.* 2003; Hackspacher *et al.* 2004). South of the SRGS, thermochronometry of the Uruguay basement has revealed early Mesozoic regional exhumation associated with the opening of the South Atlantic as well (Hueck *et al.* 2017). In contrast, studies in the Florianópolis region, north of the SRGS (Fig. 6.1a), indicated a complex thermotectonic history, representing a limit between the record of pre-rift exhumation in the south and post-rift exhumation in the north. Cooling in this region records pre- and post-rift exhumation of different blocks, limited by NW-SE fault zones (Jelinek *et al.* 2003; Karl *et al.* 2013) and affected by the thermal overprint of the Paraná-Etendeka LIP (Hueck *et al.* 2018a). Our models show that this cooling phase in the SRGS persisted from the Permian through the Jurassic, suggesting regional exhumation until the Early Cretaceous magmatism of the Paraná-Etendeka LIP. Quirk & Rüpke (2018) stated that melt trapped in the asthenosphere could increase buoyancy of the continental plate before rifting, uplifting progressively thinner lithosphere before plate breakup and melt release. The voluminous magmatism of the Paraná-Etendeka LIP, with extrusive peak at c. 134 Ma, and whose feeding dykes cut through the shield (Fig. 6.1b), is a strong indication of a mantle anomaly acting below or in the vicinity of the SRGS. Previous work attributed this LIP and the Pangaea breakup to the influence of the Tristan da Cunha mantle plume in the region (Turner *et al.* 1994; Dalziel *et al.* 2000; Meisling *et al.* 2001; Hoernle *et al.* 2015). Breakup and sea-floor spreading did not advance further north of Florianópolis until late Aptian

(Chang *et al.* 1992; Meisling *et al.* 2001; Stica *et al.* 2014), which concentrated the thermotectonic stress in the vicinity of the SRGS during the Early Cretaceous. This protracted cooling phase ended in the Cretaceous, when the majority of our samples reached stability at temperatures close to 60 °C, although a few samples possibly reached surface temperature. During the Cretaceous the SRGS was a significant source of sediments for adjacent basins (Ladeira 2014), such as the Paraná Basin, in which the Botucatu Formation aeolian sandstone deposits (Gondwana III Supersequence) display a reduction in thickness towards the SRGS, suggesting that the shield was a topographic high and sediment source (Scherer 2000).

During the Late Cretaceous, our models from the PB suggest a discrete reheating phase, raising temperatures to around 70 °C (Fig. 6.7), in a similar behaviour to several models for the PB from de Oliveira *et al.* (2016). This reheating persisted until the last magmatic episode in the SRGS, represented the emplacement of several alkaline plugs between 99 and 76 Ma, with a NW-SE alignment, located in the TiT (Barbieri *et al.* 1987). Borehole samples from the Camaquã Basin, subjected to zircon fission track analysis by de Oliveira *et al.* (2016), suggest partial resetting of ages during Pangaea breakup, indicating temperatures up to c. 250 °C at subsurface. In the Florianópolis region, ZHe ages were partially reset during the Paraná-Etendeka LIP magmatism (Hueck *et al.* 2018a). In a study on the conjugate African side of the Atlantic Ocean, Brown *et al.* (2014) suggested that the LIP magmatism was sufficient to raise temperature to partial annealing of apatite fission tracks. Considering this, we suggest that the heat influence of the Tristan da Cunha plume, the mantle uplift linked to initiation of rifting, plus the Paraná-Etendeka magmatism, were responsible for a disturbance in the geothermal gradient under the SRGS. This disturbance was more intense in the eastern part of the shield, closer to the Atlantic rift, where temperatures increased some 10 to 20 °C, but was not enough to reset any of the analysed thermochronometers.

Final cooling (phase III) towards surface conditions affected the whole SRGS after the Palaeocene, at rates between 20 and 35 m/Ma for most samples. This post-rift cooling phase corresponds to 1,000 to 2,000 m denudation, moving samples from the colder limit of the AFTPRZ (60°C) to surface temperature. Models by de Oliveira *et al.* (2016) and de Borba *et al.* (2002, 2003) indicate similar exhumation event in the shield, as those of Brown *et al.* (2014) on the African conjugate margin. Coeval cooling was also observed along the SE Brazilian coast, which resulted in the uplift of the Serra do Mar range and sediment progradation in the marginal basins (de Borba *et al.* 2003;

Hackspacher *et al.* 2004; Hiruma *et al.* 2010; Cogné *et al.* 2012). Therefore, the final cooling phase observed along both sides of the Atlantic margin is possibly related to plate adjustments after Atlantic rifting, which changed the spreading rate and geometry in the Late Cretaceous and resulted in stresses that were transferred to the continent (Brown *et al.* 2014; de Oliveira *et al.* 2016). Moreover, flexural compensation caused by the accumulation of sediments in the coastal basin and subsidence of the cooling oceanic crust might have contributed to coastal uplift (de Oliveira *et al.* 2016). Finally, Müller *et al.* (2018) suggested an increase in the uplift of the South America margin over the last 50 Ma driven by mantle convection.

There is considerable uncertainty in our estimates of the long-term total denudation of the SRGS, given the probable variability of the geothermal gradient in the region during the Phanerozoic, in consequence of the Palaeozoic orogenies nearby and the Mesozoic Atlantic rifting. In any case, using a constant geothermal gradient of 25 °C/km, we estimated a total denudation of c. 6000 m since the Devonian – Carboniferous for the SRGS. This value was calculated based on the ZHe results of samples from the Camaquã Basin, SGT and PB, considering that the exhumation timing and rates are different in each portion of the shield, with the western part of the shield having an earlier phase of exhumation compared to the eastern.

6.8 Conclusions

Our set of new AFT, AHe and ZHe data for the Sul-Rio-Grandense Shield, supported by published work of more restricted scope, unveils the Phanerozoic thermotectonic evolution of the SRGS and the thermal effects of the pre-, syn- and post-Pangaea breakup. Inverse modelling allowed the reconstruction of three main distinct cooling phases in the SRGS (Fig. 6.9), and indicated a positive thermal effect on the east margin of the shield related to South Atlantic rifting and Pangaea breakup.

1) The oldest cooling phase affected the western part of the SRGS, reflecting exhumation of rocks from the São Gabriel Terrane and Camaquã Basin from the Devonian to Carboniferous. This phase is related to the successive orogenies occurring in the SW portion of West Gondwana, which caused uplift of western area of the shield, as well of the adjacent Paraná Basin, possibly in response to intraplate stress caused by processes at the collisional plate boundary.

2) A widespread cooling phase affects most of the shield from Permian to Jurassic times, during which most of our samples cooled to temperatures around 60°C, the upper limit of the AFTPRZ. This cooling episode is most likely the result of

lithospheric thinning and uplift preceding Pangaea breakup, although factors such as Gondwana deglaciation and late stage evolution of the Gondwanan Orogeny might have contributed to crustal exhumation and uplift, evidenced by structural reactivation of Brasiliano Orogeny lineaments and flexure along the shield.

3) During the Late Cretaceous a subtle reheating event is inferred, mostly in the eastern part of the SRGS. The Paraná-Etendeka LIP magmatism, linked to the Tristan da Cunha mantle plume and Atlantic rifting, possibly caused an increase in the regional geothermal gradient, which was most effective in the Pelotas Batholith, closer to the rift margin, but not high enough to reset the ages of the thermochronometers analysed.

4) Final exhumation took place since the Paleogene, acting over the whole SRGS, likely related to plate adjustments after Atlantic opening and flexural response to the subsidence of cooling oceanic crust adjacent to the shield.

6.9 Acknowledgments

The authors gratefully acknowledge the support from Shell Brasil through the “BG05: UoA-UFRGS-SWB Sedimentary Systems” project at UFRGS, the strategic importance of the support given by ANP through the R&D levy regulation, and the CNPq scholarship (SWE 204254/2017-5) during the exchange period at the University of Aberdeen. We also thank Peter W. Reiners and his team at the Baja Arizona Radiogenic Helium Dating Laboratory (US) for the (U-Th)/He analyses and assistance. We are grateful for the suggestions of Léo A. Hartmann and Chong Ma that significantly improved the manuscript.

6.10 References

- Almeida, F.F.M. de & Hasui, Y. 1984. *O Pré-Cambriano Do Brasil*. São Paulo, Editora Edgar Blucher.
- Almeida, F.F.M. De, Brito Neves, B.B. De & Dal Ré Carneiro, C. 2000. The origin and evolution of the South American platform. *Earth Science Reviews*, **50**, 77–111, <https://doi.org/10.1080/02841850802647039>.
- Barbieri, M., Beccaluva, L., et al. 1987. The Phonolite Suite From Piratini, RS. *Geochimica Brasiliensis*, **1**.
- Basei, M.A.S., Frimmel, H.E., Campos Neto, M. da C., de Araujo, C.E.G., de Castro, N.A. & Passarelli, C.R. 2018. The Tectonic History of the Southern Adamastor Ocean Based on a Correlation of the Kaoko and Dom Feliciano Belts. In: *Geology of Southwest Gondwana*. Springer International Publishing, 63–85., https://doi.org/10.1007/978-3-319-68920-3_3.
- Bicca, M.M., Chemale, F., Jelinek, A.R., de Oliveira, C.H.E., Guadagnin, F. & Armstrong, R. 2013. Tectonic evolution and provenance of the Santa Bárbara Group, Camaquã Mines region, Rio Grande

- do Sul, Brazil. *Journal of South American Earth Sciences*, **48**, 173–192, <https://doi.org/10.1016/j.jsames.2013.09.006>.
- Borba, A.W. de & Mizusaki, A.M.P. 2003. Santa Bárbara Formation (Caçapava do Sul, southern Brazil): depositional sequences and evolution of an Early Paleozoic postcollisional basin. *Journal of South American Earth Sciences*, **16**, 365–380, [https://doi.org/10.1016/S0895-9811\(03\)00102-0](https://doi.org/10.1016/S0895-9811(03)00102-0).
- Borba, A.W. de, Vignol-Lelarge, M.L.M. & Mizusaki, A.M.P. 2002. Uplift and denudation of the Caçapava do Sul granitoids (southern Brazil) during Late Paleozoic and Mesozoic: constraints from apatite fission-track data. *Journal of South American Earth Sciences*, **15**, 683–692, [https://doi.org/10.1016/S0895-9811\(02\)00086-X](https://doi.org/10.1016/S0895-9811(02)00086-X).
- Borba, A.W. de, Lima, E.F. De, Vignol-Lelarge, M.L.M., Mizusaki, A.M.P., Sparrenberg, I. & Barros, C.E. de. 2003. Significance of Late Paleozoic Fission-track Ages in Volcanic Rocks from the Lavras Do Sul Region, Southernmost Brazil. *Gondwana Research*, **6**, 79–88, [https://doi.org/10.1016/S1342-937X\(05\)70645-6](https://doi.org/10.1016/S1342-937X(05)70645-6).
- Borsa, G.N.O., Mizusaki, A.M.P. & Menegat, R. 2017. The Triassic belt preserved in Arroio Moirão Graben, southernmost Brazil: Depositional system, sequence stratigraphy and tectonics. *Journal of South American Earth Sciences*, **77**, 123–140, <https://doi.org/10.1016/j.jsames.2017.05.002>.
- Brown, R., Summerfield, M., Gleadow, A.J.W., Gallagher, K., Carter, A., Beucher, R. & Wildman, M. 2014. Intracontinental deformation in southern Africa during the Late Cretaceous. *Journal of African Earth Sciences*, **100**, 20–41, <https://doi.org/10.1016/j.jafrearsci.2014.05.014>.
- Bueno, G.V., Zacharias, A.A., Oreiro, S.G., Cupertino, J.A., Falkenhein, F.U.H. & Martins Neto, M.A. 2007. Bacia de Pelotas. *Boletim de Geociências da Petrobras*, **15**, 551–559.
- Carlson, W.D., Donelick, R.A. & Ketcham, R.A. 1999. Variability of apatite fission-track annealing kinetics; I, Experimental results. *American Mineralogist*, **84**, 1213–1223, <https://doi.org/10.2138/am-1999-0901>.
- Carneiro, C.D.R., Almeida, F.F.M. de, Hasui, Y., Zalán, P. V. & Teixeira, J.B.G. 2012. Estágios Evolutivos do Brasil no Fanerozoico. In: Hasui, Y., Carneiro, C. D. R., Almeida, F. F. M. de & Bartorelli, A. (eds) *Geologia Do Brasil*. São Paulo, Editora Beca, 131–137.
- Cawood, P.A. 2005. Terra Australis Orogen: Rodinia breakup and development of the Pacific and Iapetus margins of Gondwana during the Neoproterozoic and Paleozoic. *Earth-Science Reviews*, **69**, 249–279, <https://doi.org/10.1016/j.earscirev.2004.09.001>.
- Chang, H.K., Kowsmann, R.O., Figueiredo, A.M.F. & Bender, A.A. 1992. Tectonics and stratigraphy of the East Brazil Rift system: an overview. *Tectonophysics*, **213**, 97–138, [https://doi.org/10.1016/0040-1951\(92\)90253-3](https://doi.org/10.1016/0040-1951(92)90253-3).
- Charrier, R., Pinto, L. & Rodríguez, M.P. 2007. Tectonostratigraphic evolution of the Andean Orogen in Chile. In: *The Geology of Chile*. Geological Society Special Publication, 21–114., <https://doi.org/10.1144>.
- Chemale, F. 2000. Evolução Geológica do Escudo Sul-rio-grandense. In: Holz, M. & De Ros, L. F. (eds) *Geologia Do Rio Grande Do Sul*. Porto Alegre, Universidade Federal do Rio Grande do Sul, 13–52.
- Cogné, N., Gallagher, K. & Cobbold, P.R. 2011. Post-rift reactivation of the onshore margin of southeast Brazil: Evidence from apatite (U-Th)/He and fission-track data. *Earth and Planetary Science Letters*, **309**, 118–130, <https://doi.org/10.1016/j.epsl.2011.06.025>.

- Cogné, N., Gallagher, K., Cobbold, P.R., Riccomini, C. & Gautheron, C. 2012. Post-breakup tectonics in southeast Brazil from thermochronological data and combined inverse-forward thermal history modeling. *Journal of Geophysical Research B: Solid Earth*, **117**, 1–16, <https://doi.org/10.1029/2012JB009340>.
- CPRM, S.G. do B. 2010. *Projeto Aerogeofísico Escudo Do Rio Grande Do Sul*, <https://doi.org/http://rigeo.cprm.gov.br/jspui/handle/doc/10948>.
- Dalziel, I.W.D., Lawver, L.A. & Murphy, J.B. 2000. Plumes, orogenesis, and supercontinental fragmentation. *Earth and Planetary Science Letters*, **178**, 1–11, [https://doi.org/10.1016/S0012-821X\(00\)00061-3](https://doi.org/10.1016/S0012-821X(00)00061-3).
- Donelick, R.A. 1993. Method of Fission Track Analysis Utilizing Bulk Chemical Etching of Apatite. 35.
- Donelick, R.A., Ketcham, R.A. & Carlson, W.D. 1999. Variability of apatite fission-track annealing kinetics; II, Crystallographic orientation effects. *American Mineralogist*, **84**, 1213–1223, <https://doi.org/10.2138/am-1999-0901>.
- Donelick, R.A., O'Sullivan, P.B. & Ketcham, R.A. 2005. Apatite Fission-Track Analysis. In: Reiners, P. W. & Ehlers, T. A. (eds) *Low-Temperature Thermochronology: Techniques, Interpretations, and Applications*. Mineralogical Society of America, 49–94.
- Farley, K.A. 2000. Helium diffusion from apatite: General behavior as illustrated by Durango fluorapatite. *Journal of Geophysical Research: Solid Earth*, **105**, 2903–2914, <https://doi.org/10.1029/1999JB900348>.
- Farley, K.A., Wolf, R.A. & Silver, L.T. 1996. The effects of long alpha-stopping distances on (U-Th)/He ages. *Geochimica et Cosmochimica Acta*, **60**, 4223–4229, [https://doi.org/10.1016/S0016-7037\(96\)00193-7](https://doi.org/10.1016/S0016-7037(96)00193-7).
- Fernandes, L.A.D., Menegat, R., et al. 1995. Evolução Tectônica do Cinturão Dom Feliciano no Escudo Sul-Rio-Grandense: Parte 1 - Uma Contribuição a Partir do Registro Geológico. *Revista Brasileira de Geociências*, **25**, 351–374, <https://doi.org/10.25249/0375-7536.1995351374>.
- Fleischer, R.L., Price, P.B. & Walker, R.M. 1975. *Nuclear Tracks in Solids: Principles and Applications*. California, University of California Press.
- Florisbal, L.M., Heaman, L.M., Janasi, V. de A. & Bitencourt, M. de F. 2014. Tectonic significance of the Florianópolis Dyke Swarm, Paraná–Etendeka Magmatic Province: A reappraisal based on precise U–Pb dating. *Journal of Volcanology and Geothermal Research*, **289**, 140–150, <https://doi.org/10.1016/j.jvolgeores.2014.11.007>.
- Flowers, R.M. 2009. Exploiting radiation damage control on apatite (U–Th)/He dates in cratonic regions. *Earth and Planetary Science Letters*, **277**, 148–155, <https://doi.org/10.1016/j.epsl.2008.10.005>.
- Flowers, R.M. & Kelley, S.A. 2011. Interpreting data dispersion and ‘inverted’ dates in apatite (U–Th)/He and fission-track datasets: An example from the US midcontinent. *Geochimica et Cosmochimica Acta*, **75**, 5169–5186, <https://doi.org/10.1016/j.gca.2011.06.016>.
- Flowers, R.M., Shuster, D.L., Wernicke, B.P. & Farley, K.A. 2007. Radiation damage control on apatite (U–Th)/He dates from the Grand Canyon region, Colorado Plateau. *Geology*, **35**, 447, <https://doi.org/10.1130/G23471A.1>.
- Flowers, R.M., Ketcham, R.A., Shuster, D.L. & Farley, K.A. 2009. Apatite (U–Th)/He thermochronometry using a radiation damage accumulation and annealing model. *Geochimica et Cosmochimica Acta*, **73**, 2347–2365, <https://doi.org/10.1016/j.gca.2009.01.015>.

- Galbraith, R.F. 1981. On statistical models for fission track counts. *Journal of the International Association for Mathematical Geology*, **13**, 471–478, <https://doi.org/10.1007/BF01034498>.
- Galbraith, R.F. & Green, P.F. 1990. Estimating the component ages in a finite mixture. *International Journal of Radiation Applications and Instrumentation. Part D. Nuclear Tracks and Radiation Measurements*, **17**, 197–206, [https://doi.org/10.1016/1359-0189\(90\)90035-V](https://doi.org/10.1016/1359-0189(90)90035-V).
- Galbraith, R.F., Laslett, G.M., Green, P.F. & Duddy, I.R. 1990. Apatite fission track analysis: geological thermal history analysis based on a three-dimensional random process of linear radiation damage. *Philosophical Transactions of the Royal Society of London. Series A: Physical and Engineering Sciences*, **332**, 419–438, <https://doi.org/10.1098/rsta.1990.0124>.
- Gallagher, K. 2012. Transdimensional inverse thermal history modeling for quantitative thermochronology. *Journal of Geophysical Research: Solid Earth*, **117**, 1–16, <https://doi.org/10.1029/2011JB008825>.
- Gallagher, K., Hawkesworth, C.J. & Mantovani, M.S.M. 1994. The denudation history of the onshore continental margin of SE Brazil inferred from apatite fission track data. *Journal of Geophysical Research: Solid Earth*, **99**, 18117–18145, <https://doi.org/10.1029/94JB00661>.
- Gallagher, K., Hawkesworth, C.. & Mantovani, M.S.. 1995. Denudation, fission track analysis and the long-term evolution of passive margin topography: application to the southeast Brazilian margin. *Journal of South American Earth Sciences*, **8**, 65–77, [https://doi.org/10.1016/0895-9811\(94\)00042-Z](https://doi.org/10.1016/0895-9811(94)00042-Z).
- Gallagher, K., Brown, R. & Johnson, C. 1998. Fission track analysis and its applications to geological problems. *Annual Reviews of Earth and Planetary Sciences*, **26**, 519–572, <https://doi.org/10.1146/annurev.earth.26.1.519>.
- Gallagher, K., Charvin, K., Nielsen, S., Sambridge, M. & Stephenson, J. 2009. Markov chain Monte Carlo (MCMC) sampling methods to determine optimal models, model resolution and model choice for Earth Science problems. *Marine and Petroleum Geology*, **26**, 525–535, <https://doi.org/10.1016/j.marpetgeo.2009.01.003>.
- Gastal, M. do C.P., Lafon, J.M., Hartmann, L.A. & Koester, E. 2005. Sm–Nd isotopic compositions as a proxy for magmatic processes during the Neoproterozoic of the southern Brazilian shield. *Journal of South American Earth Sciences*, **18**, 255–276, <https://doi.org/10.1016/j.jsames.2004.11.009>.
- Gaucher, C., Frei, R., et al. 2011. Mesoproterozoic evolution of the Río de la Plata Craton in Uruguay: At the heart of Rodinia? *International Journal of Earth Sciences*, **100**, 273–288, <https://doi.org/10.1007/s00531-010-0562-x>.
- Gleadow, A.J.W. 1981. Fission-track dating methods: What are the real alternatives? *Nuclear Tracks*, **5**, 3–14, [https://doi.org/10.1016/0191-278X\(81\)90021-4](https://doi.org/10.1016/0191-278X(81)90021-4).
- Gleadow, A.J.W., Duddy, I.R., Green, P.F. & Lovering, J.F. 1986a. Confined fission track lengths in apatite: a diagnostic tool for thermal history analysis. *Contributions to Mineralogy and Petrology*, **94**, 405–415, <https://doi.org/10.1007/BF00376334>.
- Gleadow, A.J.W., Duddy, I.R., Green, P.F. & Hegarty, K.A. 1986b. Fission track lengths in the apatite annealing zone and the interpretation of mixed ages. *Earth and Planetary Science Letters*, **78**, 245–254, [https://doi.org/10.1016/0012-821X\(86\)90065-8](https://doi.org/10.1016/0012-821X(86)90065-8).

- Glorie, S., Agostino, K., et al. 2017. Thermal history and differential exhumation across the Eastern Musgrave Province, South Australia: Insights from low-temperature thermochronology. *Tectonophysics*, **703–704**, 23–41, <https://doi.org/10.1016/j.tecto.2017.03.003>.
- Goddéris, Y., Donnadieu, Y., Carretier, S., Aretz, M., Dera, G., Macouin, M. & Regard, V. 2017. Onset and ending of the late Palaeozoic ice age triggered by tectonically paced rock weathering. *Nature Geoscience*, **10**, 382–386, <https://doi.org/10.1038/ngeo2931>.
- Green, P.F. 1986. On the thermo-tectonic evolution of Northern England: Evidence from fission track analysis. *Geological Magazine*, **123**, 493–506, <https://doi.org/10.1017/S0016756800035081>.
- Green, P.F. & Duddy, I. 2018. Apatite (U-Th-Sm) / He thermochronology on the wrong side of the tracks. *488*, 21–33, <https://doi.org/10.1016/j.chemgeo.2018.04.028>.
- Green, P.F. & Duddy, I.R. 2006. Interpretation of apatite (U–Th)/He ages and fission track ages from cratons. *Earth and Planetary Science Letters*, **244**, 541–547, <https://doi.org/10.1016/j.epsl.2006.02.024>.
- Green, P.F., Duddy, I., Gleadow, A.J., Tingate, P. & Laslett, G. 1986. Thermal annealing of fission tracks in apatite. *Chemical Geology: Isotope Geoscience section*, **59**, 237–253, [https://doi.org/10.1016/0168-9622\(86\)90074-6](https://doi.org/10.1016/0168-9622(86)90074-6).
- Guenther, W.R., Reiners, P.W., Ketcham, R.A., Nasdala, L. & Giester, G. 2013. Helium diffusion in natural zircon: radiation damage, anisotropy, and the interpretation of zircon (U–TH)/He thermochronology. *American Journal of Science*, **313**, 145–198, <https://doi.org/10.2475/03.2013.01>.
- Hackspacher, P.C., Ribeiro, L.F.B., Ribeiro, M.C.S., Fetter, A.H., Hadler Neto, J.C., Tello, C.E.S. & Dantas, E.L. 2004. Consolidation and break-up of the South American Platform in southeastern Brazil: Tectonothermal and denudation histories. *Gondwana Research*, **7**, 91–101, [https://doi.org/10.1016/S1342-937X\(05\)70308-7](https://doi.org/10.1016/S1342-937X(05)70308-7).
- Hackspacher, P.C., Godoy, D., Ribeiro, L.F.B., Hadler Neto, J.C. & Franco, A.O.B. 2007. Modelagem térmica e geomorfologia da borda sul do Cráton do São Francisco: termocronologia por traços de fissão em apatita. *Brazilian Journal of ...*, **37**, 76–86.
- Hall, J.W., Glorie, S., Collins, A.S., Reid, A., Evans, N., McInnes, B.I.A. & Foden, J. 2016. Exhumation history of the Peake and Denison Inliers: insights from low-temperature thermochronology. *Australian Journal of Earth Sciences*, **63**, 805–820, <https://doi.org/10.1080/08120099.2016.1253615>.
- Hartmann, L.A., Leite, J.A.D., et al. 2000. Advances in SHRIMP geochronology and their impact on understanding the tectonic and metallogenic evolution of southern Brazil. *Australian Journal of Earth Sciences*, **47**, 829–844, <https://doi.org/10.1046/j.1440-0952.2000.00815.x>.
- Hartmann, L.A., Campal, N., Santos, J.O.S., McNaughton, N.J., Bossi, J., Schipilov, A. & Lafon, J.M. 2001. Archean crust in the Rio de la Plata Craton, Uruguay - SHRIMP U-Pb zircon reconnaissance geochronology. *Journal of South American Earth Sciences*, **14**, 557–570, [https://doi.org/10.1016/S0895-9811\(01\)00055-4](https://doi.org/10.1016/S0895-9811(01)00055-4).
- Hartmann, L.A., Chemale, F. & Philipp, R.P. 2007. Evolução Geotectônica do Rio Grande do Sul no Precambriano. In: Iannuzzi, R. & Frantz, J. C. (eds) *50 Anos de Geologia*. Porto Alegre, Editora Comunicação e Identidade.
- Hartmann, L.A., Liu, D., Wang, Y., Massonne, H.-J. & Santos, J.O.S. 2008. Protolith age of Santa Maria Chico granulites dated on zircons from an associated amphibolite-facies granodiorite in

- southernmost Brazil. *Anais da Academia Brasileira de Ciências*, **80**, 543–551, <https://doi.org/10.1590/S0001-37652008000300014>.
- Hartmann, L.A., Lopes, W.R. & Savian, J.F. 2016. Integrated evaluation of the geology, aerogammaspectrometry and aeromagnetometry of the Sul-Riograndense Shield, southernmost Brazil. *Anais da Academia Brasileira de Ciências*, **88**, 75–92, <https://doi.org/10.1590/0001-3765201520140495>.
- Hasui, Y. 2010. A grande colisão Pré-Cambrian do sudeste brasileiro e a estruturação regional. *Geociências - UNESP*, **29**, 141–169.
- Hasui, Y. 2012. Sistema Orogenico Mantiqueira. In: Hasui, Y., Carneiro, C. D. R., Almeida, F. F. M. de & Bartorelli, A. (eds) *Geologia Do Brasil*. São Paulo, Editora Beca, 331–373.
- Hiruma, S.T., Riccomini, C., Modenesi-Gauttieri, M.C., Hackspacher, P.C., Neto, J.C.H. & Franco-Magalhães, A.O.B. 2010. Denudation history of the Bocaina Plateau, Serra do Mar, southeastern Brazil: Relationships to Gondwana breakup and passive margin development. *Gondwana Research*, **18**, 674–687, <https://doi.org/10.1016/j.gr.2010.03.001>.
- Hoernle, K., Rohde, J., Hauff, F., Garbe-Schönberg, D., Homrighausen, S., Werner, R. & Morgan, J.P. 2015. How and when plume zonation appeared during the 132Myr evolution of the Tristan Hotspot. *Nature Communications*, **6**, <https://doi.org/10.1038/ncomms8799>.
- Hueck, M., Oriolo, S., et al. 2017. Phanerozoic low-temperature evolution of the Uruguayan Shield along the South American passive margin. *Journal of the Geological Society of London*, <https://doi.org/10.1144/jgs2016-101>.
- Hueck, M., Dunkl, I., Heller, B., Angelo, M., Basei, S. & Siegesmund, S. 2018a. (U-Th)/ He Thermochronology and Zircon Radiation Damage in the South American Passive Margin : Thermal Overprint of the Paraná LIP ? 1–18, <https://doi.org/10.1029/2018TC005041>.
- Hueck, M., Oyhantçabal, P., Philipp, R.P., Angelo, M., Basei, S. & Siegesmund, S. 2018b. *The Dom Feliciano Belt in Southern Brazil and Uruguay*. Siegesmund, S., Basei, M. A. S., Oyhantçabal, P. & Oriolo, S. (eds). Cham, Springer International Publishing, Regional Geology Reviews, <https://doi.org/10.1007/978-3-319-68920-3>.
- Hurford, A.J. 1990. Standardization of Fission-Track Dating Calibration - Recommendation by the Fission-Track Working Group of the IUGS Subcommission on Geochronology. *Chemical Geology*, **80**, 171–178 ST-Standardization of Fission-Track Dat.
- Hurford, A.J. & Green, P.F. 1983. The zeta age calibration of fission-track dating. *Chemical Geology*, **41**, 285–317, [https://doi.org/10.1016/S0009-2541\(83\)80026-6](https://doi.org/10.1016/S0009-2541(83)80026-6).
- Hurter, S.J. & Pollack, H.N. 1996. Terrestrial heat flow in the Parana Basin, southern Brazil. *Journal of Geophysical Research*, **101**, 8659–8671, <https://doi.org/10.1029/95jb03743>.
- Jelinek, A.R., Cezar, A., Neto, B. & Poupeau, G. 2003. Análise Por Traços De Fissão Em Apatitas Do Distrito Fluorítico De Santa Catarina : Relações Entre Hidrotermalismo E Evolução Da Margem Continental. *Recherche*, **33**, 289–298.
- Jelinek, A.R., Chemale, F., van der Beek, P.A., Guadagnin, F., Cupertino, J.A. & Viana, A. 2014. Denudation history and landscape evolution of the northern East-Brazilian continental margin from apatite fission-track thermochronology. *Journal of South American Earth Sciences*, **54**, 158–181, <https://doi.org/10.1016/j.jsames.2014.06.001>.

- Karl, M., Glasmacher, U.A., Kollenz, S., Franco-Magalhaes, A.O.B., Stockli, D.F. & Hackspacher, P.C. 2013. Evolution of the South Atlantic passive continental margin in southern Brazil derived from zircon and apatite (U-Th-Sm)/He and fission-track data. *Tectonophysics*, **604**, 224–244, <https://doi.org/10.1016/j.tecto.2013.06.017>.
- Kasanzu, C.H. 2017. Geoscience Frontiers Apatite fission track and (U-Th) / He thermochronology from the Archean Tanzania Craton : Contributions to cooling histories of Tanzanian basement rocks. *Geoscience Frontiers*, **8**, 999–1007, <https://doi.org/10.1016/j.gsf.2016.09.007>.
- Kasanzu, C.H., Linol, B., Wit, M.J., Brown, R., Persano, C. & Stuart, F.M. 2016. From source to sink in central Gondwana: Exhumation of the Precambrian basement rocks of Tanzania and sediment accumulation in the adjacent Congo basin. 2034–2051, <https://doi.org/10.1002/2016TC004147>.Received.
- Ketcham, R.A., Carter, A., Donelick, R.A., Barbarand, J. & Hurford, A.J. 2007. Improved modeling of fission-track annealing in apatite. *American Mineralogist*, **92**, 799–810, <https://doi.org/10.2138/am.2007.2281>.
- Ksienzyk, A.K., Dunkl, N., Jacobs, J., Fossen, H. & Kohlmann, F. 2014. From orogen to passive margin : constraints from fission track and (U – Th) / He analyses on Mesozoic uplift and fault reactivation in SW Norway.
- Ladeira, F.S.B. 2014. *Gondwana Landscapes in Southern South America*. Rabassa, J. & Ollier, C. (eds). Dordrecht, Springer Netherlands, <https://doi.org/10.1007/978-94-007-7702-6>.
- Lal, D., Rajan, R.S. & Tamhane, A.S. 1969. Chemical Composition of Nuclei of Z > 22 in Cosmic Rays using Meteoritic Minerals as Detectors. *Nature*, **211**, 33–37, <https://doi.org/10.1038/221033a0>.
- Luchi, M.G.L. de, Dopico, C.I.M., Wemmer, K. & Siegesmund, S. 2018. Untangling the Neoproterozoic-Early Paleozoic Tectonic Evolution of the Eastern Sierras Pampeanas Hidden in the Isotopical Record. In: *Geology of Southwest Gondwana*. Springer International Publishing, 433–466., https://doi.org/10.1007/978-3-319-68920-3_16.
- Mandal, S., Fellin, M., Burg, J.-P. & Maden, C. 2015. Geochemistry, Geophysics, Geosystems. 3626–3648, <https://doi.org/10.1002/2015GC005977>.Received.
- Maraschin, A.J., Mizusaki, A.M., Zwingmann, H., Borba, A.W. de & Sbrissa, G.F. 2010. Illite authigenesis in sandstones of the Guaritas Allogroup (Early Paleozoic): Implications for the depositional age, stratigraphy and evolution of the Camaquã Basin (Southern Brazil). *Journal of South American Earth Sciences*, **29**, 400–411, <https://doi.org/10.1016/j.jsames.2009.07.007>.
- Matos, R.M.D. de. 1999. History of the northeast Brazilian rift system: kinematic implications for the break-up between Brazil and West Africa. *Geological Society, London, Special Publications*, **153**, 55–73, <https://doi.org/10.1144/GSL.SP.1999.153.01.04>.
- Meisling, K.E., Cobbold, P.R. & Mount, V.S. 2001. Segmentation of an obliquely rifted margin, Campos and Santos basins,southeastern Brazil *AAPG Bulletin*, **85**, 1903–1924, <https://doi.org/10.1306/8626D0B3-173B-11D7-8645000102C1865D>.
- Milani, E.J. 1997. *Evolução Tectono-Estratigráfica Da Bacia Do Paraná e Seu Relacionamento Com a Geodinâmica Fanerozóica Do Gondwana Sul-Ocidental*. Universidade Federal do Rio Grande do Sul.
- Milani, E.J. & Wit, M.J. De. 2014. Correlations between the classic Paraná and Cape – Karoo sequences of South America and southern Africa and their basin infills flanking the Gondwanides : du Toit

- revisited □and Cape – Karoo Correlations between the classic Parana sequences of South Amer, <https://doi.org/10.1144/SP294.17>.
- Milani, E.J., Melo, J.H.G. de, Souza, P.A. De, Fernandes, L.A. & França, A.B. 2007. Bacia do Paraná. *Boletim de Geociências da Petrobras*, **8**, 265–287.
- Miller, D.J., Ketzer, J.M., et al. 2015. Natural gas hydrates in the Rio Grande Cone (Brazil): A new province in the western South Atlantic. *Marine and Petroleum Geology*, **67**, 187–196, <https://doi.org/10.1016/j.marpetgeo.2015.05.012>.
- Montañez, I.P. & Poulsen, C.J. 2013. The Late Paleozoic Ice Age: An Evolving Paradigm. *Annual Review of Earth and Planetary Sciences*, **41**, 629–656, <https://doi.org/10.1146/annurev.earth.031208.100118>.
- Müller, R.D., Hassan, R., Gurnis, M., Flament, N. & Williams, S.E. 2018. Dynamic topography of passive continental margins and their hinterlands since the Cretaceous. *Gondwana Research*, **53**, 225–251, <https://doi.org/10.1016/j.gr.2017.04.028>.
- Murray, K.E., Orme, D.A. & Reiners, P.W. 2014. Effects of U–Th-rich grain boundary phases on apatite helium ages. *Chemical Geology*, **390**, 135–151, <https://doi.org/10.1016/j.chemgeo.2014.09.023>.
- Nürnberg, D. & Müller, R.D. 1991. The tectonic evolution of the South Atlantic from Late Jurassic to present. *Tectonophysics*, **191**, 27–53, [https://doi.org/10.1016/0040-1951\(91\)90231-G](https://doi.org/10.1016/0040-1951(91)90231-G).
- Oliveira, C.H.E. de, Chemale, F., Jelinek, A.R., Bicca, M.M. & Philipp, R.P. 2014. U-Pb and Lu-Hf isotopes applied to the evolution of the late to post-orogenic transtensional basins of the dom feliciano belt, Brazil. *Precambrian Research*, **246**, 240–255, <https://doi.org/10.1016/j.precamres.2014.03.008>.
- Oliveira, C.H.E. de, Jelinek, A.R., Chemale, F. & Bernet, M. 2016. Evidence of post-Gondwana breakup in Southern Brazilian Shield: Insights from apatite and zircon fission track thermochronology. *Tectonophysics*, **666**, 173–187, <https://doi.org/10.1016/j.tecto.2015.11.005>.
- Oriolo, S., Oyhantçabal, P., Basei, M.A.S., Wemmer, K. & Siegesmund, S. 2016. The Nico Pérez Terrane (Uruguay): From Archean crustal growth and connections with the Congo Craton to late Neoproterozoic accretion to the Río de la Plata Craton. *Precambrian Research*, **280**, 147–160, <https://doi.org/10.1016/j.precamres.2016.04.014>.
- Oriolo, S., Hueck, M., Oyhantçabal, P., Goscombe, B., Wemmer, K. & Siegesmund, S. 2018. Shear Zones in Brasiliano-Pan-African Belts and Their Role in the Amalgamation and Break-Up of Southwest Gondwana. In: *Geology of Southwest Gondwana*. Springer International Publishing, 593–613., <https://doi.org/10.1007/978-3-319-68920-3>.
- Paim, P.S.G., Chemale, F. & Wildner, W. 2014. Estágios Evolutivos da Bacia do Camaguã (RS). *Ciência e Natura*, **36**, 1–11, <https://doi.org/10.5902/2179460X13748>.
- Pankhurst, R.J., Rapela, C.W., Fanning, C.M. & Márquez, M. 2006. Gondwanide continental collision and the origin of Patagonia. *Earth-Science Reviews*, **76**, 235–257, <https://doi.org/10.1016/j.earscirev.2006.02.001>.
- Persano, C., Stuart, F.M., Bishop, P. & Barfod, D.N. 2002. Apatite (U-Th)/ He age constraints on the development of the Great Escarpment on the southeastern Australian passive margin. **200**, 79–90.
- Philipp, R.P., Machado, R. & Jr, Chemale, F. 2003. Reavaliação e novos dados geocronológicos (Ar/Ar, Rb/Sr e Sm/Nd) do Batólito Pelotas no Rio Grande do Sul: implicações petrogenéticas e idade de

- reativação das zonas de cisalhamento. *Geologia USP. Série Científica*, **3**, 71–84, <https://doi.org/10.5327/S1519-874X2003000100006>.
- Philipp, R.P., Lusa, M. & Nardi, L.V.S. 2008. Petrology of dioritic, tonalitic and trondhjemite gneisses from Encantadas Complex, Santana da Boa Vista, southernmost Brazil: paleoproterozoic continental-arc magmatism. *Anais da Academia Brasileira de Ciências*, **80**, 735–748, <https://doi.org/10.1590/S0001-37652008000400013>.
- Philipp, R.P., Massonne, H.J. & de Campos, R.S. 2013. Peraluminous leucogranites of the Cordilheira Suite: A record of Neoproterozoic collision and the generation of the Pelotas Batholith, Dom Feliciano Belt, Southern Brazil. *Journal of South American Earth Sciences*, **43**, 8–24, <https://doi.org/10.1016/j.jsames.2012.10.006>.
- Philipp, R.P., Pimentel, M.M. & Chemale, F. 2016. Tectonic evolution of the Dom Feliciano Belt in Southern Brazil: Geological relationships and U-Pb geochronology. *Brazilian Journal of Geology*, **46**, 83–104, <https://doi.org/10.1590/2317-4889201620150016>.
- Price, P.B. & Walker, R.M. 1963. Fossil tracks of charged particles in mica and the age of minerals. *Journal of Geophysical Research*, **68**, 4847–4862, <https://doi.org/10.1029/JZ068i016p04847>.
- Quirk, D.G. & Rüpke, L.H. 2018. Melt-induced buoyancy may explain the elevated rift-rapid sag paradox during breakup of continental plates. *Scientific Reports*, **8**, 9985, <https://doi.org/10.1038/s41598-018-27981-2>.
- Ramos, V.A. 2009. Anatomy and global context of the Andes: Main geologic features and the Andean orogenic cycle. In: Kay, S. M. (ed.) *Backbone of the Americas*. The Geological Society of America, ix, 278 p., [https://doi.org/10.1016/s0895-9811\(02\)00006-8](https://doi.org/10.1016/s0895-9811(02)00006-8).
- Recanati, A., Gautheron, C., et al. 2017. Helium trapping in apatite damage : Insights from (U-Th-Sm) / He dating of different granitoid lithologies. *Tectonophysics*, **470**, 116–131, <https://doi.org/10.1016/j.tecto.2017.09.002>.
- Reiners, P.W. 2005. Zircon (U-Th)/He Thermochronometry. In: *Reviews in Mineralogy and Geochemistry*. 151–179., <https://doi.org/10.2138/rmg.2005.58.6>.
- Reiners, P.W. & Farley, K.A. 2001. Influence of crystal size on apatite (U-Th)/He thermochronology: An example from the Bighorn Mountains, Wyoming. *Earth and Planetary Science Letters*, **188**, 413–420, [https://doi.org/10.1016/S0012-821X\(01\)00341-7](https://doi.org/10.1016/S0012-821X(01)00341-7).
- Reiners, P.W., Farley, K.A. & Hickes, H.J. 2002. He diffusion and (U-Th)/He thermochronometry of zircon: Initial results from Fish Canyon Tuff and Gold Butte. *Tectonophysics*, **349**, 297–308, [https://doi.org/10.1016/S0040-1951\(02\)00058-6](https://doi.org/10.1016/S0040-1951(02)00058-6).
- Reiners, P.W., Spell, T.L., Nicolescu, S. & Zanetti, K.A. 2004. Zircon (U-Th)/He thermochronometry: He diffusion and comparisons with 40Ar/39Ar dating. *Geochimica et Cosmochimica Acta*, **68**, 1857–1887, <https://doi.org/10.1016/j.gca.2003.10.021>.
- Renne, P.R., Deckart, K., Ernesto, M., Feautaud, G. & Piccirillo, E.M. 1996. Age of the Ponta Grossa dike swarm (Brazil), and implications to Paraná flood volcanism. *Earth and Planetary Science Letters*, **144**, 199–211, [https://doi.org/10.1016/0012-821X\(96\)00155-0](https://doi.org/10.1016/0012-821X(96)00155-0).
- Rossetti, L.M., Lima, E.F., Waichel, B.L., Scherer, C.M. & Barreto, C.J. 2014. Stratigraphical framework of basaltic lavas in Torres Syncline main valley, southern Parana-Etendeka Volcanic Province. *Journal of South American Earth Sciences*, **56**, 409–421, <https://doi.org/10.1016/j.jsames.2014.09.025>.

- Saalmann, K., Hartmann, L.A., Remus, M.V.D., Koester, E. & Conceição, R.V. 2005. Sm–Nd isotope geochemistry of metamorphic volcano-sedimentary successions in the São Gabriel Block, southernmost Brazil: evidence for the existence of juvenile Neoproterozoic oceanic crust to the east of the Rio de la Plata craton. *Precambrian Research*, **136**, 159–175, <https://doi.org/10.1016/j.precamres.2004.10.006>.
- Saenz, C.A.T., Hackspacher, P.C., Hadler Neto, J.C., Iunes, P.J., Guedes, S., Ribeiro, L.F.B. & Paulo, S.R. 2003. Recognition of Cretaceous, Paleocene, and Neogene tectonic reactivation through apatite fission-track analysis in Precambrian areas of southeast Brazil: association with the opening of the south Atlantic Ocean. *Journal of South American Earth Sciences*, **15**, 765–774, [https://doi.org/10.1016/S0895-9811\(02\)00131-1](https://doi.org/10.1016/S0895-9811(02)00131-1).
- Scherer, C.M.. 2000. Eolian dunes of the Botucatu Formation (Cretaceous) in southernmost Brazil: morphology and origin. *Sedimentary Geology*, **137**, 63–84, [https://doi.org/10.1016/S0037-0738\(00\)00135-4](https://doi.org/10.1016/S0037-0738(00)00135-4).
- Schmitt, R. da S., Fragoso, R.D.A. & Collins, A.S. 2018. Suturing Gondwana in the Cambrian: The Orogenic Events of the Final Amalgamation. In: *Geology of Southwest Gondwana*. Springer International Publishing, 411–432., https://doi.org/10.1007/978-3-319-68920-3_15.
- Shuster, D.L., Flowers, R.M. & Farley, K.A. 2006. The influence of natural radiation damage on helium diffusion kinetics in apatite. *Earth and Planetary Science Letters*, **249**, 148–161, <https://doi.org/10.1016/j.epsl.2006.07.028>.
- Soares, C.J., Guedes, S., Jonckheere, R., Hadler, J.C., Passarella, S.M. & Dias, A.N.C. 2016. Apatite fission-track analysis of Cretaceous alkaline rocks of Ponta Grossa and Alto Paranaíba Arches, Brazil. *Geological Journal*, **51**, 805–810, <https://doi.org/10.1002/gj.2694>.
- Stica, J.M., Zalán, P. V. & Ferrari, A.L. 2014. The evolution of rifting on the volcanic margin of the Pelotas Basin and the contextualization of the Paraná-Etendeka LIP in the separation of Gondwana in the South Atlantic. *Marine and Petroleum Geology*, **50**, 1–21, <https://doi.org/10.1016/j.marpetgeo.2013.10.015>.
- Stockli, D.F. 2005. Application of low-temperature thermochronometry to extensional tectonic settings. In: Reiners, P. W. & Ehlers, T. A. (eds) *Low-Temperature Thermochronology: Techniques, Interpretations, and Applications*. Mineralogical Society of America, 411–448.
- Tagami, T. & O'Sullivan, P.B. 2005. Fundamentals of fission-track thermochronology. In: Reiners, P. W. & Ehlers, T. A. (eds) *Low-Temperature Thermochronology: Techniques, Interpretations, and Applications*. Mineralogical Society of America, 19–48.
- Turner, S., Regelous, M., Kelley, S., Hawkesworth, C. & Mantovani, M. 1994. Magmatism and continental break-up in the South Atlantic: high precision ^{40}Ar - ^{39}Ar geochronology. *Earth and Planetary Science Letters*, **121**, 333–348, [https://doi.org/10.1016/0012-821X\(94\)90076-0](https://doi.org/10.1016/0012-821X(94)90076-0).
- Vermeesch, P. 2009. RadialPlotter: a Java application for fission track, luminescence and other radial plots. *Radiation Measurement*, 409–410 <http://www.ucl.ac.uk/~ucfbpve/radialplotter/>.
- Wagner, G.A., Gleadow, A.J.W. & Fitzgerald, P.G. 1989. The significance of the partial annealing zone in apatite fission-track analysis: Projected track length measurements and uplift chronology of the transantarctic mountains. *Chemical Geology: Isotope Geoscience section*, **79**, 295–305, [https://doi.org/10.1016/0168-9622\(89\)90035-3](https://doi.org/10.1016/0168-9622(89)90035-3).

- Wildman, M., Brown, R., et al. 2016. The chronology and tectonic style of landscape evolution along the elevated Atlantic continental margin of South Africa resolved by joint apatite fission track and (U-Th-Sm)/He thermochronology. *Tectonics*, **35**, 511–545, <https://doi.org/10.1002/2015TC004042>.
- Wildner, W., Lima, E.F. De, Nardi, L.V.S. & Sommer, C.. 2002. Volcanic cycles and setting in the Neoproterozoic III to Ordovician Camaquã Basin succession in southern Brazil: characteristics of post-collisional magmatism. *Journal of Volcanology and Geothermal Research*, **118**, 261–283, [https://doi.org/10.1016/S0377-0273\(02\)00259-7](https://doi.org/10.1016/S0377-0273(02)00259-7).
- Wildner, W., Ramgrab, G.E., Lopes, R. da C. & Iglesias, C.M. da F. 2008. Mapa Geológico do Estado do Rio Grande do Sul 1:750.000.
- Wolf, R.A., Farley, K.A. & Silver, L.T. 1996. Helium diffusion and low-temperature thermochronometry of apatite. *Geochimica et Cosmochimica Acta*, **60**, 4231–4240, [https://doi.org/10.1016/S0016-7037\(96\)00192-5](https://doi.org/10.1016/S0016-7037(96)00192-5).
- Wolf, R.A., Farley, K.A. & Kass, D.M. 1998. Modeling of the temperature sensitivity of the apatite (U-Th)/He thermochronometer. *Chemical Geology*, **148**, 105–114, [https://doi.org/10.1016/S0009-2541\(98\)00024-2](https://doi.org/10.1016/S0009-2541(98)00024-2).
- Zalán, P. V. 1991. Influence of Pre-Andean Orogenies on the Intracratonic Basins of South America. *Asociación Colombiana de Geólogos y Geofísicos del Petróleo*.
- Zalán, P. V. 2004. Evolução Fanerozóica das Bacias Sedimentares Brasileiras. In: Mantesso-Neto, V., Bartorelli, A., Carneiro, C. D. R. & Neves, B. B. de B. (eds) *Geologia Do Continente Sul-Americano: Evolução Da Obra de Fernando Flávio Marques de Almeida*. Beca Produções Culturais Ltda, 595–612.
- Zerfass, H., Chemale, F., Leandro, C. & Lavina, E. 2004. Tectonics and sedimentation in Southern South America during Triassic. *Tectonics*, **166**, 265–292, <https://doi.org/10.1016/j.tecto.2003.12.008>.

6.11 Email de publicação

Segue abaixo a confirmação de publicação do artigo no periódico *Journal of the Geological Society*.

L lcgsi-mailer@alerts.stanford.edu
Mon 11/11/2019 11:35
SILVEIRA LUIZ MACHADO, JOAO PACIFICO (PGR); eprints@geolsoc.org.uk ↗
CAUTION: This email contains web links. Do NOT click on these links unless you recognise the sender and know the content is safe.

Dear author,

As a thank you for your contribution to Journal of the Geological Society, we are pleased to provide you with PDF e-prints of your recently published paper. These e-prints are available from the following URL:
<http://jgs.lyellcollection.org/cgi/reprint/176/6/1056.pdf?ijkey=lmmk6JA0mYgzRET&keytype=finite>

Please note the following important points:

1. Unless your article is published as Open Access, these e-prints may NOT be used for commercial purposes or posted on openly accessible websites, and are subject to the terms and conditions described here: https://www.geolsoc.org.uk/author_terms. For information about the use of Open Access articles please visit: <https://www.geolsoc.org.uk/Open-Access#whatcanido>
2. Please forward this message to your co-authors so that they can access the paper (they will not get a separate email).
3. You may also share the article with colleagues for legitimate research purposes. More information can be found here: <https://www.geolsoc.org.uk/sharing>
4. The article URL might break between 2 lines in this email. Please make sure you copy the complete URL into your browser.
5. If you encounter difficulty downloading the PDF, please email us at jgs-feedback@highwire.stanford.edu.
6. You have also been signed up for alerts that will notify you when/if the following events occur:
*Your article is cited by another article hosted by HighWire Press.
*A correction for your article is posted.

Thank you for publishing with the Geological Society - we look forward to the opportunity to work with you again in the future.

Yours sincerely
Geological Society Publishing House team

Apêndices

A1 - Seismostratigraphy of the Pelotas Basin

Nota explicativa

Este apêndice corresponde a um manuscrito em fase avançada de preparação. O texto aqui apresentado foi integrado como um capítulo da tese na University of Aberdeen (UK), por isso há passagens que fazem referência aos resultados de termocronologia. Este manuscrito deverá ser aprimorado e adaptado após a defesa da tese em ambas universidades, contando com as contribuições das bancas de doutorado. O produto final deverá ser submetido a um periódico de nível internacional.

Abstract

The Pelotas Basin is a passive margin continental basin adjacent to Uruguay and southernmost Brazil. It was formed as result of the South Atlantic opening after West Gondwana breakup. To this day no economically viable hydrocarbon reserves have been found in the basin, and its framework and development are still poorly explored. Based on a dataset of seventeen seismic lines and several well logs, and supported by previous studies, a general history of the basin development is presented here. The pre-rift and syn-rift stages are difficult to distinguish due the continuity of the igneous activity responsible for the deposits of these stages. Thick and broad seaward-dipping reflectors suggest intense volcanism during break-up. The post-rift stage corresponds to the main infill of the basin, accumulating more than 7,500 m of sediments in the southern part of the mapped area. This stage was divided into nine seismic units, with variable depositional time frames and sites. The mapping and interpolation of these units allowed estimation of trends, areas and volumes of deposition. An initial shallow water environment with a carbonate platform was developed over the basin area, followed by thermal subsidence and creation of accommodation space, later filled by a thick sedimentary package. Subsidence rates and deposition within the basin decreased until the Palaeocene. Preserved sediments suggest a substantial increase in the deposition rates and volumes after the Eocene. Although cyclic base-level changes and the action of waves and sea currents appear to be the main control over the depositional trends, periods of continental uplift may be related to the observed patterns.

A1.1 Introduction

The proposal of this research assumed a balance between the time and rate of the continental basement exhumation and the Meso-Cenozoic foundation and filling of the adjacent oceanic basin. It was expected that the ZHe data would constrain the beginning of the basement cooling preceding the rift, the AFT data would mark the accelerated uplift during the rift climax, and the AHe data would provide information about the regional exhumation post-rift. Unfortunately, the obtained thermochronometry results in southernmost Brazil and Uruguay do not allow such direct correlation, generally because they are considerably older than the late Mesozoic Pelotas Basin. The ZHe data provide information from the early to middle Palaeozoic, the AFT data constrain mostly the exhumation pre-rift (late Palaeozoic to early Mesozoic), and the AHe data are too disperse and complex to define adequately the late Mesozoic to Cenozoic thermal history of the continental basement.

Nonetheless, an attempt to characterize the basin fill and correlate it to the Cenozoic exhumation of the Uruguayan and Sul-Rio-Grandense shields was made. A semi-qualitative evaluation of the Pelotas Basin volcano-sedimentary deposits can be used to constrain the variation of the depositional rate through time, which in turn could be linked and elucidate the potential influence of the onshore cooling/erosion in the sediment availability. Here the results from a systematic mapping of seismic units across the Pelotas Basin are presented. The seismic investigation was focused between the Rio Grande Terrace (sometimes as Torres Terrace) at north and the Rio Grande Cone at south, along the Rio Grande do Sul state margin, southernmost Brazil (Fig. A1.1).

A1.2 Method and Dataset

The Pelotas Basin does not have 3D seismic surveys, and only a dozen exploration wells were drilled in the basin by the end of the last century. This scarcity of data already represents a challenge to a proper characterization of the basin architecture. The quantity and quality of the data provided by ANP imposed particular obstacles to the development of the analysis. The dataset comprised processed post-stack time-migrated 2D seismic reflection data and some exploration well logs. A 2D seismic reflection dataset was provided by the Agência Nacional de Petróleo, Gás Natural e Biocombustíveis (ANP, Brazil), consisting of six strike and eleven dip seismic lines. The lines sum more than 5,000 km in extension and cover an area of

approximately 229,000 km² (Fig A1.1). This dataset consisted of processed post-stack time-migrated 2D seismic reflection data, with signal usually down to 10,000 ms or less in two-way-travel time (TWT). The grid spacing between the strike lines varies between 25 and 90 km, and between 18 and 120 km for the dip lines. Additionally, data from six exploration wells offshore and three onshore were provided, with an inconsistent variability of logs suites (e.g. gamma ray, sonic, resistivity) in each well. Onshore wells reached less than 1,000 m deep, while the offshore ones reached between 2,300 and 6,200 m deep and were drilled in the shelf portion of the margin. Four wells (2BPS6, 2RSS1, 2RSS2, 1BPS8) intersected the seismic lines within the dataset. Formation well tops and checkshot data were available in the well 2BPS6. Interpretation of the dataset was performed with Petrel Interpretation Software 2017, by Schlumberger.

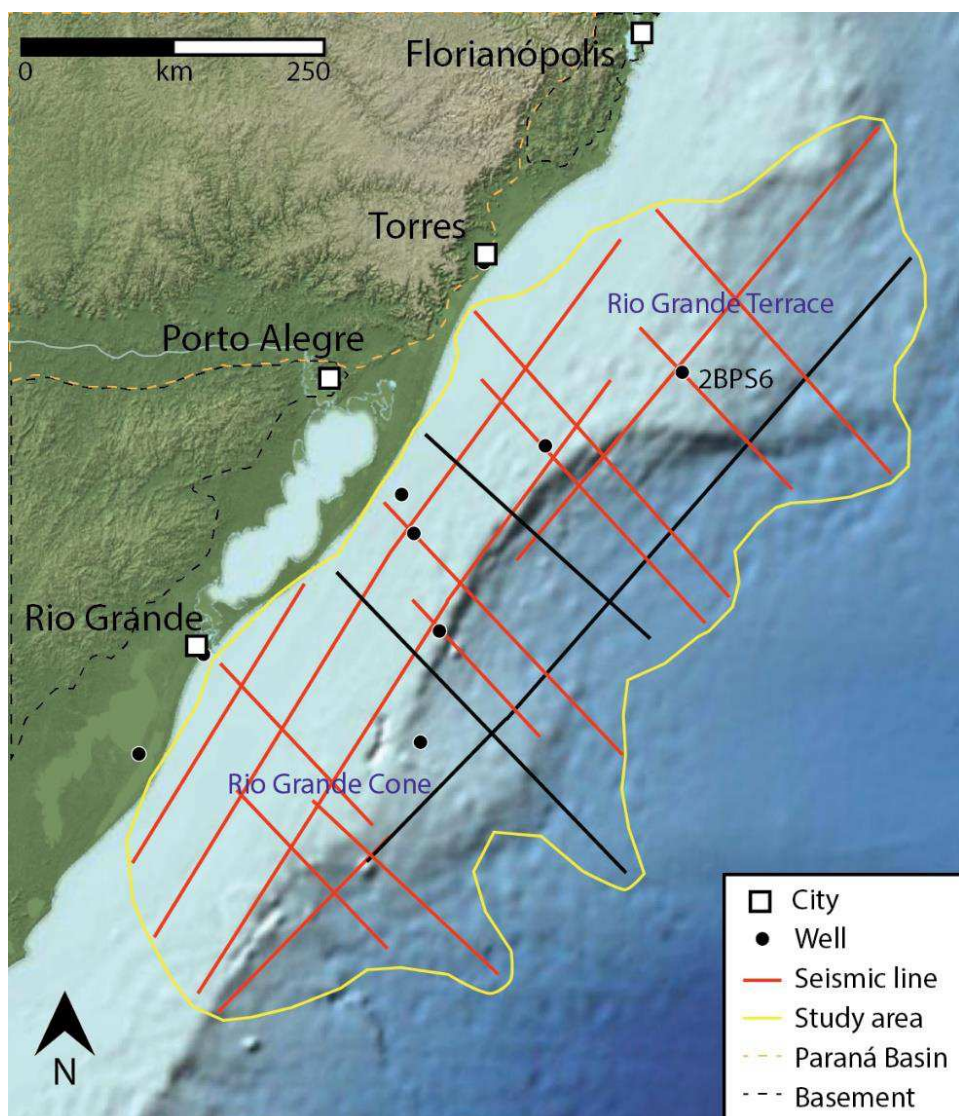


Figure A1.1: Distribution of the dataset along southernmost Brazil, used for the Pelotas Basin analysis. Note the two bathymetric highs, Rio Grande Terrace and Rio Grande Cone, which represent important structures within the basin. Black seismic lines are shown in figures A1.3 and A1.6.

Identification of the seismic horizons was based on the works of Holz *et al.* (2008) and Contreras *et al.* (2010), both of which discuss the seismostratigraphy of the Pelotas Basin. Both studies consider the same seismic line (228-0317), which was also in the dataset of this research and allowed a comparison between them and the present work. Although both studies largely agree in the selected reflectors that limit the seismic units within the basin, there are some differences in the quantity of seismic units and time frame of each of them. Contreras *et al.* (2010) defined fourteen units based on one seismic line (line 228-0317) and six wells, while Holz *et al.* (2008) defined ten units based on 259 seismic lines, nine wells and geophysical data. Assuming that the significantly larger volume of data used by Holz *et al.* (2008) would permit a more refined analysis of the basin, it was used as the main reference during the present analysis of the seismic lines.

The seismic horizons defined by the aforementioned works were extended throughout the seismic lines of this thesis using the loop-tie method, and their positioning was recognized according to the terminations of seismic reflectors. This method of analysis was formalized by Payton (1977) and has been continually refined since then, proving itself successful in the characterization of a basin framework. The fundamental concepts of this method are that seismic reflectors have a temporal connotation, i.e. they represent depositional or erosional surfaces rather than lithological continuous bodies, and that the patterns observed on the terminations (edges) of the seismic reflectors (Fig. A1.2) allow defining the variations of depositional patterns and accommodation space within the basin through time.

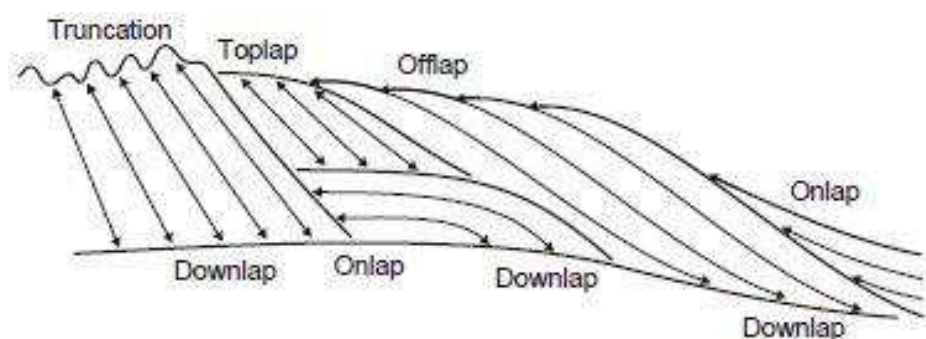


Figure A1.2: Types of seismic reflector terminations. The identification of these patterns allows to infer depositional trends, which reflect variations of the base-level and shoreline shifts. From Catuneanu (2006).

The expansion of the seismic horizons throughout the study area consisted of: 1) recognition and mapping of the seismic horizons on the reference dip line (228-0317); 2) propagation of these seismic horizons to the adjacent dip line through the loop-tie method, done using strike lines that cross both dip lines, the reference one and the

adjacent one; 3) identification of the seismic reflectors terminations against the propagated seismic horizons in the new dip line (the adjacent one), making adjustments in the transported seismic horizons according to the geometry of the new line; 4) mapping of the extrapolated seismic horizons in the entire new line; 5) repeat steps 2 to 4 until cover the whole seismic survey. In the cases where a seismic line intercepts a well, the evaluation of sudden breaks and patterns on the gamma ray and sonic logs of the well were used to support the correct positioning of the seismic horizons.

Amongst the seismic lines provided, those in the dip direction along the Rio Grande Cone had been processed to highlight only the very shallow (1 to 2 ms) stratigraphy, obliterating most of the basin infill underneath, thus being of limited value for the present research purposes. The well information was provided in the outdated *.lis* format, not readable by modern programs used for seismic analysis (e.g. Petrel). To work with the well data, files were converted to the *.dilis* format, a file format that is commonly readable by modern seismic analysis programs. The conversion likely caused the segregation and/or duplication of several logs, and the loading of these logs into the seismic analysis program was not a trivial task. Attempts to use the checkshot data from well 2BPS6 to calibrate the sonic log and improve the time-depth relation were unsuccessful. The obtained time-depth relations from these attempts resulted in basin infill thickness surpassing 11 km, a value not supported by published works. Thus, only the sonic log was used to tie the seismic data with wells and to estimate the depths and thickness of the seismic units identified. The results of the sonic/seismic tie satisfactorily agreed with the works that were used as reference. Having overcome these initial challenges, the dataset provided a good overall coverage of the Pelotas Basin and allowed regional mapping of the seismic units.

A1.3 Seismic units

The seismic units mapped in this work are based on the works from Holz *et al.* (2008) and Contreras *et al.* (2010). Both studies largely agreed in the selected horizons that limit the seismic units within the basin, but there are some differences in the distribution and time frame of each seismic unit (Table A1.1). These divergences may be a consequence of the different datasets used in each work, and indicate the necessity of additional seismic surveys, exploration wells and research within the basin to constrain more precisely the ages and boundaries of each seismic unit.

The analysis of the seismic profiles and well logs available for this work led to the identification of three major seismic successions in the Pelotas Basin: the Pre-, Syn- and Post-rift successions (Fig. A1.3). The Pre-rift Succession includes reflectors of chaotic geometry that represent the undifferentiated basement of the basin. The top surface of this succession is problematic to define, as there is a continuity in the nature of the deposits (mostly igneous) between the Pre- and Syn-rift successions (see Chapter 2, section Rift related basins), thus their limits are often ambiguous. The Syn-rift Succession comprises the half-grabens of the Cassino Formation (recognized in one seismic line with support of well data) and the seaward-dipping reflectors (SDRs) of the Imbituba Formation. Despite the ambiguous transition from the Pre- to the Syn-rift succession, the Syn-rift Succession is somewhat easily recognized because of the nature of its reflectors, usually of high amplitude, subparallel stacking with good lateral continuity, and wedge shapes limited by antithetic faults. The thickening of the wedges against these faults suggest syn-depositional tectonism. This Syn-rift Succession is limited on the top by an angular unconformity, marked by the truncation of the reflectors against an erosional surface. The Post-rift Succession corresponds to almost the entire infill of the Pelotas Basin and lies above the erosional surface that truncates the reflectors below (from the Syn-rift Succession). This Post-rift Succession contains several key surfaces related to cyclic variations on the basin base-level, and it was subdivided into nine seismic units (Table A1.1).

Table A1.1: Comparative between the different interpretations of the seismic units within the Pelotas Basin that were used as reference in this work. Chart not scaled and time interval for each unit is approximated, considering the differences between both works (usually less than 4 Ma for each unit).

Epoch	Holz et al. (2008)	Contreras et al. (2010)	This work	Interval (Ma)	Tectonic context				
Holocene	Seq 4g	SP14	SU9	6	Passive margin				
Pleistocene									
Pliocene		SP13	SU8	6					
Miocene Up									
Miocene Mid	Seq 4f	SP12	SU7	8					
Miocene Low	Seq 4e	SP11	SU6	5					
Oligocene Up	SP10	SU5	10						
Oligocene Low									
Eocene Up	Seq 4c	SP9	SU4	15					
Eocene Mid		SP8							
Eocene Low		SP7							
Palaeocene	Seq 4b	SP6	SU3	15	Carbonate platform				
Maastrichtian	Seq 4a	SP5	SU2	20					
Campanian		SP4							
Santonian									
Coniacian		SU1	25						
Turonian						SP3			
Cenomanian									
Albian									
Aptian	Seq 2	SP2	Syn-rift	15	Rift				
Barremian	Seq 1	SP1	Pre-rift	-	Pre-rift				

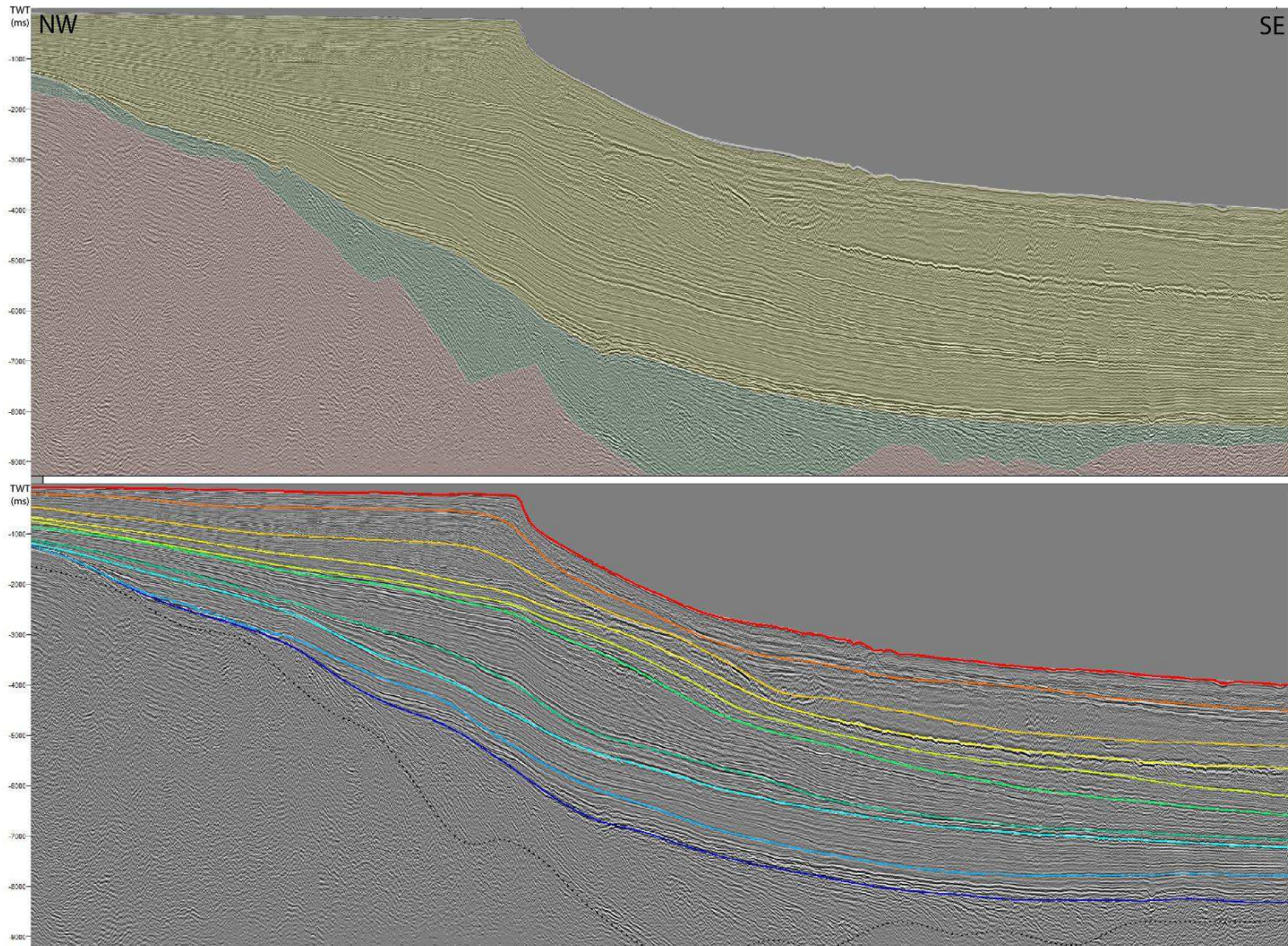


Figure A1.3: Seismic line of dip direction located between the Rio Grande Terrace and Rio Grande Cone. On the top, the red, green and yellow colours represent the Pre-, Syn and Post-rift successions, respectively. On the bottom, the coloured lines represent the top surface of each seismic unit mapped.

The horizons limiting the seismic units represent sequence boundaries related to base-level falls, associated to glacioeustatic cycles and tectonism. These surfaces usually truncate (because of erosion) the unit below them, especially in the shelf region, while the unit developed afterwards, above the surface, often present an onlap pattern on the proximal part of the basin and a downlap towards the slope. Details of each seismic unit are described below:

- SU1: This unit represents the first volcano-sedimentary sequence post-rift, and includes the volcanic rocks of the Curumim Formation, evaporites from the Ariri Formation, and the carbonate and siliciclastic deposits from the Porto Belo and Atlântida formations. These formations are not individualized here, and together they represent an environment of shallow waters (continental to oceanic) that was progressively drowned during a marine transgression. The reflectors within this unit show a vertical variation; usually the bottom ones present high amplitude, low frequency and good lateral continuity, grading upwards to reflectors with lower amplitude but similar continuity. This variation likely is a response to the change of volcanic rocks to carbonate deposits and a progressive increase of clastic sediments with basin drowning;
- SU2: This unit and the following ones correspond to the Imbé and Cidreira formations, both siliciclastic deposits of medium to fine grain and which correspond to the main infill of the Pelotas Basin. The seismic horizons that limit this and the following units correspond to regressive surfaces associated with cycles of base-level rise and fall. Reflectors of the SU2 show medium to low amplitude and frequency, parallelism or minor undulations, and good lateral continuity, with an onlap pattern in the proximal part of the basin;
- SU3: The base of this unit is marked by a bright reflector recognized in most of the seismic lines available. On the proximal part of the basin, reflectors within this unit onlap this basal bright horizon, while in the distal part this unit thins and present low amplitude parallel reflectors;
- SU4: On the shelf part of the basin, reflectors of this unit onlap the regressive surface below, while in the lower slope some downlap terminations were identified. The reflectors present a high amplitude in the shelf and slope, grading to lower amplitudes in the abyssal plain. This unit is relatively thick below the slope;

- SU5: This unit contains reflectors with low to medium amplitude, undulated to laterally continuous, the latter especially in the distal part of the basin. It is the thinner seismic unit mapped, either due to a low rate of deposition or to a pervasive erosional event, and in the shelf and upper slope its reflectors onlap the seismic horizon below;
- SU6: This unit is also thin and poorly preserved. Reflectors show medium to high amplitude, are mostly undulated, have good lateral continuity and onlap on the proximal region against the seismic horizon below;
- SU7: Reflectors within this unit are of medium amplitude, being parallel in the shelf, undulated in the slope and parallel again in the distal part of the basin, where the amplitude of the reflectors also diminishes. This unit highlights the early stages of the development of the Rio Grande Cone, in the southern part of the basin.
- SU8: Reflectors of this unit downlap onto the bottom surface in the shelf, and some onlaps are recognized in the very proximal part of the basin. On the top of the unit offlaps terminations are apparent. While in the proximal region the reflectors present high frequency, medium to high amplitude and their continuity is disrupted by compactional faults, in the distal part reflectors show low amplitude and poor continuity, sometimes of chaotic nature;
- SU9: The top unit of the Pelotas Basin infill, it presents reflectors of high frequency, low amplitude and good lateral continuity, often disrupted by compactional faults. Downlap terminations are common in the shelf and slope, while horizontal reflectors dominate the deep basin. This unit is also affected by sea-bottom simulator reflectors, an indicative of the presence of gas hydrate reserves.

Despite the lack of 3D seismic surveys in the Pelotas Basin, the systematic 2D mapping of the seismic successions/units described above allowed creation of maps of the top surface of each unit throughout the basin. This was done expanding each seismic horizon in the space between adjacent seismic lines. The generated maps were in time unit (ms), but making use of the time-depth relationship obtained from the sonic logs it was possible to estimate the depths in meters. Figure A1.4 shows estimates of the depth to each seismic unit (i.e. to their top surface), which facilitates observing changes in the basin architecture throughout its development.

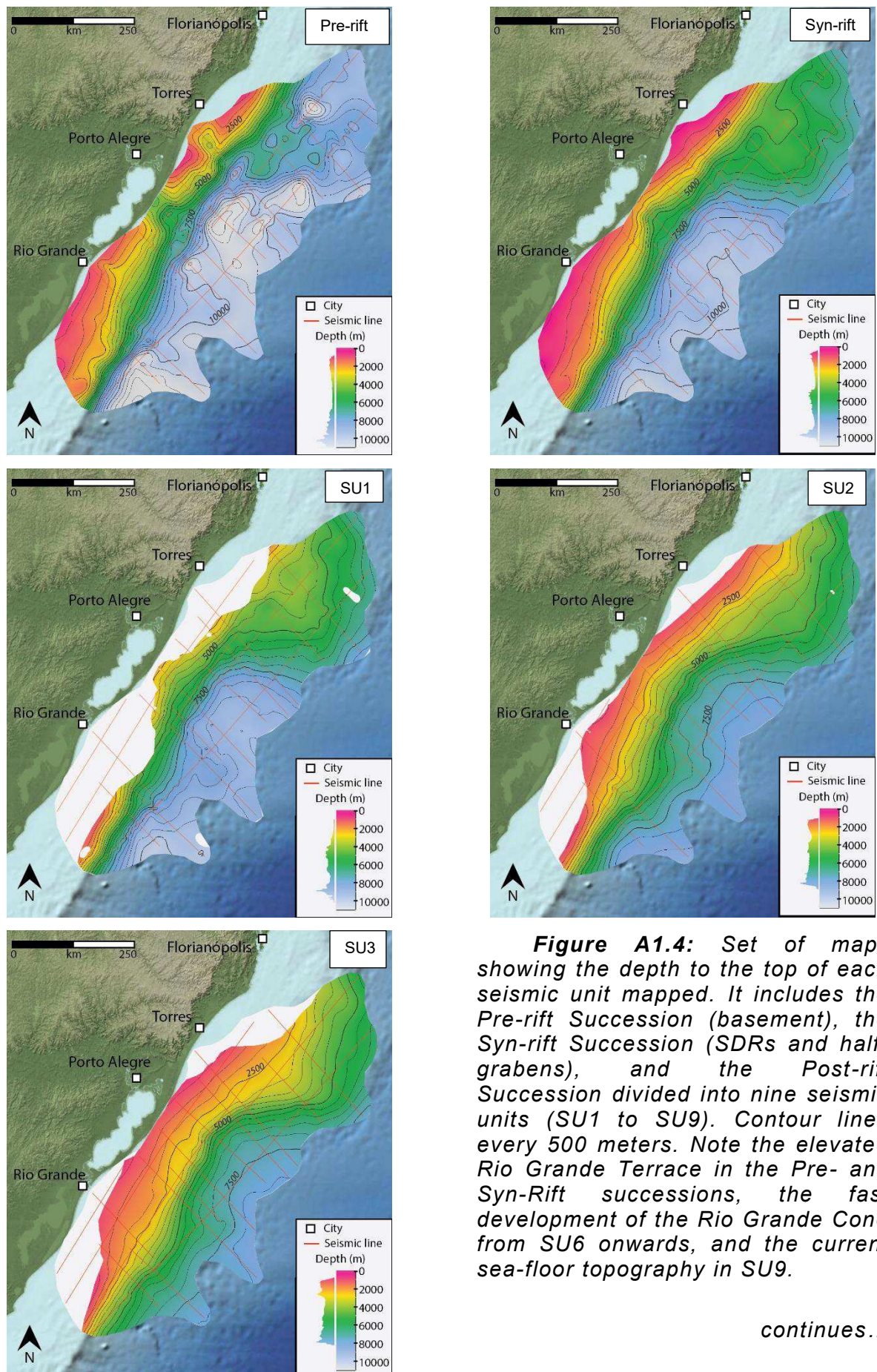
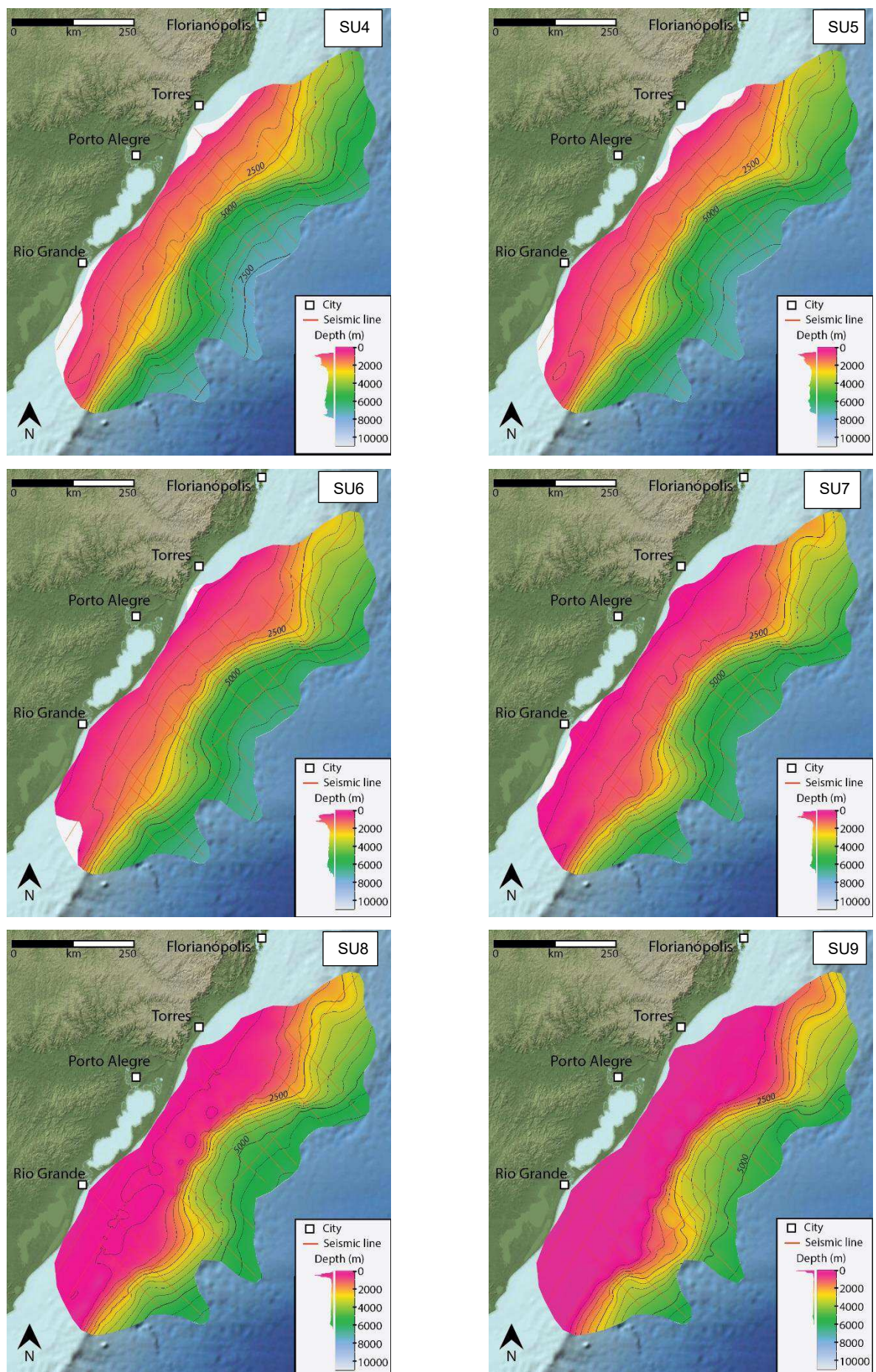


Figure A1.4: Set of maps showing the depth to the top of each seismic unit mapped. It includes the Pre-rift Succession (basement), the Syn-rift Succession (SDRs and half-grabens), and the Post-rift Succession divided into nine seismic units (SU1 to SU9). Contour lines every 500 meters. Note the elevated Rio Grande Terrace in the Pre- and Syn-Rift successions, the fast development of the Rio Grande Cone from SU6 onwards, and the current sea-floor topography in SU9.

continues...



A1.4 Depositional sequences

Each seismic unit defined here (e.g. SU1) is bound by two seismic horizons, thus the sedimentary package limited by these successive horizons correspond to the thickness of the seismic unit in the seismic line analysed. The systematic mapping of these horizons and the interpolation of them between adjacent seismic lines allows estimation of the variability of the thickness of the seismic unit throughout the mapped area. Therefore, the creation of thickness maps (isopach maps) for every seismic unit enables the visualization of spatial and temporal changes in the depocenters of the basin (Fig. A1.5). The isopach maps also permit observing the locations where the sediments of each unit did not accumulate during the unit deposition (bypass zone) or where they were eroded during a base level fall.

In Figure A1.5 it is possible to observe the total thickness of the Pelotas Basin infill and the thickness of each one of the Post-rift succession units (SU1 to SU9). Although the surface map from SU9 in Figure A1.4 shows a fairly uniform sea bottom, Figure A1.5 highlights the variability of the thickness of sediments accumulated in each seismic unit along the mapped area. The thickest volcano-sedimentary succession accumulated since the formation of the Pelotas Basin is located in the southern part of the studied area and represents the Rio Grande Cone, where more than 7,500 meters of the stratigraphic column are preserved.

The transition between the rift and drift regimes started in the basin in the Aptian, when oceanic lithosphere cooling and subsidence led to a base-level rise and to the creation of accommodation space within the basin (Contreras *et al.* 2010). This favoured an initial build-up of carbonates over most of the basin, followed by a fast deepening, especially in the south, and the aggradation/retrogradation terrigenous deposits (Holz *et al.* 2008; Schattner *et al.* 2019).

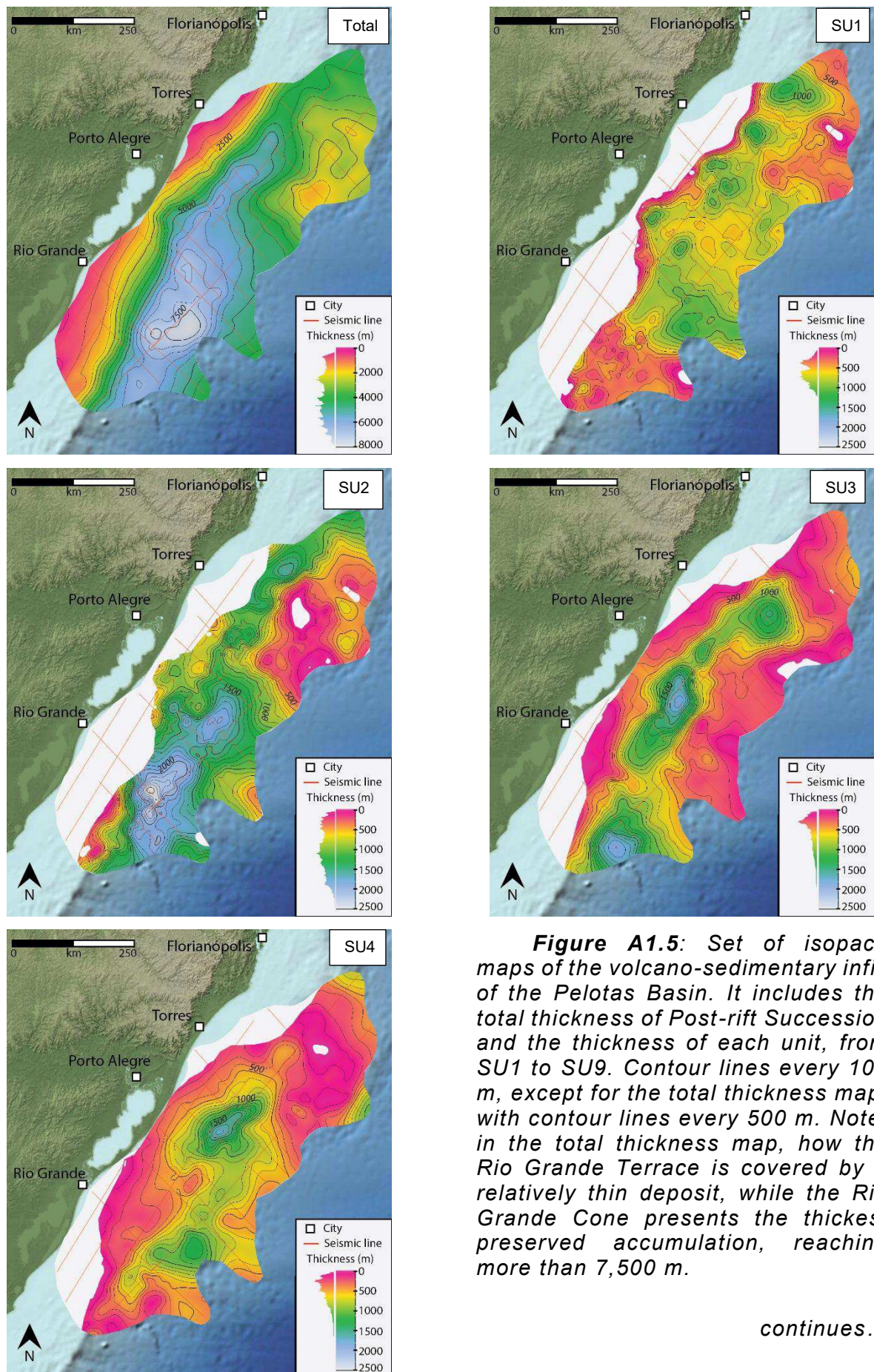
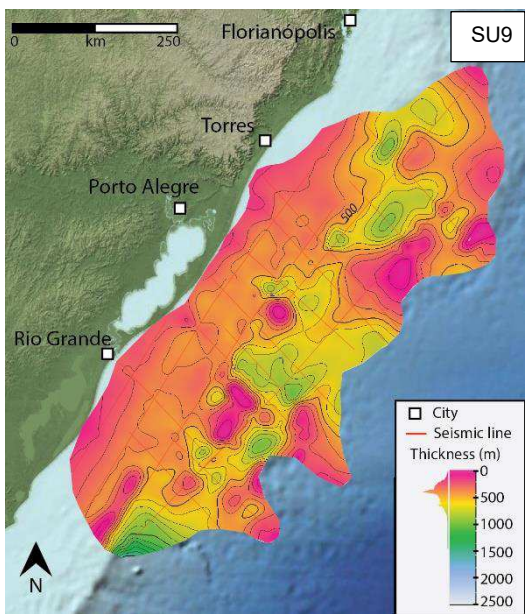
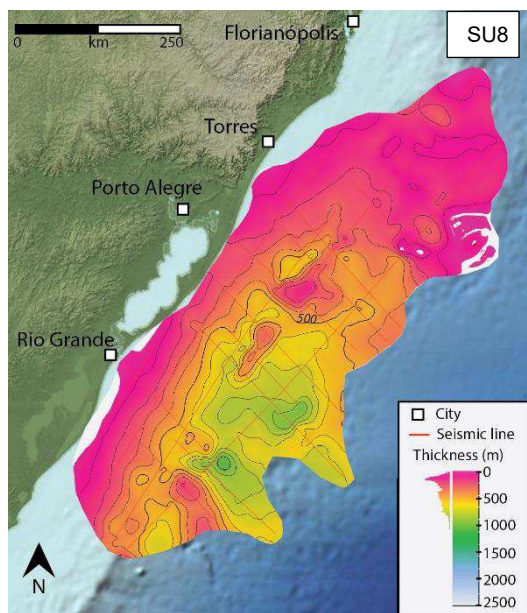
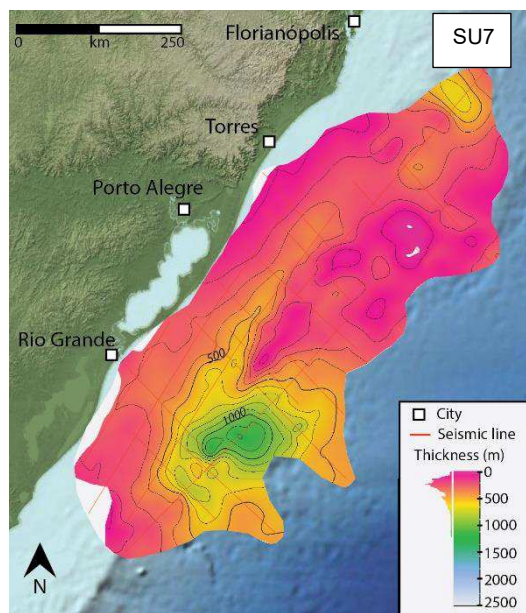
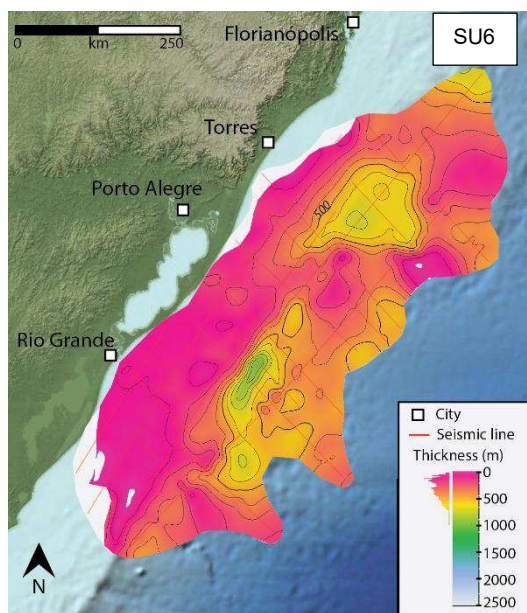
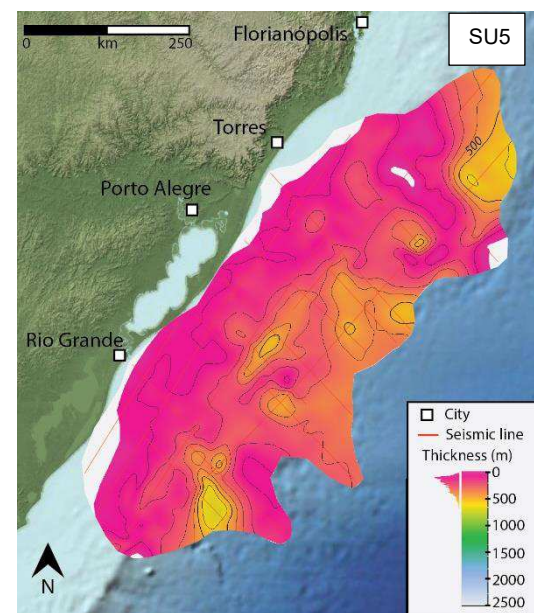


Figure A1.5: Set of isopach maps of the volcano-sedimentary infill of the Pelotas Basin. It includes the total thickness of Post-rift Succession and the thickness of each unit, from SU1 to SU9. Contour lines every 100 m, except for the total thickness map, with contour lines every 500 m. Note, in the total thickness map, how the Rio Grande Terrace is covered by a relatively thin deposit, while the Rio Grande Cone presents the thickest preserved accumulation, reaching more than 7,500 m.

continues...



The subsidence rate decreased during the Late Cretaceous (Contreras *et al.* 2010), but this was accompanied by a global sea-level rise (Haq *et al.* 1987), with transgression of the coast line, which created further accommodation space and maintained the depositional pattern until the Palaeocene (Barboza *et al.* 2008). From the Eocene onwards, the subsidence rate increased, likely favoured by isostasy due to sediment loading, but it was accompanied by a gradual sea level fall and a general regression trend, which led to the development of aggradation/progradation stacking patterns (Holz *et al.* 2008; Barboza *et al.* 2008; Contreras *et al.* 2010; Schattner *et al.* 2019). This general behaviour during the post-rift stage was affected by high frequency base-level changes, which caused the formation of the sequence boundaries mapped between the seismic units.

The deposits within the basin provide insights about variations in the sedimentary supply and tectonic evolution, even though parts of the seismic units were eroded during the cyclic base level falls. The preserved thickness of each seismic unit can be combined with its area to estimate the volume occupied by the deposit, a bulk volume of the unit (Table A1.2). Considering that most of the basin infill is composed of fine siliciclastic sediments, and that porosity decreases with depth due to compaction caused by the overburden pressure, it is necessary to assess the porosity and its variation with depth in the volume estimates. For now, the porosity-depth curves for shales and carbonates from Allen & Allen (2013) and the depth to each seismic unit according to well BPS6 were used to infer the minimum and maximum porosity and volume of each seismic unit. Because of the broad scale of the mapped area and the limited dataset, the calculated values must be carefully considered and should be used more as a semi-qualitative estimate.

Table A1.2: Estimates of the extension of each seismic unit mapped. Area and total volume of the seismic units was obtained from the surface and isopach maps. The total volume considers the seismic unit as a solid block, without any porosity, thus a bulk volume. Depths to each seismic unit based on information from well BPS6. The estimates of the porosity are based on curves of depth against porosity from Allen & Allen (2013). The minimum and maximum volumes refer only to sediments, discounted the inferred porosity. Note the high bulk volume occupied by SU2, deposited in the Late Cretaceous during thermal subsidence of the basin. Seismic units afterwards tend to have lower bulk volumes until SU5, after which they gradually increase. When considering the porosity and the approximate interval of deposition of each seismic unit, a similar pattern is observed, with a decrease of the deposited volumes between SU2 and SU5, followed by a general increase to SU9.

Seismic unit	Area (m ²)	Total volume (m ³)	Depth (m)	Porosity max (%)	Porosity min (%)	Minimum volume (m ³)	Maximum volume (m ³)	Start (Ma)	Interval (Ma)	Vol./Ma (m ³ /Ma)	Vol.min./Ma (m ³ /Ma)	Vol.max./Ma (m ³ /Ma)
SU9	2,28E+11	1,04E+14	-360	55	25	4,66E+13	7,77E+13	6	6	1,73E+13	7,77E+12	1,30E+13
SU8	2,24E+11	8,24E+13	-800	45	13	4,53E+13	7,17E+13	12	6	1,37E+13	7,55E+12	1,19E+13
SU7	2,22E+11	7,77E+13	-1020	40	10	4,66E+13	6,99E+13	20	8	9,71E+12	5,83E+12	8,74E+12
SU6	2,18E+11	6,89E+13	-1390	35	7	4,48E+13	6,40E+13	25	5	1,38E+13	8,95E+12	1,28E+13
SU5	2,16E+11	4,99E+13	-2050	28	5	3,59E+13	4,74E+13	35	10	4,99E+12	3,59E+12	4,74E+12
SU4	1,96E+11	9,52E+13	-2290	25	4	7,14E+13	9,14E+13	50	15	6,35E+12	4,76E+12	6,09E+12
SU3	1,94E+11	1,07E+14	-2730	22	3	8,38E+13	1,04E+14	65	15	7,16E+12	5,59E+12	6,95E+12
SU2	1,72E+11	1,74E+14	-3900	16	2	1,46E+14	1,70E+14	85	20	8,68E+12	7,29E+12	8,51E+12
SU1	1,73E+11	1,09E+14	-4370	17	2	9,04E+13	1,07E+14	113	28	3,89E+12	3,23E+12	3,81E+12

A1.5 Discussion

The tectono-sedimentary evolution of the Pelotas Basin can be inferred from the identification of the seismic horizons and units within it. Spatial and temporal changes in the depositional pattern within the basin, as well as the basement topography above which the volcano-sedimentary succession was deposited, has been observed from the systematic mapping of key seismic horizons. Two features stand out in the during the analysis: the Rio Grande Terrace and the Rio Grande Cone. These two entities are easily recognized in Figure A1.6, which displays an along-strike seismic line that transects almost the entire study region.

In the north of the mapped area, the notable topographic high that precedes the deposition of the Post-rift Succession corresponds to the Rio Grande Terrace (Figs. A1.4 and A1.2. Syn-rift). It can be considered a basement high within the Pelotas Basin, in which the Pre- and Syn-rift successions are of difficult visual distinction. The well BPS6 was drilled on the Terrace and reached volcanic rocks from the Imbituba Formation (Syn-Rift) at 5,368 m. The limit between these igneous rocks and volcanic rocks of the Serra Geral Formation (Paraná Basin) is not clear on the seismic lines. The reflectors under the central part of the Terrace are mostly chaotic, while sub-parallel reflectors appear on the edges of this basement high, often dipping laterally and occasionally bounded by faults (Fig. A1.6). Some of these reflectors might represent intrusions (sills), as they appear to form packages of sub-parallel reflectors in between chaotic ones, but most of them seem to represent subaerial volcanism, related to the SDRs, but with lateral dip, away from the central high. The seismic units from the Post-Rift Succession, above the Imbituba Formation, are usually thinner in the Terrace than in the rest of the basin, and often are eroded on the structure's southern edge.

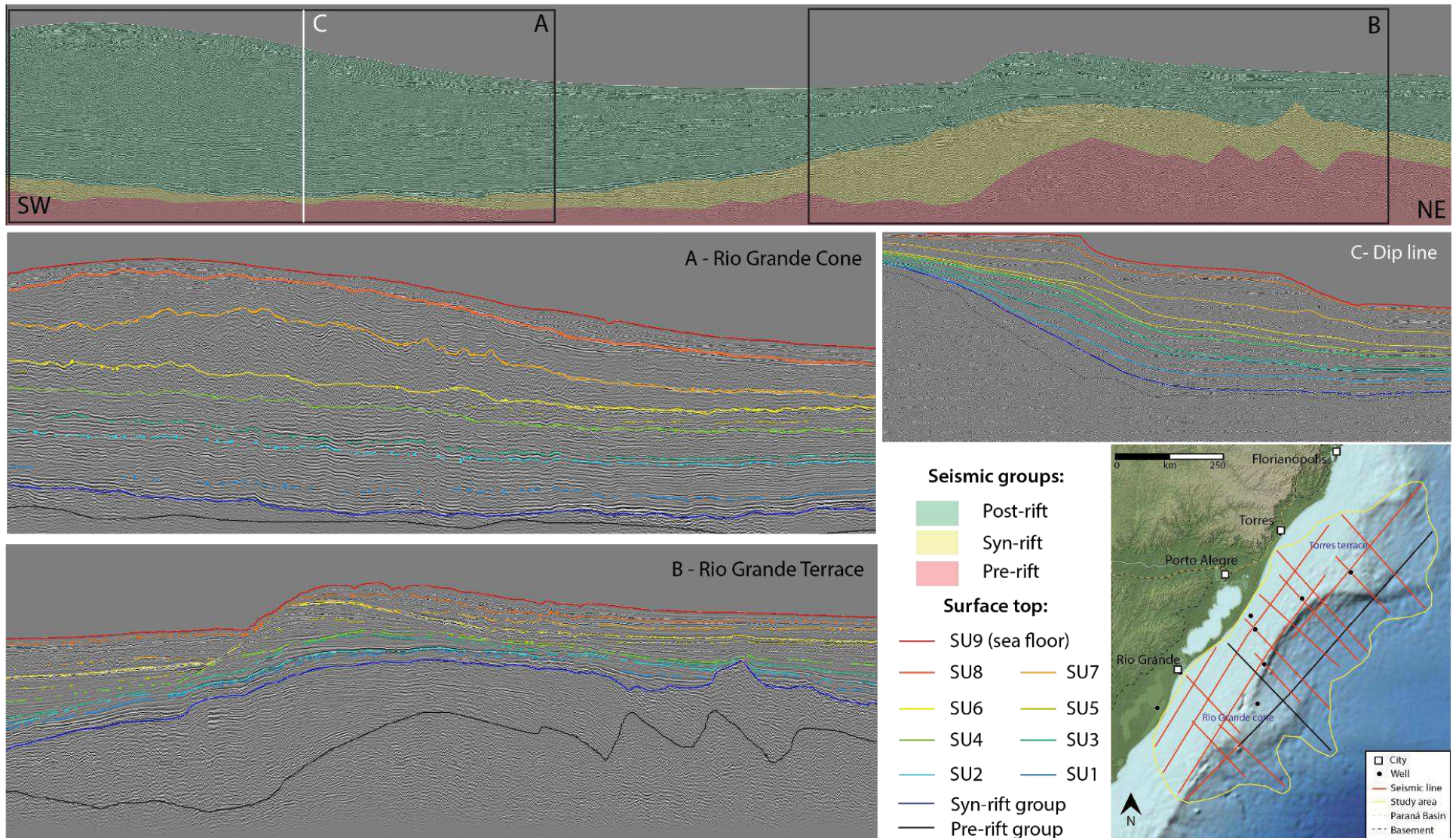


Figure A1.6: Panel of representative seismic lines, indicated as black lines in the mini map. On the top, strike line that cuts the Rio Grande Cone and the Rio Grande Terrace, showing the variable thickness of the seismic successions. On the lower left, details of the two features, showing the seismic horizons mapped as the surface top of each seismic unit. On the right, dip line of the edge from the Rio Grande Cone used for comparison with the works from Holz et al. (2008) and Contreras et al. (2010).

On the other extreme, in the southern part of this seismic line it is possible to identify the Rio Grande Cone, a bathymetric high representative of the volcano-sedimentary package of the Post-Rift Succession. In this region the seismic survey barely images the basement of the basin, and the sedimentary package reaches more than 7,500 m. The mapping of the seismic units within the Rio Grande Cone indicates a thick SU2 in the area and an increase in the sedimentary input after the SU6, which correspond to the seismic units deposited from the Miocene onwards. This result is supported by Schattner *et al.* (2019), who estimates at least 1 km of sedimentary deposition since the Mid-Miocene. Such rapid accumulation probably led to gravitational instability of the sediments (Beglinger *et al.* 2012), which likely caused mass movements that disrupt the seismic reflectors resulting in a chaotic pattern and poor lateral continuity.

The systematic mapping of the seismic units within the Pelotas Basin also allowed definition of the areal distribution and volume of each depositional sequence (Fig. A1.3). Although the obtained values are approximations, they provide insights about the variability of the sediment supply and rate of accumulation (m^3/Ma) in the basin throughout the Cenozoic (Table A1.2). After the formation of SU1, correlated to a shallow water environment (Ceolin *et al.* 2011), the results suggest the deposition of the voluminous SU2 at a high rate in the Late Cretaceous, filling the slope and the southern part of the basin. During this period the basin was thermally subsiding, accompanied by a rise of relative sea-level, which favoured the deposition and preservation of a thick sedimentary package. The following seismic units (SU3 to SU5), deposited until the Oligocene, accumulated mostly in the slope region and show a gradual decrease in their volumes and depositional rates. By the late Oligocene - early Miocene timespan, the depositional rate began to increase, in a trend that persists until the present time and can be observed between seismic units SU6 and SU9. During this time sedimentation prevailed in the southern part of the mapped region, leading to the development of the Rio Grande Cone. Such high sedimentary input in a relatively short period of time probably led to the formation of depositional macroforms, such as deltas, what is suggested by a lateral change in the thickness (depocenters) between SU7 and SU8 (Fig. A1.3). Because of the lack of seismic lines in the region of the Rio Grande Cone, it is not possible to confirm such a geometry.

The geographical nature of the Pelotas Basin must be accounted for during the evaluation of the deposited volumes of each seismic unit. Being open to the sea and with low relief along the coast, the Pelotas Basin has been subject to intense sediment

reworking by the action of sea waves and currents. Several ocean bottom currents act in the region and erode, transport and distribute sediments within the basin (Schattner *et al.* 2019). On the subaerial part of the Pelotas Basin, four lagoon-barrier systems are exposed and were developed in the last 0.5 Ma, probably because of high frequency glacioeustatic cycles (Rosa *et al.* 2017). However, it is suggested that some epeirogenic uplift of the margin might have happened during this time as well (Carreño *et al.* 1999). The apparent increase input of sediments into the basin from the Miocene onwards might not, therefore, be a direct consequence of accelerated uplift and erosion of the continent. In any case, the Miocene increase in the sedimentary input can be tentatively related to continental uplift.

A1.6 Summary & Conclusions

The analysis of seventeen seismic lines permitted evaluation of the framework and development history of the Pelotas Basin. Sequence boundaries were recognized and seismic units were defined, allowing assessment of the intrabasinal depositional patterns. The interpolation of the seismic horizons between seismic lines permitted creation of isopach and surface maps of each seismic unit, which, in turn, allowed easy visualization of spatial and temporal variations during the depositional history of the basin. Moreover, the created maps enabled estimations of the volume and rate of deposition of each seismic unit in a large part of the Pelotas Basin. Despite the limitations and complexity of the dataset available for this work, the obtained results highlight important changes in the basin filling trend during the late Mesozoic and Cenozoic:

- 1) Two bathymetric highs were recognized within the basin, and their origin is very distinct. The northern one corresponds to the Rio Grande Terrace, a basement high developed in the early stages of basin formation. The southern one is the Rio Grande Cone, a sedimentary macroform developed mostly from the Miocene onwards.
- 2) The Rio Grande Terrace represents a topographic obstacle to the deposition and preservation of sediments on the Pelotas Basin, favouring the accumulation of sediments in the southern part of the basin; also it is possibly linked to the Florianópolis High, which bound the Pelotas Basin further north and is a structure that limited the oceanic waters flow to Santos and Campos basins during the Cretaceous, leading to the formation of evaporitic deposits within them.
- 3) The pre- and syn-rift stages of the Pelotas Basin are characterized by intense magmatism, in a way that the transition between both stages is ambiguous in the

seismic images. However, the syn-rift stage is characterized by seaward-dipping reflectors (SDRs) bounded by antithetic faults. The systematic mapping of these faults could possibly be a criterion for defining the limit between both stages.

4) Siliciclastic deposits of the syn-rift stage are very scarce, being recognized only in the proximal part of the basin and with the support of data from an exploration well. The Pelotas Basin was probably above sea-level during this stage, with subaerial magmatism and limited siliciclastic deposition, so most of the basin fill represents post-rift deposition.

5) The post-rift succession includes the vast majority of the volcano-sedimentary infill of the Pelotas Basin. In the southern mapped region, the total thickness surpasses 7,500 meters. The post-rift succession comprises nine seismic units limited by erosive surfaces in the shelf and their correlative units in the deeper basin. These units show variable thicknesses and depocenters, recording changes in the intrabasinal depositional pattern during the Cenozoic.

6) Volumetric estimates suggest an initial low depositional rate, corresponding mostly to carbonate lithologies (SU1). This was followed by siliciclastic sedimentation, with a peak in late Cretaceous (SU2) and a subsequent decrease in the depositional rate until the Eocene (SU2 to SU5). The period between late Cretaceous and Eocene is characterized by a global high sea level, which favoured the creation of accommodation space and the accumulation of the sedimentary packages.

7) After the period of reduction in the sedimentary influx, the deposits suggest a progressive increase in the sedimentation rates from the Oligocene onwards, accumulating mostly in the southern part of the basin.

8) The Pelotas Basin appears to be tectonically inactive during the Cenozoic, and its post-rift deposits might be related mainly to glacioeustatic cycles and ocean bottom currents. However, the increase in the sedimentation rate after the Oligocene might be linked to continental uplift and erosion, providing more sediments to the margin.

A1.7 References

- Allen, P.A. & Allen, J.R. (2013). Basin Analysis: Principles and applications to petroleum play assessment. Wyley-Blackwell, 3rd Edition. United Kingdom.
- Barboza, E. G., Rosa, M. L. C. C., & Ayup-Zouain, R. N. (2008). Cronoestratigrafia da Bacia de Pelotas: uma revisão das seqüências deposicionais. *Gravel*, 6(1), 125-138.
- Beglinger, S. E., Doust, H., & Cloetingh, S. (2012). Relating petroleum system and play development to basin evolution: West African South Atlantic basins. *Marine and Petroleum Geology*, 30(1), 1-25.

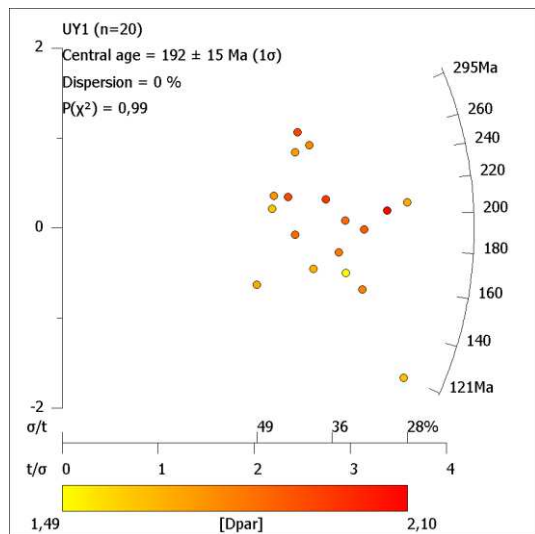
- Carreño, A. L., Coimbra, J. C., & Do Carmo, D. A. (1999). Late Cenozoic sea level changes evidenced by ostracodes in the Pelotas Basin, southernmost Brazil. *Marine Micropaleontology*, 37(2), 117-129.
- Catuneanu, O. (2006). *Principles of sequence stratigraphy*. Elsevier.
- Contreras, J., Zühlke, R., Bowman, S., & Bechstädt, T. (2010). Seismic stratigraphy and subsidence analysis of the southern Brazilian margin (Campos, Santos and Pelotas basins). *Marine and Petroleum Geology*, 27(9), 1952-1980.
- Haq, B. U., Hardenbol, J. A. N., & Vail, P. R. (1987). Chronology of fluctuating sea levels since the Triassic. *Science*, 235(4793), 1156-1167.
- Holz, M. et al. (2008). Reavaliação dos Sistemas Petrolíferos da Bacia de Pelotas. *Projeto BAPEL*. Internal report of ANP (Agência Nacional de Petróleo, Gás Natural e Bicombustíveis), available under request. <http://www.anp.gov.br/exploracao-e-producao-de-oleo-e-gas/estudos-geologicos-e-geofisicos/plano-plurianual-de-estudos-de-geologia-e-geofisica/ppa-2007-2014/resultados-por-bacia>
- Payton, C. E. (Ed.). (1977). Seismic stratigraphy: applications to hydrocarbon exploration (Vol. 26, pp. 1-516). Tulsa, OK: American Association of Petroleum Geologists.
- Rosa, M. L. C. D. C., Barboza, E. G., Abreu, V. D. S., Tomazelli, L. J., & Dillenburg, S. R. (2017). High-Frequency Sequences in the Quaternary of Pelotas Basin (coastal plain): a record of degradational stacking as a function of longer-term base-level fall. *Brazilian Journal of Geology*, 47(2), 183-207.
- Schattner, U., José Lobo, F., López-Quirós, A., dos Passos Nascimento, J. L., & de Mahiques, M. M. (2019). What feeds shelf-edge clinoforms over margins deprived of adjacent land sources? An example from southeastern Brazil. *Basin Research*.

A2 Uruguay data

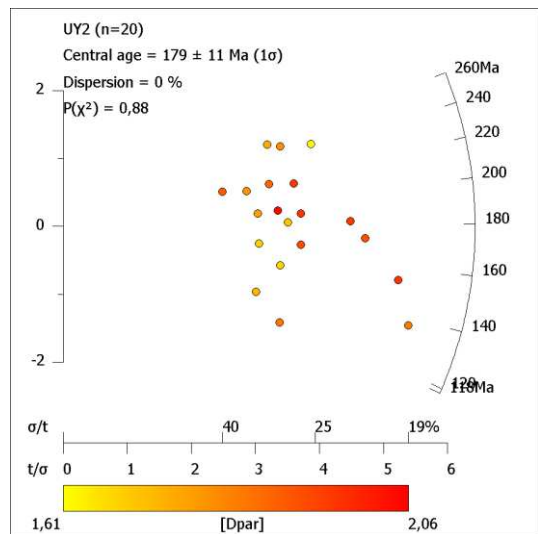
A2.1 Uruguay radial plots

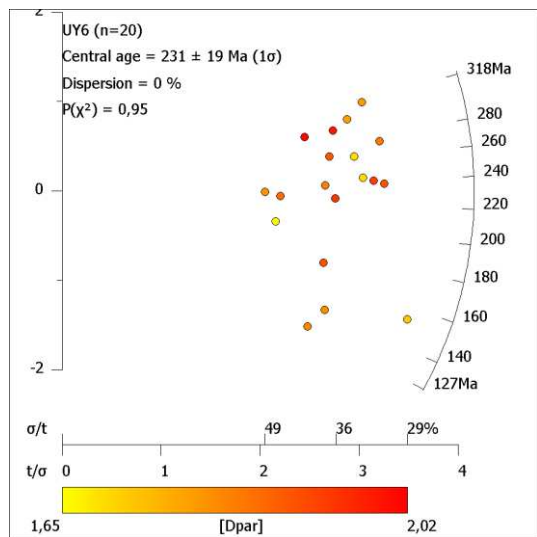
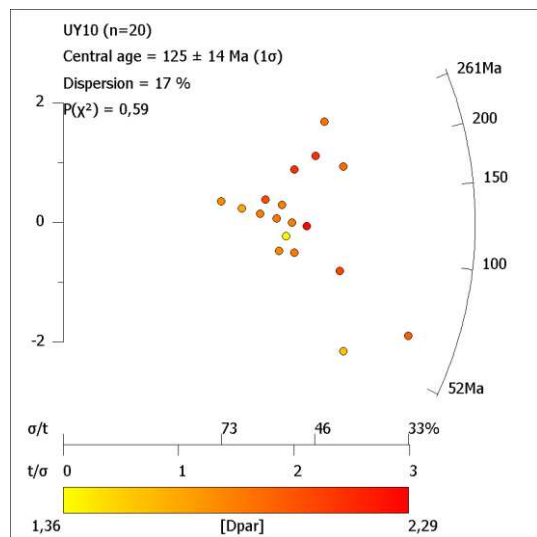
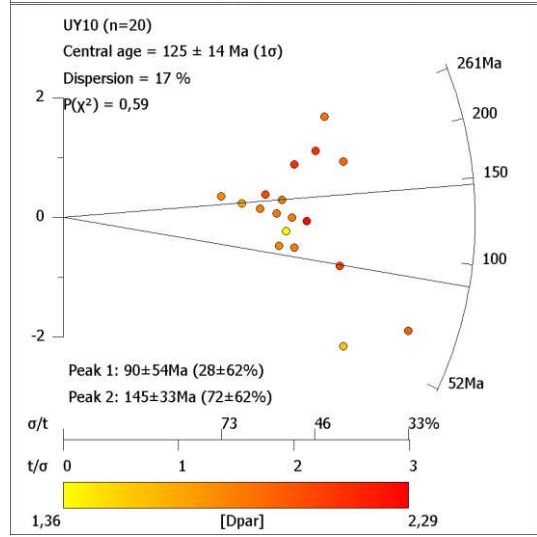
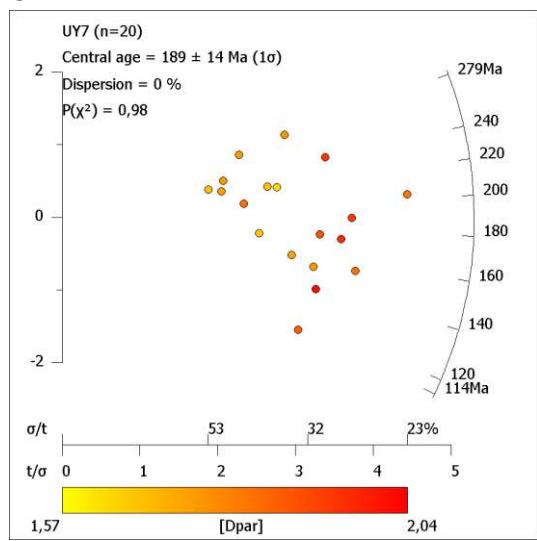
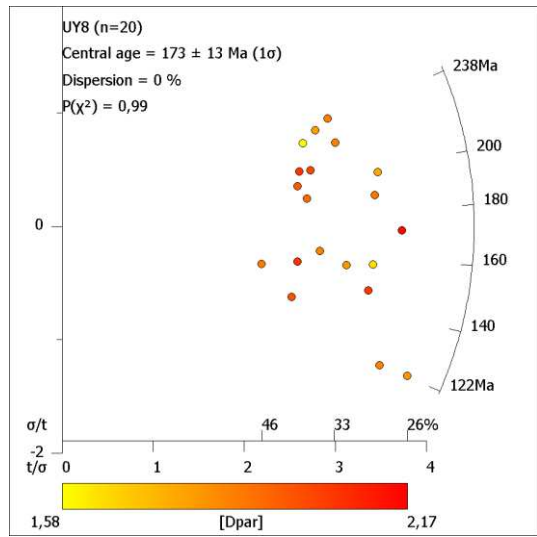
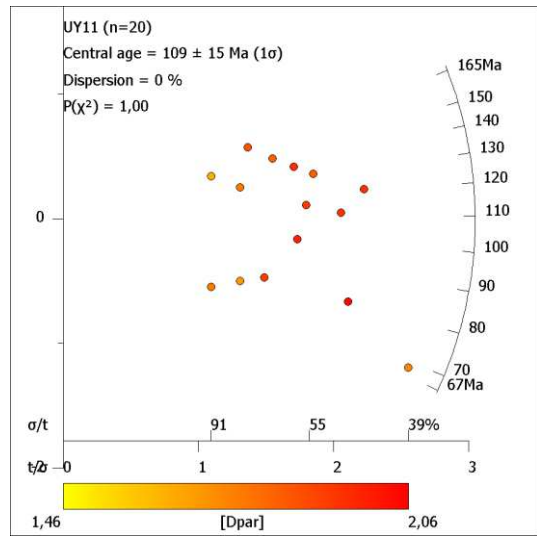
Radial plots, made with RadialPlotter 9.0, of single crystal AFT ages for each sample can be found below. All samples passed the homogeneity chi-square test ($P(\chi^2) > 5\%$) and generally do not show age dispersion, which means that the central ages obtained correspond to single populations. Three samples presented minor age dispersion (UY10 = 17%, UY19 = 18% and UY32 = 18%) that could indicate a mix of apatite populations, but because they passed the chi-square test, are derived from granites, and their central ages agree with neighborhood samples, we considered them as single population as well. For any point, the age is given by extrapolating the radius through it to the circular scale. The vertical scale indicates ± 2 standard errors associated with any single estimate. The horizontal scale indicates approximate percent relative standard errors. For further information see Galbraith (1981), Galbraith & Green (1990) and Vermeesch (2009).

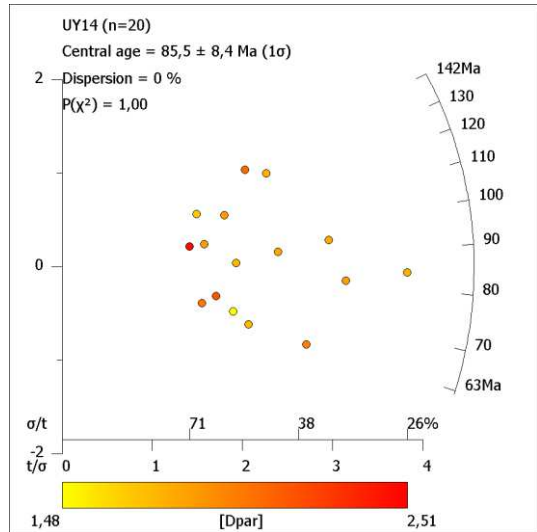
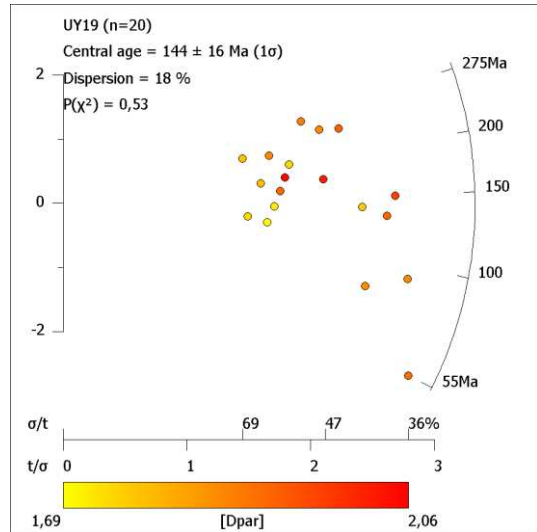
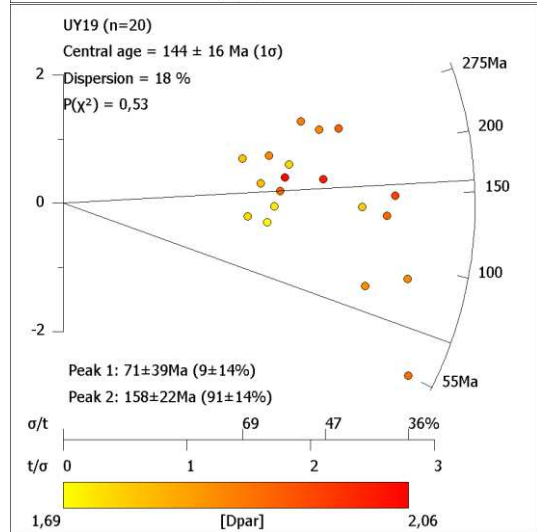
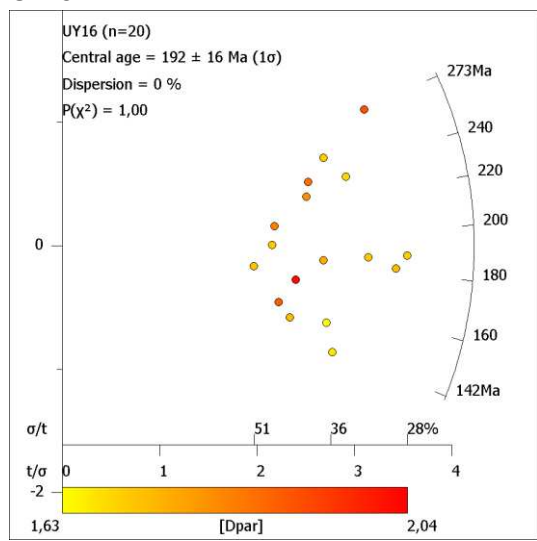
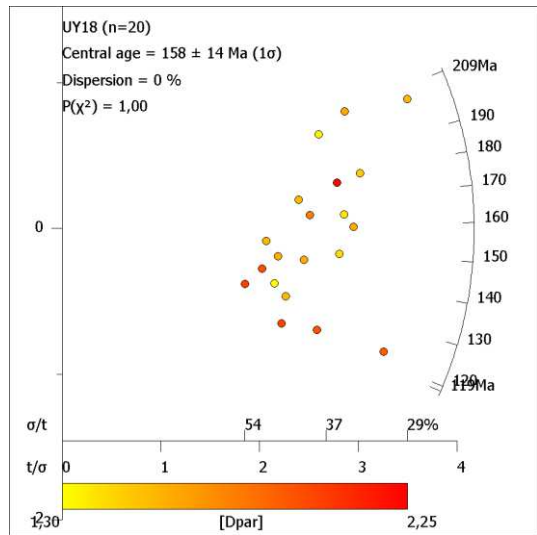
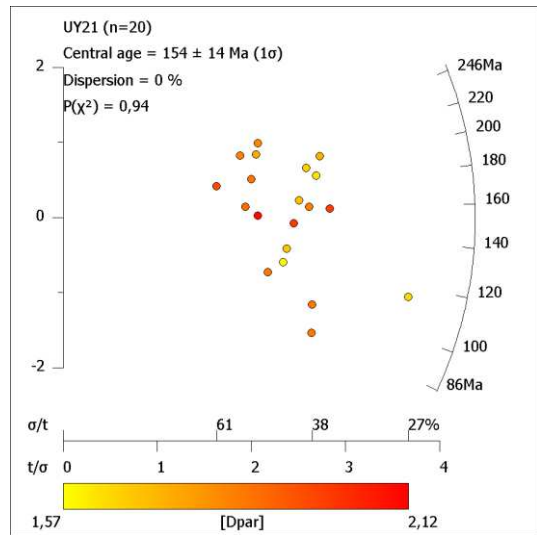
UY1 –

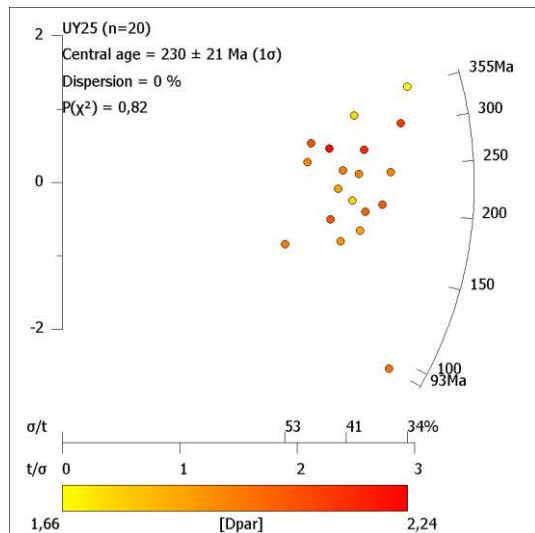
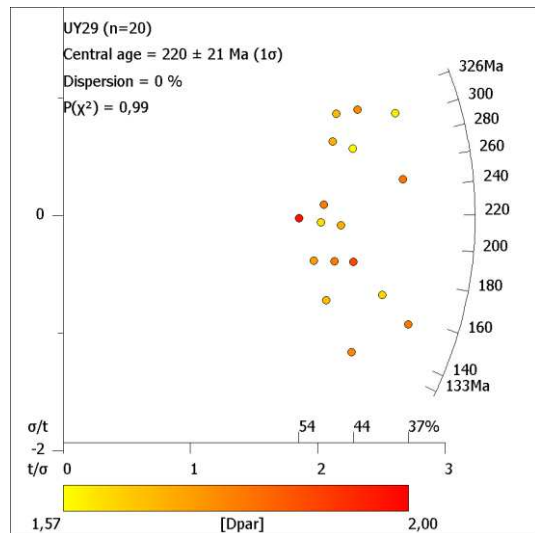
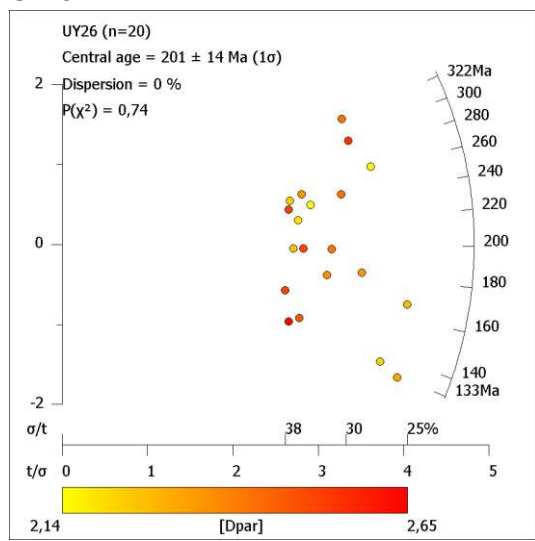
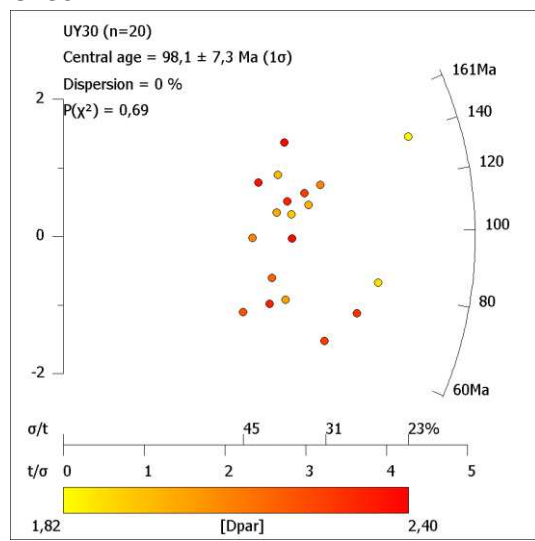
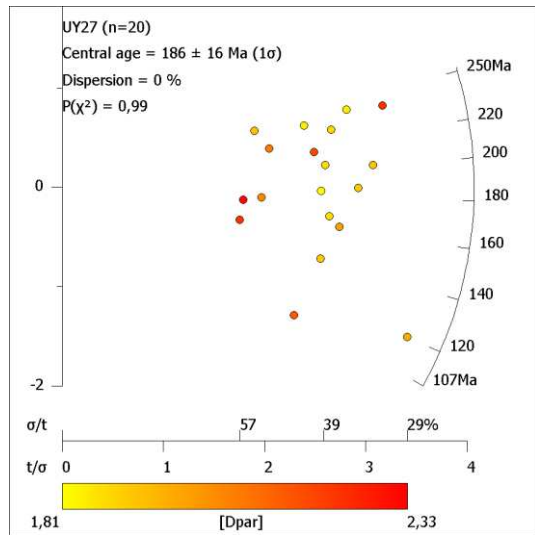
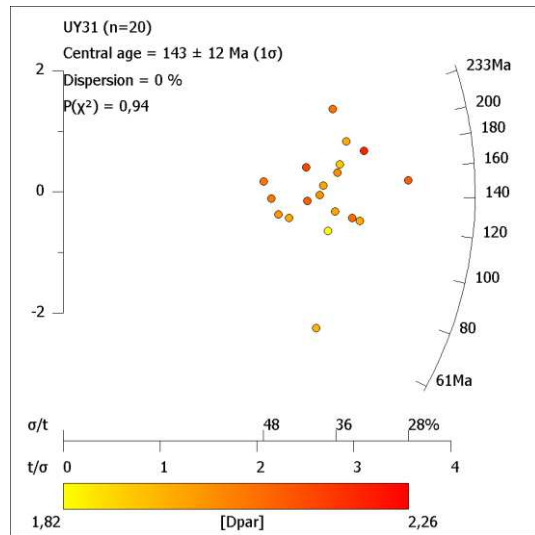


UY2 –

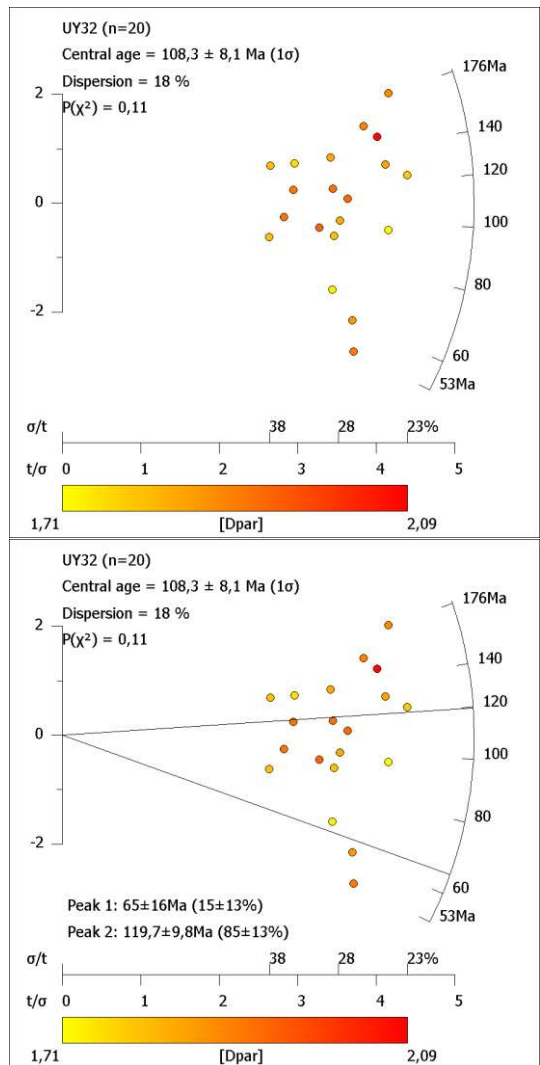


UY6 –**UY10 –****UY7 –****UY8 –****UY11 –**

UY14 -**UY19 -****UY16 -****UY18 -****UY21 -**

UY25 –**UY29 –****UY26 –****UY30 –****UY27 –****UY31 –**

UY32 –

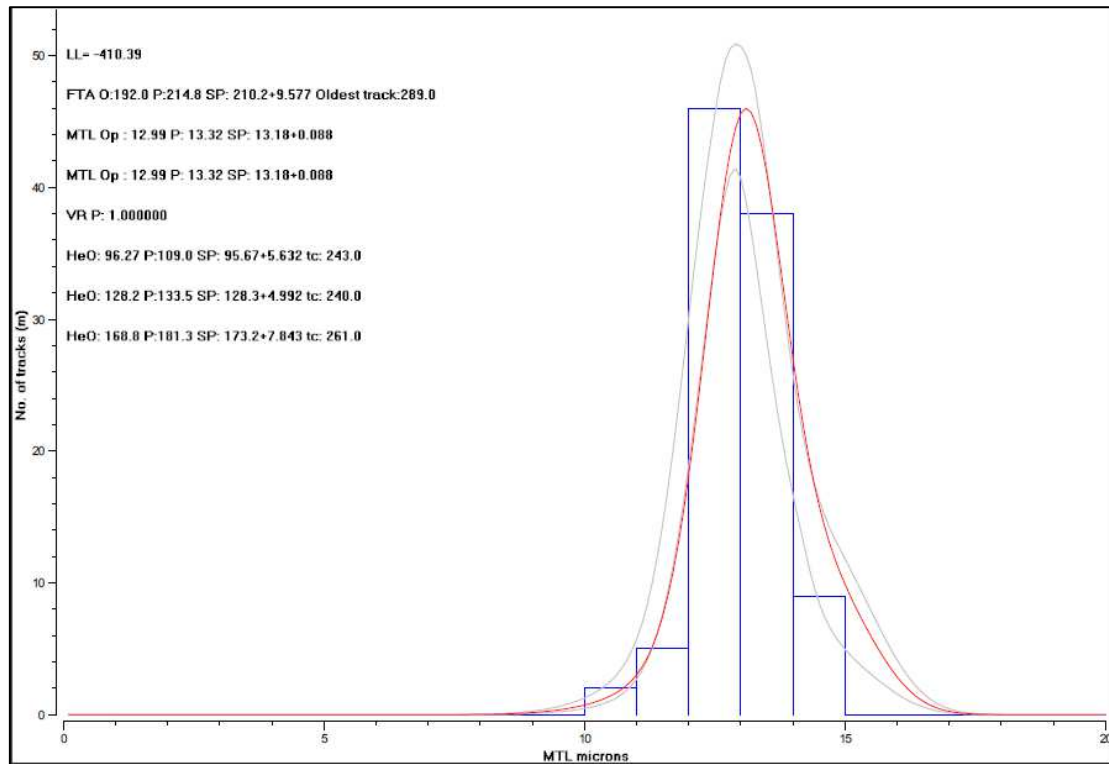


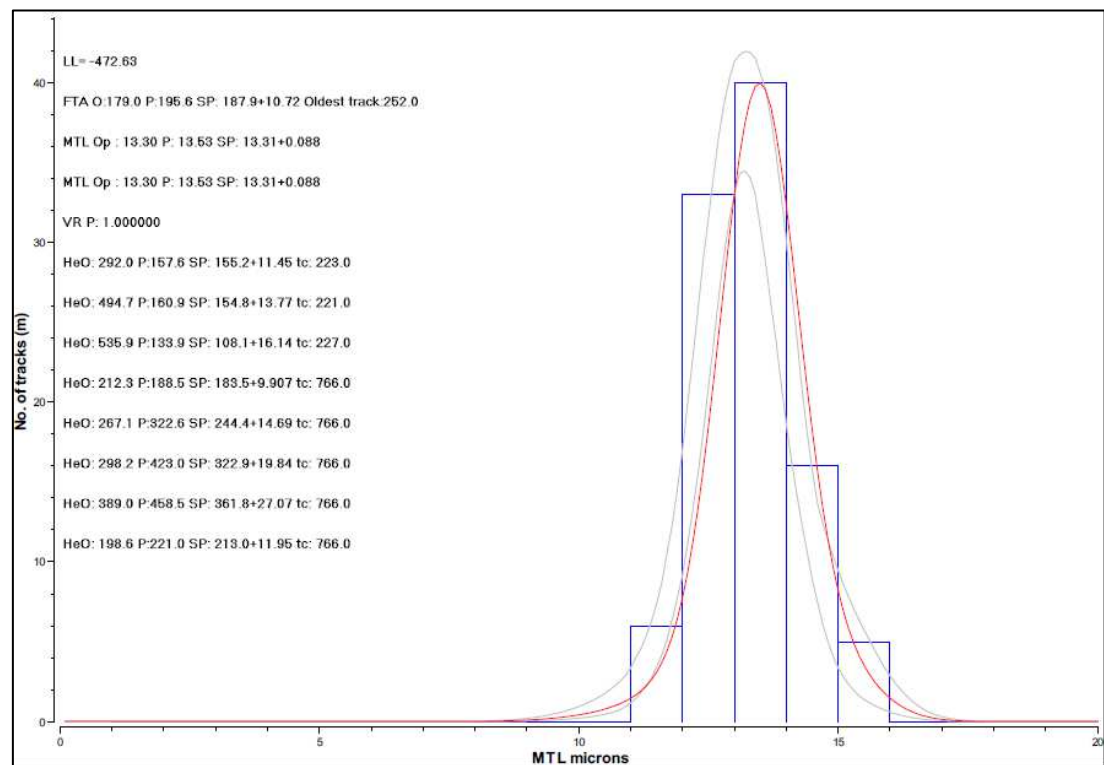
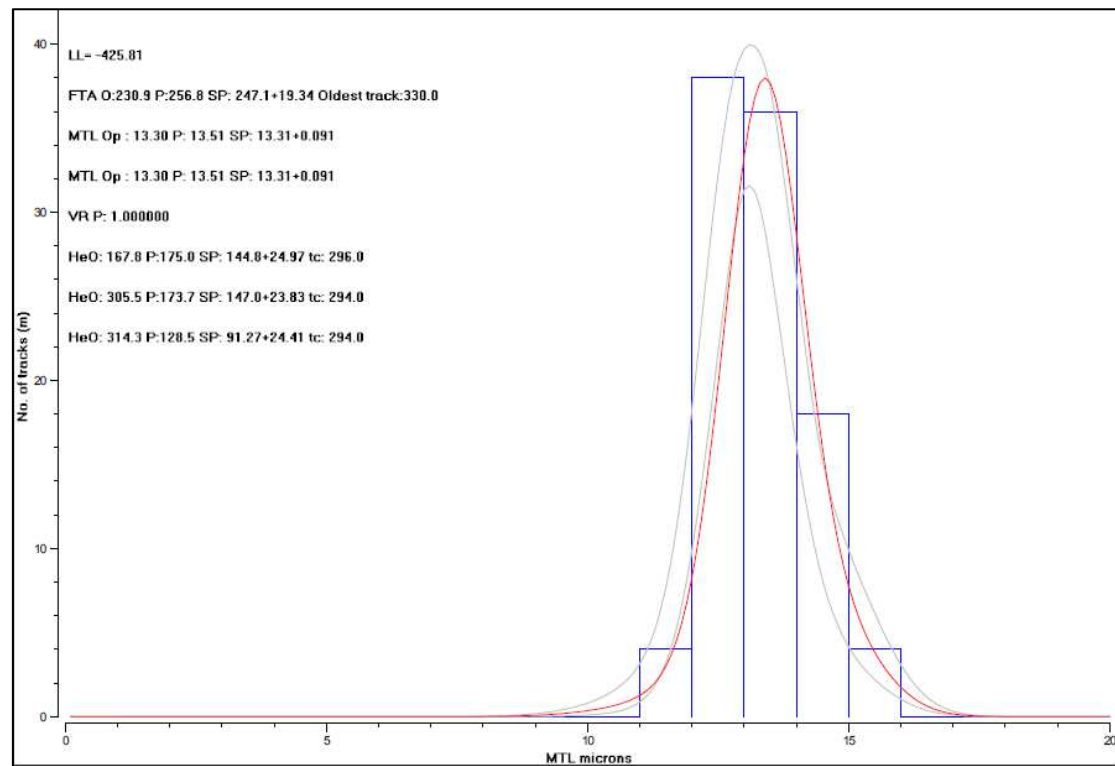
A2.2 Uruguay fission-tracks distribution

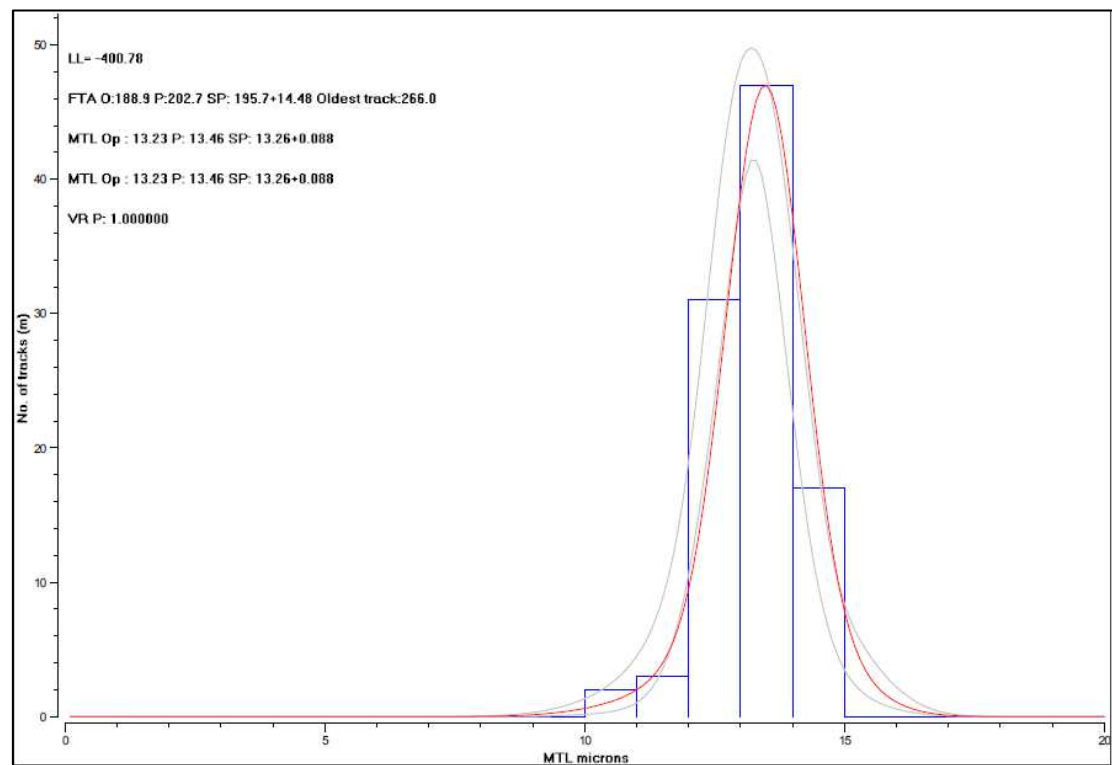
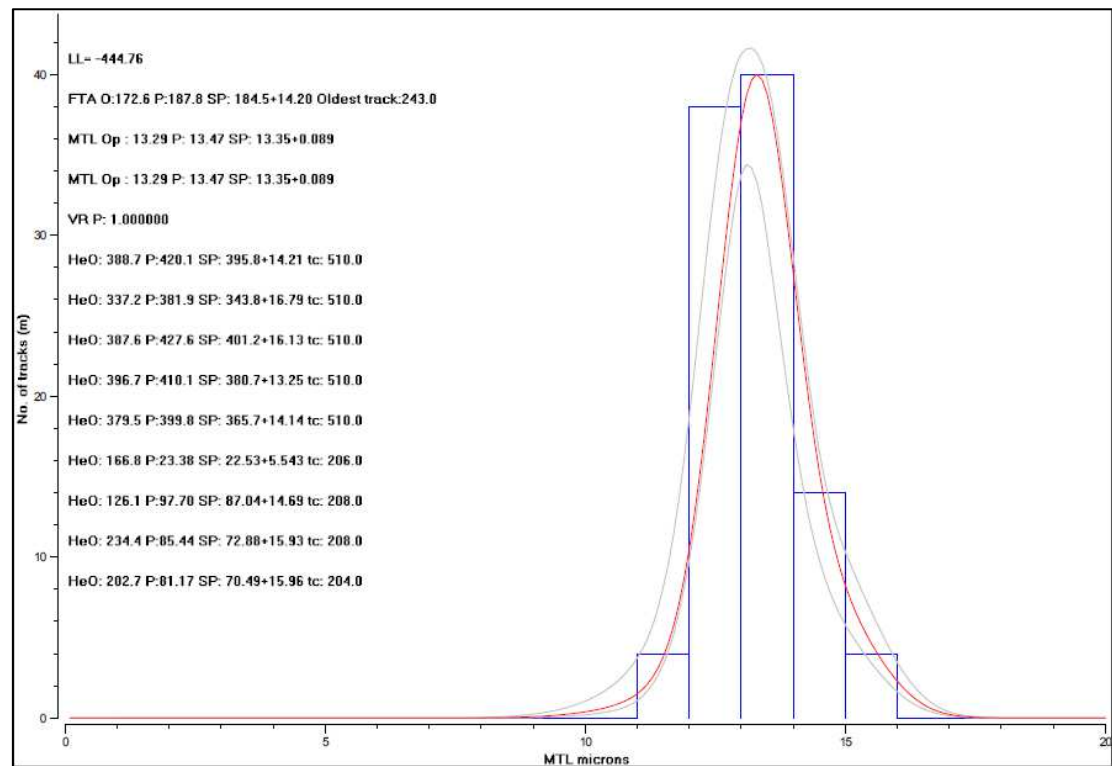
The *c*-axis corrected confined track length distribution (MTL) of each sample can be found below. The lengths scattering tends to be unimodal for all samples but UY29, which displays a bimodal distribution and a distinct old AFT age in SSE coastal region (CDT). In most cases, the track lengths distribution is Gaussian around the mean value or negatively skewed, with a larger proportion of longer tracks than shorter ones. The gray lines define the range of track length distribution calculated during the inverse modeling, while the red line represents the length distribution calculated for the mean trajectory of the model (*i.e.* the length distribution that corresponds to the trajectories shown in figures 5.8 and 5.9). The total number of confined tracks (N) is indicated as well. For further information see Gallagher 2009, 2012 and QTQt User Guide v5.7.

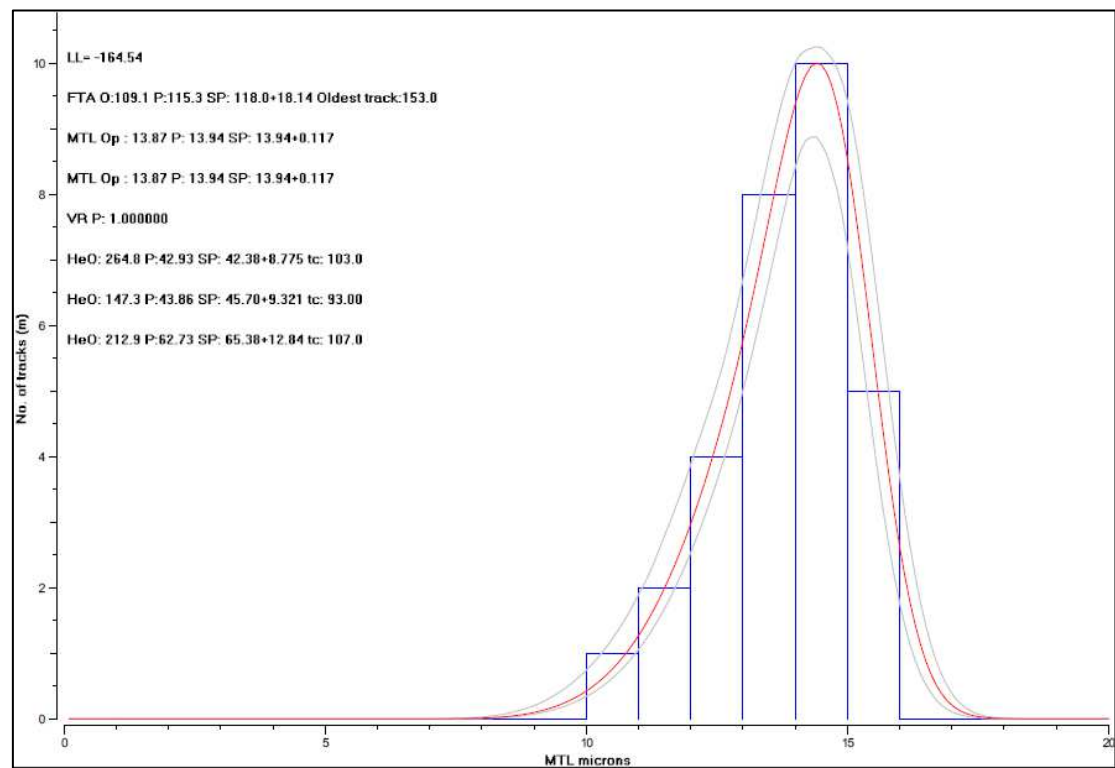
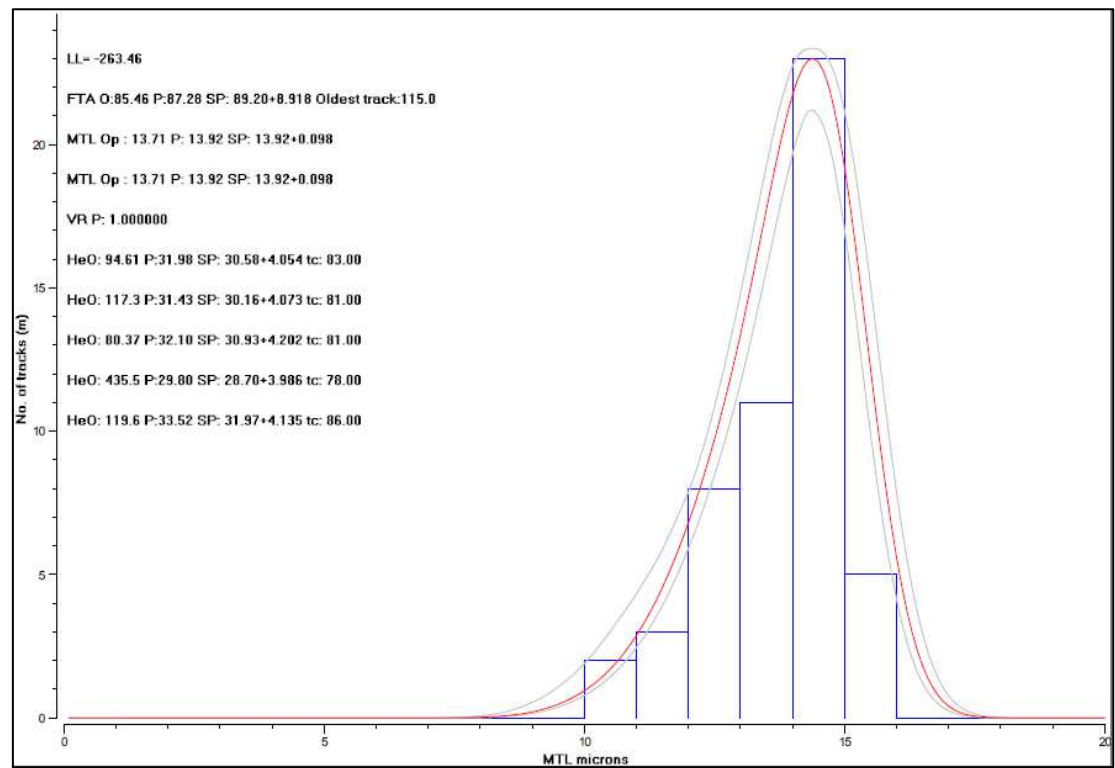
UY1 – AFT, AHE

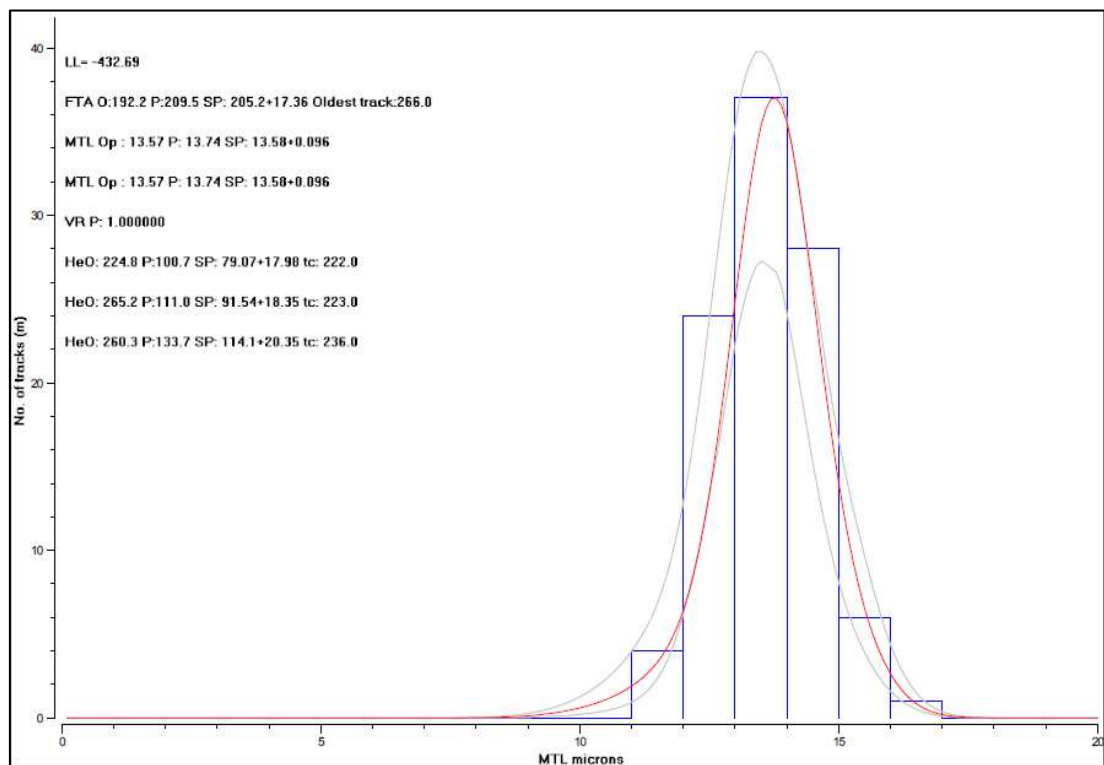
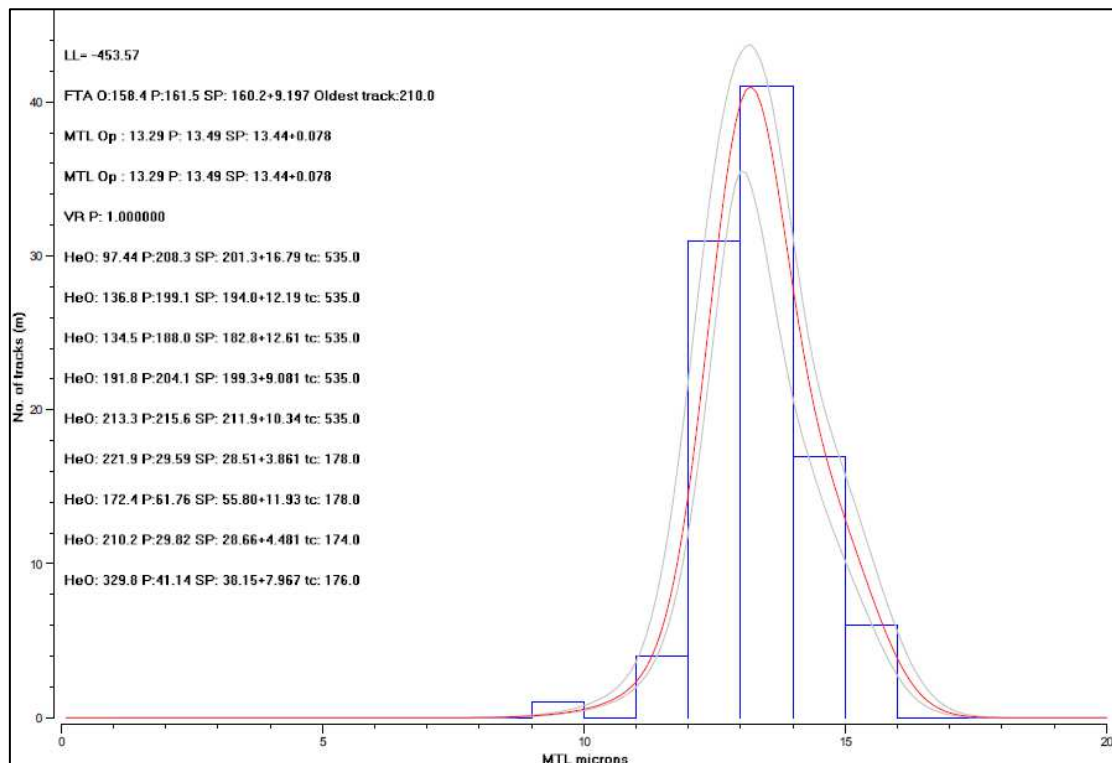
N= 100

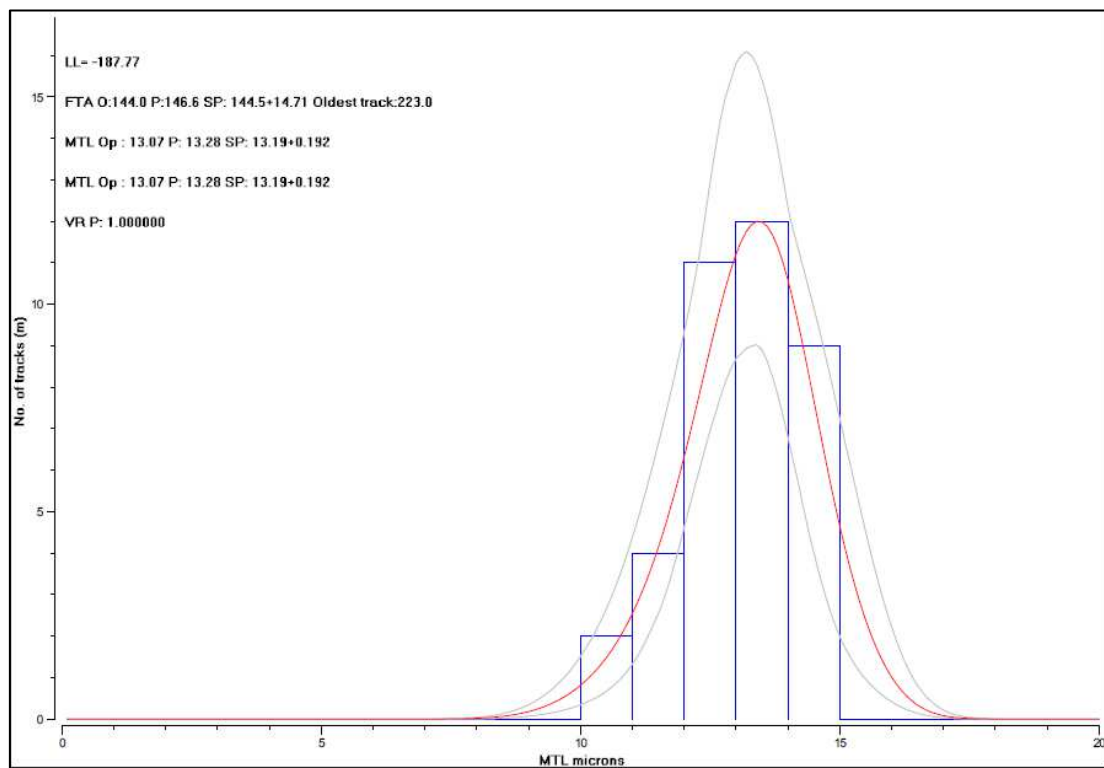
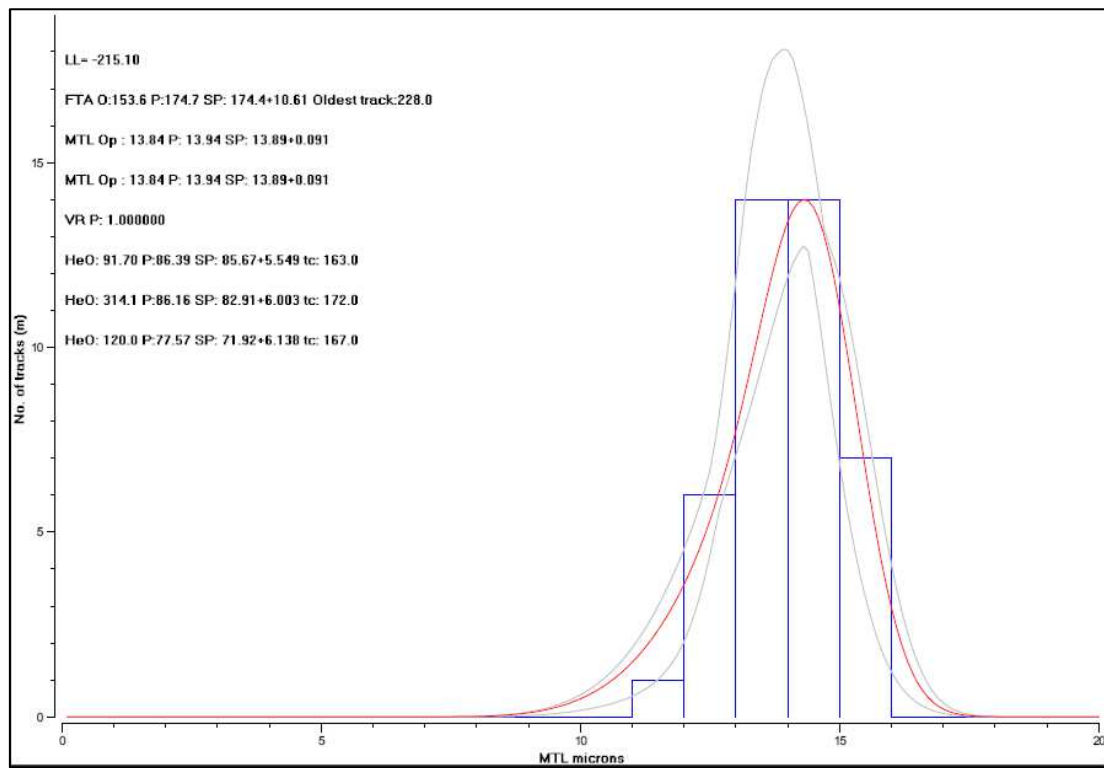


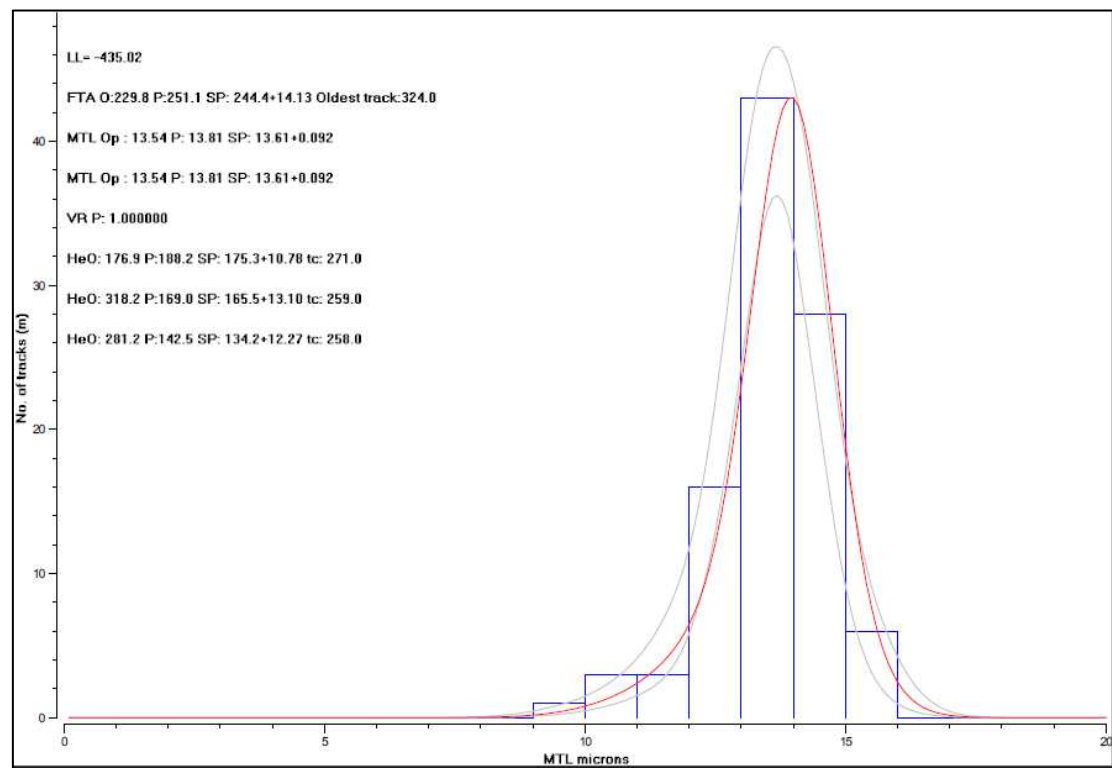
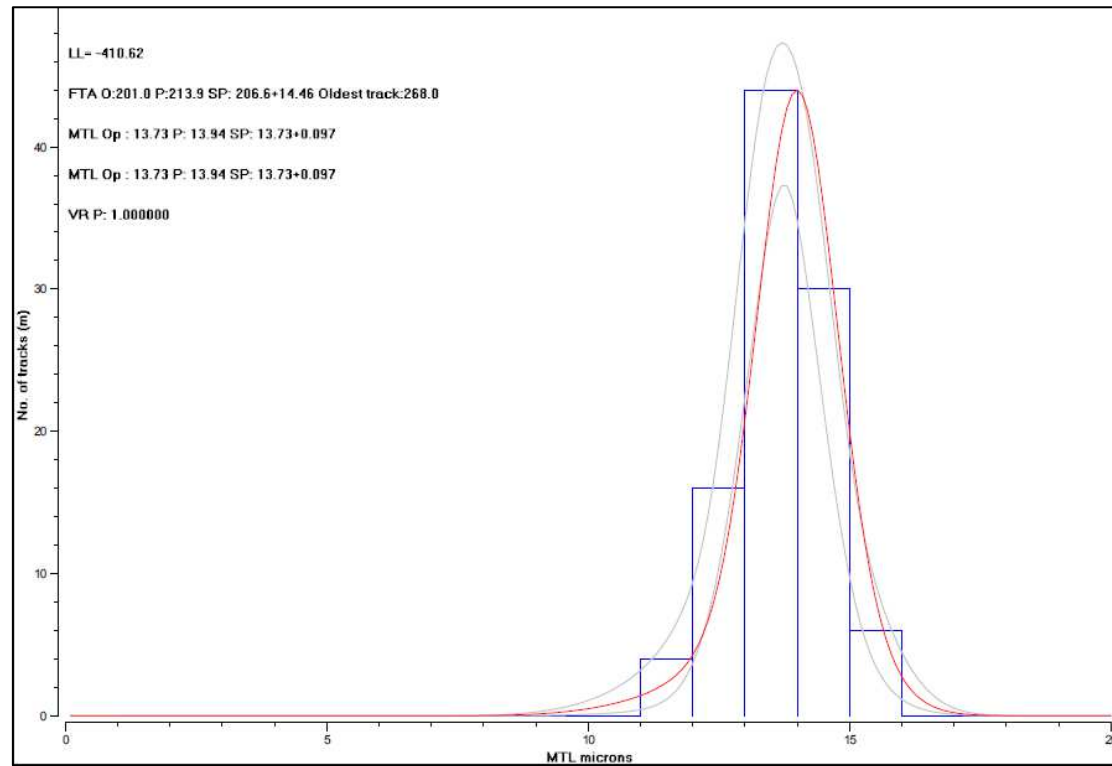
UY2 – AFT, AHE, ZHE**N= 100****UY6 – AFT, AHE****N= 100**

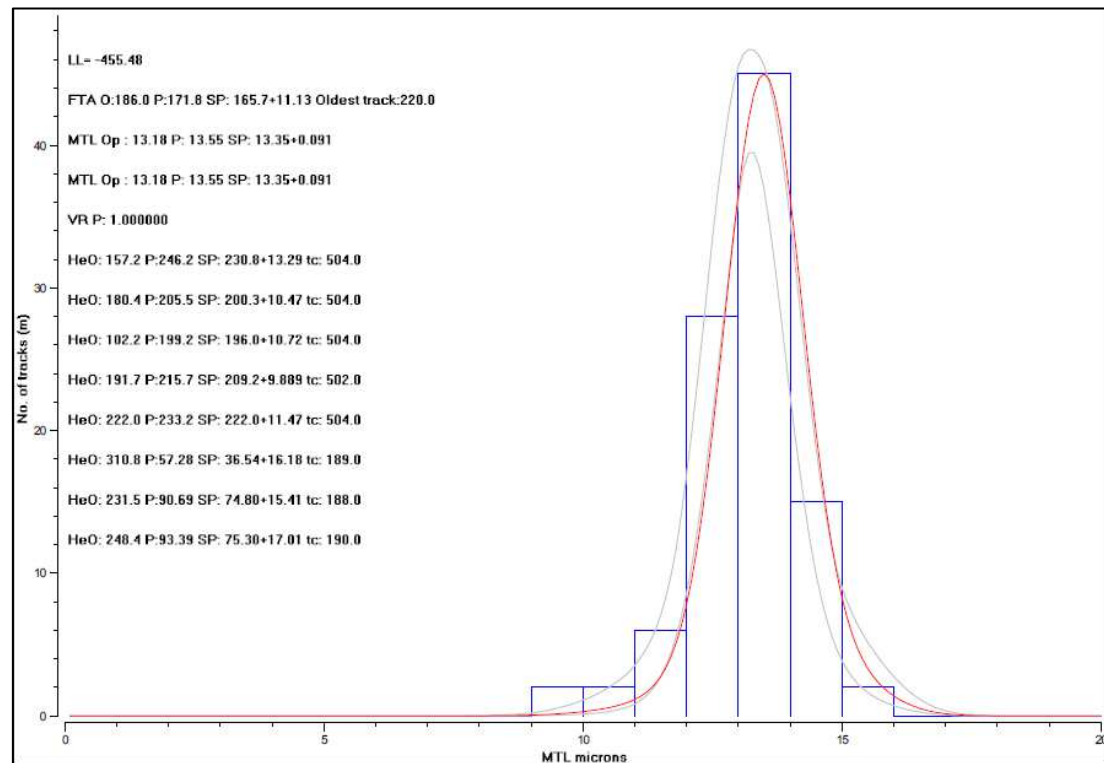
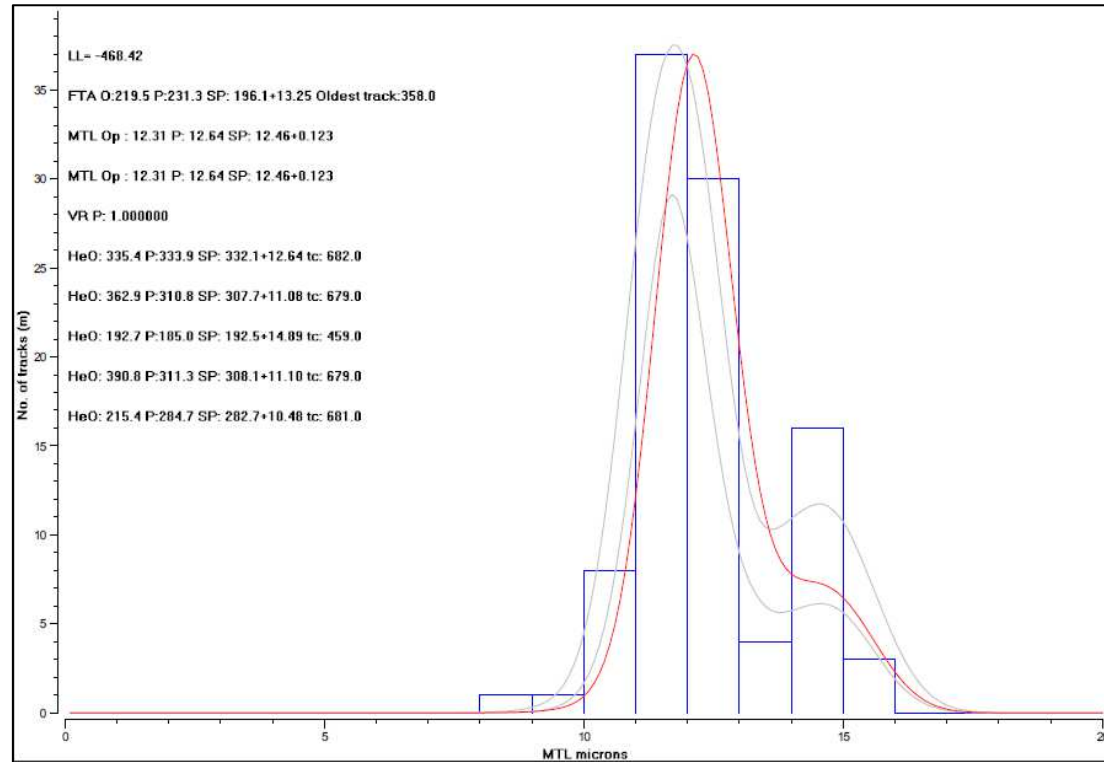
UY7 – AFT**N= 100****UY8 – AFT, AHE, ZHE****N= 100**

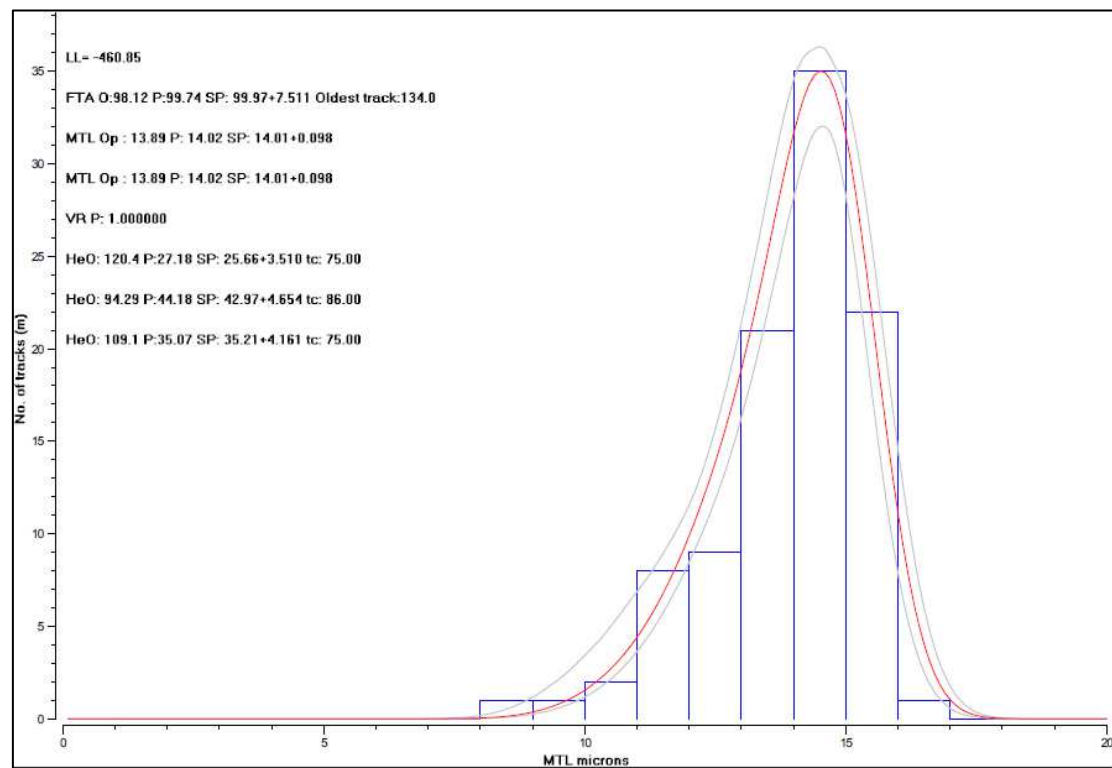
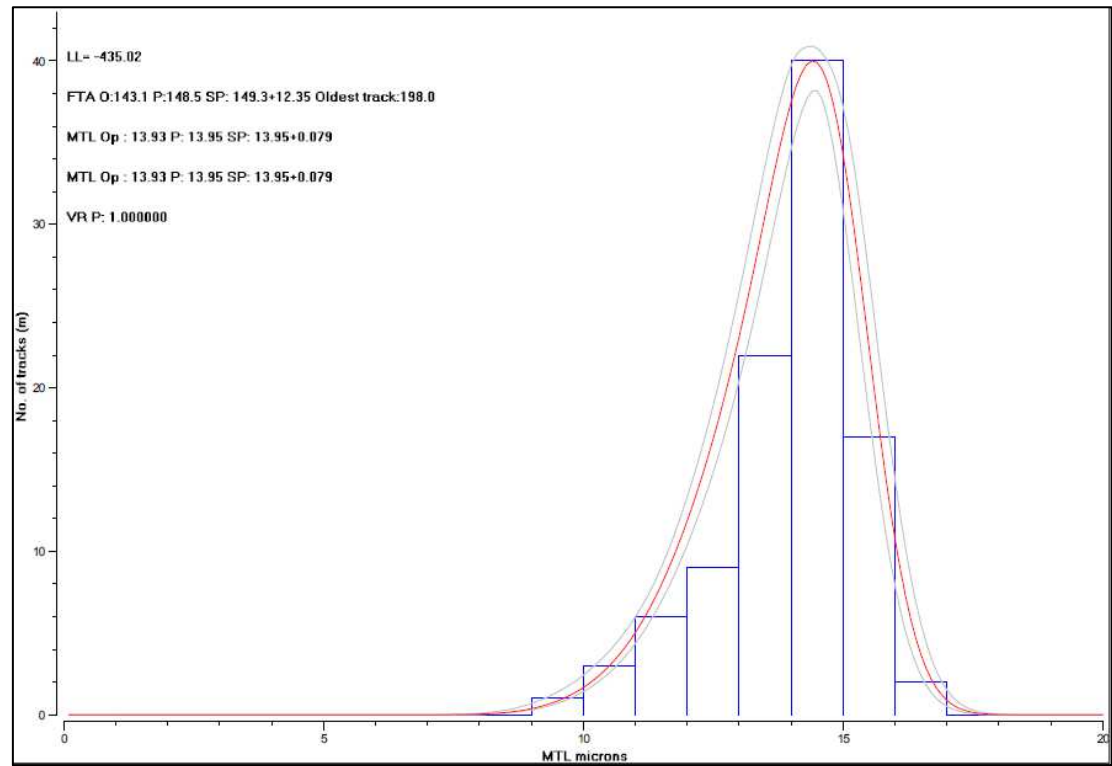
UY11 – AFT, AHE**N= 30****UY14 – AFT, AHE****N= 52**

UY16 – AFT, AHE**N= 100****UY18 – AFT, AHE, ZHE****N= 100**

UY19 – AFT**N= 38****UY21 – AFT, AHE****N= 42**

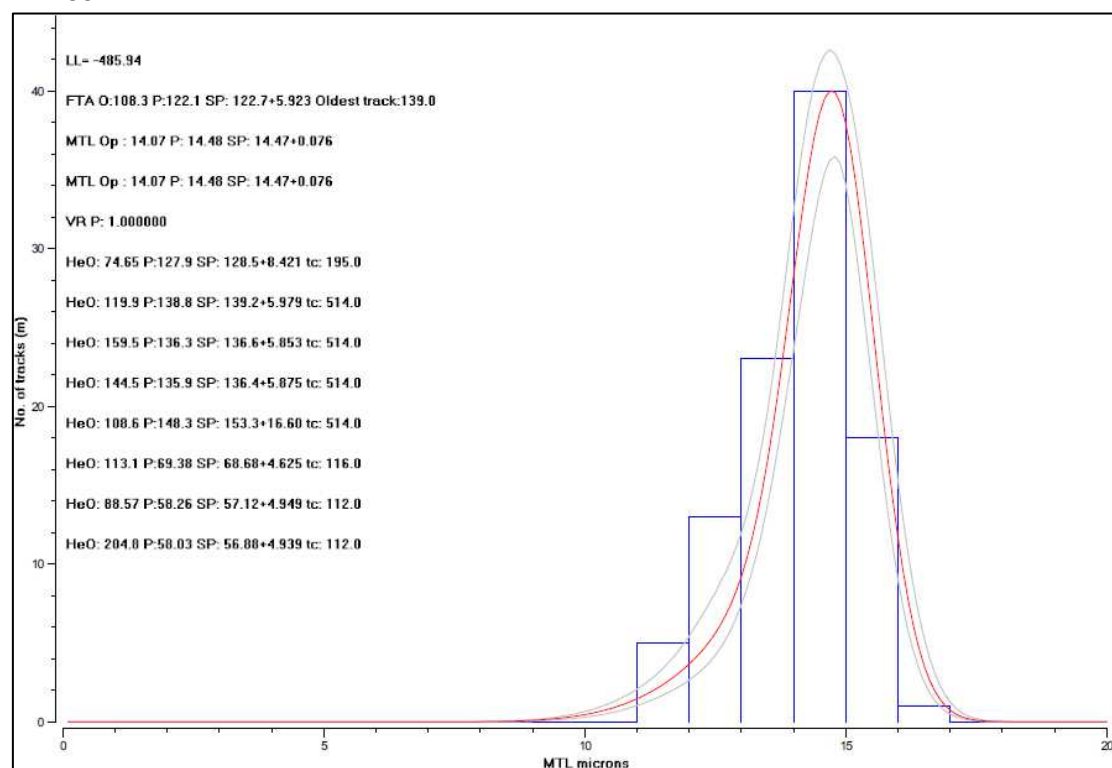
UY25 – AFT, AHE**N= 100****UY26 – AFT****N= 100**

UY27 – AFT, AHE, ZHE**N= 100****UY29 – AFT, ZHE****N= 100**

UY30 – AFT, AHE**N= 100****UY31 – AFT****N= 100**

UY32 – AFT, AHE, ZHE

N= 100

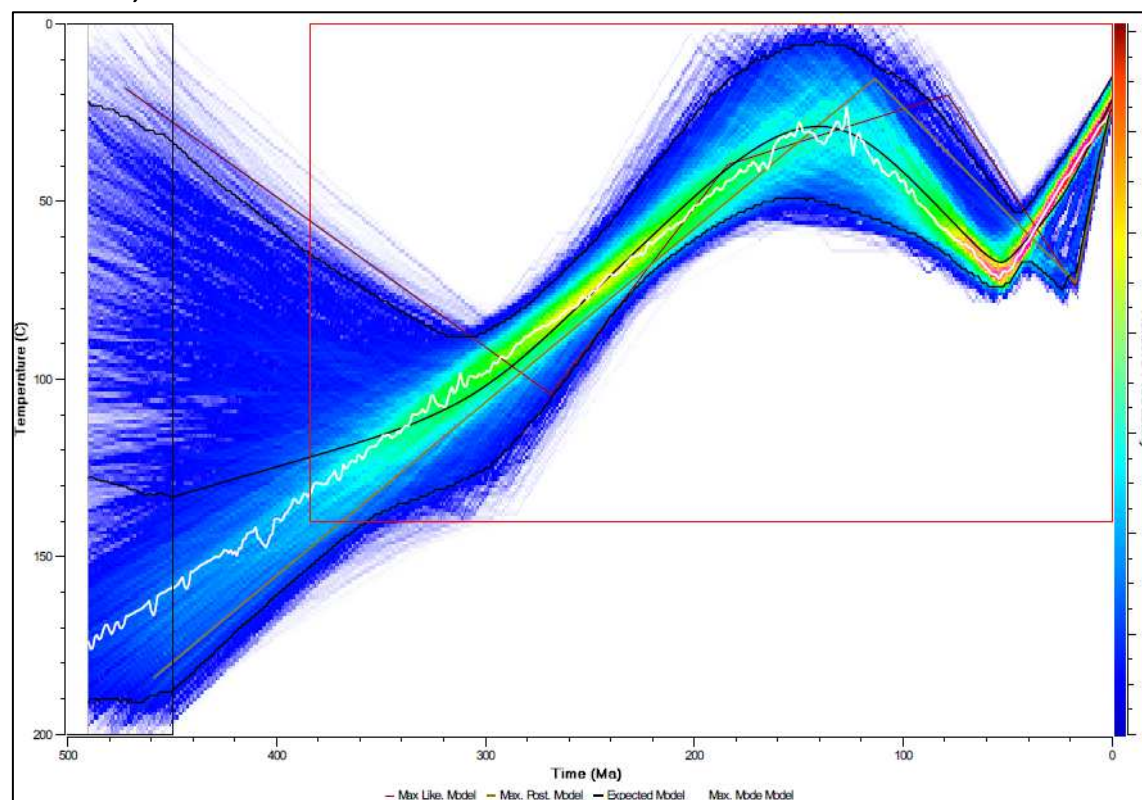


A2.3 Uruguay inverse models

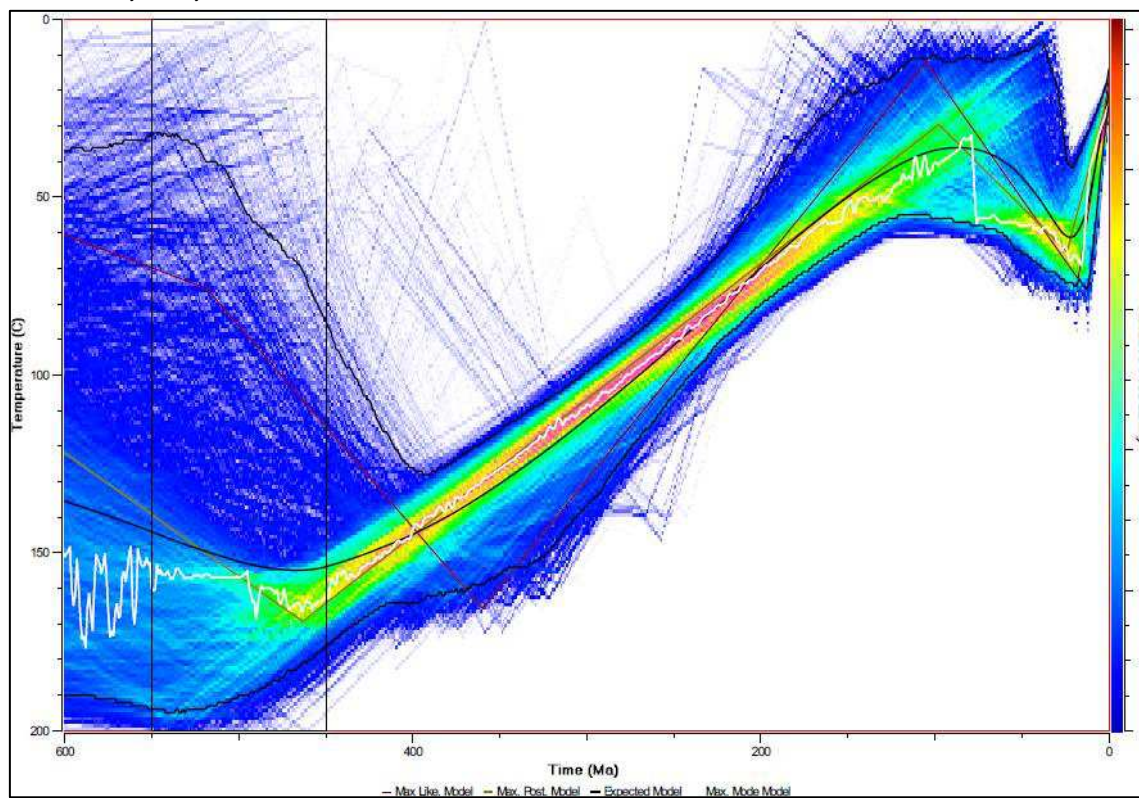
The final inverse model of each sample can be found below. Final models were run with all data available for the sample, as indicated. Black line represents the expected model, that is, a weighted mean model, where the weighting is provided by the posterior probability for each model (for further information see Gallagher 2009, 2012 and QTQt User Guide v5.7).

The expected model is the one displayed in figures 5.8 and 5.9 of this thesis. Confidence intervals represent the 95% probability range, with relative probability inside this range indicated with the color scale.

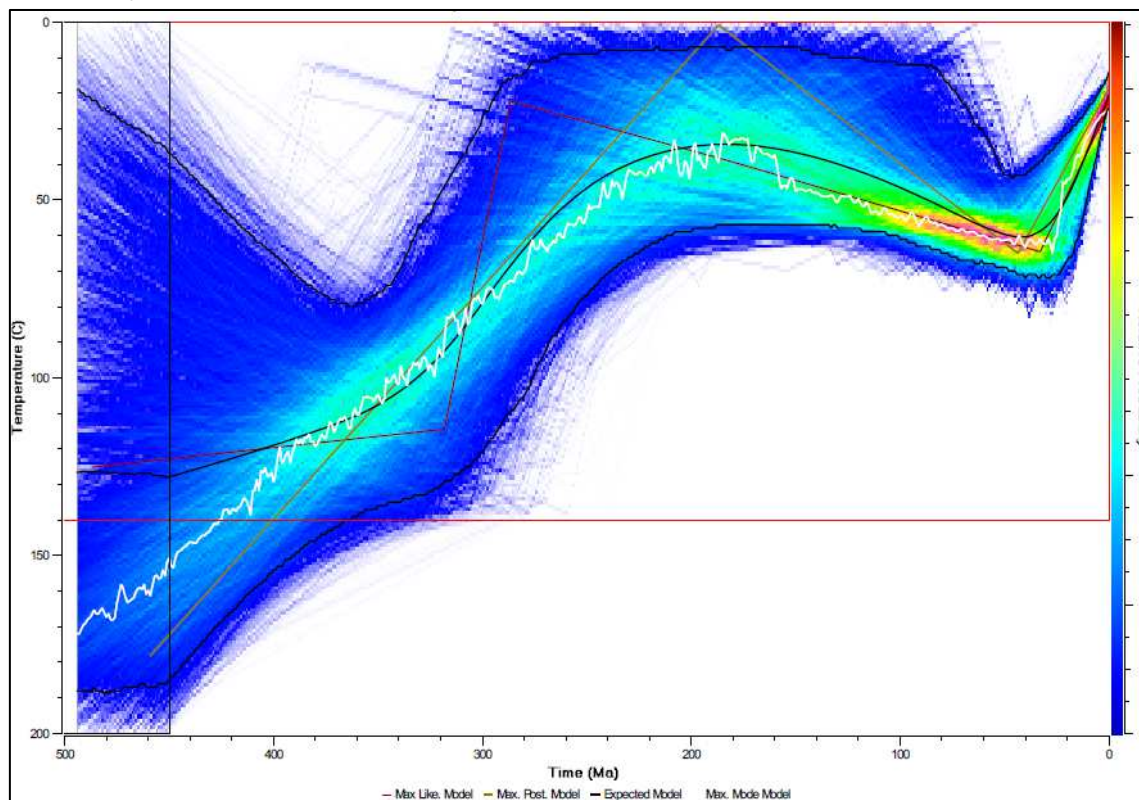
UY1 – AFT, AHE

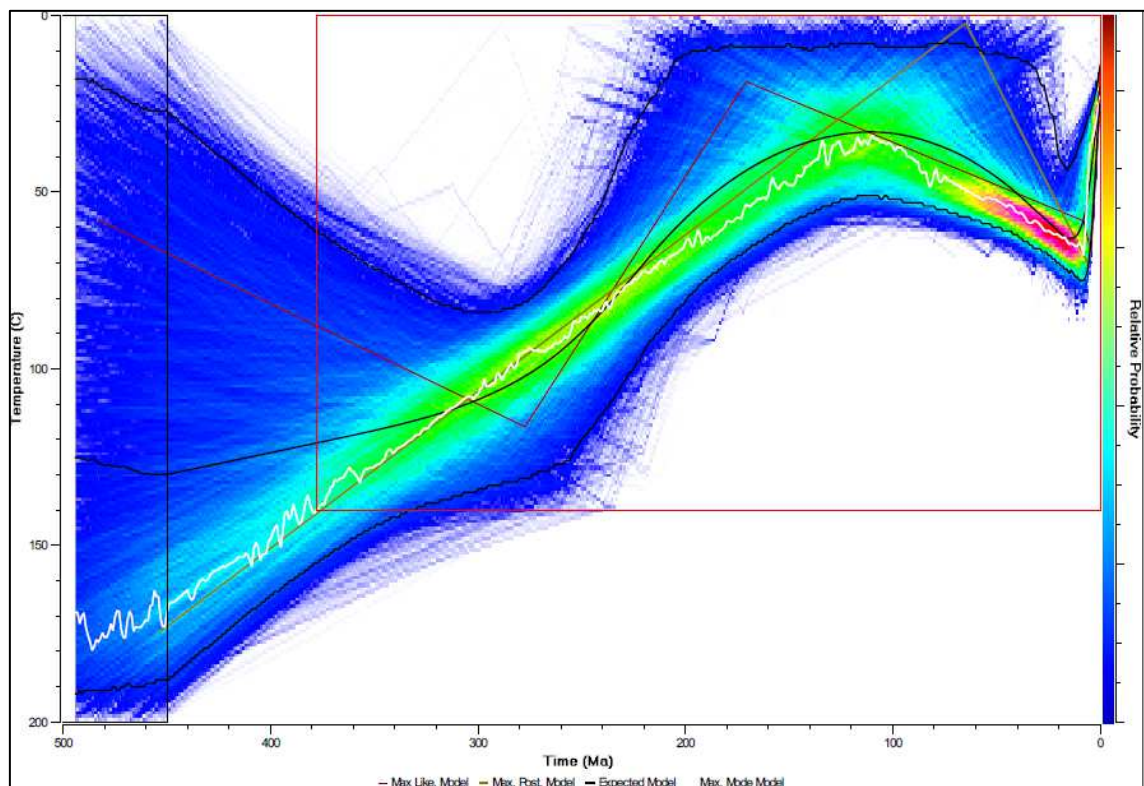
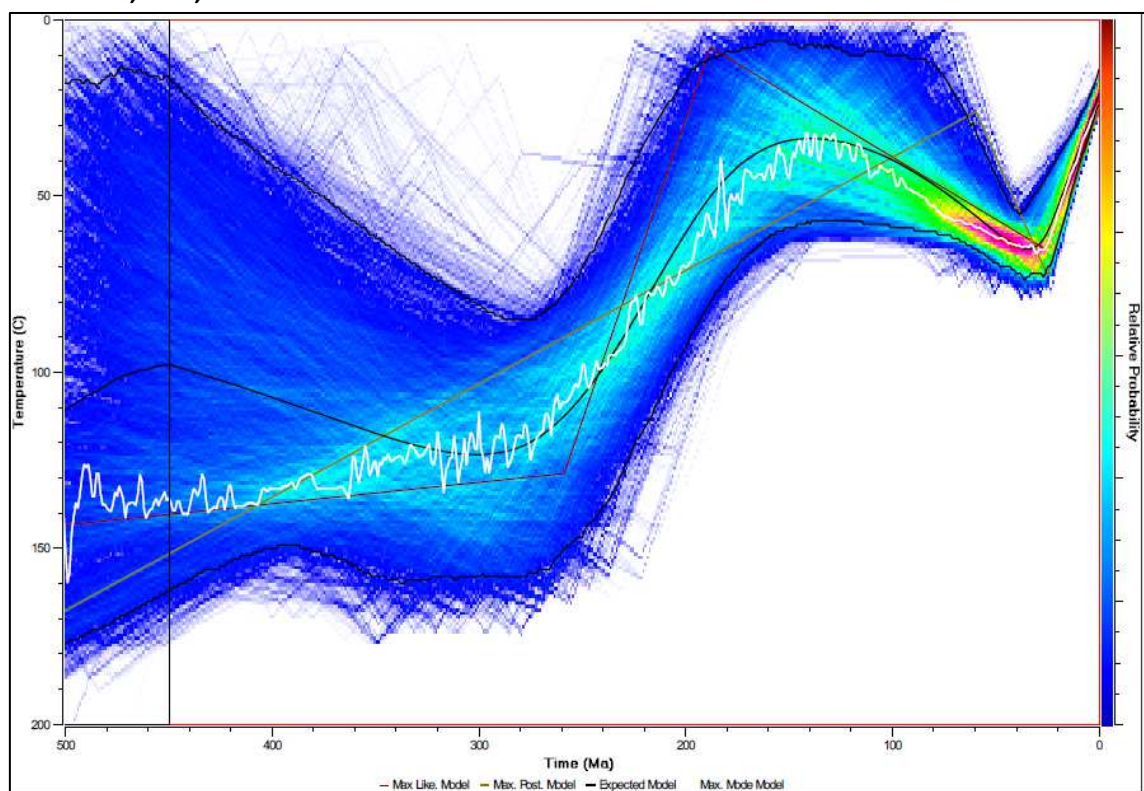


UY2 – AFT, AHE, ZHE

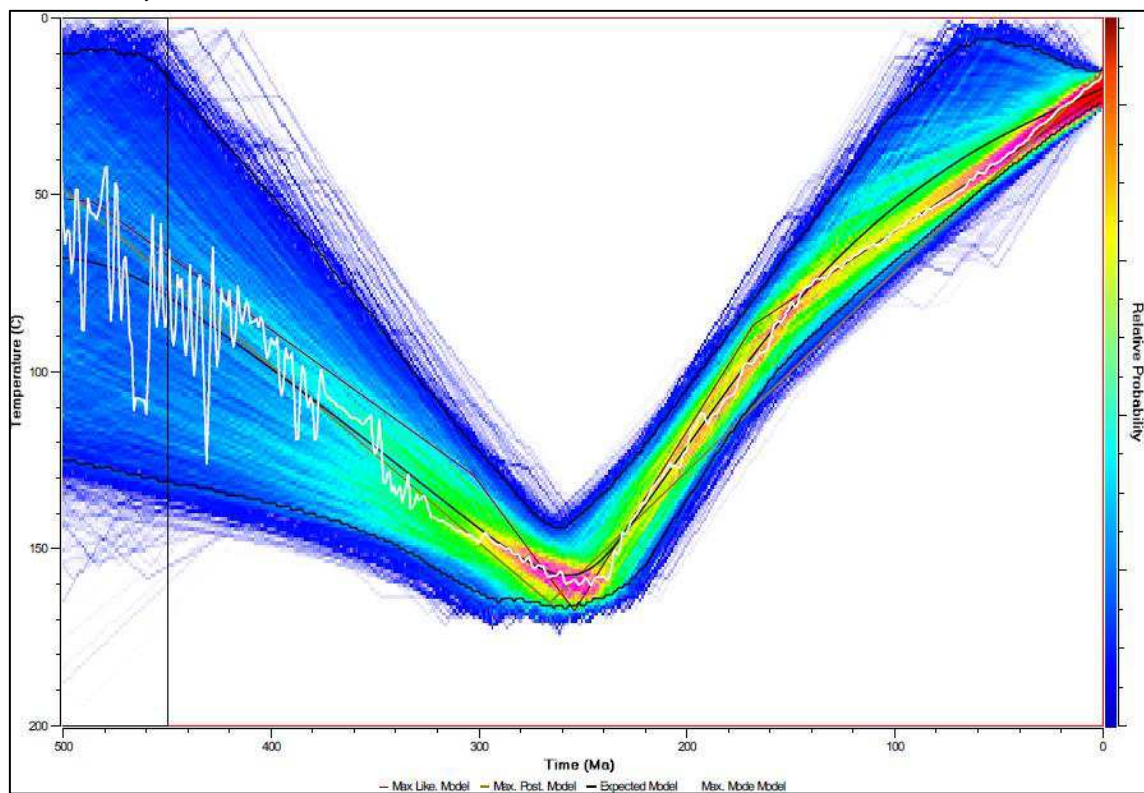


UY6 – AFT, AHE

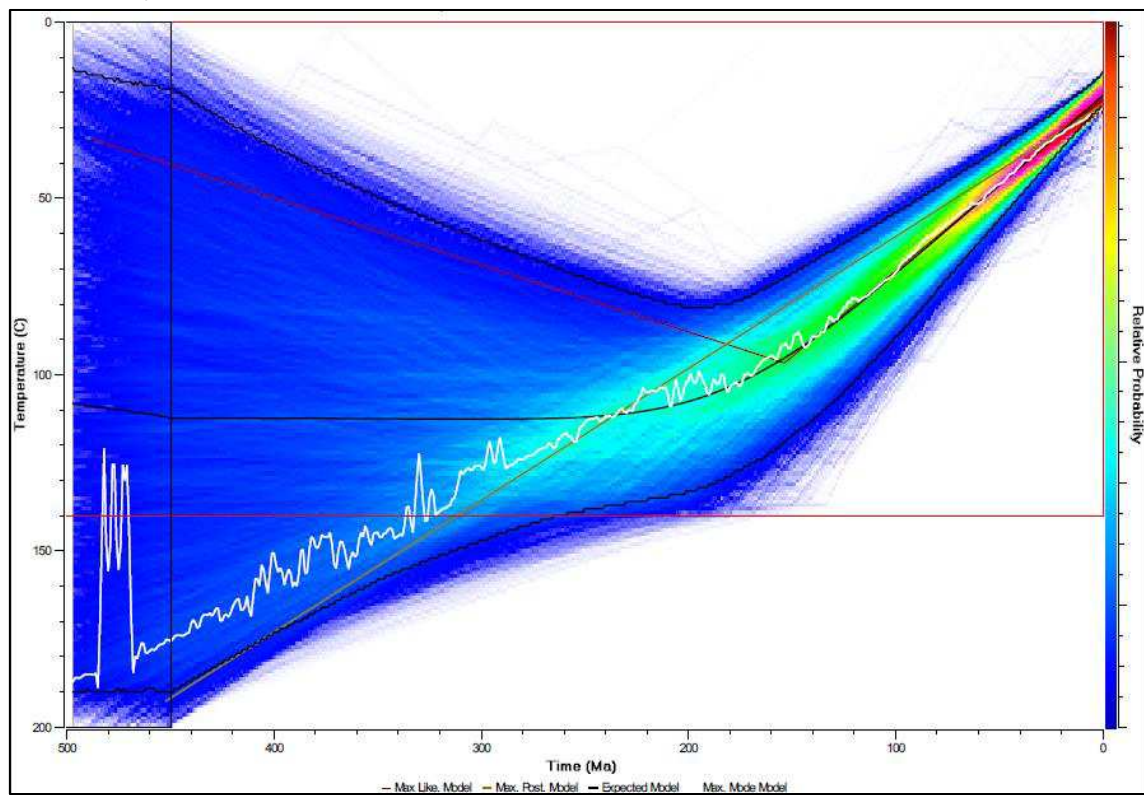


UY7 - AFT**UY8 – AFT, AHE, ZHE**

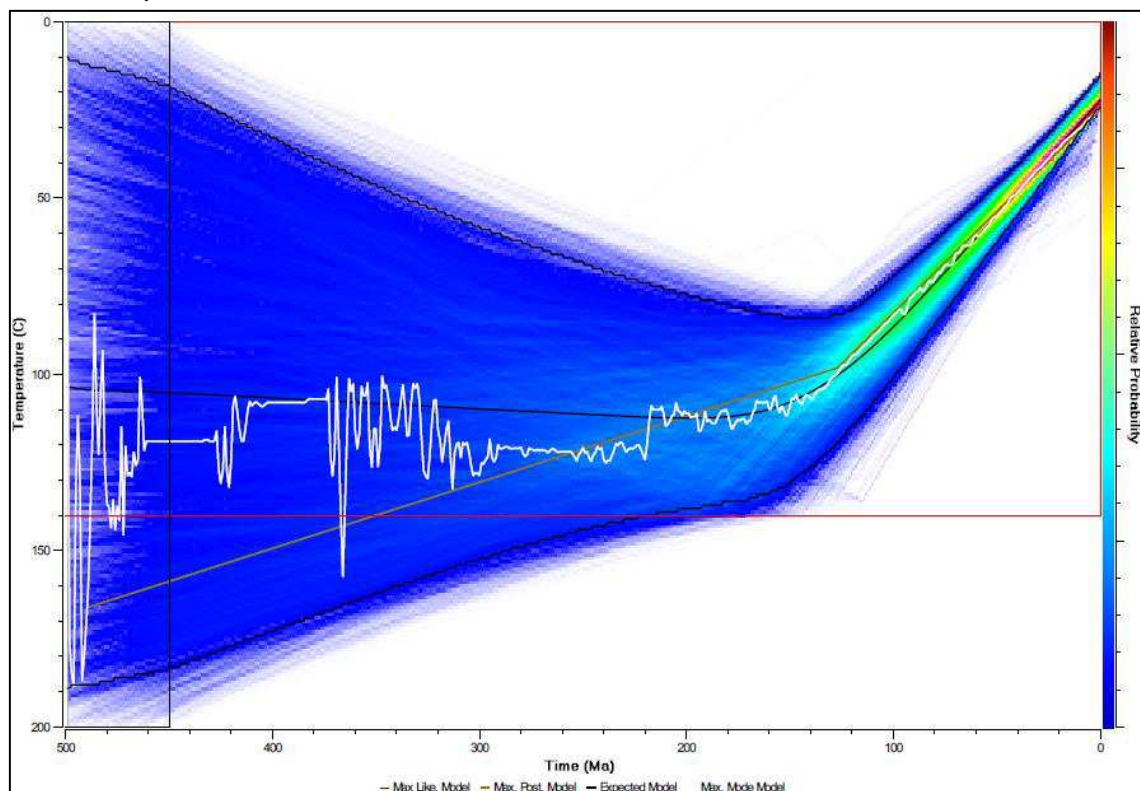
UY10 – AFT, ZHE



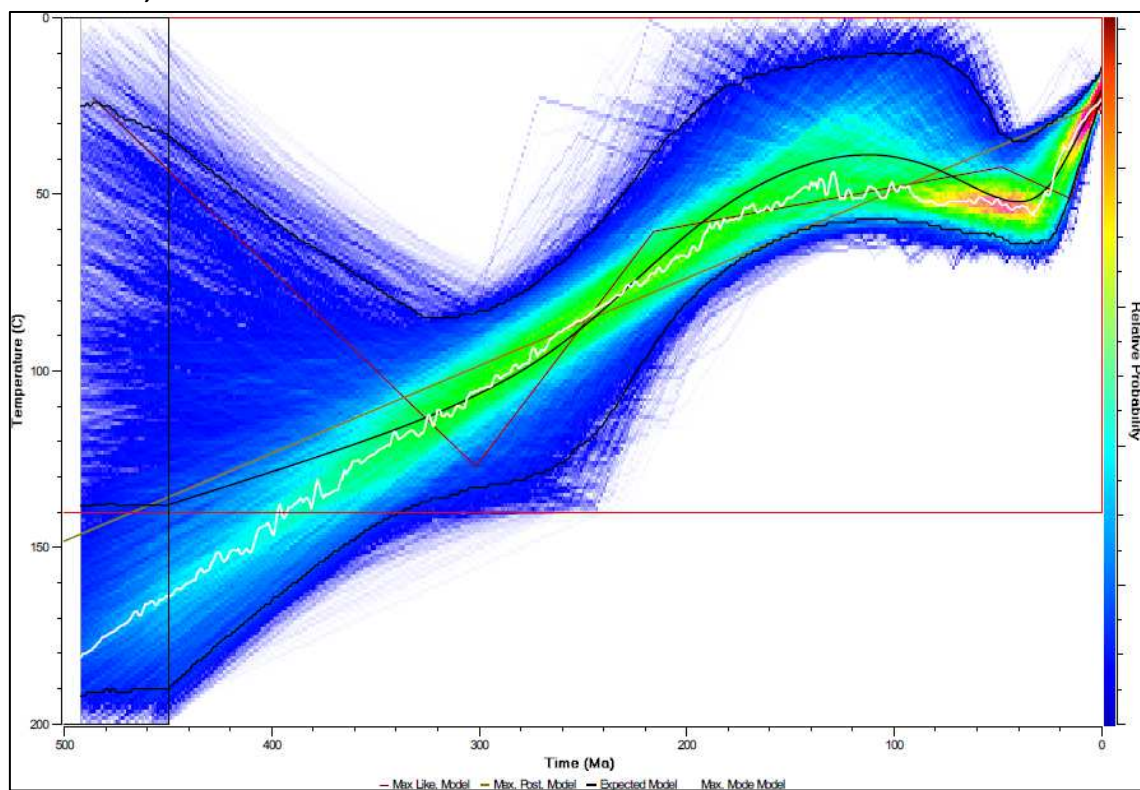
UY11 – AFT, AHE



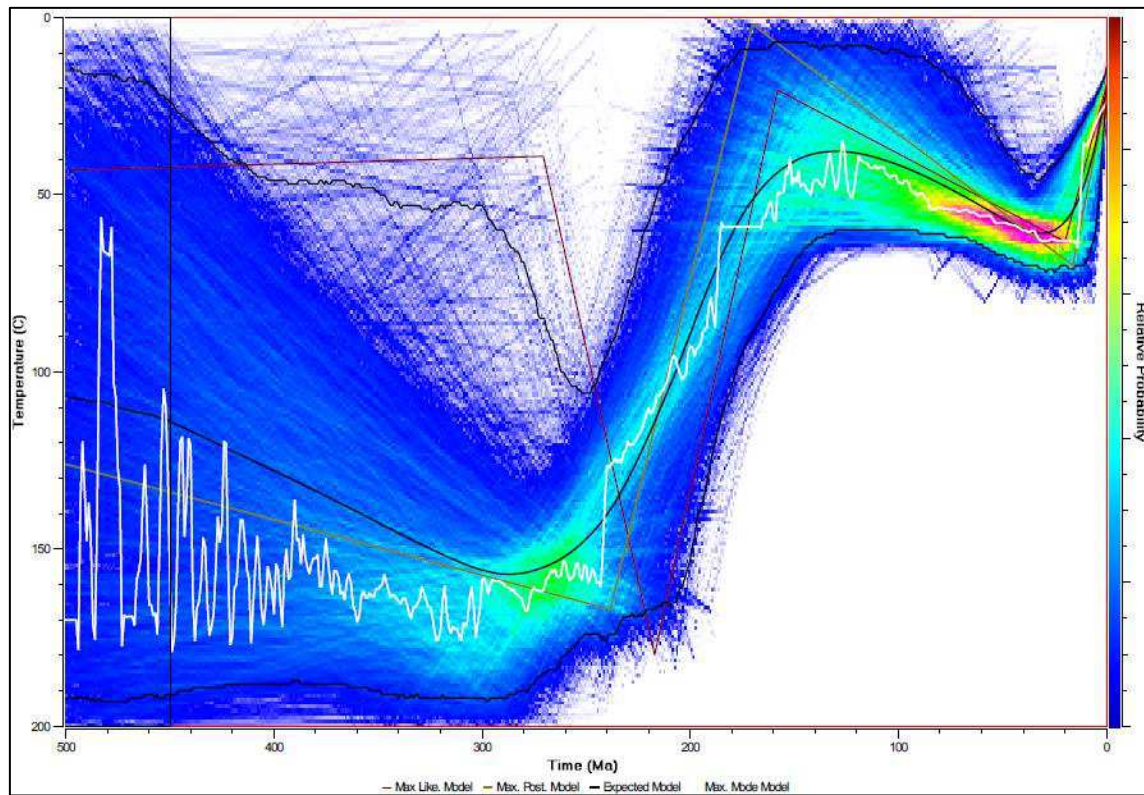
UY14 – AFT, AHE



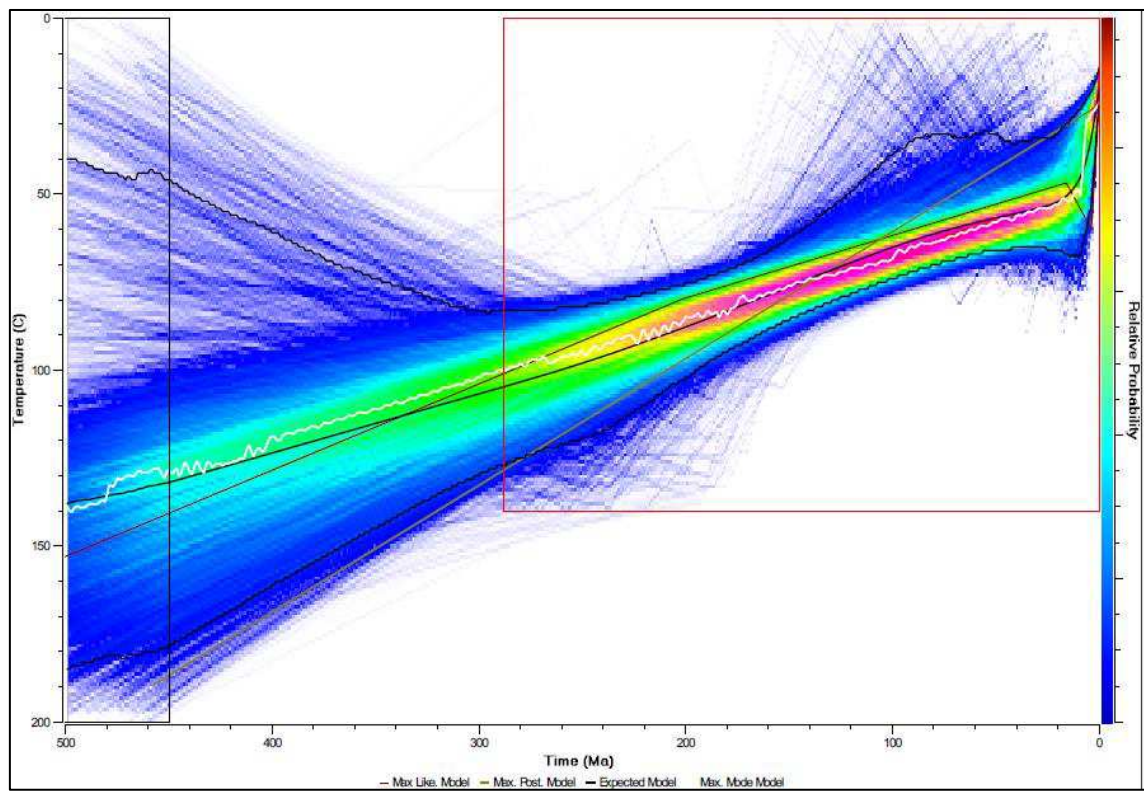
UY16 – AFT, AHE



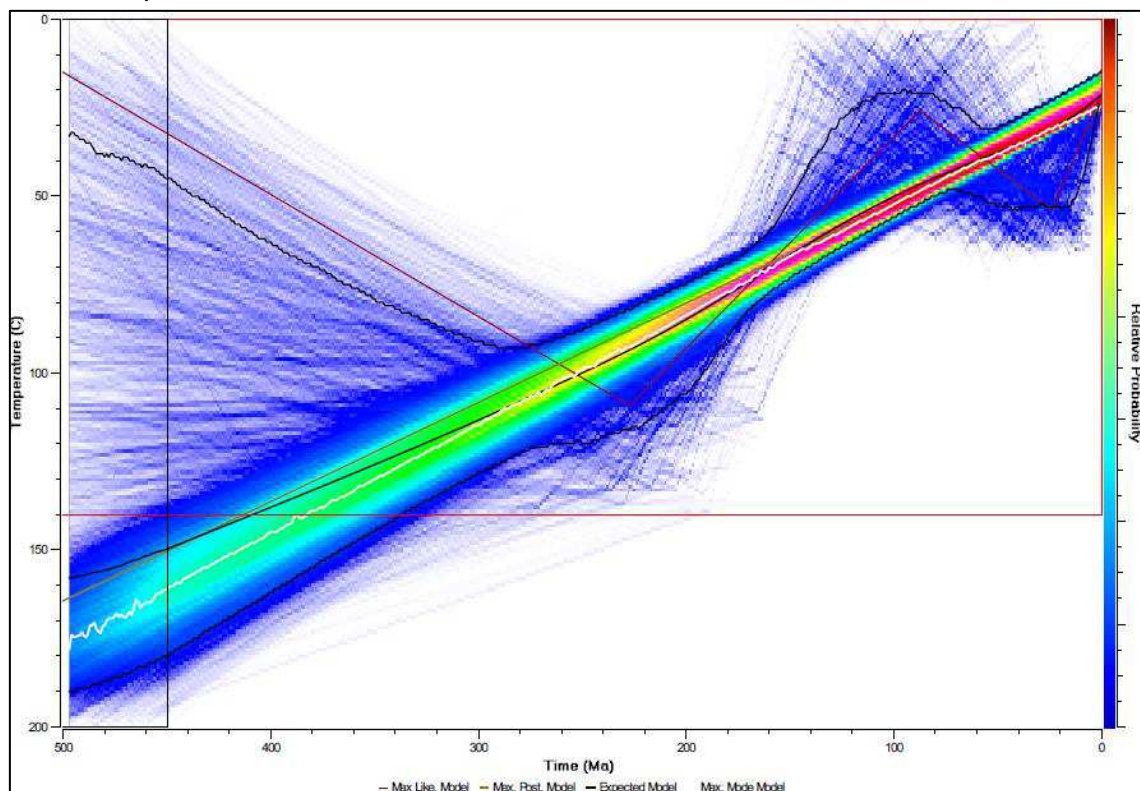
UY18 – AFT, AHE, ZHE



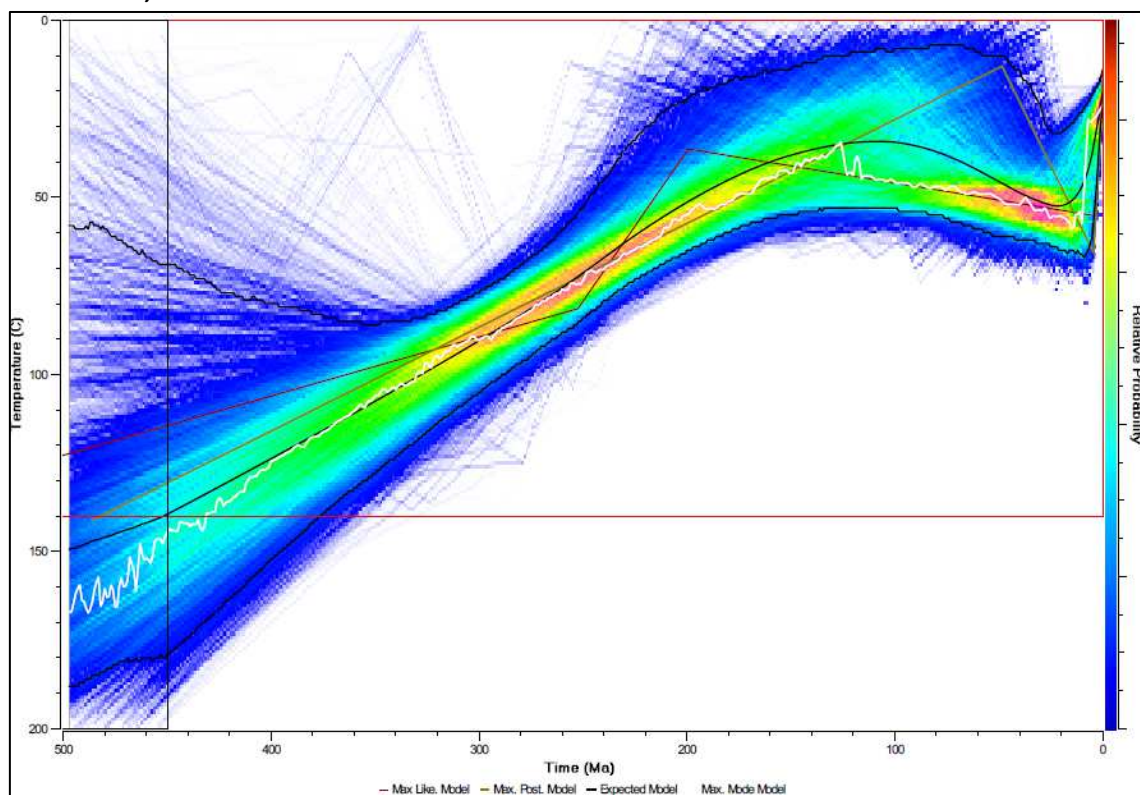
UY19 - AFT



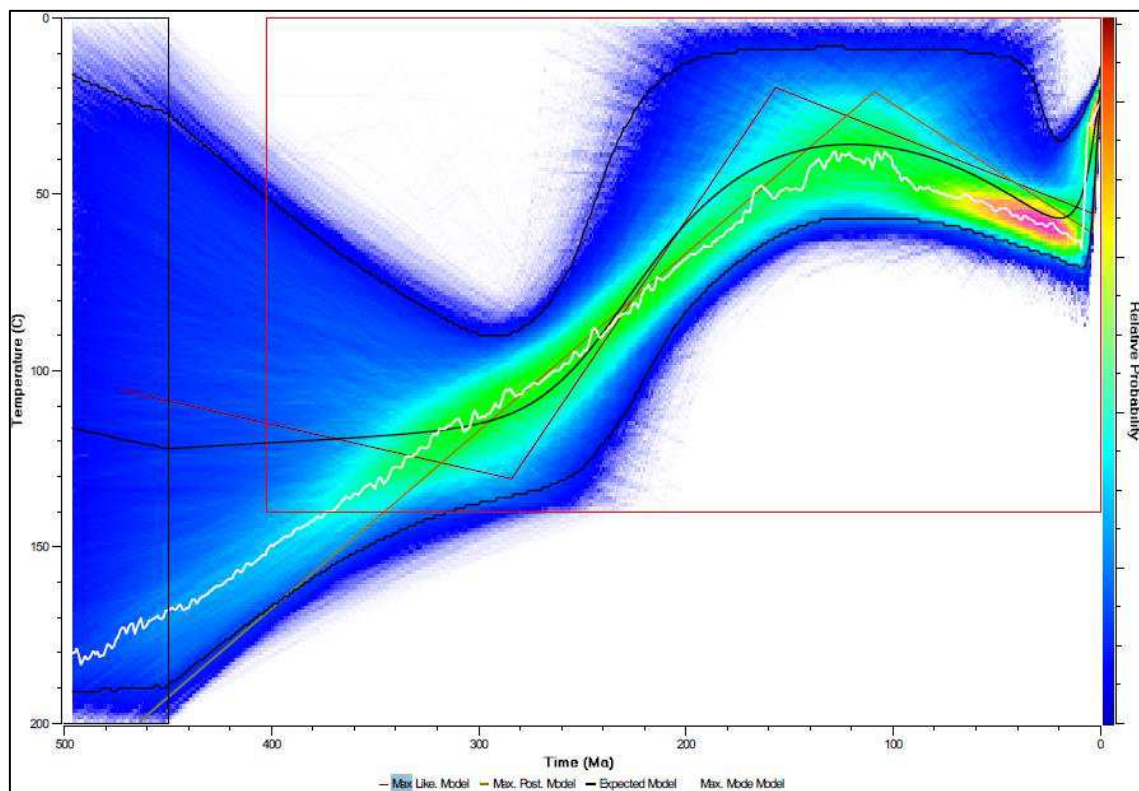
UY21 – AFT, AHE



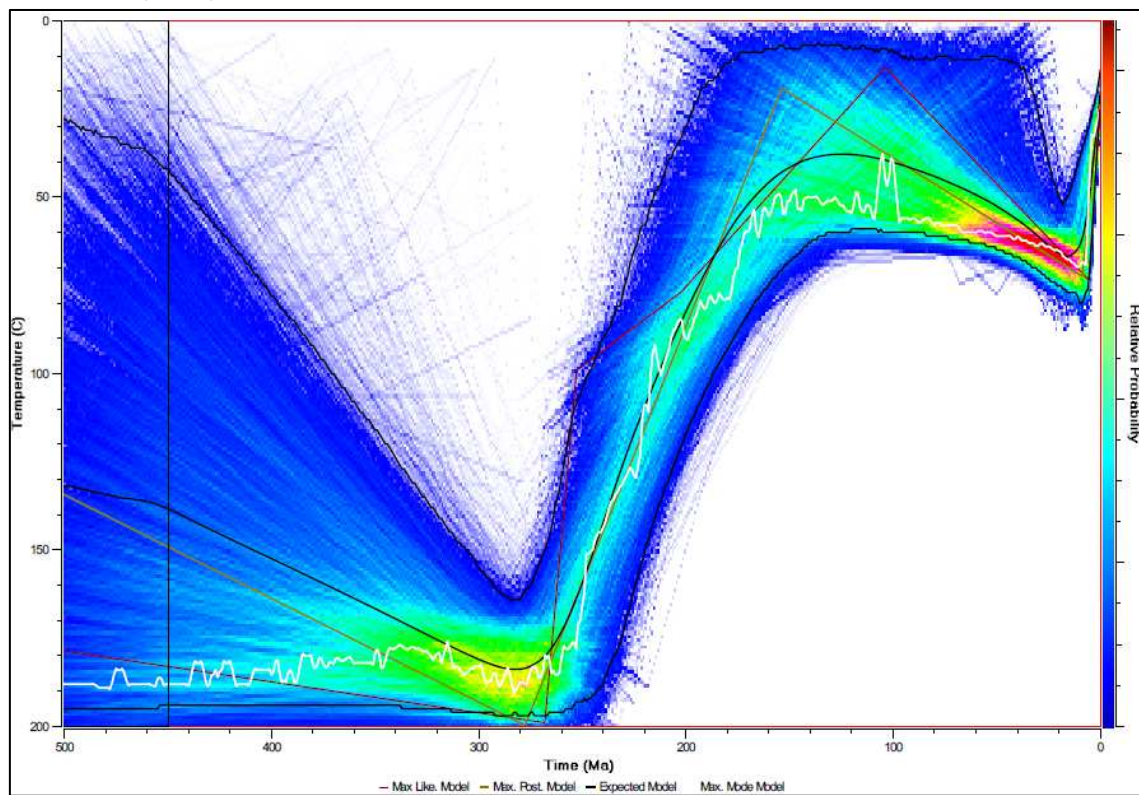
UY25 – AFT, AHE



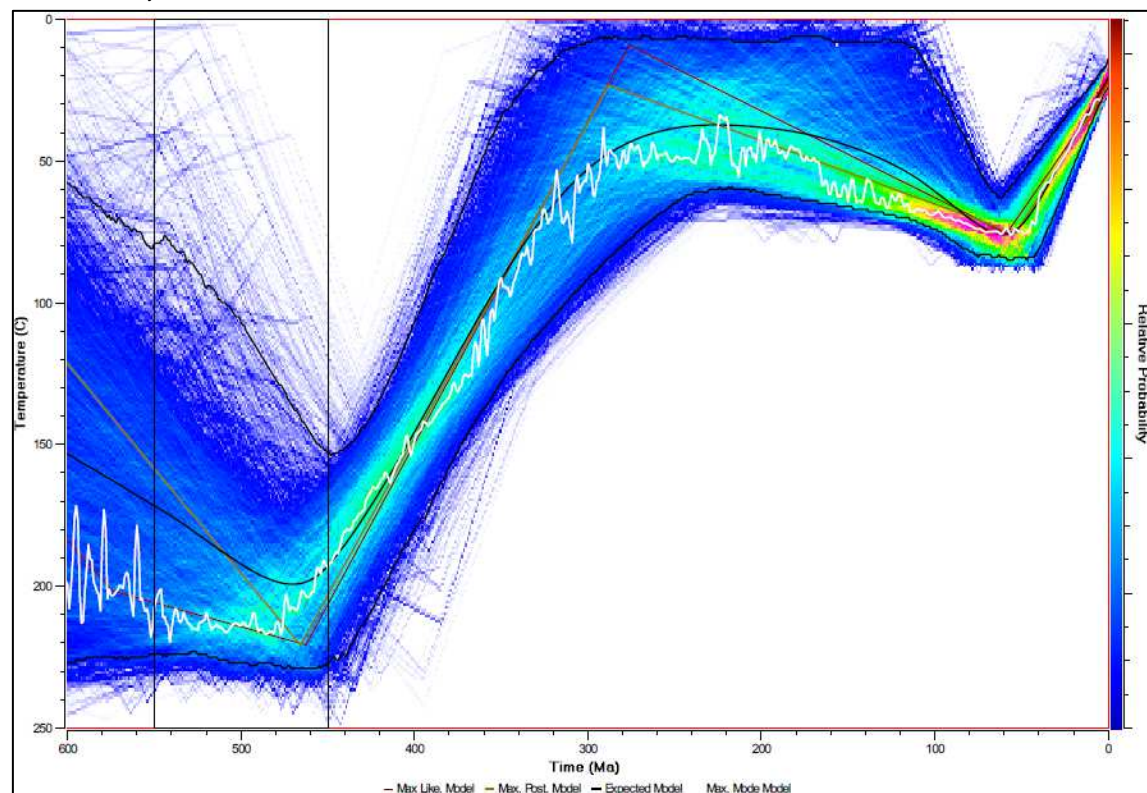
UY26 - AFT



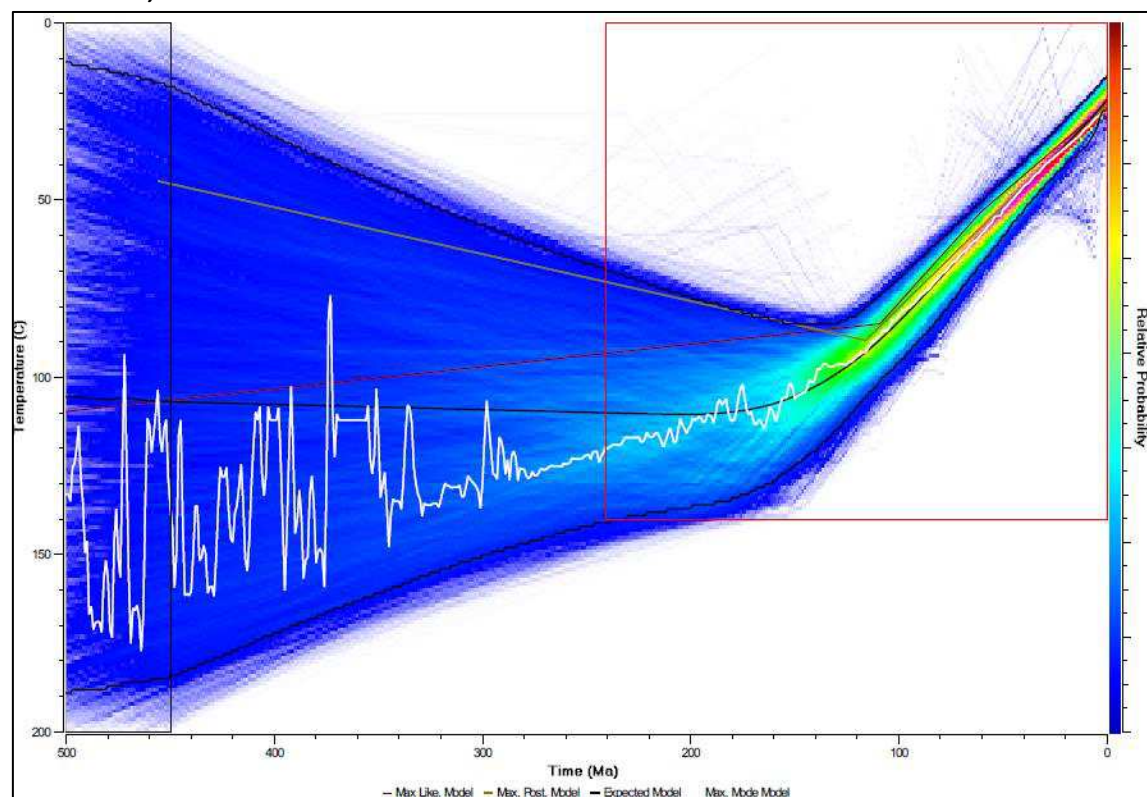
UY27 – AFT, AHE, ZHE

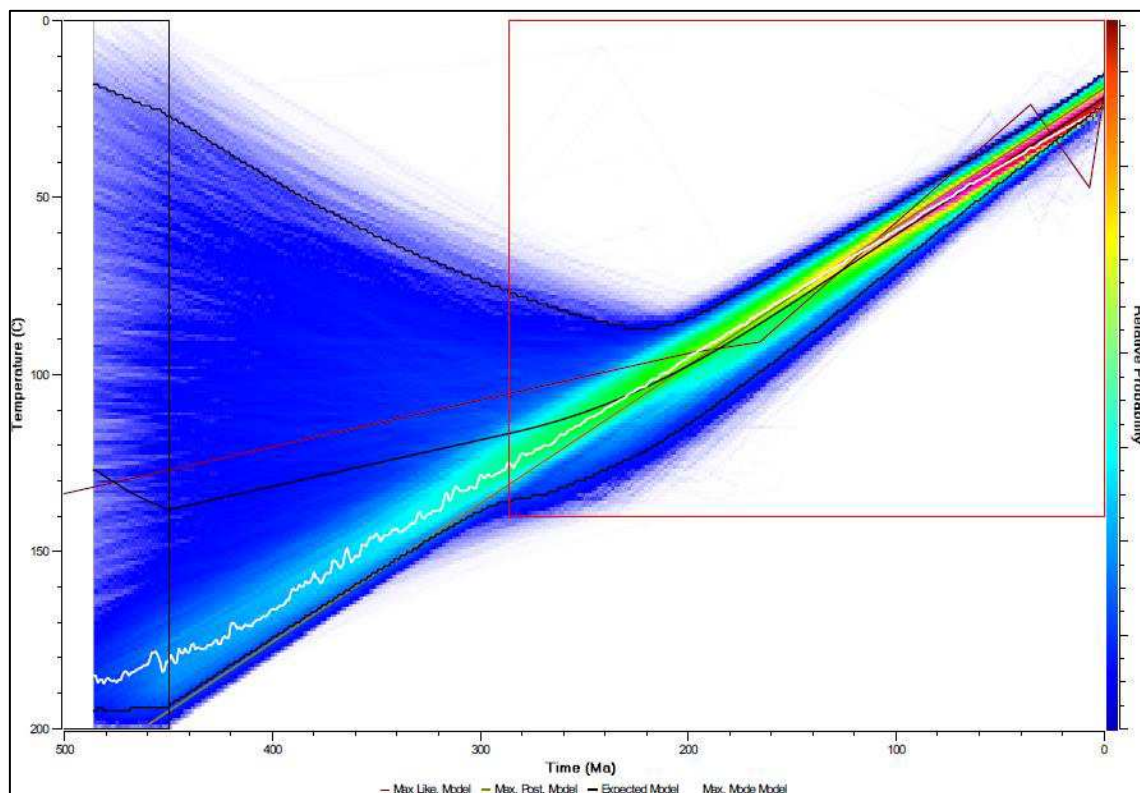
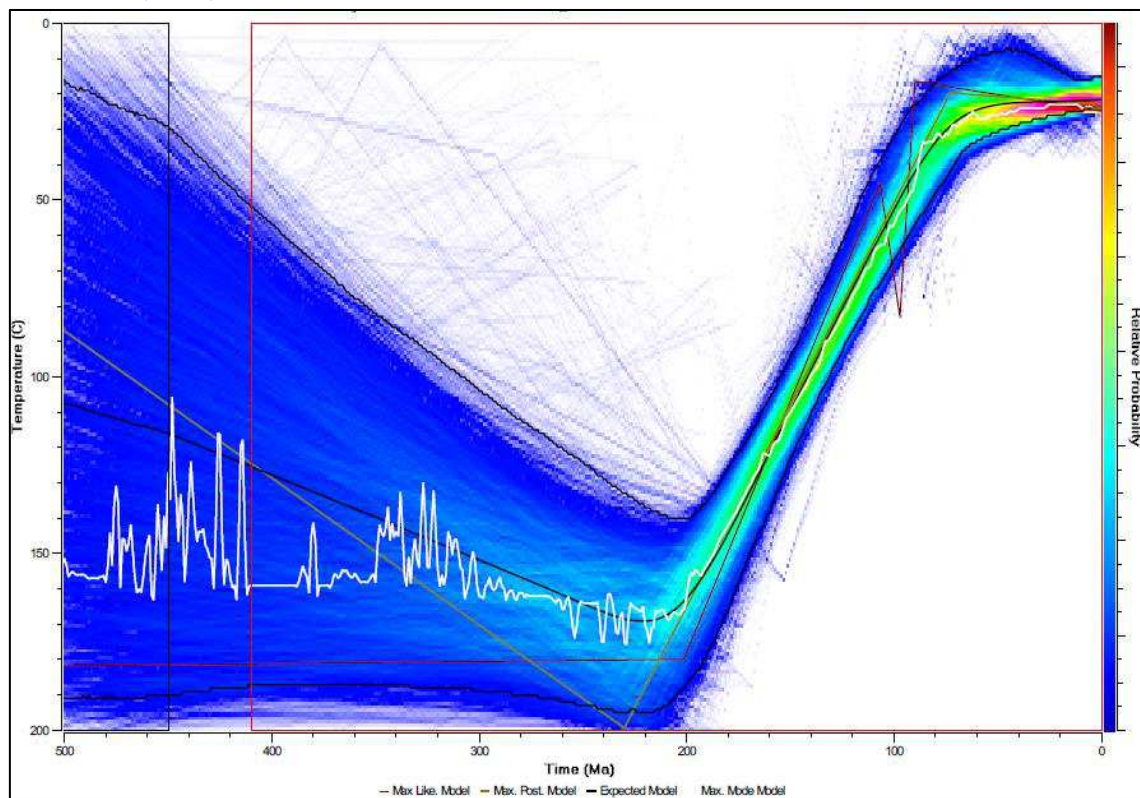


UY29 – AFT, ZHE



UY30 – AFT, AHE



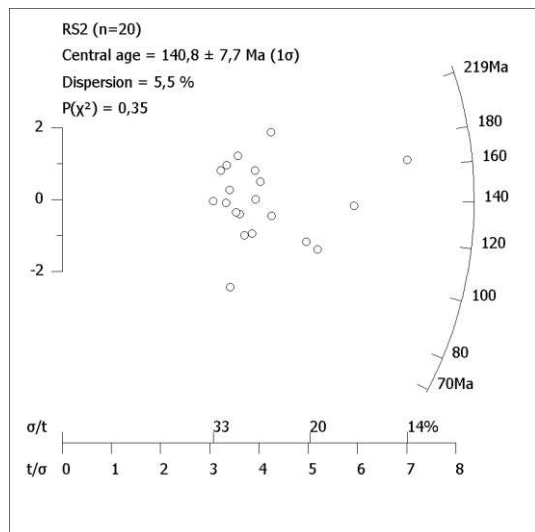
UY31 - AFT**UY32 – AFT, AHE, ZHE**

A3 Rio Grande do Sul data

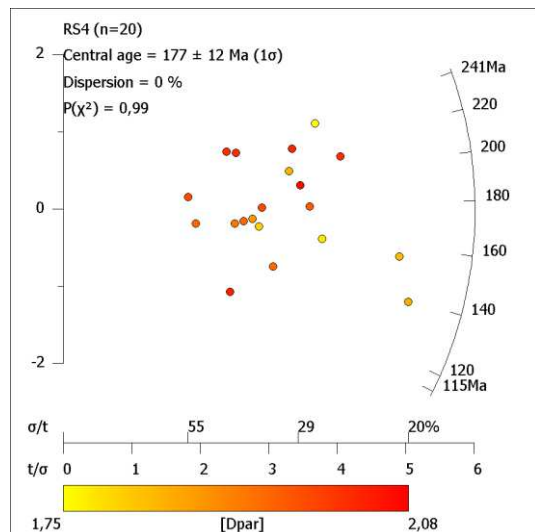
A3.1 Rio Grande do Sul radial plots

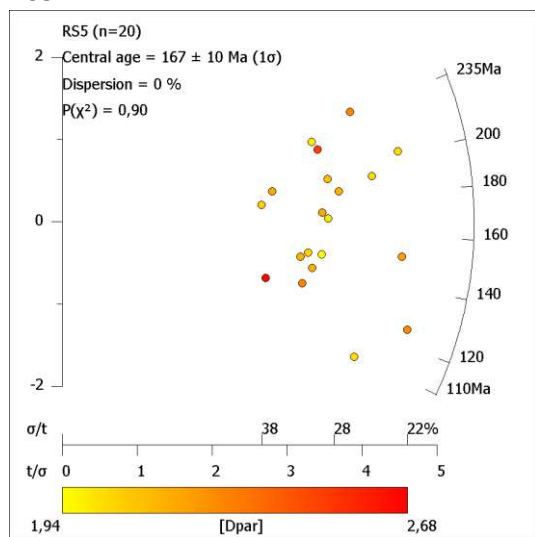
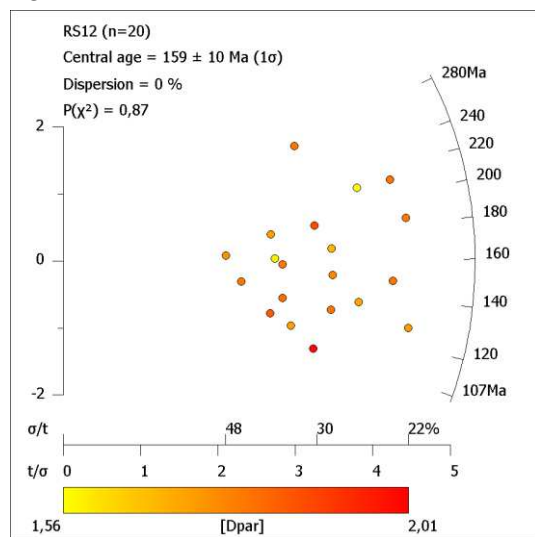
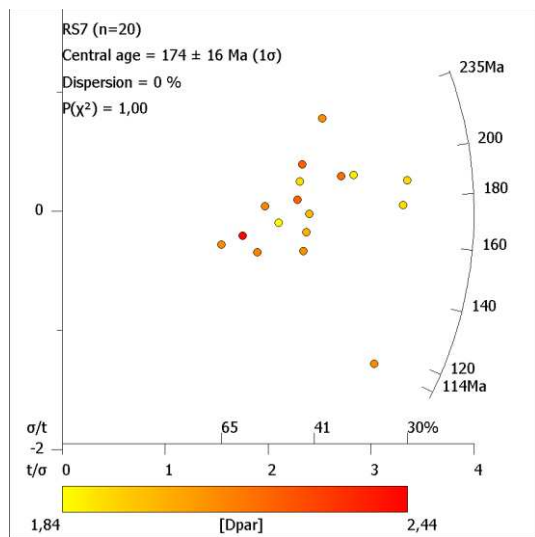
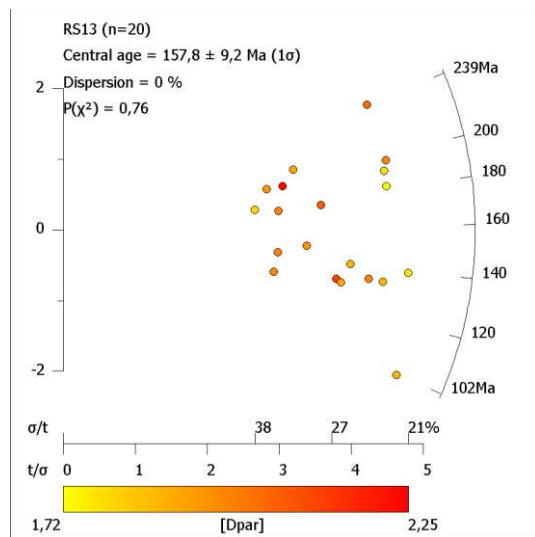
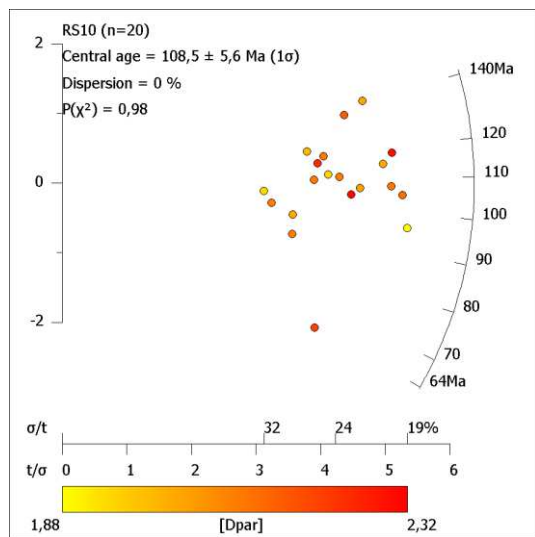
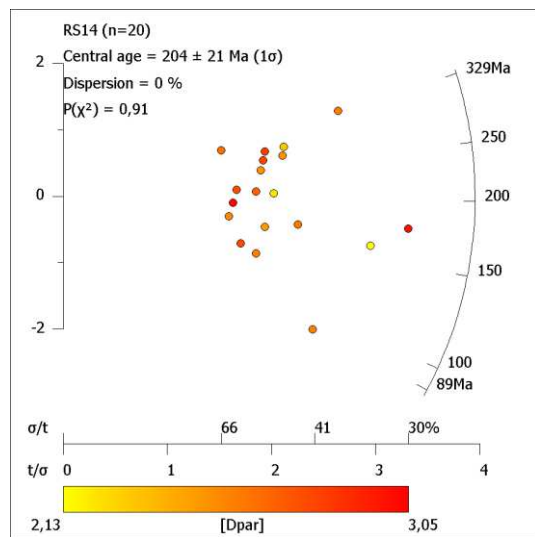
Radial plots, made with RadialPlotter 9.0, of single crystal AFT ages for each sample can be found below. All samples passed the homogeneity chi-square test ($P\chi^2 > 5\%$) and generally do not show age dispersion, even for the sedimentary samples (RS21 and RS22), which means that the central ages obtained correspond to single populations. Single crystal age dispersion is low (<5%) for all samples except RS23 and RS29, with 7% and 24% of dispersion, respectively. This dispersion could indicate a mix of apatite populations, but because they passed the chi-square test and their central ages agree with neighborhood samples, we considered them as single population as well. For any point, the age is given by extrapolating the radius through it to the circular scale. The vertical scale indicates ± 2 standard errors associated with any single estimate. The horizontal scale indicates approximate percent relative standard errors. For further information see Galbraith (1981), Galbraith & Green (1990) and Vermeesch (2009).

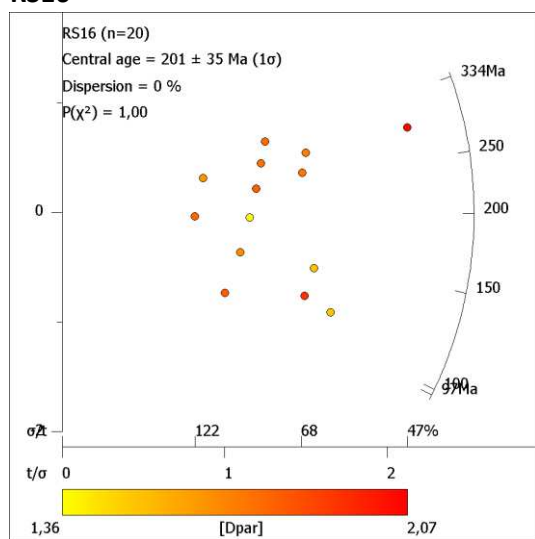
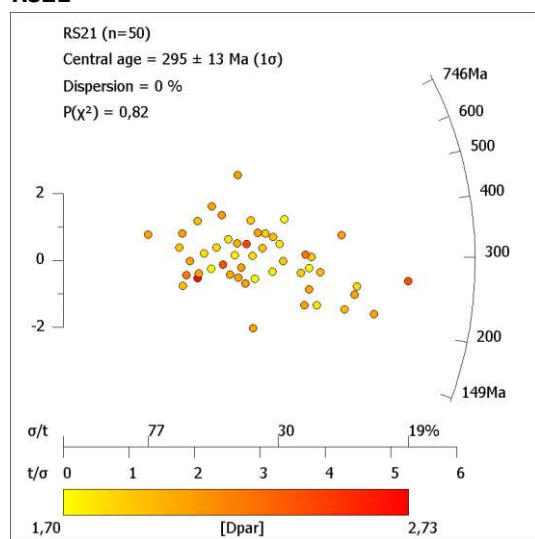
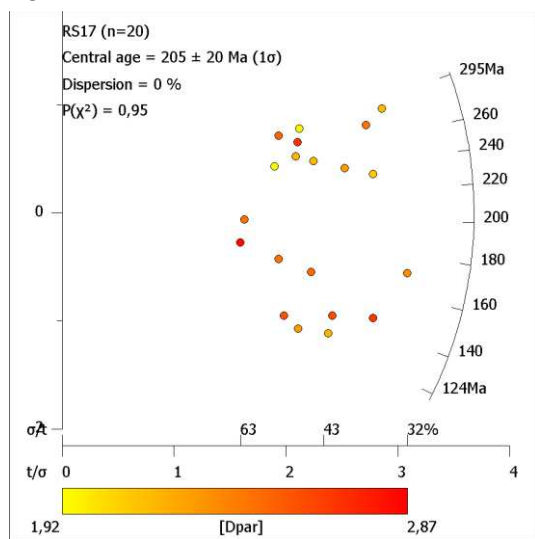
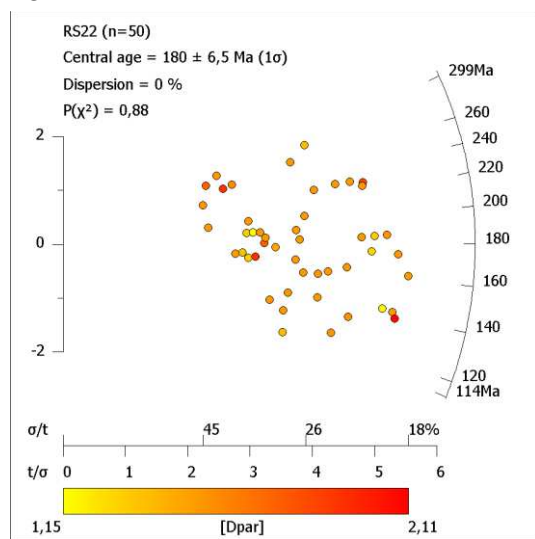
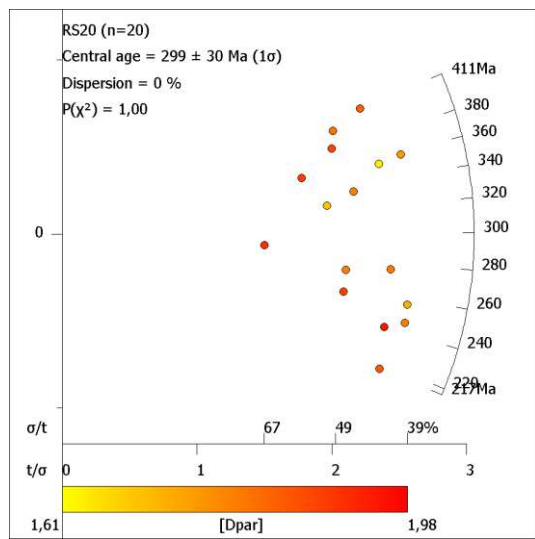
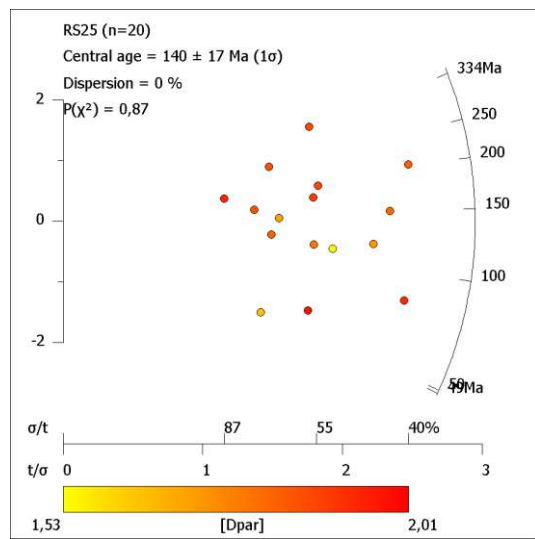
RS2 –

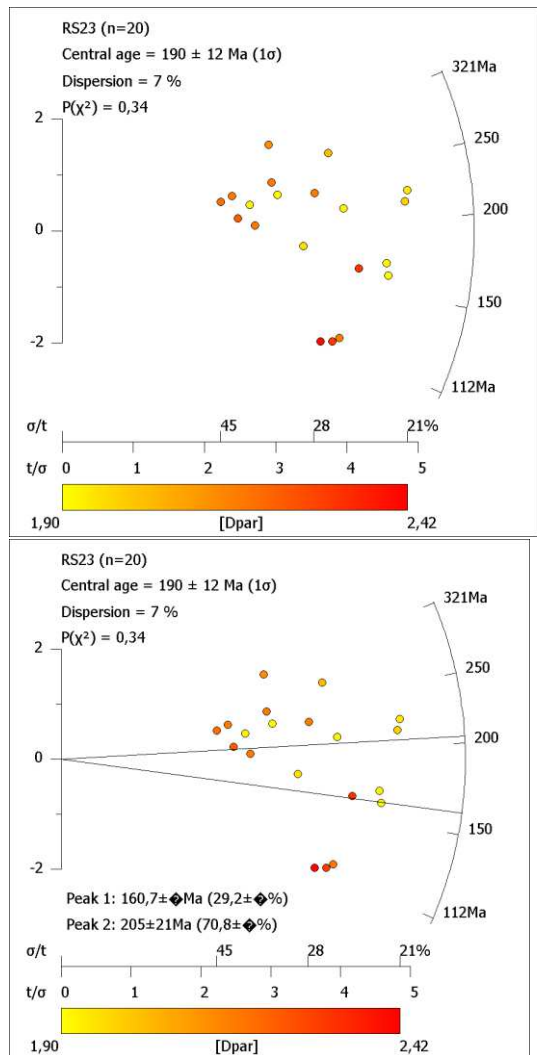
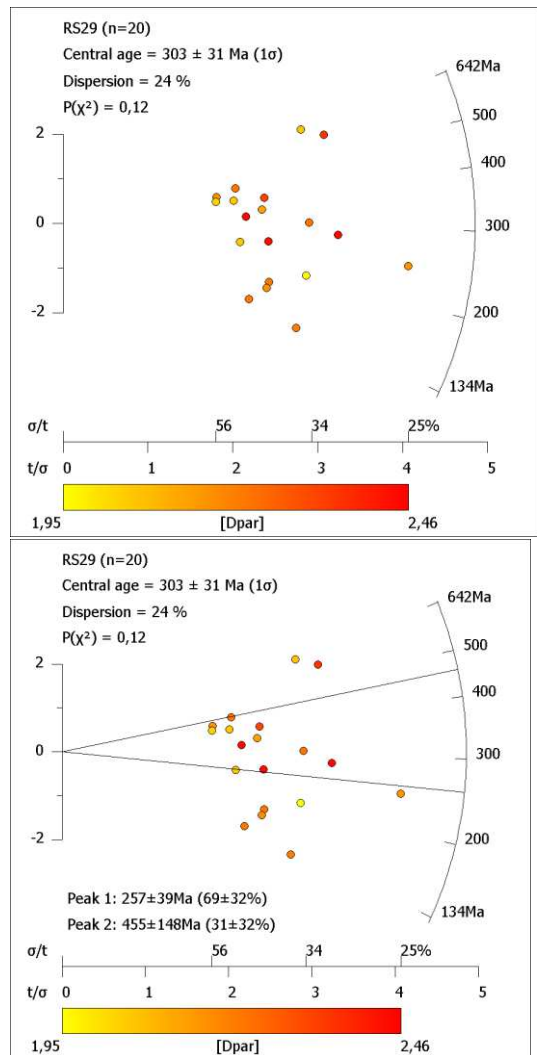
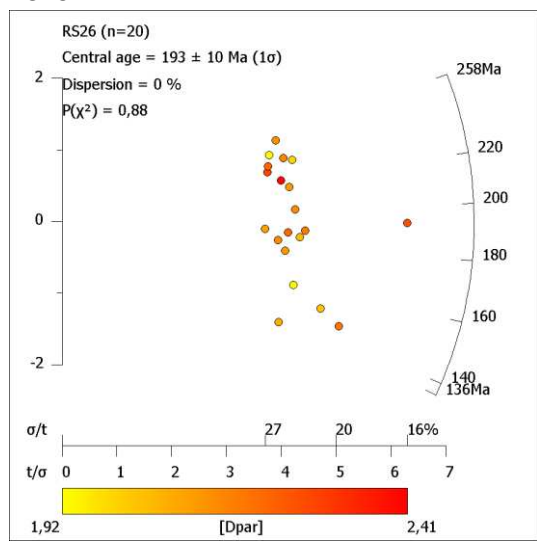


RS4 –



RS5 -**RS12 -****RS7 -****RS13 -****RS10 -****RS14 -**

RS16 –**RS21 –****RS17 –****RS22 –****RS20 –****RS25 –**

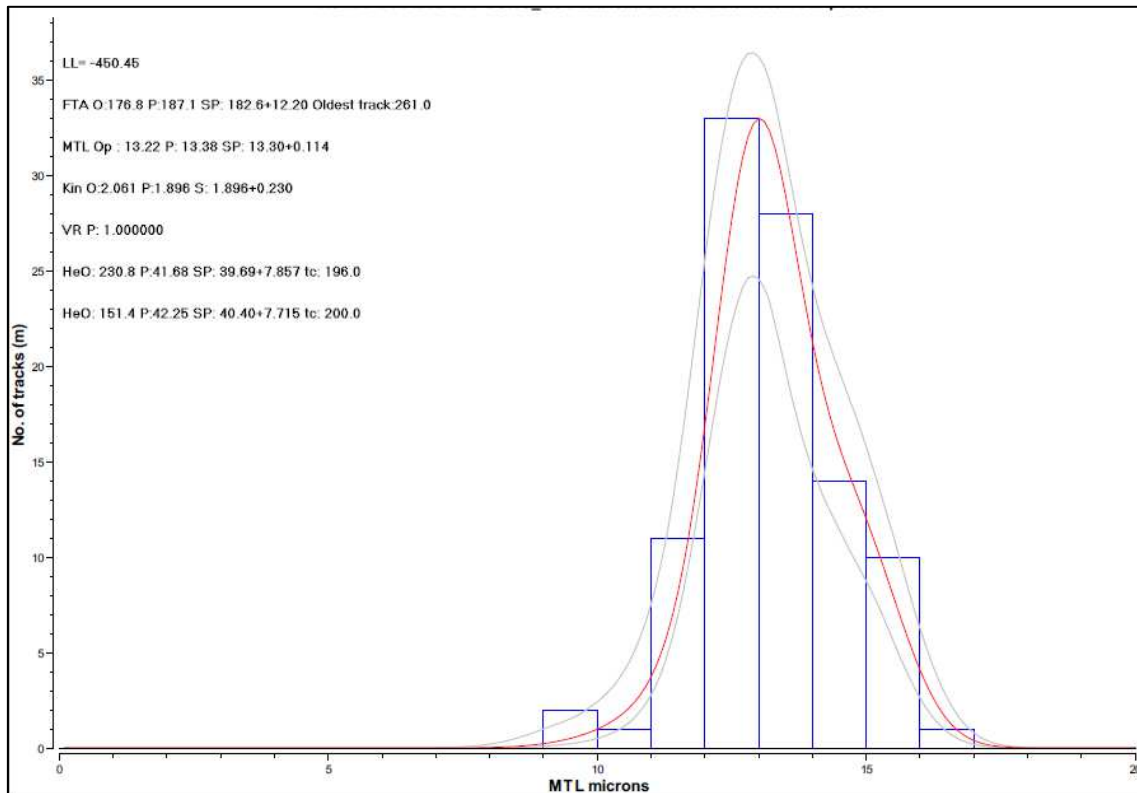
RS23 -**UY29 -****RS26 -**

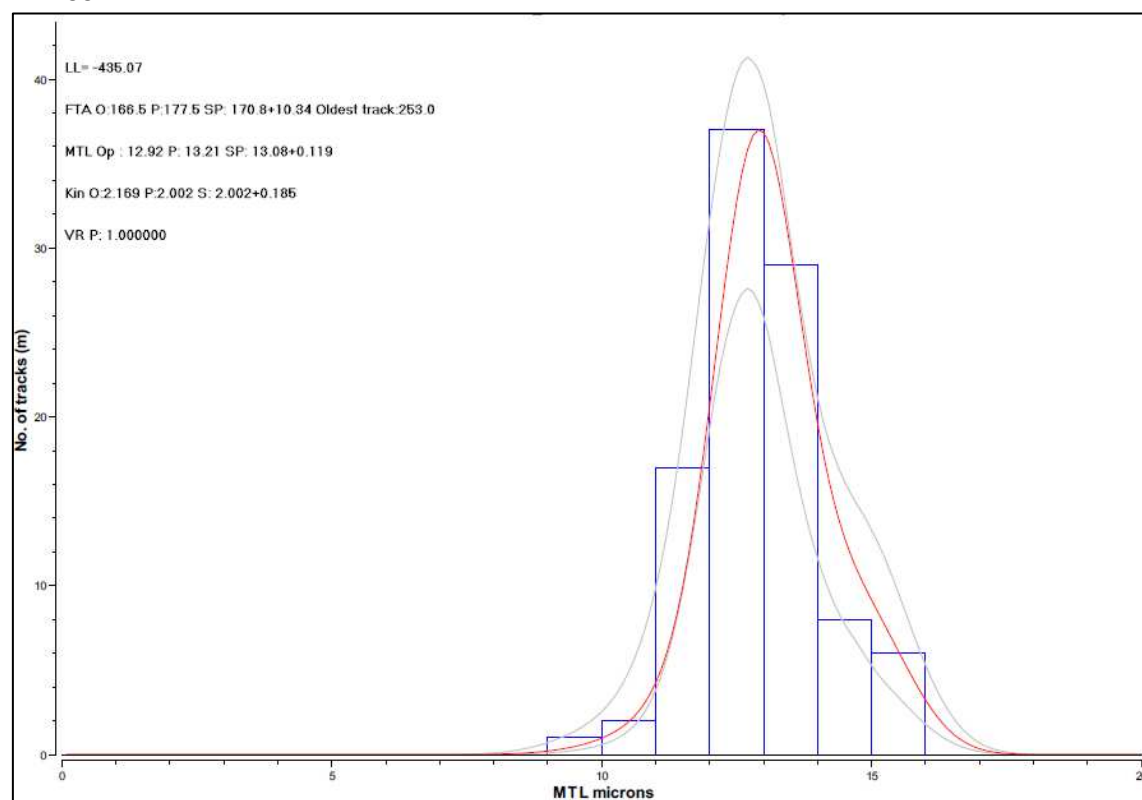
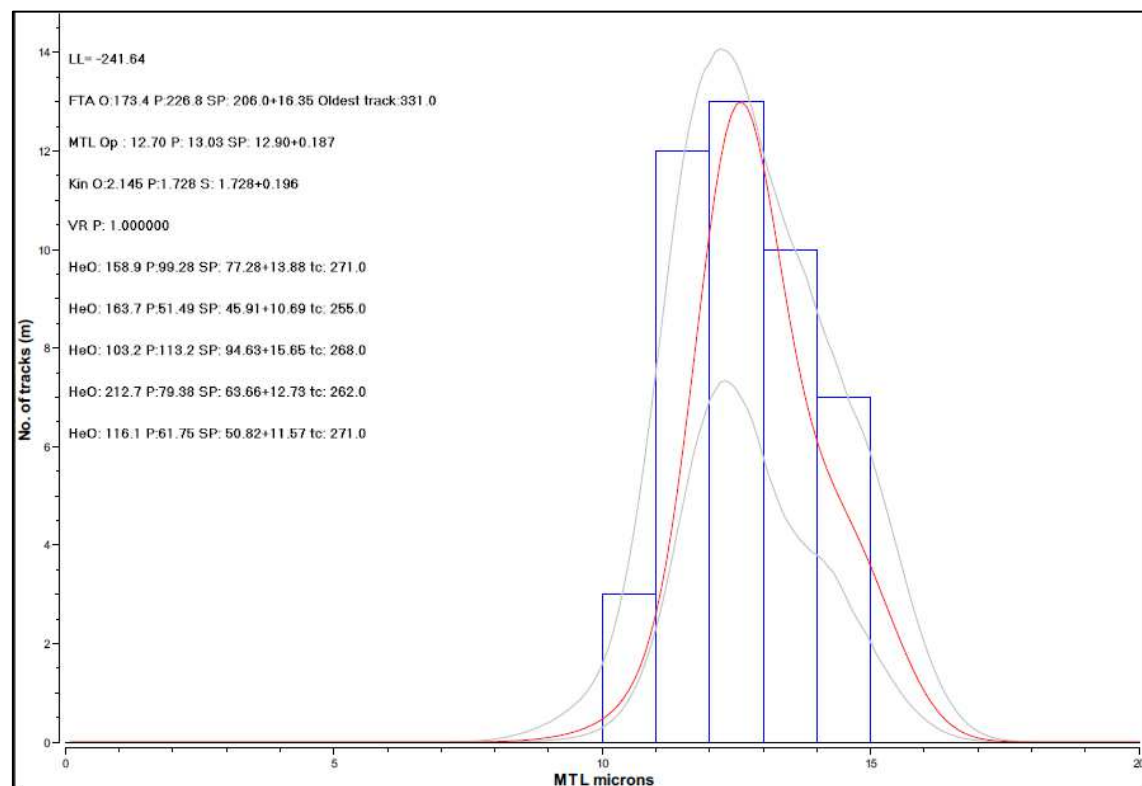
A3.2 Rio Grande do Sul fission-tracks distribution

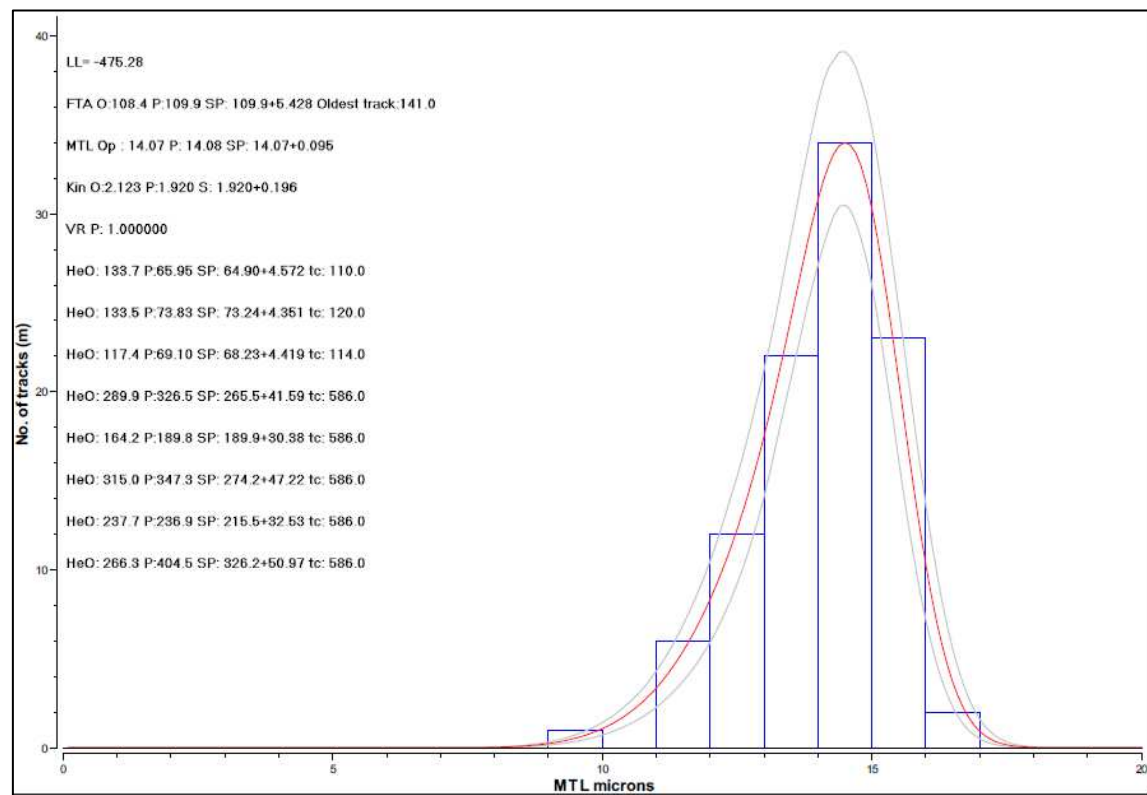
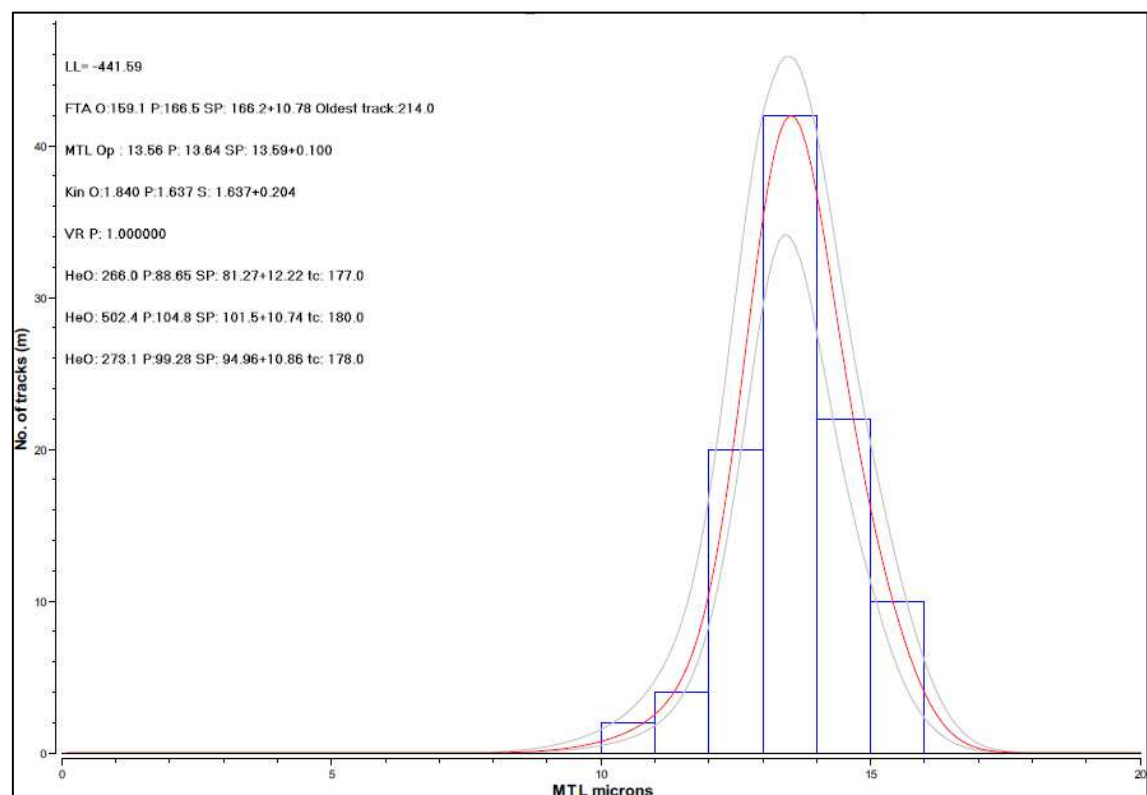
The *c*-axis corrected confined track length distribution (MTL) of each sample can be found below. The lengths scattering tends to be unimodal for all samples. In most cases, the track lengths distribution is Gaussian around the mean value. The gray lines define the range of track length distribution calculated during the inverse modeling, while the red line represents the length distribution calculated for the mean trajectory of the model (*i.e.* the length distribution that corresponds to the trajectories shown in figures 6.6 and 6.7). The total number of confined tracks (N) is indicated as well. For further information see Gallagher 2009, 2012 and QTQt User Guide v5.7)

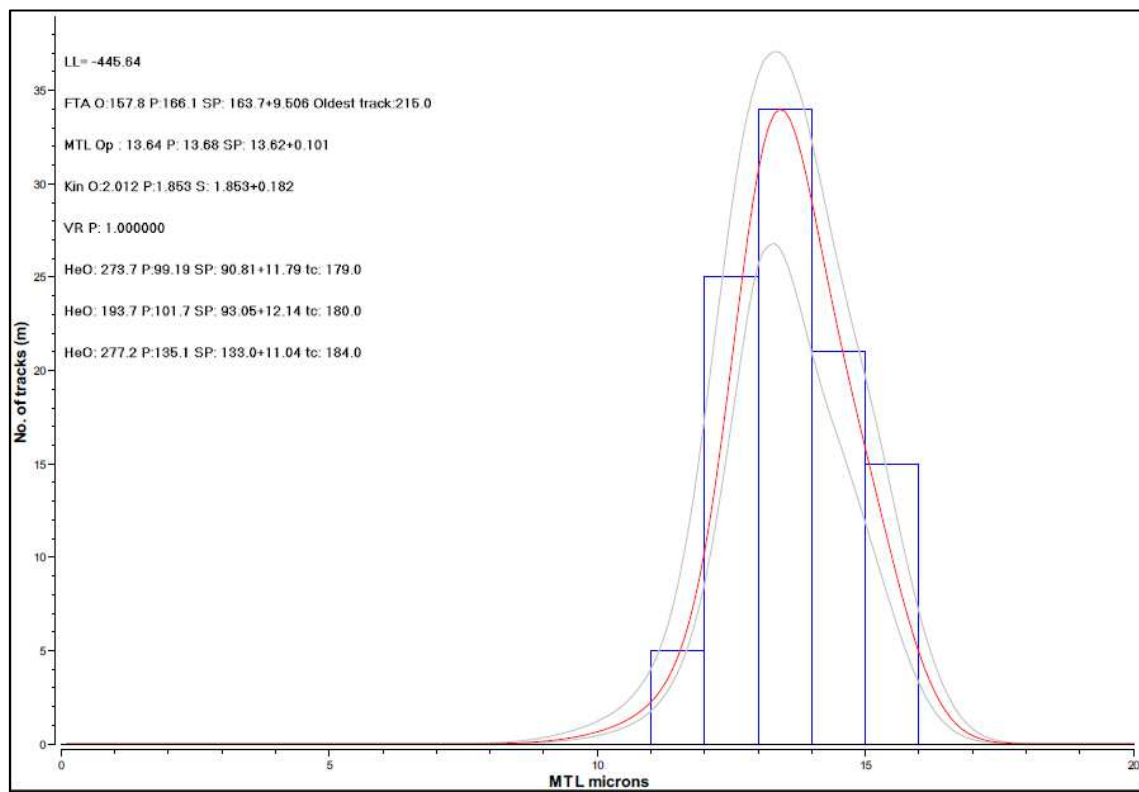
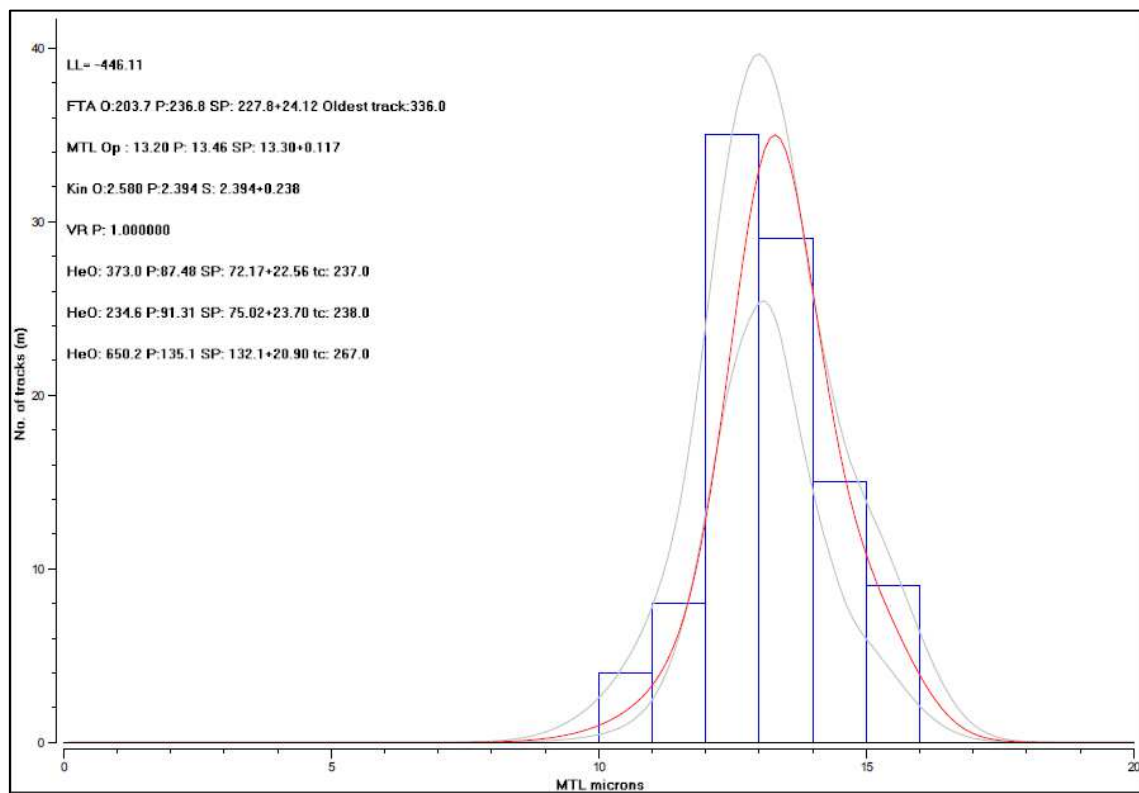
RS4 – AFT, AHE, ZHE

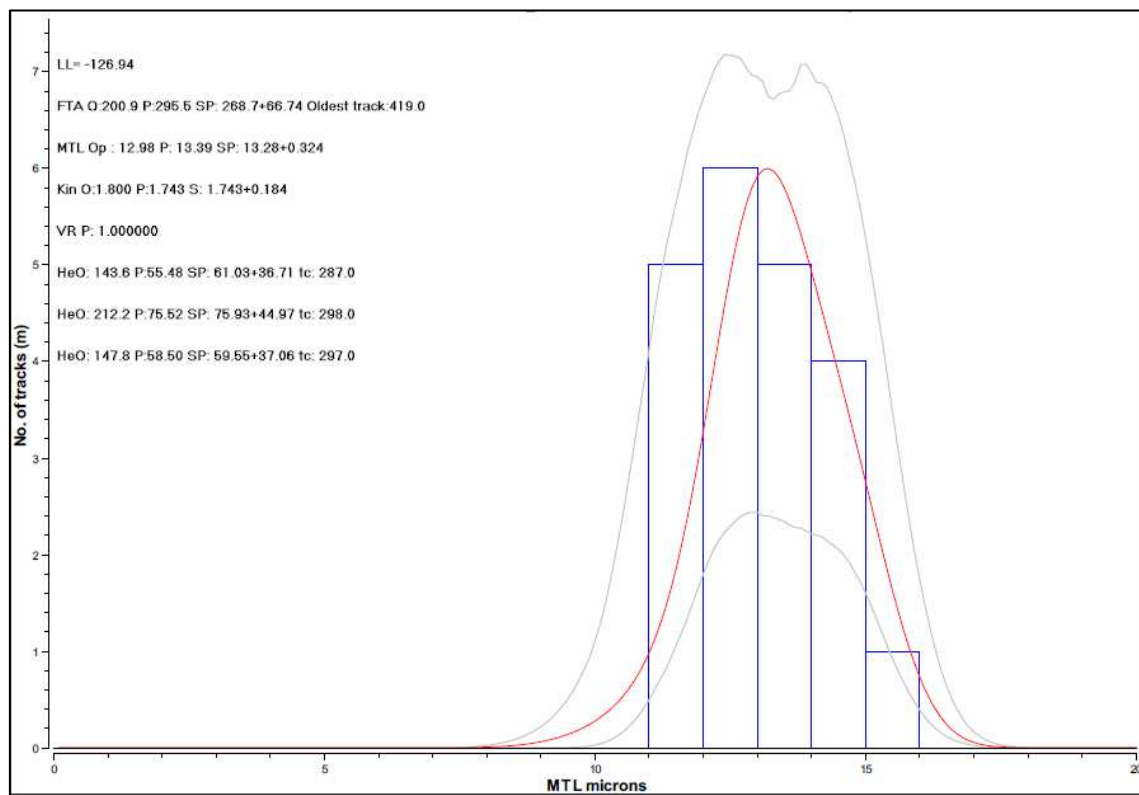
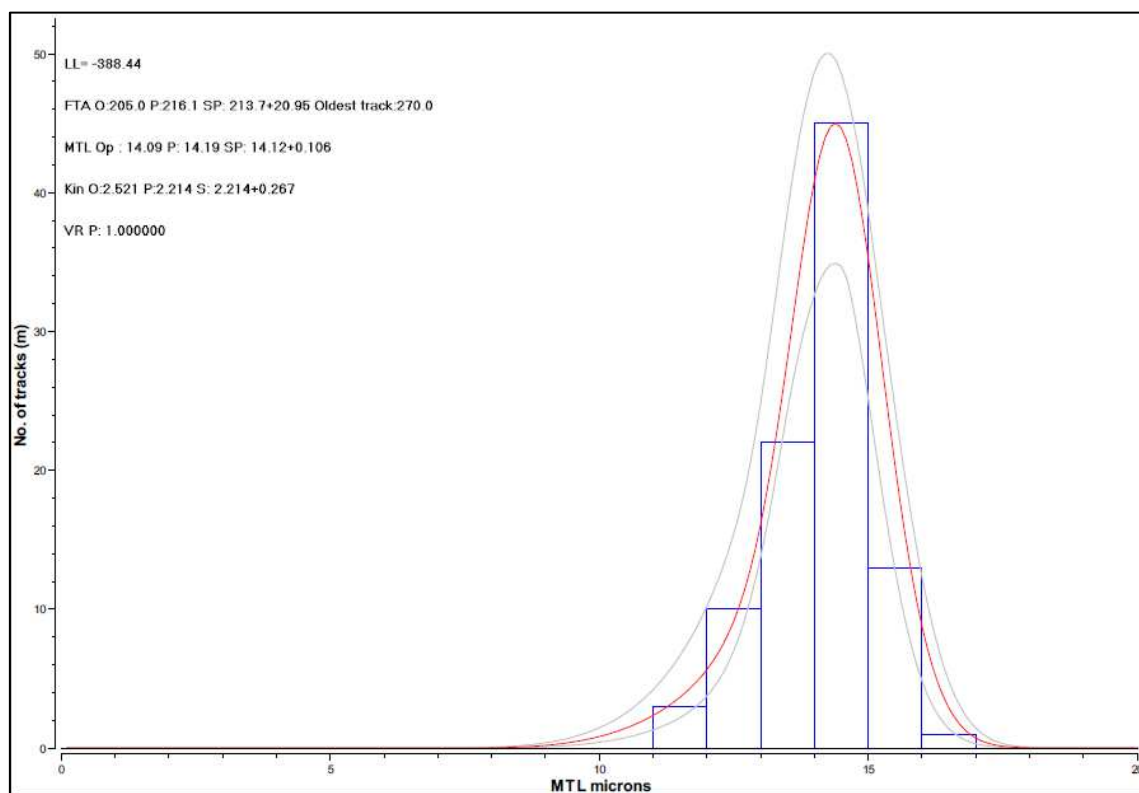
N= 100

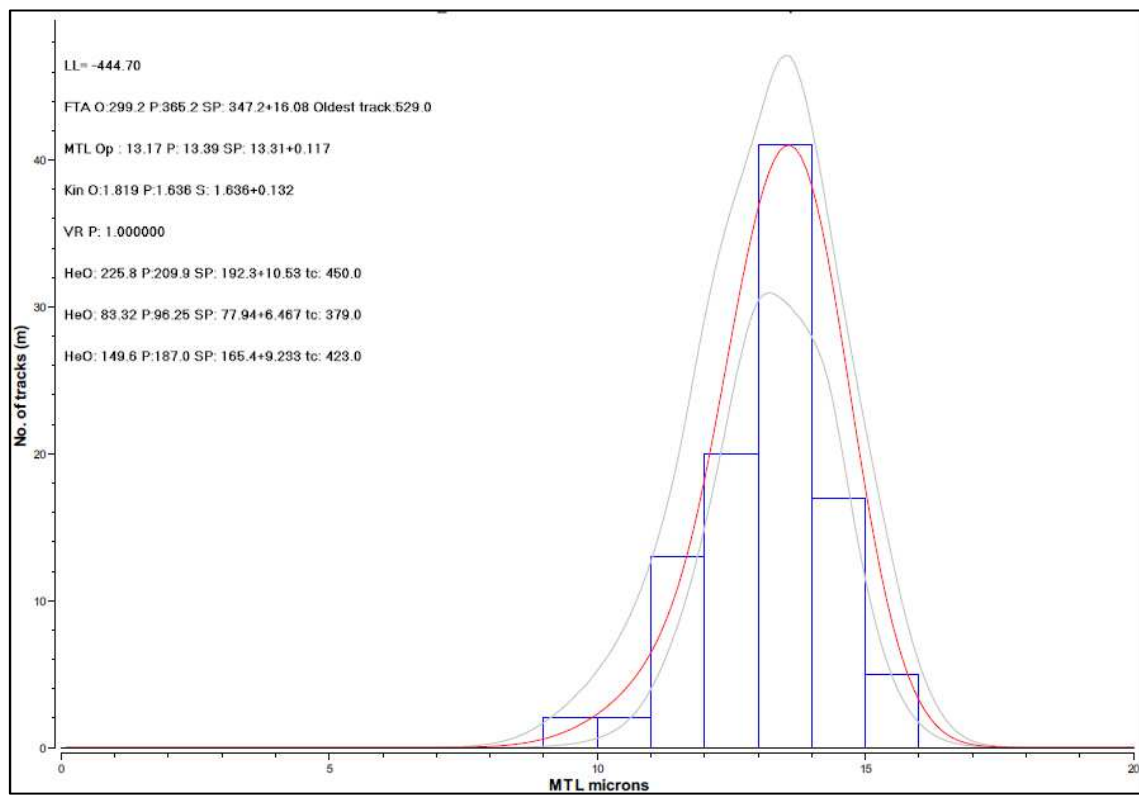
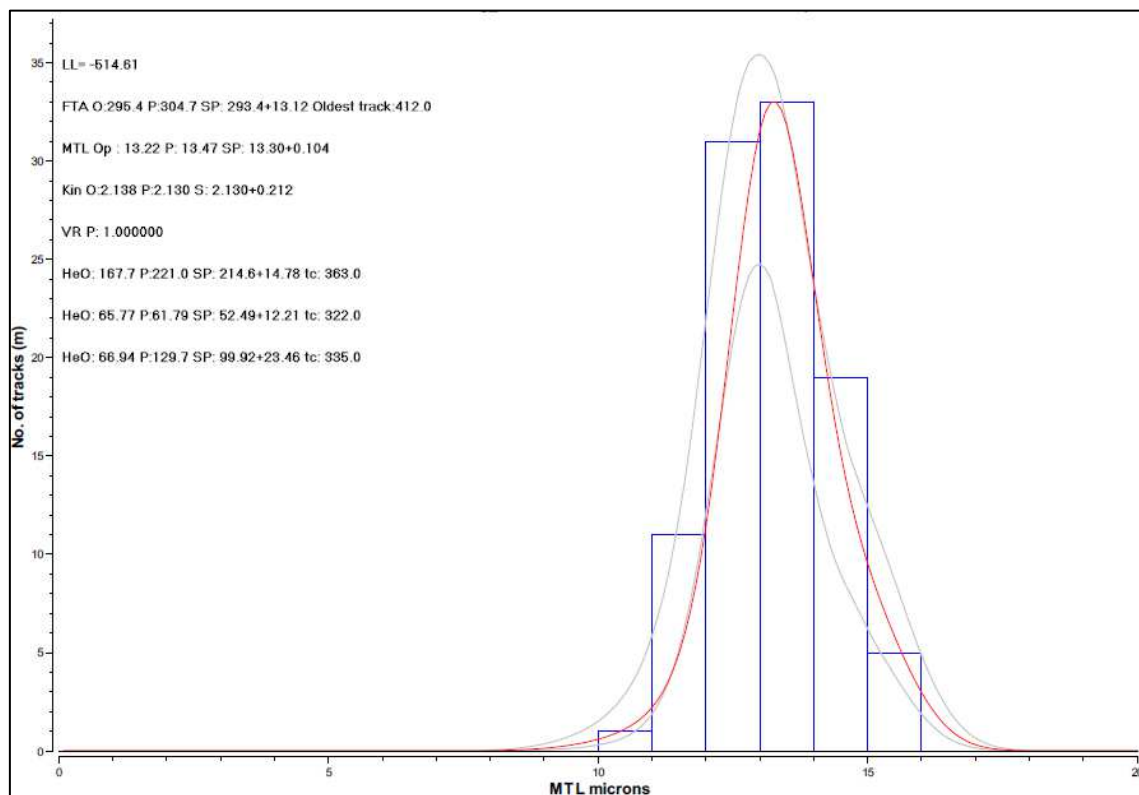


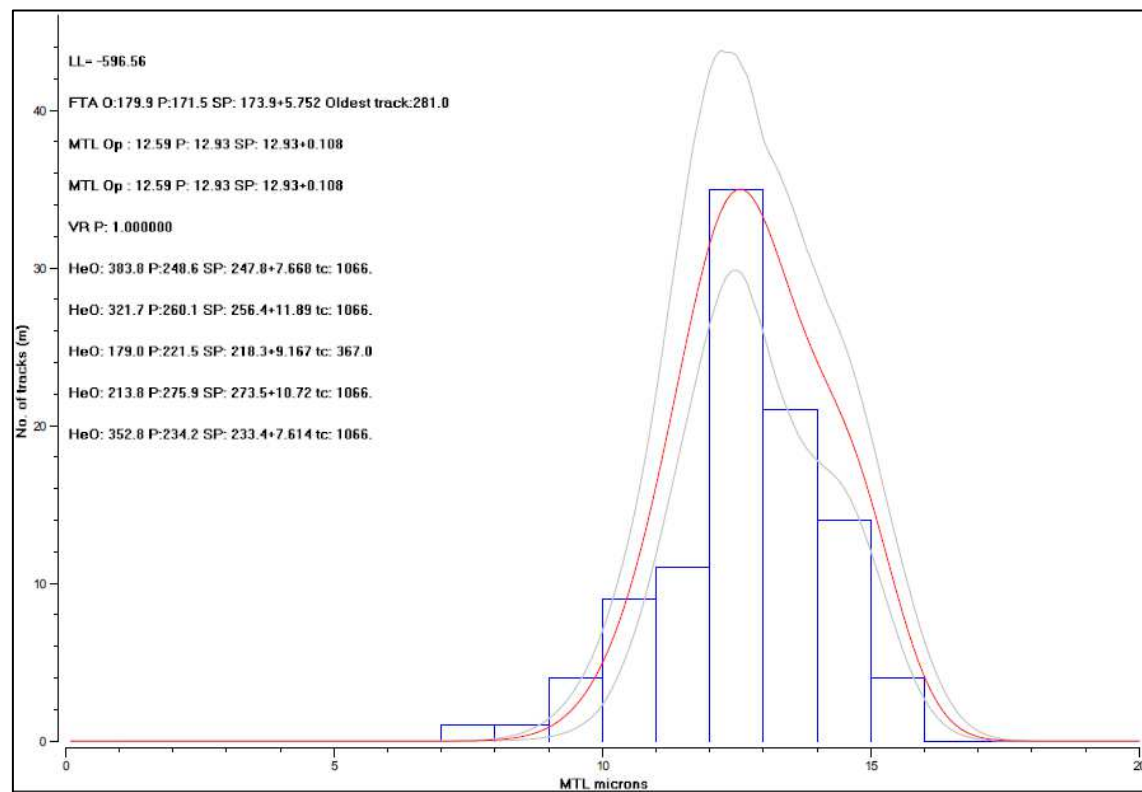
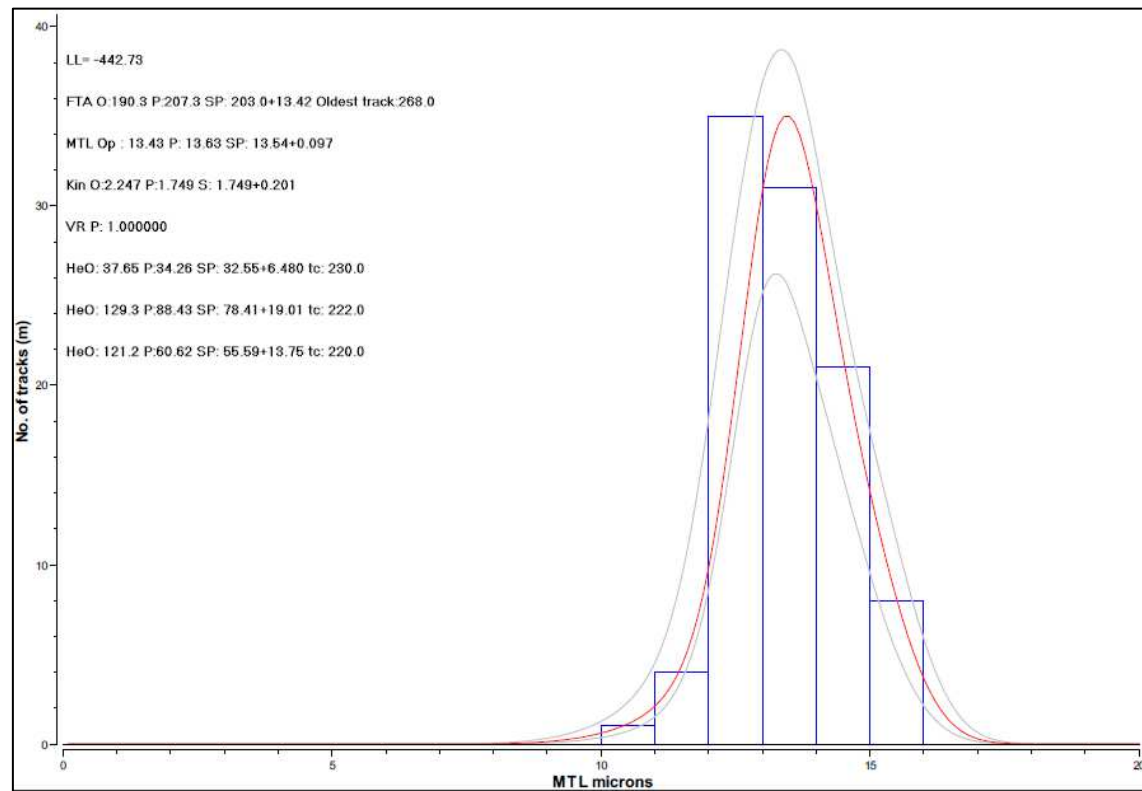
RS5 – AFT**N= 100****RS7 – AFT, AHE****N= 45**

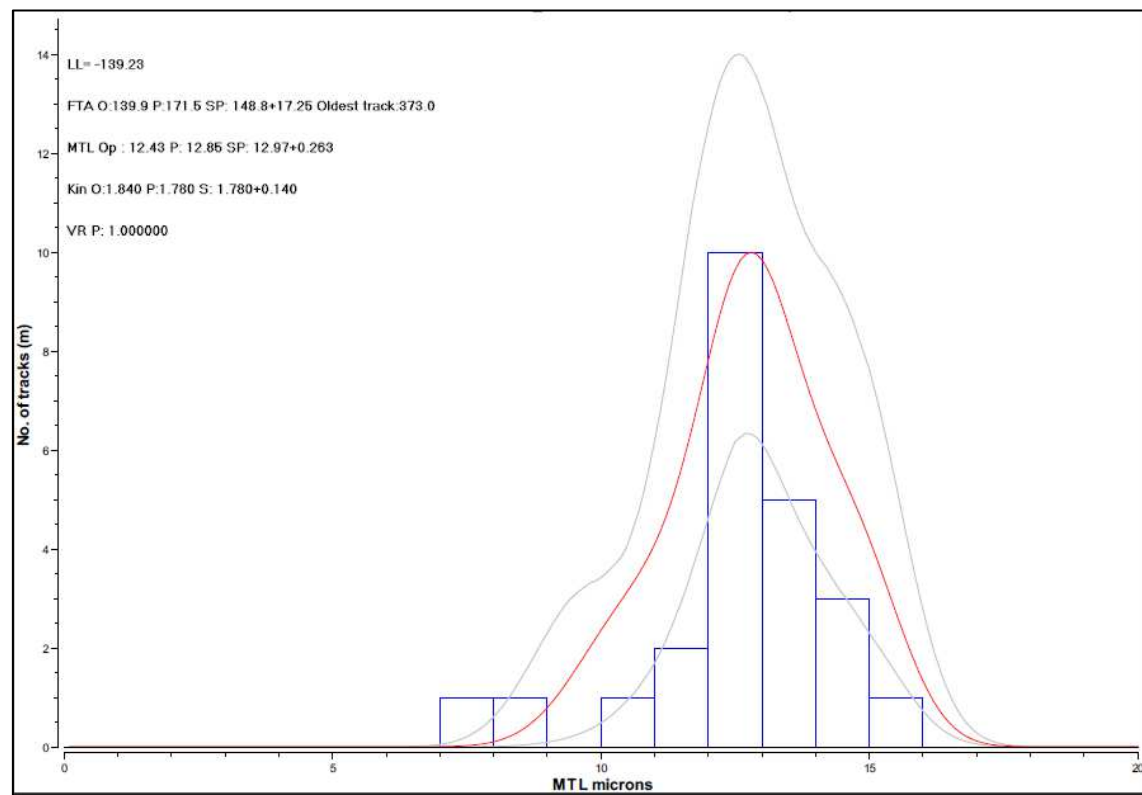
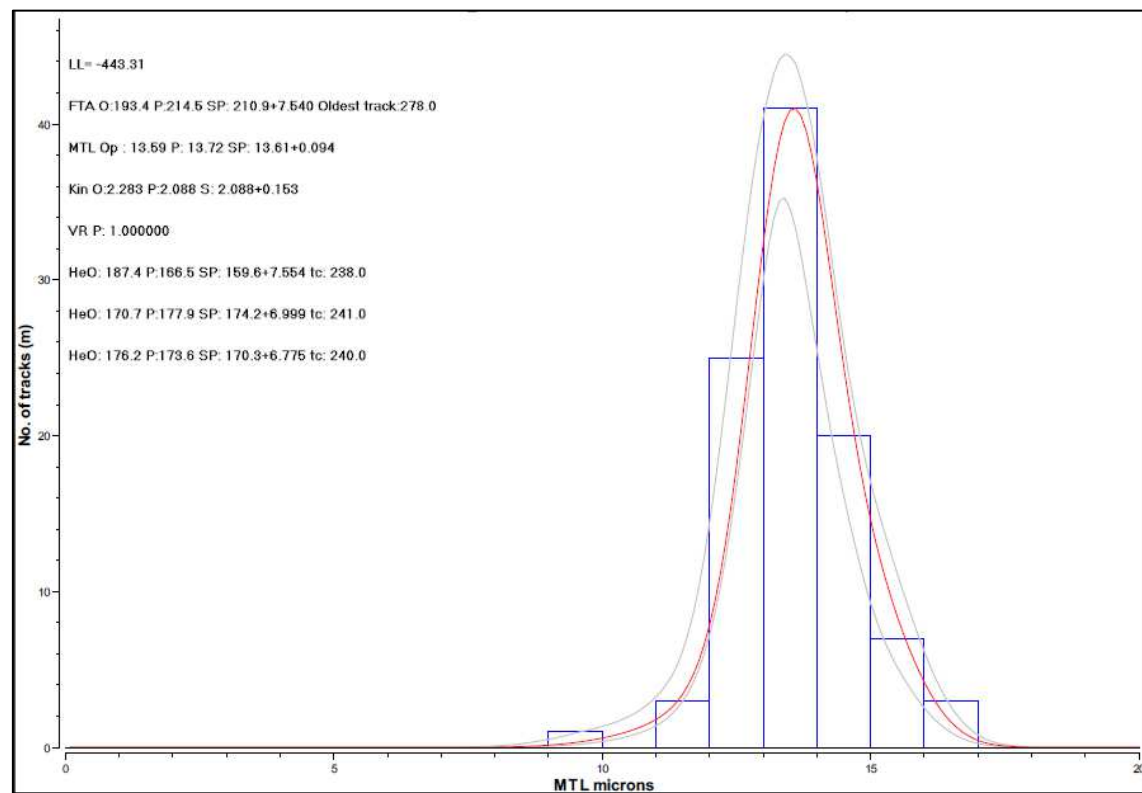
RS10 – AFT, AHE, ZHE**N= 100****RS12 – AFT, AHE****N= 100**

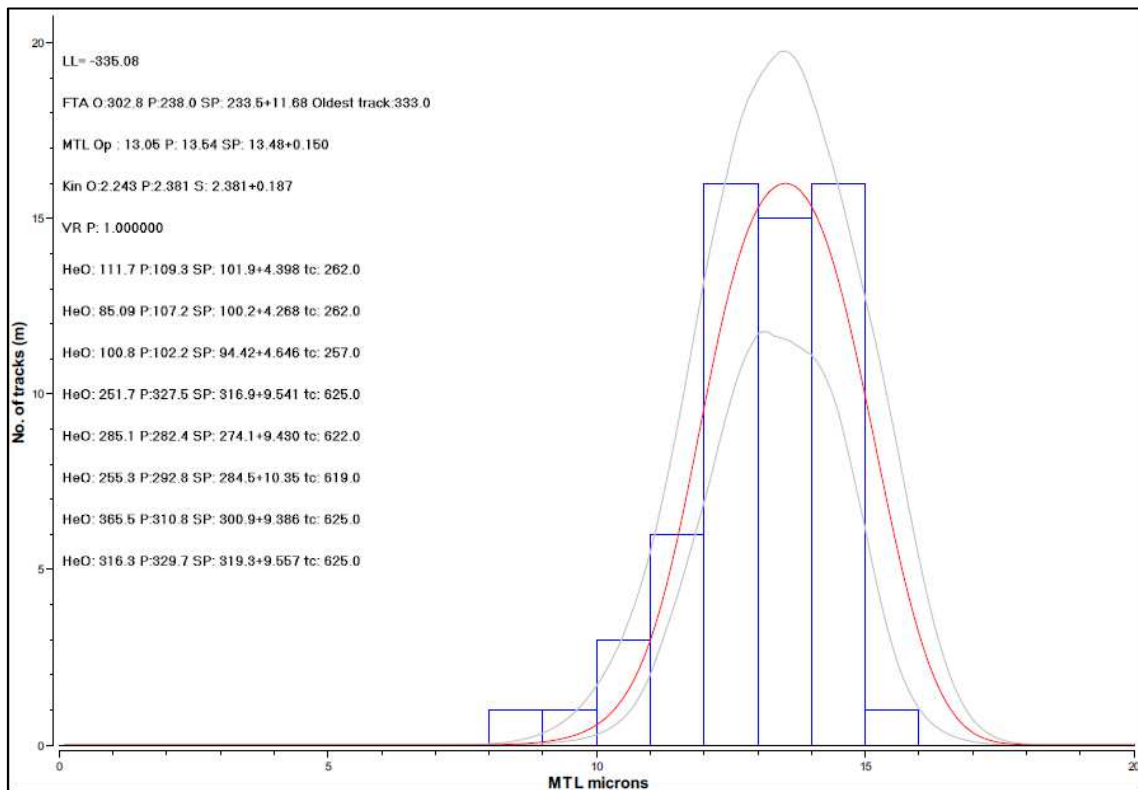
RS13 – AFT, AHE, ZHE**N= 100****RS14 – AFT, AHE****N= 100**

RS16 – AFT, AHE**N= 21****RS17 – AFT****N= 94**

RS20 – AFT, AHE**N= 100****RS21 – AFT, AHE****N= 100**

RS22 – AFT, ZHE**N= 100****RS23 – AFT, AHE****N= 100**

RS25 – AFT, AHE**N= 24****RS26 – AFT, AHE****N= 100**

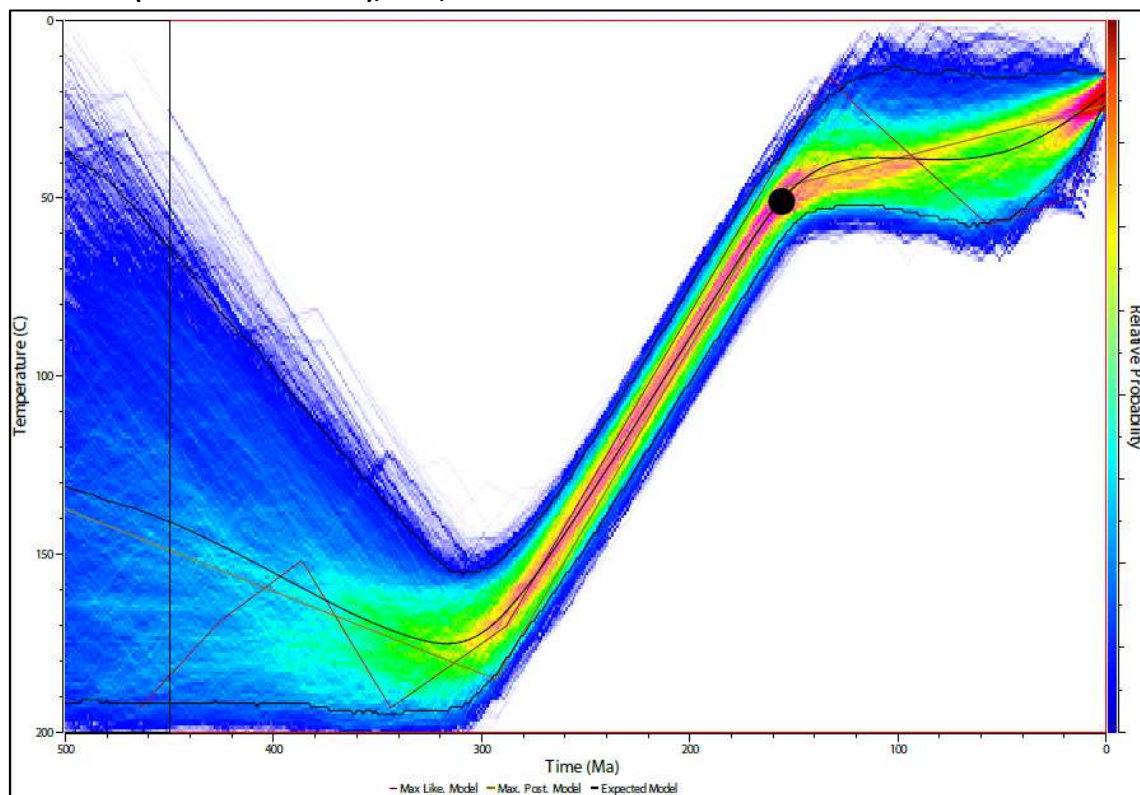
RS29 – AFT, AHE, ZHE**N= 59**

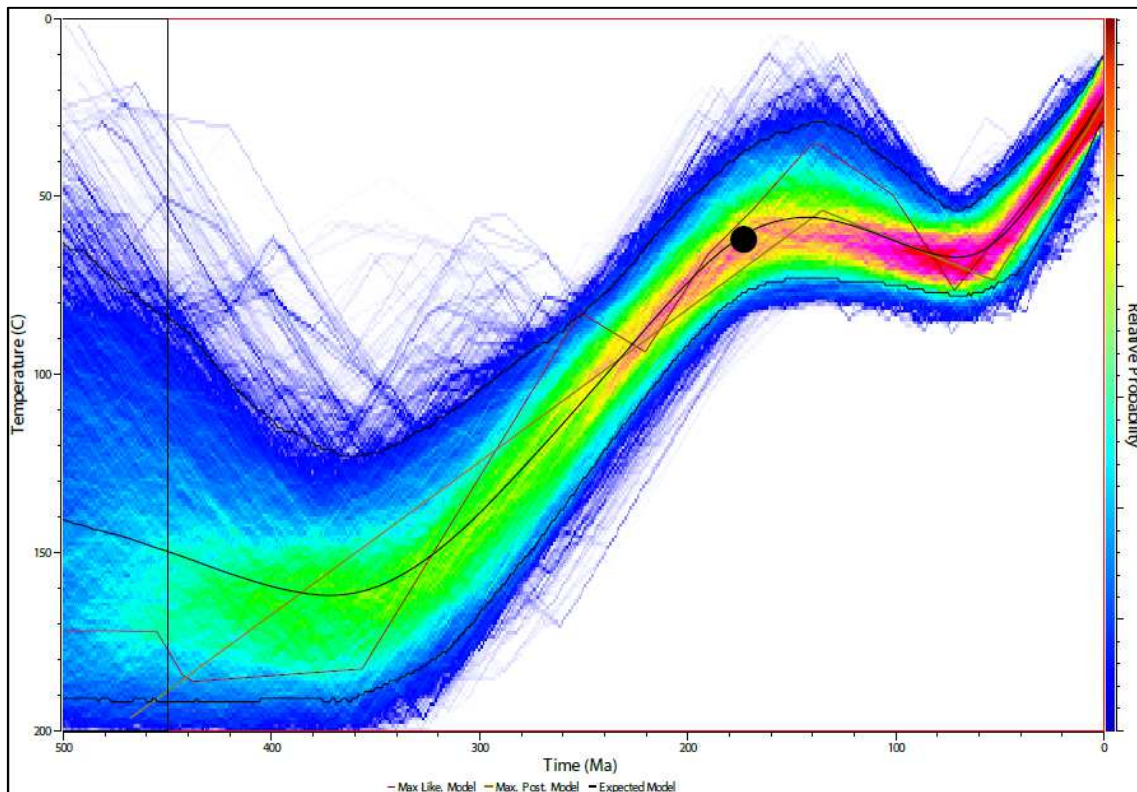
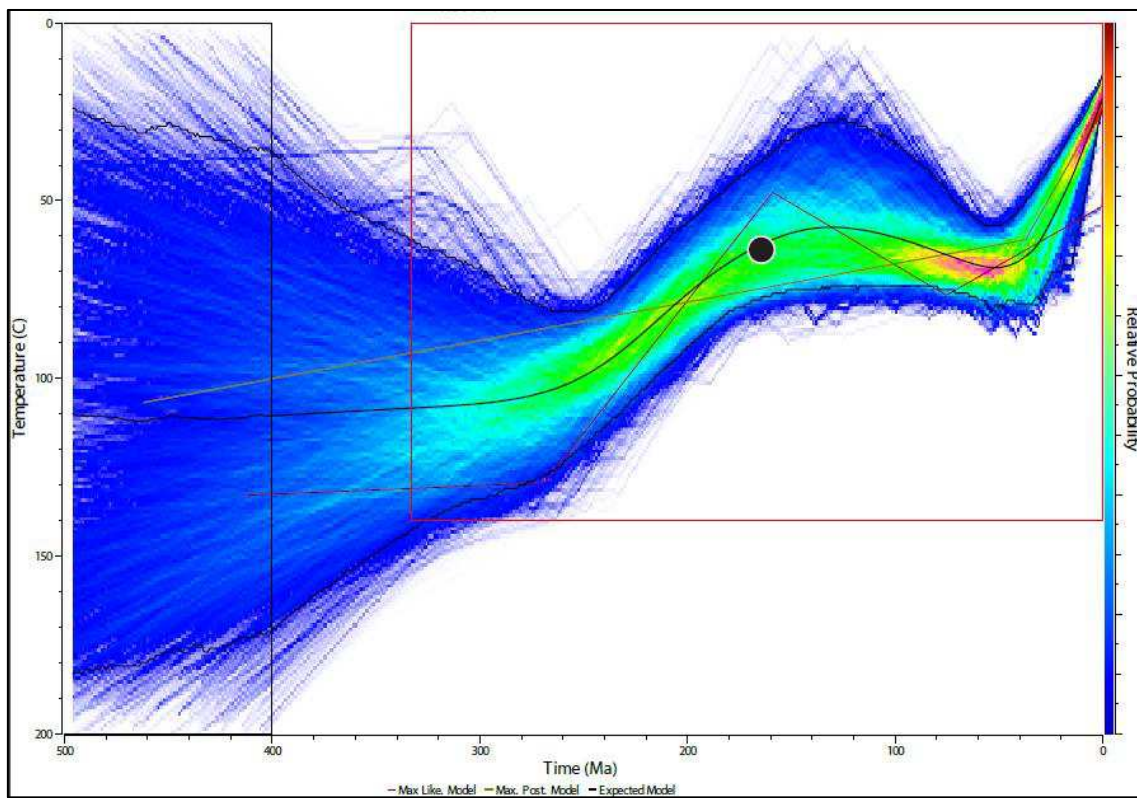
A3.3 Rio Grande do Sul inverse models

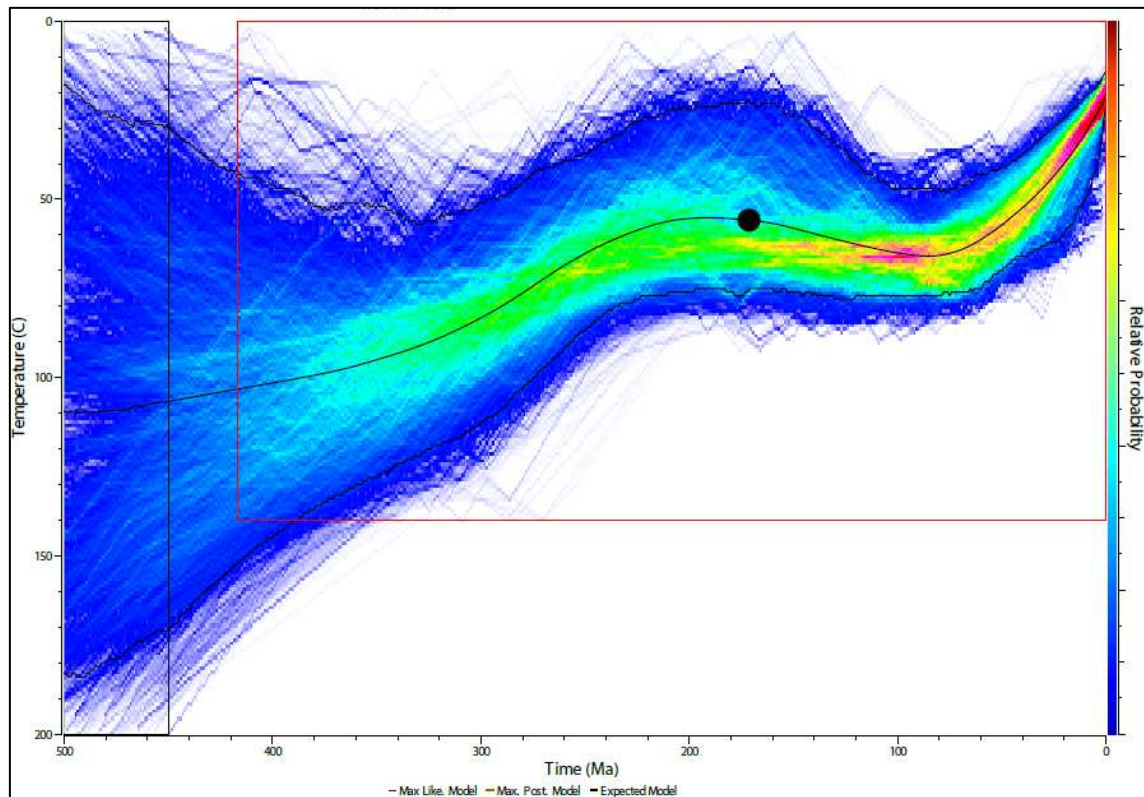
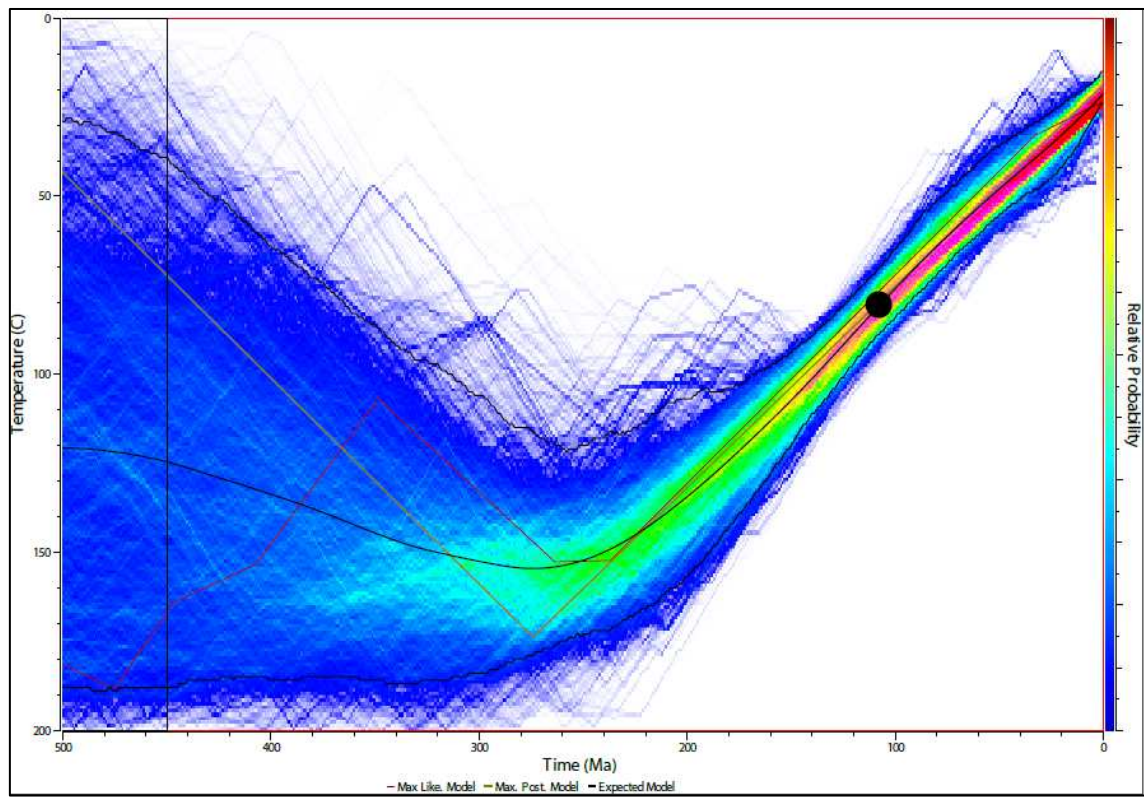
The final inverse model of each sample can be found below. Final models were run with all data available for the sample, as indicated. Black line represents the expected model, that is, a weighted mean model, where the weighting is provided by the posterior probability for each model (for further information see Gallagher 2009, 2012 and QTQt User Guide v5.7).

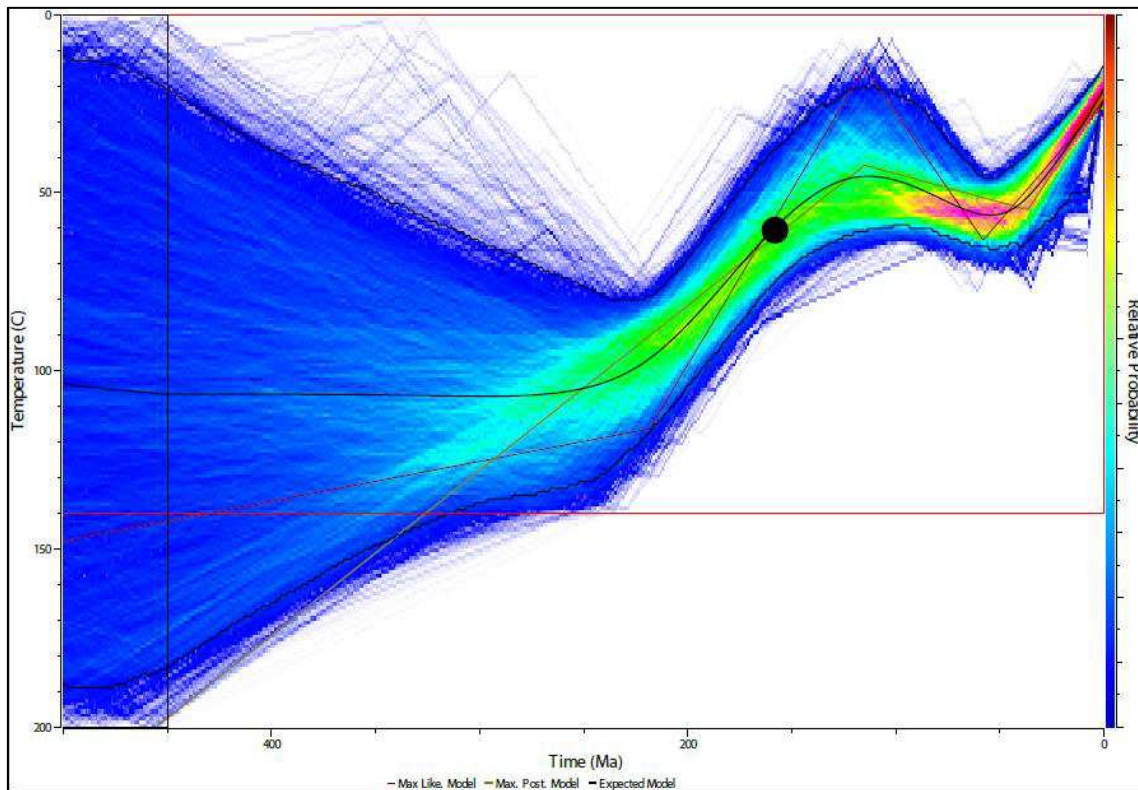
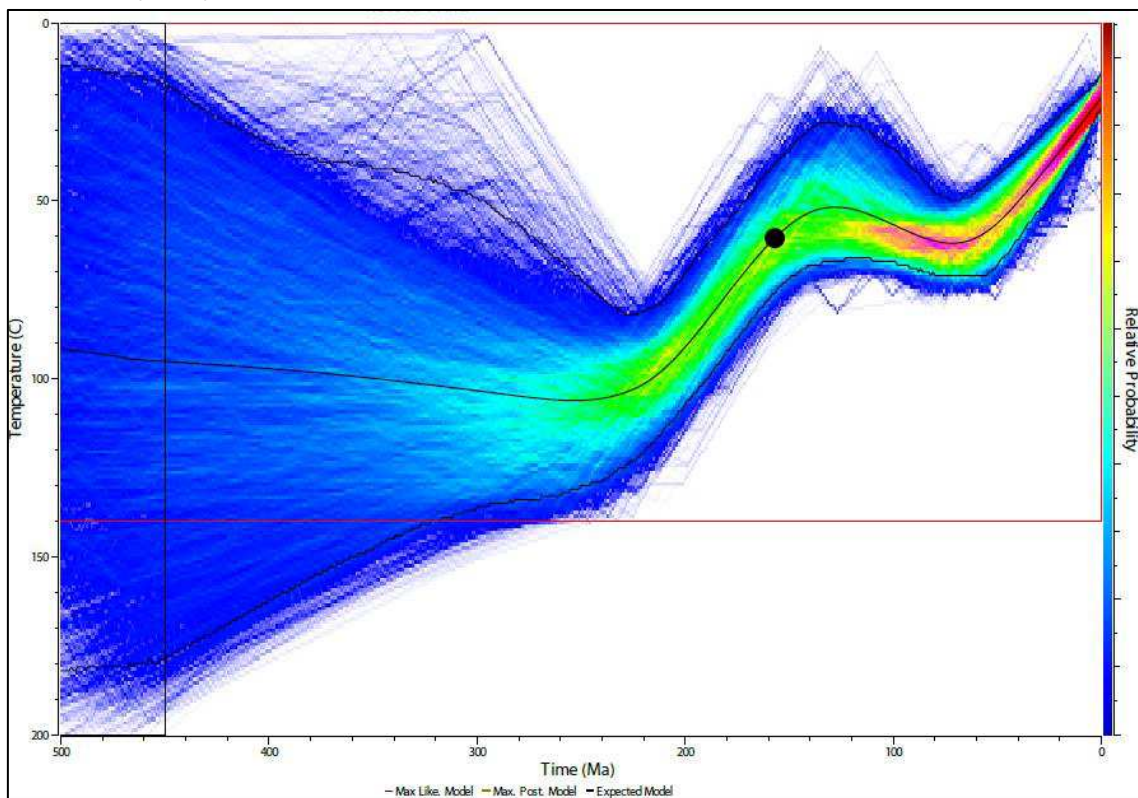
The expected model is the one displayed in figures 6.6 and 6.7 of the paper. Confidence intervals represent the 95% probability range, with relative probability inside this range indicated with the color scale.

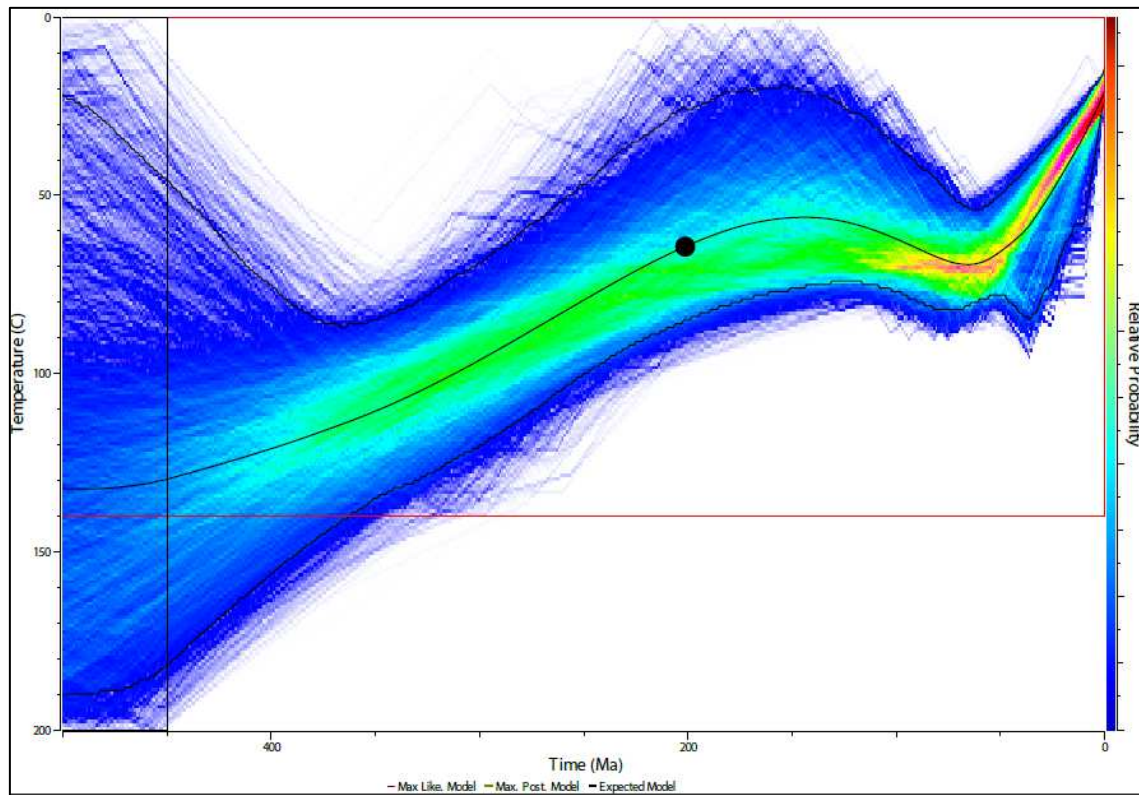
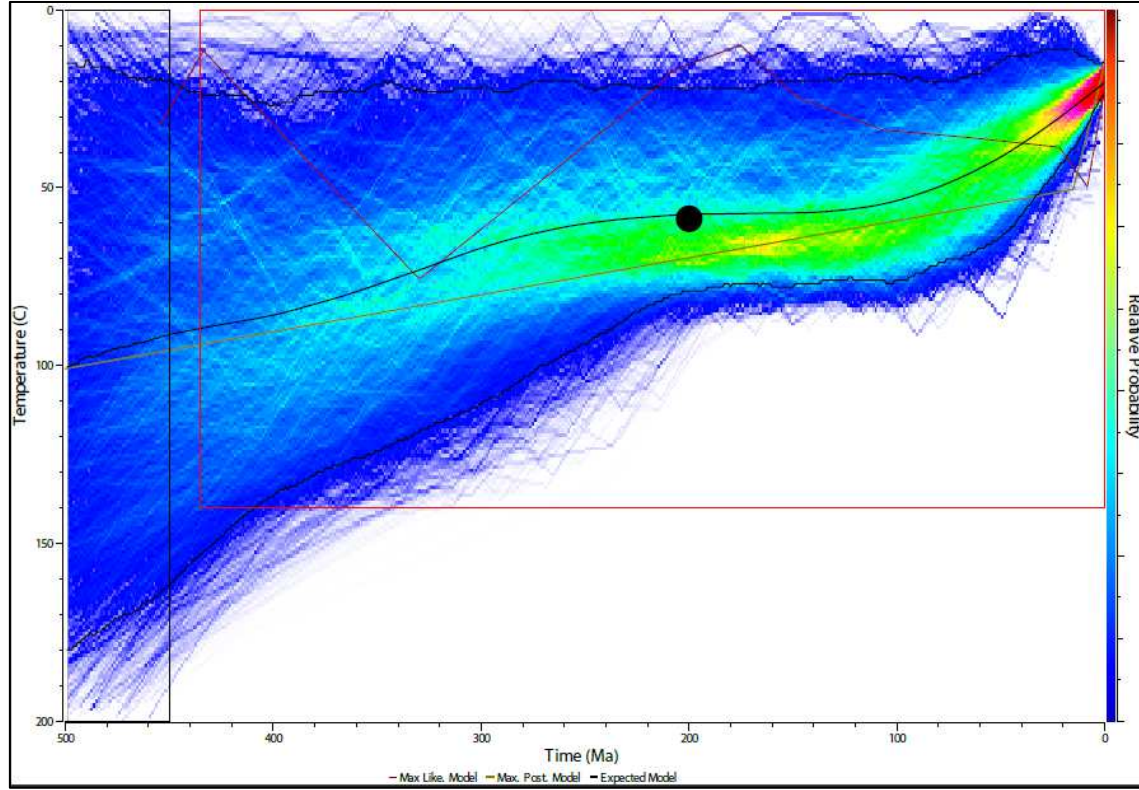
RS2 – AFT (no confined tracks), AHE, ZHE



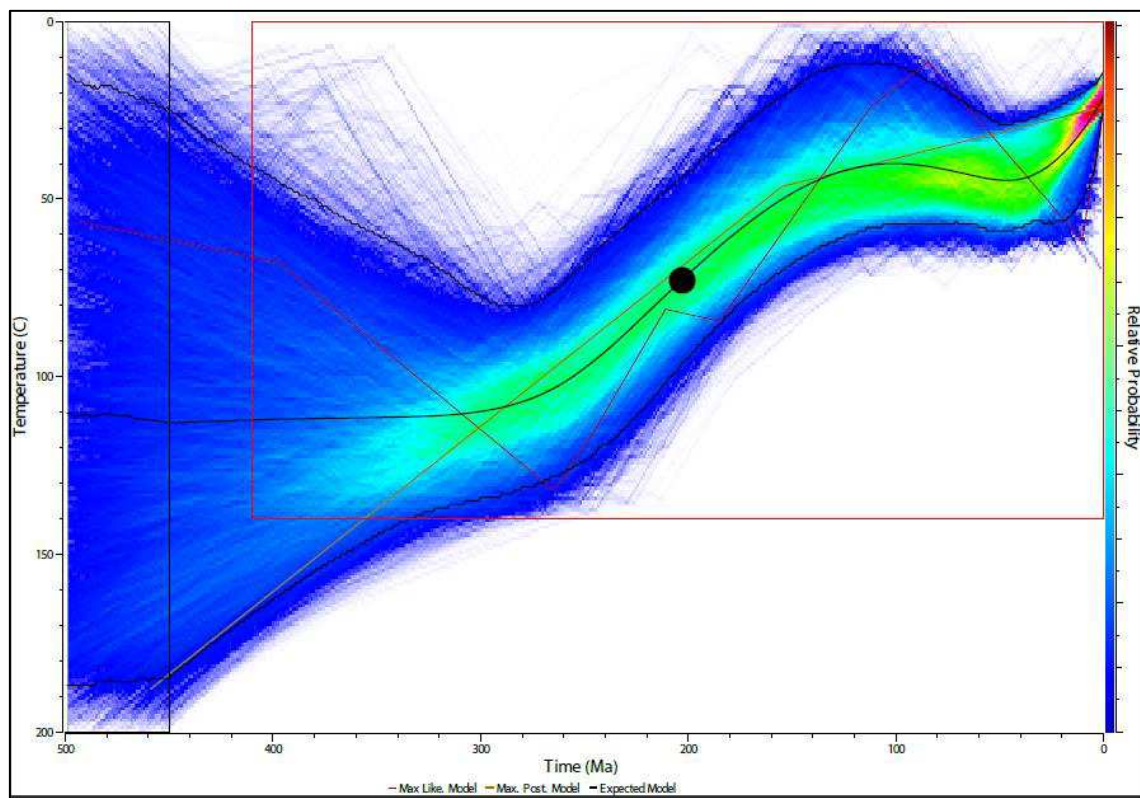
RS4 – AFT, AHE, ZHE**RS5 – AFT**

RS7 – AFT, AHE**RS10 – AFT, AHE, ZHE**

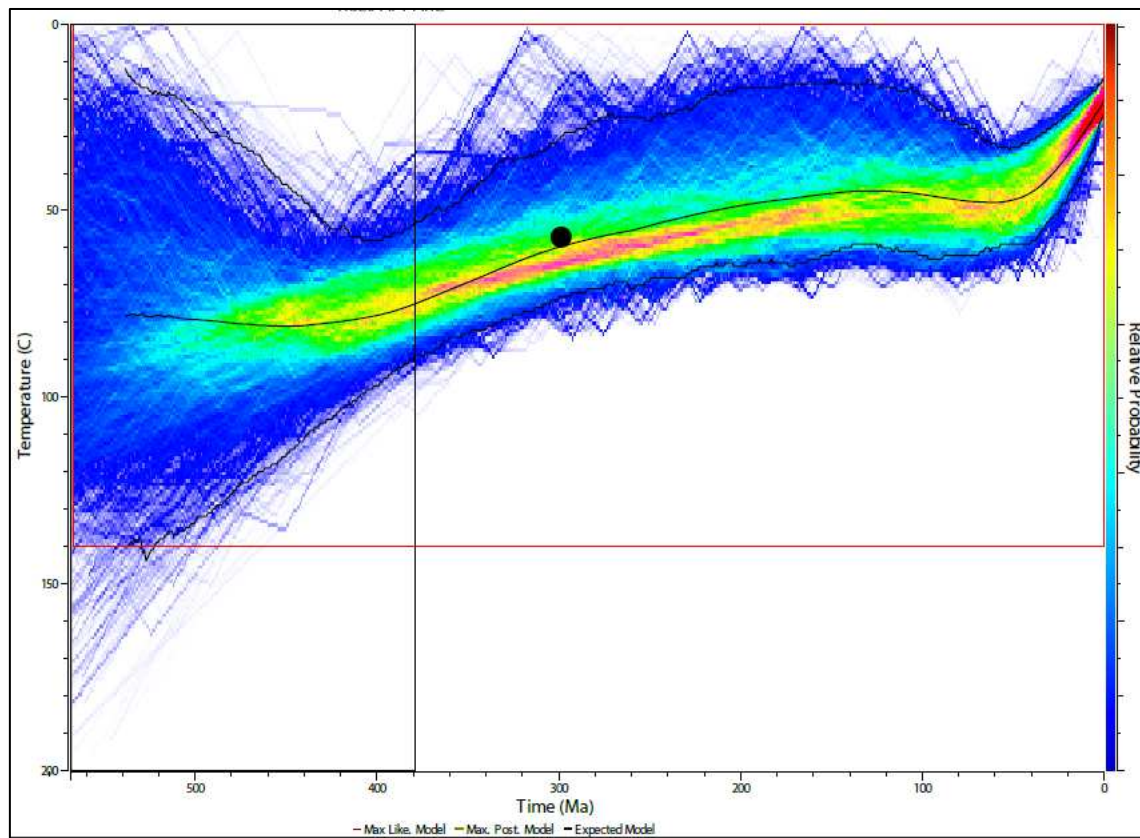
RS12 – AFT, AHE**RS13 – AFT, AHE, ZHE**

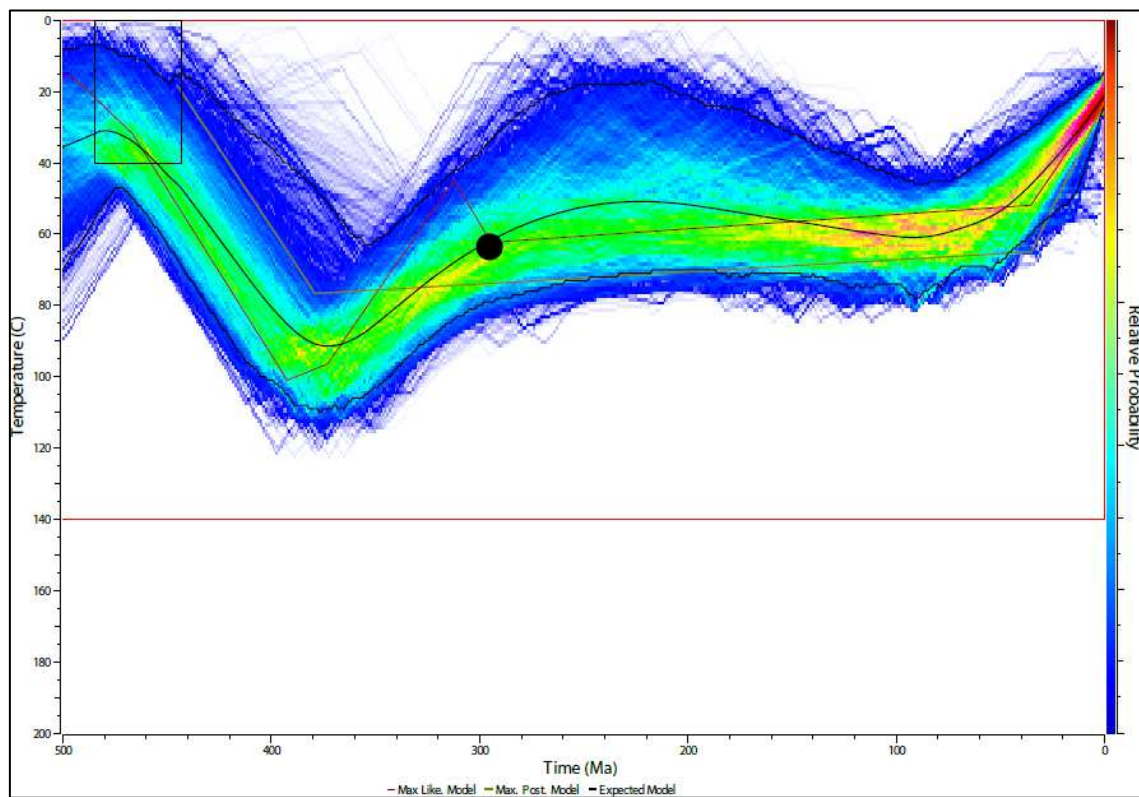
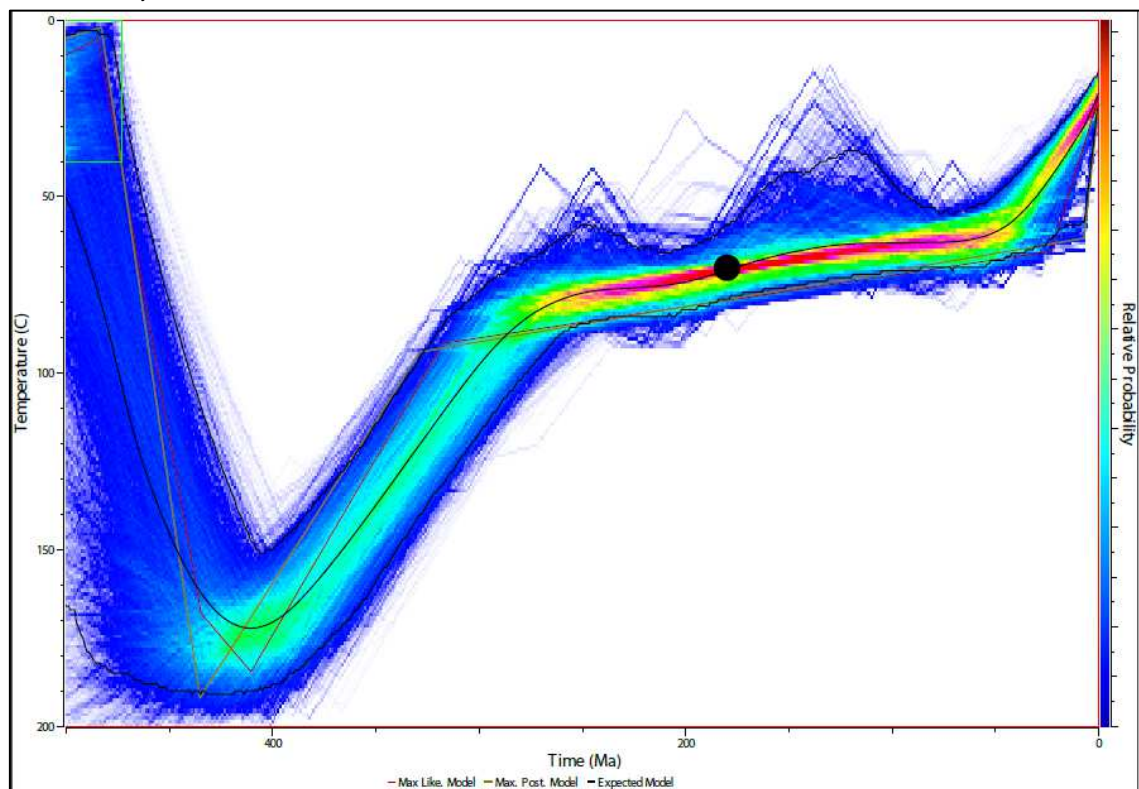
RS14 – AFT, AHE**RS16 – AFT, AHE**

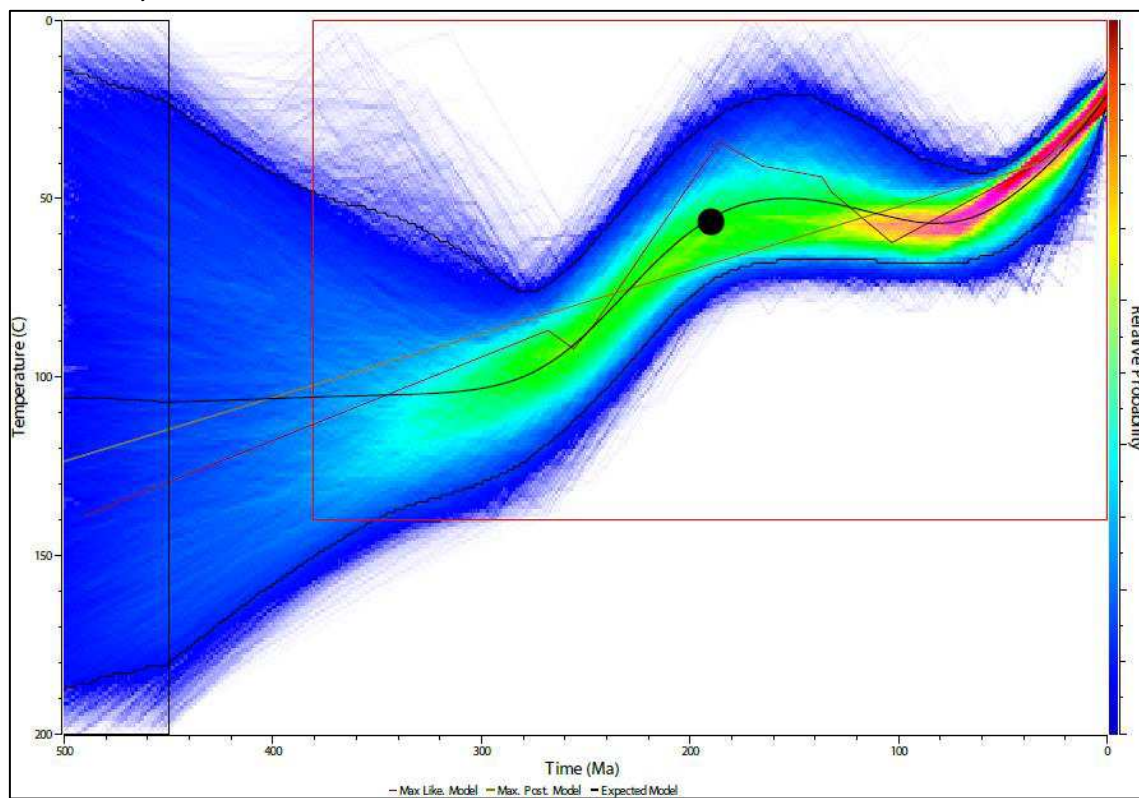
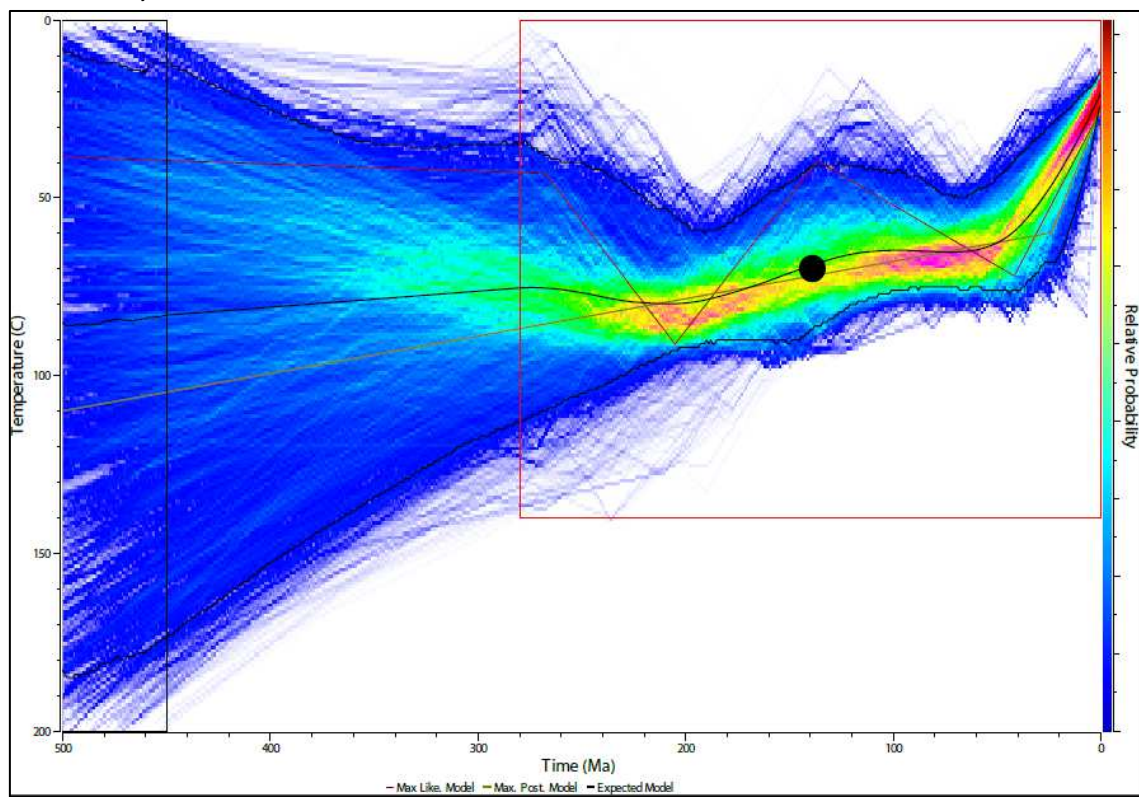
RS17 – AFT

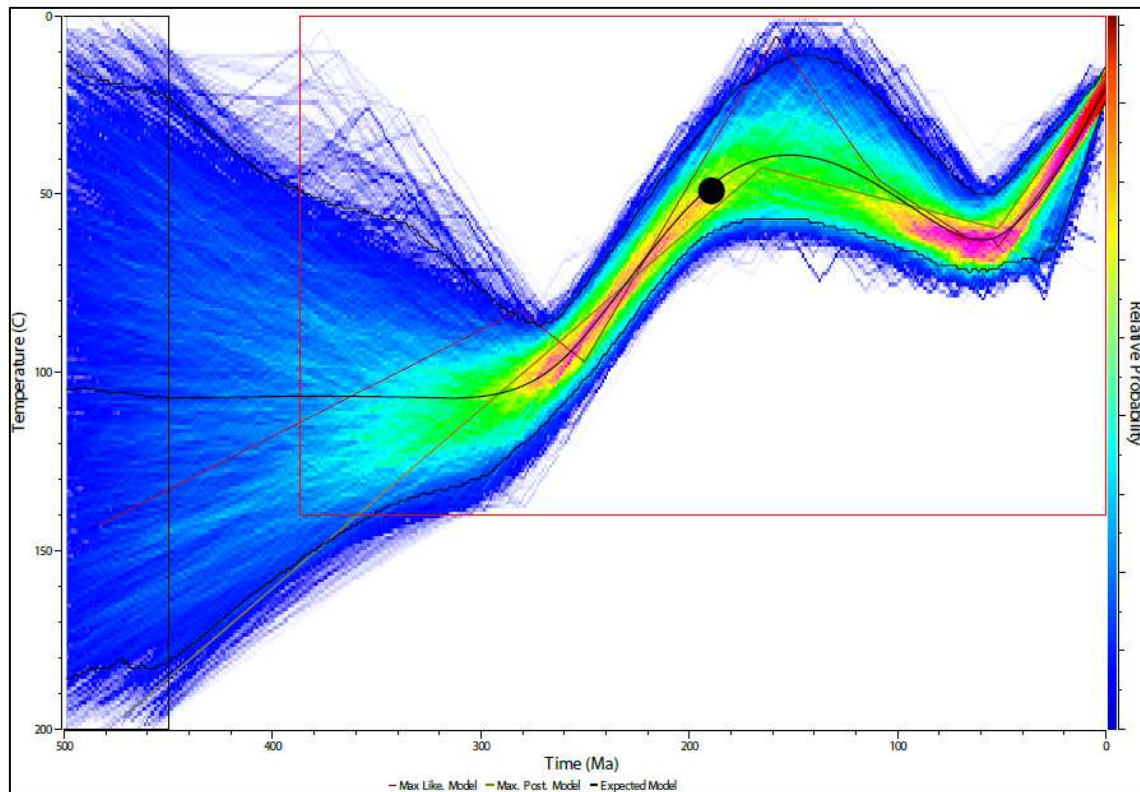
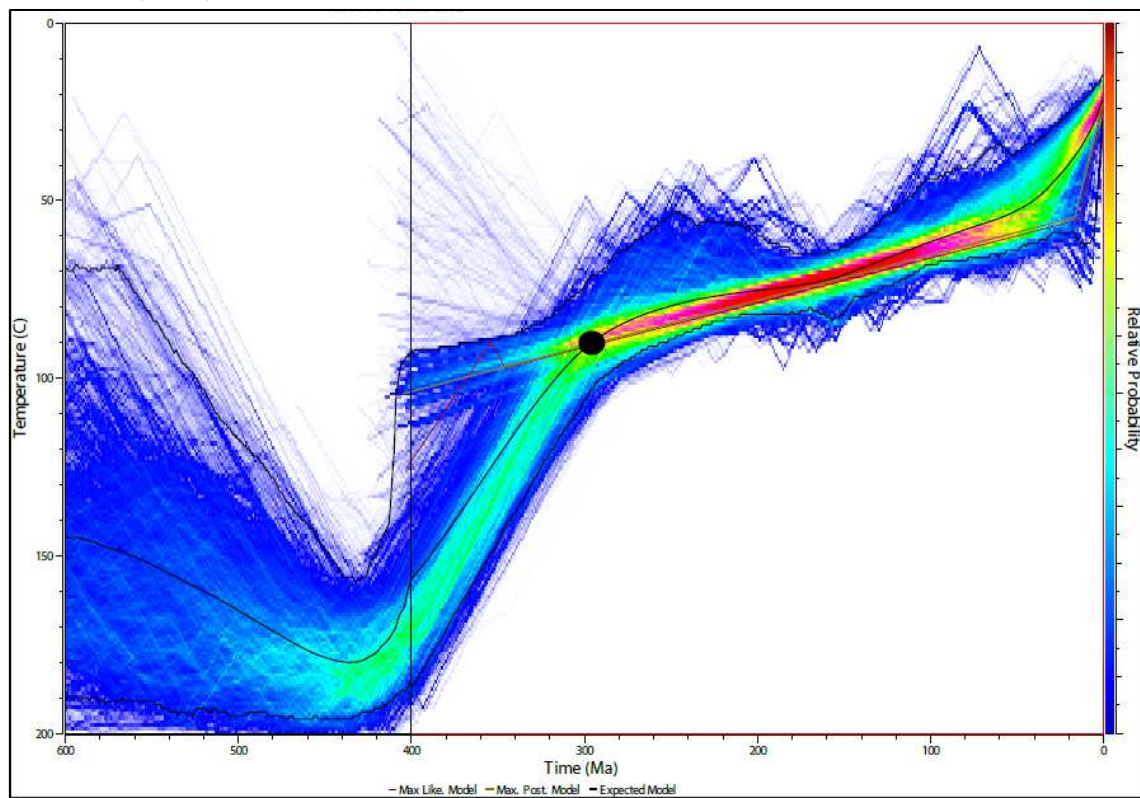


RS20 – AFT, AHE



RS21 – AFT, AHE**RS22 – AFT, ZHE**

RS23 – AFT, AHE**RS25 – AFT, AHE**

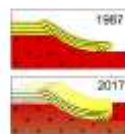
RS26 – AFT, AHE**RS29 – AFT, AHE, ZHE**

A4 Resumos publicados

A4.1 XVI Simpósio Nacional De Estudos Tectônicos



XVI SIMPÓSIO NACIONAL DE ESTUDOS TECTÔNICOS
X INTERNATIONAL SYMPOSIUM ON TECTONICS
22 a 24 de maio de 2017 | Salvador - BA - Brasil



NOVAS PERSPECTIVAS DE ESTUDOS TERMOTECTÔNICOS NO RS & UY

João Pacifico S. L. Machado¹, Marcos Müller Bicca¹, Claudio Gaucher², Letícia Chiglino², Andréa Ritter Jelinek¹

¹ Universidade Federal do Rio Grande do Sul, Porto Alegre, Brasil, email: joao.machado@ufrgs.br

² Universidad de la República, Montevideo, Uruguay

³ Universidade do Vale do Rio dos Sinos, São Leopoldo, Brasil

1. INTRODUÇÃO

O resumo aqui apresentado visa expor o desenvolvimento do projeto de doutorado de João Pacifico Machado. Tal projeto encontra-se em fase inicial e versa sobre “Estudos Tectônicos de Desenvolvimento de Bacias Utilizando Termocronologia de Baixa Temperatura e Análises Sismicas”, com foco na Bacia de Pelotas (BP) e área continental adjacente.

1.1. Caracterização do Problema

A margem continental atlântica sul-americana apresenta ampla variação em seu relevo e geologia, sendo que as mudanças geomorfológicas tendem a não ser graduais, mas a concentrar-se em zonas de transição, marcadas por grandes estruturas. Além disso, por vezes as variações no relevo continental parecem de alguma forma refletir os lineamentos e estruturas observadas na crosta oceânica. Em Santa Catarina temos o exemplo do Alto de Florianópolis, representado por uma região de terrenos mais elevados no continente e por um lineamento oceânico, o qual delimita duas bacias costeiras de evolução distinta. O projeto aqui proposto busca relacionar feições geomorfológicas continentais com zonas de fraturas oceânicas, processos geodinâmicos e termotectônicos de exumação do continente e por fim, o vínculo desses fatores com o desenvolvimento da BP.

1.2. Justificativa & Objetivos

A configuração da margem continental exerce influência direta no desenvolvimento de bacias sedimentares *offshore*, visto que o continente consiste como área-fonte dos sedimentos para o preenchimento das bacias, e estas representam o *locus* principal das reservas de hidrocarbonetos no Brasil. A natureza da margem na porção sul brasileira e uruguaiã carece de informações termocronológicas, as quais tem o potencial de esclarecer processos de soerguimento e denudação no continente e, por consequência, auxiliar na estimativa do volume sedimentar disponível para preenchimento das bacias marginais.

Trabalhos com enfoque em termocronologia, como o de Karl *et al.* (2013), evidenciam a importância de antigas zonas de fraturas regionais, de direção NW-SE, no desenvolvimento de blocos crustais com evoluções termotectônicas dispares na margem brasileira. Os autores demonstram que a Zona de Fratura Florianópolis representa um limite entre dois blocos crustais com padrões de exumação e resfriamento distintos, sendo que o bloco ao sul do lineamento apresenta uma evolução termotectônica complexa e carente de informações para uma adequada compreensão. Além dos lineamentos NW-SE, na margem leste do continente sul-americano são predominantes as estruturas de direção NE-SW (e.g. Zona de Cisalhamento Dorsal de Canguçu), as quais podem ter sofrido reativações recentes. Nesse projeto trabalha-se com a hipótese de que estruturas regionais, como por exemplo a Sincinal de Torres, o Arco de Rio Grande e a Zona de Cisalhamento Dorsal de Canguçu/ Sierra Ballena (figuras 1 e 2) funcionam como limites de blocos que sofreram comportamentos verticais distintos, e que como consequência afetaram o desenvolvimento da BP.

Através de uma análise da relação *source-to-sink*, o objetivo é investigar a atuação de processos tectônicos sobre os domínios tectonoestratigráficos compreendidos entre as cidades de Florianópolis e Montevidéu, e sua correlação com o desenvolvimento e preenchimento da BP. Essa comparação parte do pressuposto de que eventos de soerguimento epigenéticos regionais amplificam os eventos erosivos, o que acaba por incrementar o influxo siliciclástico na bacia. No projeto serão realizadas 1) análises termocronológicas de baixa temperatura, a fim de elucidar movimentações verticais de blocos crustais distintos em torno das estruturas tectônicas continentais, e 2) análises sismicas, a fim de avaliar a arquitetura deposicional da BP e a influência de estruturas geológicas no seu desenvolvimento. Os métodos termocronológicos de traços de fissão e (U-Th)/He permitirão avaliar épocas e taxas relativas aos movimentos verticais da crosta, o que possibilita o

desenvolvimento de modelos de exumação e a estimativa de volumes de erosão continental. As análises sísmicas permitirão avaliar a arquitetura deposicional da bacia, a fim de reconstruir sua evolução cronoestratigráfica. Espera-se assim reconhecer uma íntima relação entre períodos de acelerado soerguimento e denudação continental, que gerariam maiores volumes de sedimentos, com a deposição de espessos pacotes sedimentares correlatos na bacia. Com isso será possível criar um modelo termotectônico de evolução da margem costeira com ênfase no desenvolvimento da BP, algo inédito na região. Na atual etapa do projeto foi realizada a coleta e preparo das amostras para as análises termocronológicas, assunto sobre o qual trata o restante desse resumo.

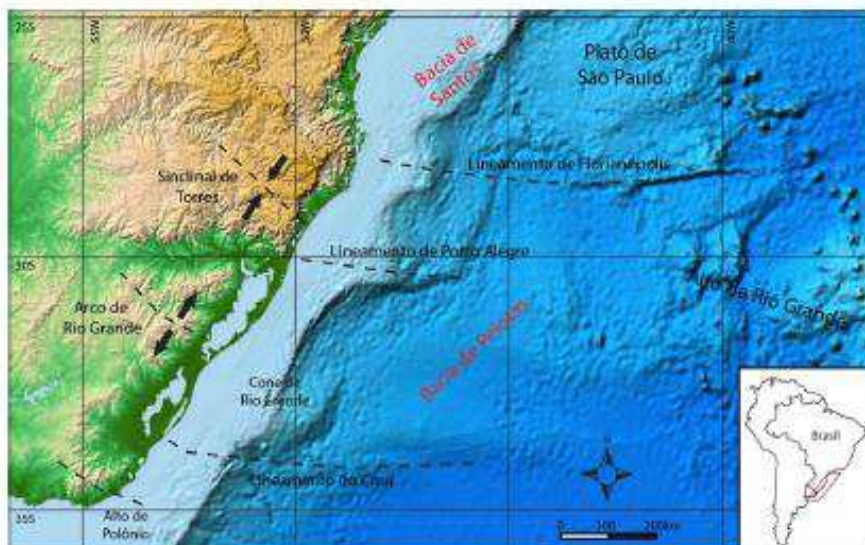


Figura 1: Principais estruturas oceânicas da porção sul do Brasil. Mapa-base topográfico obtido na National Oceanic and Atmospheric Administration - NOAA (Amante & Eakins, 2009).

2. CONTEXTO GEOLÓGICO

A área de estudo aparenta uma continuidade de seus terrenos tectonoestratigráficos, desde Florianópolis até o Uruguai, limitados por zonas de cisalhamento regionais (figura 2). Cada terreno apresenta uma complexidade e evolução distinta, sendo que os processos de aglutinação dos terrenos ainda são motivos de debate. A colagem dos terrenos ocorreu até a formação do Gondwana (final do Neoproterozóico ao Cambriano), e se manteve durante o processo de abertura do Oceano Atlântico (Cretáceo). De maneira resumida, pode-se dividir o Uruguai, de oeste para leste, nos terrenos 1) Piedra Alta, 2) Tandilia, 3) Nico Pérez e 4) Cuchilla Dionísio. No Brasil encontram-se, no mesmo sentido, os terrenos 1) Taquarembó, 2) São Gabriel, 3) Luis Alves, 4) Tijucas e 5) Pelotas.

Tangente aos terrenos supracitados, a BP tem sua evolução associada à separação do Gondwana e abertura do assoalho oceânico. A BP é limita ao norte pelo Alto de Florianópolis e ao sul pelo Alto de Polônio, e alcança mais de 12km de profundidade em seu depocentro. De natureza siliciclastica, sem deformações por halocinese, a BP apresenta padrões retrogradacionais no Cretáceo-Paleógeno e progradacionais no Neógeno (Contreras *et al.* 2010). As estruturas transversais mais importantes da bacia são o Lineamento de Florianópolis, o Lineamento de Porto Alegre e o Lineamento do Chui (Corrêa *et al.*, 2007).

3. MÉTODOS

Os métodos de investigação empregados neste trabalho serão análises termocronológicas de baixa temperatura (traços de fissão e $(U-Th)/He$) em cristais de apatita e zircão, e análises sísmicas na BP. A adequada coleta e preparo das amostras são cruciais para as análises termocronológicas, e são abordadas a seguir.

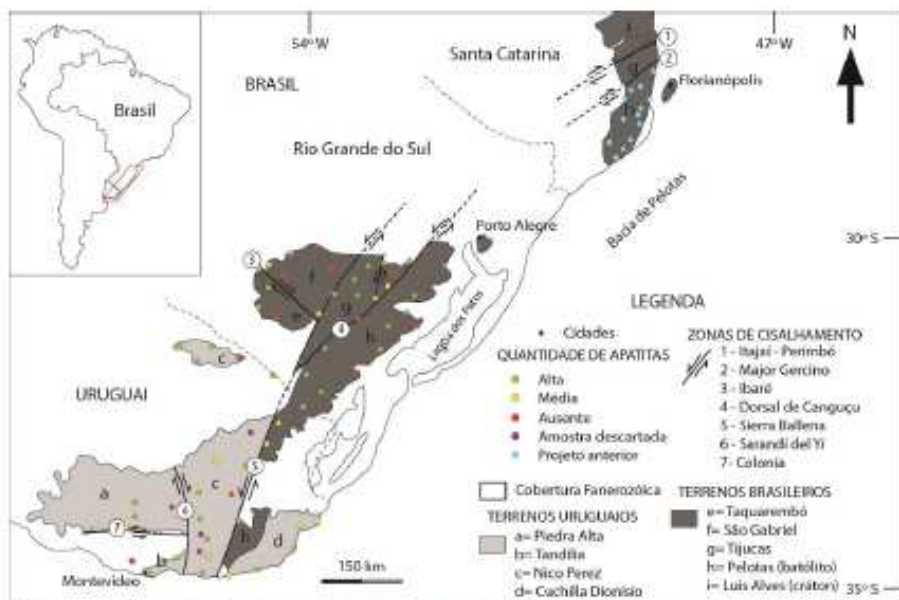


Figura 2: Mapa simplificado dos terrenos tectonoestratigráficos e principais zonas de cisalhamento que os limitam. Pontos coloridos indicam posição aproximada das amostras coletadas e quantidade de apatitas recuperadas. Baseado em Bossi & Gaucher (2014), Neves *et al.* (2014), Philipp *et al.* (2016), entre outros.

A primeira etapa de campo foi realizada em fevereiro/2016, com a coleta de amostras do embasamento no RS e UY. Aproximadamente 6.000 km foram percorridos em 15 dias, totalizando 62 afloramentos visitados e mais de 300kg de amostras coletados. Para localização dos melhores afloramentos, foi realizado um estudo prévio da área a partir de mapas geológicos regionais e imagens do *Google Earth Pro*. Foram priorizadas as litologias que comumente possuem abundância nos minerais alvo, na sua maioria granítoides. Cada ponto teve cerca de 5kg de amostra coletados, e com o auxílio de aparelho de GPS foram registrados o posicionamento e a altitude do ponto, fundamentais para as análises termocronológicas.

A cominuição das amostras e posterior separação mineral foi realizada na infraestrutura da UFRGS. Após uma etapa de fragmentação manual, as amostras foram submetidas a um britador de mandíbulas e um moinho de pratos, o que resultou na desagregação dos minerais da rocha. A essa etapa seguiu-se um peneiramento em peneiras de 500 μm , concentrando assim a porção mais fina da amostra.

Para a concentração dos cristais de apatita e zircão, o material fino resultante da cominuição passou por uma separação densimétrica com batéia. Dessa forma concentrou-se a mineralogia pesada (densa) em relação aos minerais leves (essencialmente quartzo e feldspato), reduzindo drasticamente o volume da amostra. O concentrado de minerais pesados foi então submetido à separação magnética com o Separador Isodinâmico Frantz®, com amperagens de 0,4, 0,8, 1,2 e 1,8A, e inclinação lateral -15° e frontal 25°. Dessa forma as frações magnéticas foram retiradas do concentrado, que passou a conter principalmente os minerais alvo. Por fim ocorreu a concentração gravimétrica por líquidos densos, utilizando-se bromofórmio ($\rho = 2,9 \text{ g/cm}^3$), separando assim apatitas ($\rho = 3,1 \text{ g/cm}^3$) e zircões ($\rho = 4,6 \text{ g/cm}^3$) de quaisquer minerais leves restantes. Posteriormente, em alguns casos, foi utilizado o diodometano ($\rho = 3,3 \text{ g/cm}^3$), o que permitiu separar as apatitas dos zircões.

4. RESULTADOS

Das 62 amostras coletadas, foram processadas 59 e três descartadas. Em relação a apatitas, apenas 33 amostras resultaram em 200 ou mais cristais do mineral. Outras 12 amostras possuíam apatitas em pequena quantidade (<200) e 13 amostras não possuíam o mineral. No geral, os granítoides com maior teor de feldspato alcalino foram os que menos possuíam apatitas. Por exemplo, dos 10 sienogranitos amostrados, apenas um

continha mais de 200 apatitas, sendo que em 7 amostras dessa litologia não houve recuperação alguma. No quesito morfológico dos cristais, as apatitas recuperadas mostraram uma grande variação, desde formatos pequenos e aciculares até fragmentos hexagonais de cristais maiores que foram fragmentados durante a cominuição, passando por apatitas arredondadas por abrasão das amostras sedimentares. Não foi encontrado um padrão cristalográfico das apatitas relacionado à litologia de proveniência. Em janeiro/2017 foram enviadas para irradiação, no reator nuclear do IPEN-SP, as apatitas de 45 amostras, reunidas em 33 pastilhas.

No que diz respeito aos zircões, 40 amostras possuíam cristais em quantidades adequadas para análises termocronológicas, resultado esperado tendo em vista a comum ocorrência desse mineral em granitóides. Por apresentar maior resistência ao intemperismo do que as apatitas, os cristais de zircão também foram encontrados em todas as amostras sedimentares. As características morfológicas dos cristais variam amplamente, da mesma forma que as apatitas. Suas colorações também são diversas, desde quase incolores até castanhos e acinzentados, provavelmente devido ao acúmulo de danos no retículo cristalino em virtude do decaimento, visto que as litologias amostradas são pré-Cambrianas em sua maioria.

5. PRÓXIMAS ETAPAS

Devido à necessidade de atenuação dos níveis radioativos das amostras irradiadas, será possível trabalhar com essas a partir do final do semestre 2017/1. A datação pelo método dos traços de fissão exige a contagem dos traços fósseis nas apatitas e dos traços induzidos nas respectivas micas. Esse processo será realizado na UFRGS, junto da medição dos traços confinados e outros parâmetros, necessários para o modelamento termocronológico. Ainda em 2017/1 espera-se realizar a datação por (U-Th)/He em outras apatitas das mesmas amostras. De posse das informações dos dois métodos termocronológicos, será possível realizar o modelamento tectonotectônico de cada amostra. Posteriormente, os dados obtidos serão avaliados em conjunto com informações relativas a processos geotectônicos e climáticos que atuaram na região. Dessa forma, espera-se poder correlacionar os padrões de exumação às zonas de cisalhamento presentes na região, na busca de semelhanças entre as amostras situadas num mesmo terreno tectonoestratigráfico. A partir dos modelamentos de cada amostra e de suas relações com amostras adjacentes, será possível estimar as épocas e taxas de maior erosão continental. Por sua vez, as análises sísmicas da BP focarão no reconhecimento de estruturas tectônicas que possam ser um prolongamento daquelas encontradas no continente. Ademais, através de uma análise sismoestratigráfica e modelamentos, espera-se poder estimar as épocas e volumes de maior aporte sedimentar na BP. Ao final espera-se correlacionar os padrões de exumação e erosão continentais com o volume e épocas de maior aporte sedimentar na Bacia de Pelotas.

6. REFERÊNCIAS BIBLIOGRÁFICAS

- Amante, C. & Eakins, B. W. (2009). *ETOPO1 1 Arc-Minute Global Relief Model: Procedures, Data Sources and Analysis*. NOAA Technical Memorandum NESDIS NGDC-24. National Geophysical Data Center, NOAA. [15/fev/17].
- Bossi, J., & Gaucher, C. (2014). *Estratigrafia del Predevónico del Uruguay*. Em: *Geología del Uruguay - Tomo 1: Predevónico*, págs 19-43. Montevideo.
- Contreras, J., Zühlke, R., Bowman, S., & Bechstädt, T. (2010). *Seismic stratigraphy and subsidence analysis of the southern Brazilian margin (Campos, Santos and Pelotas basins)*. Marine and Petroleum Geology, 27(9), 1952-1980.
- Corrêa, I. C. S., Toldo Jr, E. E., Weschenfelder, J., Baitelli, R., Ayup-Zouain, R. N., Dehnhardt, B. A., & Martins, L. R. S. (2007). *Plataforma e talude continental do Rio Grande do Sul: síntese dos conhecimentos*. 50, 341e354.
- Karl, M., Glasmacher, U. A., Kollenz, S., Franco-Magalhaes, A. O., Stockli, D. F., & Hackspacher, P. C. (2013). *Evolution of the South Atlantic passive continental margin in southern Brazil derived from zircon and apatite (U-Th-Sm)/He and fission-track data*. Tectonophysics, 604, 224-244.
- Neves, B. B. d. B., Fuck, R. A., & Pimentel, M. M. (2014). *The Brasiliano collage in South America: a review*. Brazilian Journal of Geology, 44(3), 493-518.
- Philipp, R. P., Pimentel, M. M., & Chemale Jr, F. (2016). *Tectonic evolution of the Dom Feliciano Belt in Southern Brazil: Geological relationships and U-Pb geochronology*. Brazilian Journal of Geology, 46, 83-104.

Apoio: BG E&P Brasil

A4.2 AGU Fall Meeting 2017

T13A-0501: Low-Temperature Thermochronology Investigation in Uruguay and Southernmost Brazil: Apatite (U-Th)/He Results

Monday, 11 December 2017

13:40 - 18:00

New Orleans Ernest N. Morial Convention Center - Poster Hall D-F

Low-temperature thermochronology has successfully allowed one to reveal exhumation histories of many orogenic belts across the Earth, and lately these techniques have been applied in cratonic regions. The present study aims to constrain thermal history and exhumation of the South Atlantic Passive Margin, between Uruguay and Southernmost Brazil, a region scarce of thermochronological data. This location has become relatively stable after the Neoproterozoic Brasiliano Orogeny, being more intensely disturbed by tectonics during the Gondwana Breakup and consequent opening of the Atlantic Ocean (Jurassic - Cretaceous). Both apatite and zircon (U-Th)/He methods are being applied on basement rocks, and since those have a long cooling history, radiation damage is expected to play an important role in crystal ages. A total of 25 samples were analyzed, and preliminary apatite (U-Th)/He results reveals unweighted sample ages ranging from Permian to Lower-Cretaceous in Southernmost Brazil, with a couple of outliers with Devonian - Carboniferous ages. In Uruguay results can be grouped in two different clusters: one of samples with Jurassic to Lower-Cretaceous ages, and another of Devonian to Permian ages. This wide range of results can be assigned to variations in the uranium content of the grains, due the presence of inclusions, compositional zonation or substantial radiation damage of the crystalline lattice. In most cases, ages tend to increase with crystal eU content. No clear relationship between ages and tectonic terranes has been found so far, neither between ages and elevation, since the region does not have significant topographic variations. Younger ages are commonly found closer to the coastal region, possibly in response to the rift shoulders uplift during Gondwana breakup and further exhumation and denudation at higher rates. An anomalous concentration of older ages in the southern region of the Pelotas Batholith, close to the Brazil - Uruguay border, suggests a geotectonic stable area near the margin. A NW-trend of younger ages throughout southernmost Brazilian Shield may reflect cooling triggered by the structural reactivation of Precambrian basement fabrics. Hopefully, future work will permit a better comprehension of the regional exhumation patterns during the Phanerozoic.

Authors

João Pacifico Machado

UFRGS Federal University of
Rio Grande do Sul

Marcos Muller Bicca

UFRGS Federal University of
Rio Grande do Sul

[Find Similar](#)

View Related Events

Day: [Monday, 11 December 2017](#)

A4.3 16th International Conference on Thermochronology

 Thermo 2018 <i>16th International Conference on Thermochronology</i>	
Session 6: Thermochronologic applications to large-scale plate tectonic processes, magmatism and	

Development of the Atlantic continental margin in southernmost Brazil: insights from apatite (U-Th)/He and fission track data

João Pacífico S. L. Machado^{**}, Andréa R. Jelinek^{*}, Marcos M. Bicca^{*}, Randell Stephenson[†], David I.M. Macdonald[‡]

^{*}Universidade Federal do Rio Grande do Sul, Brazil; [†]University of Aberdeen, UK; [‡]presenting author

Through the joint use of apatite fission tracks (AFT) and (U-Th)/He (AHe) analysis, this study evaluates the thermo-tectonic evolution of the Sul-Rio-Grandense Shield (SRS), located on the western margin of the Atlantic, southernmost Brazil. The SRS is a major geotectonic feature formed during the Brasiliano/Pan-African Orogeny (Neoproterozoic), after the collision of the Rio de La Plata, Congo and Kalahari cratons, as part of the West Gondwana assemblage. Regional shear zones with NE-SW and NW-SE orientations divide the SRS into four main tectonostratigraphic Proterozoic terranes: 1) Taquarembó (SW), 2) São Gabriel (NW), 3) Tijucas (central) and 4) Pelotas (E). These terranes are partially covered by remnants of the Canaquã Basin (Late Ediacaran-Cambrian), and limited to the north and west by the intracontinental Paraná Basin (Paleo-Mesozoic), and to the east by the Atlantic Pelotas Basin (Meso-Cenozoic). After its assemblage, the SRS went through a long period of relative quiescence, and was only directly affected by tectonic events during the opening of the South Atlantic Ocean (Jurassic-Cretaceous). The SRS has a subdued topography, with low relief and peaks under 600m. Basement samples - mainly granitoids with Neoproterozoic ages - were collected from the four terranes. There are 17 sites with results; AFT ages from 14 sites in terranes 1, 3 and 4 behave similarly, with ages ranging from 108.6 ± 6.4 to 205.1 ± 20.5 Ma (Lower Jurassic-Lower Cretaceous). However, the three AFT ages obtained in terrane 2 range from 296.4 ± 14.8 to 310.11 ± 27.91 (Upper Carboniferous-Lower Permian). The mean track length of confined tracks from the SRS range from 10.7 ± 0.2 μm to 12.8 ± 0.2 μm , and ages generally show an inverse relationship with U content. AHe analysis conducted on forty apatites from thirteen locations reveal corrected ages ranging from Devonian to Cretaceous. Such a wide spread in AHe ages has been reported in other cratonic regions, where crystals have remained for long periods in the partial retention zone (PRZ). Furthermore, inversion of AFT and AHe ages is common. These results and their relation with eU, grain size, and other parameters are not clear. Inverse modeling of SRS samples indicates cooling through the PRZ beginning at the Permian for terranes 1, 3 and 4, with local variations. This timing comprises two events affecting surface dynamics of southernmost Brazil: I) End of Gondwana glaciation – led to a regional uplift due to isostatic rebound and exposed previously buried basement rocks to weathering, raising erosion/uplift rates; II) Activity of the Gondwanides Orogeny – could have caused regional uplift of the SRS in response to compressive stresses in the SW margin of Gondwana. Protracted residence at temperatures ca. 60-70°C is observed for the same samples throughout the Mesozoic, with some of them suggesting gentle reheating around 100 Ma, which might be linked to an increase of crustal heat flux in response to Gondwana break-up magmatism. Samples from São Gabriel terrane went through the PRZ since the Devonian and indicate a long residence time in the PRZ and steady rates of cooling.

A4.4 49º Congresso Brasileiro de Geologia

49º Congresso Brasileiro de Geologia
20 a 24 de agosto de 2013 – Rio de Janeiro

Evolução Fanerozoica do Escudo Sul-Rio-Grandense: Modelos Termocronológicos de Baixa Temperatura

Pacífico Machado, J.S.L.¹; Jelinek, A.R.¹; Biçca, M.M.¹; Stephenson, R.²; Macdonald, D.I.M.²

¹Universidade Federal do Rio Grande do Sul; ²University of Aberdeen

RESUMO: O presente estudo busca elucidar a evolução termotectônica do Escudo Sul-Rio-Grandense (ESRG) através de métodos termocronológicos de baixa temperatura. Situado no extremo sul do Brasil, o ESRG consolidou-se durante o ciclo orogênico Brasiliano (Neoproterozoico), a partir da colisão dos crátões Rio de La Plata, Congo e Kalahari, durante a formação do Gondwana Ocidental. Zonas de cisalhamento regionais com direções NE-SO e NO-SE seccionam o ESRG em quatro terrenos tectonoestratigráficos Proterozoicos: 1) Taquarembó (SO), 2) São Gabriel (NO), 3) Tijucas (centro) e 4) Pelotas (L). Sequências vulcâno-sedimentares remanescentes da Bacia do Camaquá (Ediacarano-Cambriano) recobrem parcialmente o ESRG, o qual também é limitado ao norte e oeste pela Bacia do Paraná (Paleo-Mesozoica), e ao leste pela Bacia de Pelotas (Meso-Cenozoica). Após sua formação, o ESRG passou por um longo período de relativa quiescência, sendo novamente afetado por eventos tectônicos mais intensos durante a abertura do Oceano Atlântico (Jurássico-Cretáceo). Foram coletadas amostras do embasamento de todos terrenos – principalmente de granitoides Neoproterozoicos – para análises por traços de fissão (TFA) e (U-Th)/He (HeA) em apatita. Esses métodos registraram o comportamento termotectônico das rochas nos quilômetros superiores da crosta (<5km), sendo que as idades obtidas correspondem à época que essas apatitas estiveram submetidas a temperaturas entre ca. 110-45°C (zona de retenção parcial – ZRP). Foram analisadas 17 amostras: 14 idades TFA provenientes dos terrenos 1, 3 e 4 apresentam o mesmo intervalo de idades, entre 108.5 ± 5.4 e 205.1 ± 20.5 Ma. Contudo, as três idades TFA obtidas no terreno São Gabriel (2) variam de 295.4 ± 14.8 a 310.11 ± 27.9 Ma. As idades TFA do ESRG apresentam uma correlação direta com a altitude e continentalidade, e inversa em relação ao teor de urânio dos cristais. Análises HeA realizadas em 40 apatitas de 13 diferentes amostras apresentaram idades concentradas entre o Permiano e o Cretáceo, apesar de uma dispersão por todo Fanerozoico. Tal comportamento é comum para idades HeA em regiões cratônicas – com estabilidade tectônica e térmica – onde as rochas residem por longos períodos na ZRP. Ademais, a variação nas idades HeA é potencializada devido às diferenças no teor de urânio e danos na estrutura das apatitas, entre outros fatores. As histórias térmicas modeladas sugerem um processo de exumação lento e gradual para o ESRG, iniciando a passagem pela ZRP durante o Permiano para os terrenos 1, 3 e 4, com variações locais. Esse período corresponde a dois eventos regionais: i) Fim da glaciação do Gondwana, que provocou o soerguimento das rochas devido à recuperação isostática, expondo o embasamento e acelerando os processos erosionais; ii) Orogênesis Gondwanides, que pode ter causado um soerguimento regional em resposta a compressão na margem SÔ do Gondwana. Os modelos também demonstraram que esses terrenos permaneceram na ZRP durante todo Mesozoico, sendo que algumas amostras sugerem um leve reaquecimento por volta de 100 Ma, que pode estar ligado ao extenso magmatismo durante a separação do Gondwana. Modelos das amostras do terreno 2 indicam um soerguimento monótono desde o Devoniano, a uma taxa constante e longo período de residência na ZRP.

PALAVRAS-CHAVE: TERMOCRONOLOGIA, MODELAGEM, ESCUDO SUL-RIO-GRANDENSE

A4.5 EGU General Assembly 2019

Geophysical Research Abstracts
 Vol. 21, EGU2019-3563, 2019
 EGU General Assembly 2019
 © Author(s) 2019. CC Attribution 4.0 license.



Thermotectonic effects of West Gondwana breakup on the southernmost Mantiqueira Province, Brazil, revealed by fission tracks and (U-Th)/He

Joao Machado (1,2), Randell Stephenson (1), Andrea Jelinek (2), and Marcos Bicca (2)

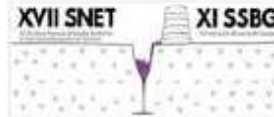
(1) School of Geosciences, Geology and Petroleum Geology, University of Aberdeen, Aberdeen, United Kingdom
 (j.luiz.machado.18@abdn.ac.uk), (2) Instituto de Geociências, Universidade Federal do Rio Grande do Sul, Porto Alegre, Brazil

Low-temperature thermochronometry has improved the understanding of the evolution of the Mantiqueira Province in the Brazilian passive margin. Most of the published investigations were conducted in the SE of the province, while the region further south, the Sul-Rio-Grandense Shield (SRGS), has had limited attention. Through the joint use of apatite fission tracks (AFT) and (U-Th)/He analysis in apatite (AHe) and zircon (ZHe), this study evaluates the thermotectonic evolution of the SRGS and the effects of the breakup of Gondwana. The SRGS was formed during the Brasiliano/Pan-African Orogeny (Neoproterozoic), after the collision of the Rio de La Plata, Congo and Kalahari cratons. Four main Proterozoic tectonostratigraphic terranes, limited by NE-SW and NW-SE shear zones, compose the SRGS: 1) Taquarembó (SW), 2) São Gabriel (NW), 3) Tijucas (central) and 4) Pelotas (E). These are partially covered by the Camaquã Basin (Late Ediacaran-Cambrian), and limited to the north and west by the intracontinental Paraná Basin (Paleo-Mesozoic), and to the east by the Atlantic Pelotas Basin (Meso-Cenozoic). Analysed samples, collected from the four terranes and the Camaquã Basin, resulted in 18 AFT, 43 AHe and 30 ZHe ages. Thirteen sites in terranes 1, 3 and 4 have similar AFT central ages, ranging from 139.9 ± 17.2 to 205.1 ± 19.7 Ma (early Jurassic-early Cretaceous). AFT ages from terrane 2 are late Carboniferous, while the Camaquã Basin has one early Permian and another early Jurassic age. The mean track length of confined tracks from the SRGS range from 10.7 ± 0.2 μm to 12.8 ± 0.2 μm , with a normal or negatively skewed distribution. AHe ages, obtained from thirteen locations, present a wide dispersion, although 70% of the mean AHe ages are Mesozoic. Similar dispersion has been reported in other cratonic regions, where apatites remained for long periods in the partial retention zone. The relation between AHe ages, eU and crystal radius is not clear. Mean ZHe ages from three sites in terrane 4 are early Permian, and present a negative correlation with eU. Terrane 2 and Camaquã Basin mean ZHe ages are Devonian. Inverse thermal modelling indicates a Devonian-Carboniferous cooling phase in the west of the SRGS, which is time correlated with two events affecting the surface dynamics of southernmost Brazil: I) end of Gondwana glaciation, which led to a regional uplift due to isostatic rebound and exposed basement rocks to weathering, raising erosion/uplift rates and II) Gondwanides Orogeny, that could have caused regional uplift of the SRGS in response to compressive stresses at the SW margin of Gondwana. A major event affects most of the SRGS between the Permian and Jurassic, slowly cooling rocks from ca. 110°C to 60°C , and is likely related to lithosphere uplift and thinning preceding Gondwana breakup and the onset South Atlantic Ocean opening (early Cretaceous). Samples from terrane 4, closer to the coast, suggest a subtle reheating after this event, probably linked to a geothermal disturbance syn- to post-breakup. A final cooling episode leading to surface temperatures affects the whole SRGS after Paleocene.

A4.6 XVII Simpósio Nacional De Estudos Tectônicos



XVII SIMPÓSIO NACIONAL DE ESTUDOS TECTÔNICOS
XI INTERNATIONAL SYMPOSIUM ON TECTONICS
XI SIMPÓSIO SUL-BRASILEIRO DE GEOLOGIA
26 a 29 de maio de 2019 | Bento Gonçalves - RS - Brasil



Evolução térmica do embasamento sul-Rio-Grandense e Uruguai investigada através de termocronômetros

João Pacifico Silveira Luiz Machado^{1,2}, Andréa Ritter Jelinek², Marcos Muller Bicca², Randell Stephenson¹

¹ University of Aberdeen, j.luizmachado.18@abdn.ac.uk

² Universidade Federal do Rio Grande do Sul, joao.machado@ufrgs.br

Através do uso de termocronômetros de baixa temperatura, o presente estudo busca investigar o comportamento térmico do embasamento cristalino Sul-Rio-Grandense (RS) e Uruguai (UR). Análises de traços de fissão em apatita (TFA) e de (U-Th)/He em apatitas (HeA) e zircões (HeZ) foram realizadas em 40 localidades, a fim de revelar fases de resfriamento/aquecimento na região e suas associações com eventos de formação do Gondwana Ocidental (Neoproterozoico-Paleozoico) e a abertura do Oceano Atlântico (Cretáceo). A região de estudo consolidou-se a partir da colisão dos cráttons Rio de La Plata, Congo e Kalahari, durante o ciclo Brasiliano (Neoproterozoico), que provocou o desenvolvimento do Cinturão Dom Feliciano entre os cráttons. Zonas de cisalhamento regionais, de direção NE-SO e NO-SE, seccionam a região em distintos terrenos tectonoestratigráficos pré-Cambrianos, e condicionaram a posterior ruptura do Gondwana. No RS foram obtidas 18 idades TFA, 43 HeA e 30 HeZ. A porção leste do RS apresenta as idades TFA mais jovens, variando entre 108 ± 6 e 203 ± 21 Ma (Cretáceo Inferior – Triássico Superior), enquanto que a porção oeste exibe idades no intervalo entre 200 ± 34 e 302 ± 31 Ma (Jurássico Inferior – Carbonífero). As idades HeA de cristais individuais apresentam grande dispersão, mesmo intra-amostra; contudo 70% das idades médias no RS são Mesozoicas. Dispersão similar em idades HeA tem sido observada em outras regiões cratônicas, onde as apatitas permaneceram por longos períodos a temperaturas $<110^{\circ}\text{C}$ e acumularam grande quantidade de danos radioativos. As idades médias HeZ da porção leste do RS são essencialmente Permianas, enquanto que a região oeste apresenta idades Devonianas. Histórias térmicas modeladas indicam uma fase de resfriamento Devoniana – Carbonifera no oeste do RS, a qual pode ser temporalmente relacionada a distintos eventos afetando a geodinâmica da região: 1) fim da glaciação do Gondwana, provocando um soerguimento regional causado pelo reajuste isostático crustal após o degelo, e expondo o embasamento a processos erosivos, e 2) ciclos orogênicos ocorrendo na margem Gondwana, causando um soerguimento local em resposta à compressão no SO do megacontinente. Uma fase de resfriamento mais abrangente ocorre no RS entre o Permiano e o Jurássico, provavelmente relacionada ao afinamento litosférico e soerguimento crustal precursores ao rompimento do Gondwana e à abertura do Oceano Atlântico. Modelos térmicos de amostras do leste do RS sugerem um sutil reaquecimento após a ruptura do Gondwana, provavelmente relacionado a uma alteração geotérmica na margem durante a ruptura e ao magmatismo Serra Geral. Uma fase final de resfriamento afeta todo o RS após o Paleoceno. Dados preliminares do UR revelam 19 idades TFA Mesozoicas, sendo as mais jovens concentradas na região costeira. As idades HeA e HeZ obtidas no UR apresentam maior dispersão quando comparadas às do RS. Imagens de catodoluminescência em apatitas do UR revelam cristais bastante fraturados, cujo fraturas ocasionalmente foram preenchidas por material potencialmente rico em urânio. O acúmulo de danos cristalinos e a possível recristalização mineral nas fraturas são fatores que influenciam a geração e difusão do He radiogênico, e consequentemente as idades HeA. Uma avaliação dos resultados de HeA e HeZ do UR, aliada à modelagem térmica das amostras, poderá revelar se a evolução térmica do embasamento Uruguai é semelhante àquela observada no Rio Grande do Sul.

Goldschmidt2019 Abstract

**Southernmost Brazil and Uruguay
basements thermal evolution
investigated with low temperature
thermochronometry**

J. P. S. L. MACHADO^{1,2*}, A. R. JELINEK², M. M. BICCA²,
R. STEPHENSON¹

¹University of Aberdeen, Aberdeen, United Kingdom

(*correspondence: j.luizmachado.18@abdn.ac.uk)

²Universidade Federal do Rio Grande do Sul, Porto Alegre,
Brazil

Through the joint use of apatite fission tracks (AFT) and (U-Th)/He analysis in apatite (AHe) and zircons (ZHe), we evaluate the Phanerozoic thermotectonic evolution of the Rio Grande do Sul (RS) and Uruguay (UY) shields. These crustal segments were assembled during the multicollisional Brasiliano/Pan-African Orogeny (NeoP), West Gondwana formation. Regional shear zones cut through them and conditioned the subsequent Atlantic Ocean opening (Jur-Cre) on the eastern margins of the shields. In RS we obtained 18 AFT, 43 AHe and 30 ZHe ages. The eastern margin presents younger AFT ages (108 ± 6 to 203 ± 21 Ma) when compared to the western hinterland (200 ± 34 to 302 ± 31 Ma). AHe single crystal ages present a wide range, even intrasample, although 70% of them are Mesozoic. Such variability is a common signature of cratonic regions, where apatites remained for long periods at $T < 110^\circ\text{C}$ and experienced complex thermal histories. Mean ZHe ages from the eastern RS are Permian, while the west presents Devonian ages. In UY we obtained 19 AFT, 45 AHe and 40 ZHe ages. UY AFT ages are Mesozoic, being younger towards the margin. UY He ages present similar dispersion to what is observed in the RS. Inverse thermal modelling indicates a Devonian-Carboniferous cooling phase in the west of the RS, time correlated with two events affecting southernmost Brazil: I) end of Gondwana glaciation, possibly leading to a regional uplift due to isostatic rebound, exposing basement rocks to weathering and raising erosion rates; II) Gondwanides Orogeny, that might have caused local uplift in response to compressive stresses at the SW margin of Gondwana. A major event affects most of the RS from the Permian to Jurassic, cooling rocks from 110°C to 50°C , likely related to lithosphere uplift and thinning preceding Gondwana breakup and Atlantic Ocean opening. Samples from the eastern RS suggest a subtle reheating afterwards, probably linked to a geothermal disturbance related to Gondwana rifting and associated magmatism. Final cooling to surface temperature affects the whole RS after the Paleocene. Future modelling will test whether UY had a similar thermotectonic history as the RS.